ABSTRACT

Title of Document:	ENTROPY CONSIDERATIONS APPLIED TO SHOCK UNSTEADINESS IN HYPERSONIC INLETS.
	Gillian Mary Harding Bussey, Ph.D, 2012
Directed By:	Professor Mark J. Lewis, Department of Aerospace Engineering

The stability of curved or rectangular shocks in hypersonic inlets in response to flow perturbations can be determined analytically from the principle of minimum entropy. Unsteady shock wave motion can have a significant effect on the flow in a hypersonic inlet or combustor. According to the principle of minimum entropy, a stable thermodynamic state is one with the lowest entropy gain. A model based on piston theory and its limits has been developed for applying the principle of minimum entropy to quasi-steady flow. Relations are derived for analyzing the time-averaged entropy gain flux across a shock for quasi-steady perturbations in atmospheric conditions and angle as a perturbation in entropy gain flux from the steady state. Initial results from sweeping a wedge at Mach 10 through several degrees in AEDC's Tunnel 9 indicates the bow shock becomes unsteady near the predicted normal Mach number. Several curved shocks of varying curvature are compared to a straight shock with the same mean normal Mach number, pressure ratio, or temperature ratio. The present work provides analysis and guidelines for designing an inlet robust to off-design flight or perturbations in flow conditions an inlet is likely to face. It also suggests that inlets with curved shocks are less robust to off-design flight than those with straight shocks such as rectangular inlets. Relations for evaluating entropy perturbations for highly unsteady flow across a shock and limits on their use were also developed. The normal Mach number at which a shock could be stable to high frequency upstream perturbations increases as the speed of the shock motion increases and slightly decreases as the perturbation size increases. The present work advances the principle of minimum entropy theory by providing additional validity for using the theory for time-varying flows and applying it to shocks, specifically those in inlets. While this analytic tool is applied in the present work for evaluating the stability of shocks in hypersonic inlets, it can be used for an arbitrary application with a shock.

ENTROPY CONSIDERATIONS APPLIED TO SHOCK UNSTEADINESS IN HYPERSONIC INLETS.

By

Gillian Mary Harding Bussey.

Dissertation submitted to the Faculty of the Graduate School of the
University of Maryland, College Park, in partial fulfillment
of the requirements for the degree of
Doctor of Philosophy
2012

Advisory Committee:
Professor Mark J. Lewis, Chair
Associate Professor Kenneth Yu
Professor Ashwani Gupta
Associate Professor James Baeder
Associate Professor Christopher Cadou

Dedication

I'd like to dedicate this to my parents Ian and Lori Harding for all their support through my years at MIT and during my time in graduate school here at the University of Maryland.

Acknowledgements

I want to thank my faculty advisor Dr. Mark Lewis for all of his encouragement, support, all that he taught me, and his friendship that helped me successfully pursue this work, made my time at College Park enjoyable, and already achieve success in my career. He has been one of the best mentors I could ever hope for and an even better friend during my time here. In addition, I would like to thank the committee members Dr. Kenneth Yu, Dr. Chris Cadou, Dr. James Baeder, and Dr. Ashwani Gupta for serving on my dissertation committee.

I would also like to extend thanks to Joe Coblish and the staff at Arnold Engineering Development Center (AEDC) Tunnel 9 who provided me data from one of their experiments. I'd particularly like to thank Dan Marren for the guidance and expertise he has provided to me during my time at University of Maryland.

I appreciate the support my employer provided in allowing me to spend a year at Maryland attending classes and conducting research and putting up with my strange hours while I continue my education. I hope they think it's been well worth it!

I would also like to thank the fellow members of my research group over the last 5 years (Josh Johnson, Jamie Meeroff, Adam Beerman, Kevin Ryan, Jeremy Knittel, Leslie Eurice, Neal Smith, and Vijay Ramasubramanian) for their advice, knowledge, laughs, and support.

Finally, my husband George is owed thanks for his putting up with my long hours.

Table of Contents

List of Tables

List of Figures

List of Symbols

S = Entropy

$\dot{S}$ = Time rate of change of entropy

t = Time

J_{th} = Thermal flux

X_{th} = Thermal force

J_{m} = Mass flux

X_{m} = Force due to mass diffusion

T = Temperature or oscillation period

p = Pressure

μ = Chemical potential or viscosity

ν = Specific volume

n = Number of moles

E = Energy

h = Specific molar enthalpy

G = Gibbs Free Energy

N = Number of species

ρ = Density

L_{ij} = Phenomenological coefficient for i and j

k = Thermal conductivity

R = Universal gas constant

c_{i} = Concentration of species i

D = Diffusivity

A_i = Chemical affinity of *i*

ξ_i = Degree of advancement of chemical reaction

ν_i = Rate of reaction of species *i*

θ = Wedge or turning angle

u = Velocity perpendicular to shock

μ_i = Thermodynamic or chemical potential of species *i*

μ = Viscosity

a = Speed of sound

a_1 = Upstream speed of sound

M = Mach number

M_n = Normal Mach number

M_1 = Upstream Mach number

M_p = Pseudo-Mach number

M_2' = Downstream Mach number in terms of upstream conditions

$\hat{M}$ = Mean of time-varying Mach number

$\hat{P}$ = Mean of time-varying pressure ratio

$\hat{\rho}_i$ = Mean of time-varying upstream (1) or downstream (2) density

P' = Unsteady component of pressure ratio

M' = Unsteady component of Mach number

ρ' = Unsteady component of density

P =Pressure ratio across shock

γ = Ratio of specific heats

β = Shock angle

C_v = Specific heat at constant volume

w = Angular frequency

ε, ϕ = Perturbation size

L =Shock volume distance

Chapter 1: Introduction

1.1 Motivation

Despite advances in computational methods for analyzing hypersonic flow problems, an analytic method to characterize unsteady hypersonic flows can provide additional insight into the performance and design of hypersonic vehicles and propulsion systems. In the present work, an analytical method is developed based on the principle of minimum entropy for determining the stability of shocks to flow perturbations and evaluated, and then applied to the problem of designing a scramjet inlet.

Unsteady or periodic shock-wave motion can have a significant effect on the flow in a hypersonic inlet or scramjet combustor. A scramjet is a supersonic combustion ramjet with supersonic flow entering the combustor that operates at Mach numbers typically above Mach 4.5 -- when ramjets lose their ability to provide thrust. An efficient inlet would be a crucial part of the operation of a scramjet-powered hypersonic vehicle and must provide efficient compression, enough mass flow, a high enough static temperature ratio, and generally uniform flow into the combustor with minimal total pressure losses. Because of the high drag, total pressure drop, and mixing losses typical in a scramjet combustor, inlet losses due to unsteady effects or poor inlet design can outweigh any thrust gains in the combustor. Numerous types of inlets have been researched for applications to hypersonic flow, with so-called "two-dimensional" inlets favored in most flight-tested designs. Additional research has focused on three-dimensional inward turning inlets -- specifically an inlet with a rectangular capture area and a circular or elliptical combustor shape or axi-symmetric Busemann inlets.

Previous work has shown that three-dimensional inlets that use a rectangular capture area with a circular combustor provide several advantages over axi-symmetric Busemann or two-dimensional rectangular inlets. The Busemann inlet is created from a flow field that obeys the Taylor–Maccoll equations for axi- symmetric flow. These inlets have several benefits including very high pressure recovery, enabling the use of a circular combustor, and are based on an inviscid flow field that is defined analytically. Some drawbacks include sensitivity to off-design conditions and their longer lengths, resulting in high viscous losses. Rectangular inlets have comparatively reduced boundary layer losses because of their shorter length and can stack without flow leakage but match to a rectangular combustor, which has several disadvantages over a circular or elliptical combustor. Circular combustors weigh less; have a lower wetted surface and hydraulic diameter; reducing drag and viscous effects in the combustor and fewer problems due to hypersonic corner flow.

Inlets with a rectangular capture area and circular combustor can offer advantages from each type of inlet without some of the disadvantages. The curved shocks in inward turning and axi-symmetric inlets have a higher entropy gain than a straight shock for the case of steady flow in similar conditions. This research will use entropy considerations to explore which types of curved shocks, if any, are inherently more forgiving to flow perturbations and off-design effects.

Changes in the flow at the capture plane of the inlet can cause inlet unstart as well as large changes in the quality of the flow downstream in the combustor.[76] An unstart in a hypersonic inlet results from a mismatch in the mass flow entering the inlet and downstream in the engine. An inlet unstart is a very unsteady and violent phenomena that typically results in an unsteady normal shock wave in the inlet, increased total pressure losses, viscous losses, flow separation, and insufficient mass flow to the engine. As the flow is perturbed from its design conditions, either by changes in angle-of-attack, turns, or travel through non-uniformities, the shock angles can change. If the shock angle increases such that the shock does not intersect the inlet, spillage can occur leading to increased vehicle drag and decreased mass flow into the combustor. On the other hand, if the shock moves inside the inlet, shock boundary-layer interactions can cause flow separation and intense localized heating. Control of the shock position on or near the cowl is thus desired to prevent destructive heating, separation losses, and maintain high enough airflow into the inlet. Understanding under what circumstances the flow is steady or stable to slight perturbations in a given inlet is therefore useful in designing scramjet inlets.

The principle of minimum entropy suggests that entropy considerations can determine whether a shock can be stable to slight perturbations. This work examines the validity of the principle of minimum entropy as a tool for such using analysis and experimental data. Assuming that the principle of minimum entropy can be applied to time-varying flows across shocks, this work compares the stability of shocks of varying curvature in a range of inlet types. Response to high and low frequency perturbations in several flow parameters a scramjet vehicle might face is also examined. A model is developed to explain the validity of methods used to compare the entropy gain to the steady state for quasi-steady shocks and to find the limits of the quasi-steady approximation with this model. A model and its limits are derived for high frequency density perturbations.

The present work provides analysis and guidelines for designing an inlet that is robust to off-design flight or likely perturbations in flow conditions. It also suggests that inlets with curved shocks are less robust to off-design flight conditions than those with straight shocks such as rectangular inlets. The present work advances the theory of the principle of minimum entropy theory for time-varying flows with application to shocks, specifically those in supersonic inlets.

1.2 Principle of Minimum Entropy

1.2.a Principle of Minimum entropy theory

The current work uses entropy considerations based on the principle of minimum entropy as developed by Prigogine[1] to analyze the stability of shocks in hypersonic inlets to flow perturbations. According to Prigogine, a stationary non-equilibrium state is characterized by an extremum principle, which states that in the stationary state, the entropy production has its minimum value compatible with the external constraints imposed on the system. Non-equilibrium thermodynamics deals with systems that are not in thermal equilibrium and/or changing in time, often because of fluxes of matter and energy between systems or chemical reactions. The principle of minimum entropy is the thermodynamic equivalent of other variational principles in physics such as the principle of least-action in mechanics and Fermat's principle in optics that light follows the shortest optical length connecting two points.

Consider the entropy production per unit time of a system with mass diffusion and heat flow, such as two vessels at different temperatures connected with a thin capillary or porous wall

$$\frac{dS}{dt} = J_{th}X_{th} + J_{m}X_{m} > 0 \tag{1}$$

as required by the Second Law of Thermodynamics, where J_m and J_{th} are the fluxes associated with diffusion and heat flow, respectively, and X_m and X_{th} are the corresponding thermodynamic forces. A thermodynamic force is an extensive variable like pressure *P* that forces a change in its conjugate intensive thermodynamic variable, which for pressure is volume *V*. The product of the thermodynamic force and a change in its conjugate equal work, such as $dU = PdV$. For a general system, the time rate of change of entropy can be written as $\dot{S} = \sum_i J_i X_i > 0$. Generalized thermodynamic fluxes *J* are linearly related to thermodynamic forces *X*.

For the heat conduction and mass diffusion system, those forces and fluxes are,

$$X_{th} = \Delta\left(\frac{1}{T}\right) = -\frac{1}{T^2}\Delta T$$
$$X_m = -\frac{(\Delta\mu_i)_T}{T} = -\frac{v_i}{T}\Delta p \tag{2}$$

$$J_{th} = \frac{dE}{dt} - h\frac{dn}{dt}$$
$$J_m = \frac{dn}{dt} \tag{3}$$

where μ_i is the chemical potential of species *i*, v_i is the specific volume, E is the energy, h is the specific molar enthalpy, and n is the number of moles. A chemical potential can be described as a potential energy that can be released or used up in a reaction and can be described as the change in Gibbs free energy *G*, as a result of a change in the number of that species with temperature, pressure, and the number of other species kept constant, $\mu_i = \left(\frac{\partial G}{\partial N_i}\right)_{T,P,N_{j\neq i}}$. For this example, entropy and Equation 1 can be written as,

$$dS = \frac{1}{T}du - \frac{\mu_i}{T}d\rho \tag{4}$$

$$dS = X_{th}(dE - hdn) - X_m d\rho \rightarrow \frac{dS}{dt} = J_{th}X_{th} + J_m X_m \tag{5}$$

where ρ is density and *u* is the internal energy and Equation 4 is the expression of entropy for an open system of a fixed size that can exchange heat and matter with an external reservoir.

The property of a stationary state of a non-equilibrium system being in a state of minimum entropy production is only valid if three general constraints are imposed:

1. **Linear:** A non-equilibrium thermodynamic process is characterized as linear if the generalized thermodynamic fluxes J_i (such as heat flow J_{th}, mass diffusion J_m, fluid deformation) are linearly related to the generalized thermodynamic forces X_i (such as temperature X_{th} or pressure gradient as in Equation 2 or chemical potential gradient X_m).

2. **Constant phenomenological coefficients:** The system must also be such that the phenomenological coefficients L_{ij}, which might be related to heat or electrical conductivity, are constants. For most real systems, this is not true in general, but this holds if the overall gradients of thermodynamic variables are small enough such that the coefficients can be assumed to be constant.[2] Thus, the principle of minimum entropy can only be applied to systems near equilibrium. For compressible flows, including those containing shock waves, the system can be considered near equilibrium locally because of the large number of particles in the small regions of interest, according to Horne et al.[3]. Prigogine[4] and others have found that if a system is far from equilibrium or non-linear, the principles governing entropy production can be quite different. In fact, Ziegler[5] proposed that entropy production be maximized for systems far from equilibrium.

The phenomenological laws are[1,2]:

$$\begin{aligned} J_{th} &= L_{11}X_{th} + L_{12}X_{m} \\ J_{m} &= L_{21}X_{th} + L_{22}X_{m} \end{aligned} \tag{6a}$$

For a basic thermodynamic system with mass transport and heat diffusion,

$$\begin{aligned} J_{th} &= L_{thth}\nabla\frac{1}{T} + L_{thm}\nabla\frac{\mu_i}{T} \\ J_{m} &= L_{mth}\nabla\frac{1}{T} + L_{mm}\nabla\frac{\mu_i}{T} \end{aligned} \tag{6b}$$

From these relationships, well-known relationships for thermal conductivity and mass transport and their corresponding coefficients can be derived. If the mass transport is zero, the heat flux reverts to a version of Fourier's law of thermal conduction with $L_{thth} = kT^2$,

$$J_{th} = L_{thth}\nabla\frac{1}{T} = -k\nabla T \tag{6c}$$

If the thermal conduction is zero, the mass transport reverts to a version of Fick's law of diffusion with $L_{mm} = \frac{D_i c_i}{RT}$ and $X_{mi} = -\frac{1}{T}\nabla\mu_i$,

$$J_{m} = -\frac{Dc_i}{RT}\nabla\mu_i \tag{6d}$$

where *i* indicates the *i*-th species, *R* is the universal gas constant, *c* is the concentration of species-*i*, and *D* is the diffusivity.

Finally, from Onsager's relations, for the stationary state,

$$J_{m} = L_{21}X_{th} + L_{22}X_{m} = 0 \tag{7}$$

3. **Satisfy Onsager's reciprocal relations:** For coupled thermodynamic processes, Onsager's reciprocal relations for the phenomenological coefficients must

be satisfied. This requires that the "interference coefficients" L_{12} and L_{21} be equal. For the mass diffusion and heat flow system, this would require that the influence of the chemical potential or the difference in concentrations of a species X_m on the heat flux J_m is equal to that of the temperature gradient X_{th} on the mass diffusion flux J_m.

Using these three relations and constraints, we can derive that the stationary state is the state of minimum entropy production. Substitute Equation 6a for J_m and J_{th} into the equation for the time rate of change of entropy using $L_{12} = L_{21}$ from Onsager's reciprocity relations:

$$\frac{dS}{dt} = L_{11}X_{th}^2 + 2L_{21}X_{th}X_m + L_{22}X_m^2 > 0 \tag{8}$$

Take the derivative of this with respect to X_m at constant X_{th},

$$\frac{1}{2}\frac{\partial}{\partial X_m}\left(\frac{dS}{dt}\right)_{X_{th}} = L_{21}X_{th} + L_{22}X_m = J_m \tag{9}$$

which is J_m from the phenomenological laws in Equation 2 for a linear relation between the fluxes and forces. From Equation 3,

$$\frac{1}{2}\frac{\partial}{\partial X_m}\left(\frac{dS}{dt}\right)_{X_{th}} = L_{21}X_{th} + L_{22}X_m = J_m = 0 \tag{10}$$

for a stationary state where $J_m = 0$. This is equivalent to a minimum in entropy production

$$\frac{\partial}{\partial X_m}\left(\frac{dS}{dt}\right)_{X_{th}} = 0 \tag{11}$$

Note that because Equation 8 is a positive definite quadratic, this corresponds to a minimum.

In this work, it is postulated that, if a stationary state in a non-equilibrium system is a state of minimum entropy, then it should be stable to perturbations from that state, as deviations would increase the entropy production. According to Prigogine, a stationary state is one that has the lowest entropy production per unit time and is stable, as it cannot leave that state by a spontaneous irreversible change. Thus, slight perturbations from that state would result in the system returning to the stationary state. Prigogine shows that irreversible processes taking place in a non-equilibrium system always lower the production of entropy per unit time. A system in the state of lowest minimum entropy production - the stationary state - cannot spontaneously deviate from that state. If an external fluctuation is imposed on the system that brings it slightly away from the stationary state, the system will adjust to bring it back to its initial stable. This state can be referred to as a "stable state".

It can be show that a system that undergoes two thermodynamic changes can only decrease entropy production per unit time over time. Prigogine presents an example with two simultaneous chemical changes[1]

$$\frac{dS}{dt} = L_{11}\left(\frac{A_1}{T}\right)^2 + 2L_{12}\frac{A_1A_2}{T^2} + L_{22}\left(\frac{A_2}{T}\right)^2 > 0 \qquad (12)$$

where A_1 and A_2 are the chemical affinities of species 1 and 2. A chemical affinity of a species is an electronic property by which dissimilar chemical species are capable of forming compounds or reacting. With the assumption that the phenomenological coefficients L_{ij} are constant in time, taking the second derivative of entropy with respect to time produces,

$$\frac{1}{2}\frac{d^2S}{dt^2}=\left(L_{11}\frac{A_1}{T}+L_{12}\frac{A_2}{T}\right)\frac{d}{dt}\left(\frac{A_1}{T}\right)+\left(L_{12}\frac{A_1}{T}+L_{22}\frac{A_2}{T}\right)\frac{d}{dt}\left(\frac{A_2}{T}\right) \tag{13}$$

$$\frac{1}{2}\frac{d^2S}{dt^2}=v_1\frac{d}{dt}\left(\frac{A_1}{T}\right)+v_2\frac{d}{dt}\left(\frac{A_2}{T}\right) \tag{14}$$

where v_i is the rate of reaction of species *i*. The chemical affinities A_i can be expressed in terms of two independent physical variables, which are taken to be pressure *p* and temperature *T* in this example, and the degree of advancement or extent of the reaction ξ_1 and ξ_2 introduced by De Donder[6] such that

$$\frac{1}{2}\frac{d^2S}{dt^2}=\frac{v_1}{T}\left[\left(\frac{\partial A_1}{\partial \xi_1}\right)_{p,T}v_1+\left(\frac{\partial A_1}{\partial \xi_2}\right)_{p,T}v_2\right]+\frac{v_2}{T}\left[\left(\frac{\partial A_2}{\partial \xi_1}\right)_{p,T}v_1+\left(\frac{\partial A_2}{\partial \xi_2}\right)_{p,T}v_2\right] \tag{15}$$

The degree of advancement measures how far a chemical reaction has progressed or how much the reactant has turned into product, and is measured in units of moles. For a simple reaction $aA \Leftrightarrow bB$ where *a* and *b* are the stoichiometric coefficients of reactant A and product B, $\xi_A=\frac{\Delta n_A}{a}$. Because chemical affinities can be written as the partial derivative of the Gibbs free energy,

$$A_i=-\left(\frac{\partial G}{\partial \xi_i}\right)_{p,T} \tag{16}$$

$$\left(\frac{\partial A_1}{\partial \xi_2}\right)_{p,T}=\left(\frac{\partial A_2}{\partial \xi_1}\right)_{p,T}=-\left(\frac{\partial^2 G}{\partial \xi_1 \xi_2}\right)_{p,T} \tag{17}$$

Equation 13 can be written as,

$$\frac{1}{2}\frac{d^2S}{dt^2}=\frac{1}{T}\left(\frac{\partial A_1}{\partial \xi_1}v_1^2+2\frac{\partial A_1}{\partial \xi_2}v_1v_2+\frac{\partial A_2}{\partial \xi_2}v_2^2\right)<0 \tag{18}$$

This is true because $\frac{\partial A_i}{\partial \xi_j} < 0$ must be satisfied for $\Delta_i S < 0$ for fluctuations from an equilibrium state. If $\Delta_i S > 0$, then the state the system fluctuated from was not an equilibrium state, because the system would spontaneously move from that state to the state with higher entropy and thus not be an equilibrium state. This result is general and applies whether temperature, pressure, or degrees of advancement is the fluctuating parameter. Although this derivation was for a closed system, the same result and a similar logic apply for an open system.[1] The inequality in Equation 18 states that over time the entropy production per unit time always decreases.

The previous development suggests that, if an unsteady flow characterized by slight perturbations from a mean has a higher entropy production than the mean, then the system would tend to seek the steady solution. Likewise, if the perturbations result in the system having a lower entropy rise than the mean steady state solution, the steady state solution would not be a stationary equilibrium state and the system would favor unsteadiness. This suggests that the principle of minimum entropy may be applied to the characterization of some time-varying flows. Entropy considerations alone do not cause the unsteadiness, which would typically be caused either by changes in flight conditions, structural deflection, vibration of the vehicle, or combustion instabilities, but rather can be used to explain whether the perturbations in the flow is likely to decay into a steady-state or persist.

1.2.b Previous work using principle of minimum entropy production theory

The principle of minimum entropy has been successfully applied to several non-convective dissipative systems.[1,7,8] Initial work explored applying it to heat conduction or mass diffusion problems through analysis. Meijir and Edwards showed that it could be applied to a system with heat conduction with two levels for arbitrary deviations.[8] Tadmor's analysis shows that entropy solutions of gas dynamics equations satisfy the principle of minimum entropy[9]. Biot found that it applies for near-equilibrium processes.[10] Endre used variational calculus to show that the minimum entropy solution agreed with energy balance for linear and quasi-linear heat conduction.[11] Borovkov found the principle of minimum entropy agreed with entropy production in a mass diffusion and heat conduction problem with two containers at different temperatures connected with a small capillary tube and a heat conduction problem with a heat-conducting layer separating two reservoirs.[12] Researchers in other fields have shown that crystal formation in snow in glaciers[13], which is driven by mass diffusion introduced by thermal gradients, and the relation between photosynthesis efficiency and chloroplast transport properties in plants[14] can be explained by the principle of minimum entropy production. Henderson and Atkinson note that many of the examples such as where the principle of minimum entropy does not apply are cases where convection is present.[15]

Several researchers have also found flow across shock waves and some viscous flow phenomena agree with the principle of minimum entropy. Helmholtz showed Newtonian flow is characterized by a minimum of viscous dissipation[16].

Horne, Smith, and Karamcheti incorporated the principle of minimum entropy production rate to identify parallel-wall channel flow, irrotational flow, incompressible channel flow, and the cylindrical vortex flow as having minimally dissipative velocity distributions[17,18]. They also found that some features of irrotational, steady, viscous flow near an airfoil, such as the effect of trailing-edge radius on circulation, are compatible with the principle of minimum entropy.

The principle of minimum entropy could also be used to interpret the stability of amplitude disturbances in initially laminar, parallel shear flows[17]. Horne, Smith, and Karamcheti found that their results were consistent with experiment and linearized hydrodynamic stability theory[17]. Shi and Zhou also found application of the principle of minimum entropy to turbulent flow in local mechanical equilibrium[19]. Kalugin proposed a variational method based on the principle of minimum entropy for calculating two-dimensional supersonic turbulent separated flows[20].

Several types of supersonic flow problems result in multiple possible solutions - for example, a strong shock and a weak shock solution - based on the conservation. equations. Flow over a wedge with an angle less than the angle at which shock detachment occurs for a given Mach number can allow for either a strong or weak shock. Several such as Carrier[21] and Henderson and Atkinson[15] linearized the time-dependent Euler equations based on linearized Rankine-Hugoniot equations at the shock subjected to boundary conditions. However, these studies did not consider other boundary conditions and did not look at entropy conditions. Work by Morgan and Salas[22] for the same problem of supersonic flow over a wedge, Salas[23] for a shock interaction with an abrupt area change, and Li and Ben-Dor[24,25] for shock reflections showed that a solution based on the principle of minimum entropy was consistent with experimental observations and numerical results for steady or pseudo-steady flows, defined as varying the Mach number and angle such that the normal Mach number was constant.

Morgan and Salas examined the stability of shock waves attached to wedges and cones when either a strong or weak shock is possible based on boundary conditions[22]. They considered a two-dimensional wedge or cone placed in a uniform supersonic flow and restricted the wedge or cone angle to less than the angle corresponding to the detachment angle. Because the flow downstream of a shock is mathematically elliptic for the strong shock and hyperbolic for the weak shock, this suggests that the solution would depend on the boundary conditions. They imposed several boundary conditions including some that are varied to allow for strong shocks. They imposed a downstream pressure for the strong shock, as an imposed condition far downstream is necessary to close an elliptic problem. In order to make the problem tractable, they assumed the solution had conical similarity, which requires changes to the Euler equations that no longer allow for a downstream pressure as boundary condition. Thus, they required a specific pressure at the wall, but allowed the wall to move as long as the normal velocity component relative to it at each time was zero and the velocity at the wall vanished as the steady state was reached asymptotically. For the hyperbolic problem (weak shock), they fixed the wall and solved for the variation of pressure in time and for the elliptic (strong shock), they fixed the pressure but moved the wall. They numerically integrated the Euler equations with the conditions and boundary conditions provided and allowed the shock to move in time, while satisfying the Rankine-Hugoniot equations at each time step.

Morgan and Salas found that their results for the stability of strong or weak shocks attached to wedges and cones were consistent with the principle of minimum entropy. They found that for the wedge, the weak solution is stable for the fixed-wall boundary conditions, while the strong solution was not. The weak shock solution corresponds to a lower pressure rise across the shock and lower entropy gain. The weak shock was also stable for the cone with a fixed pressure boundary condition. Both solutions were stable for a wedge with a fixed pressure boundary condition. The most interesting result is for a strong shock on a cone because, for a given surface pressure, multiple values of the cone deflection angle exist. Their results showed that when a surface pressure is specified between the maximum value and that of a normal shock, the stable solution corresponds to cone deflections greater than the cone deflection angle, corresponding to the maximum surface pressure. Morgan and Salas provided an example of this, which is shown in Figures 1 and 2. For a fixed surface pressure of 4.675, a cone at 12 degrees or 38.35 degrees satisfies that boundary condition. Figure 1 is for a cone with an initial angle less than 12 degrees at the start of the numerical integration. Figure 2 is for a cone with an initial angle greater than 38.35 degrees. As shown in Figure 1, the solution diverges (not stable) as the shock waves become increasingly stable and in Figure 2, the solution converges (stable). For the strong shock solution on the cone, the stable solution, which has a larger cone deflection angle, is also the minimum entropy solution. Morgan and Salas found these results consistent with experimental observations.

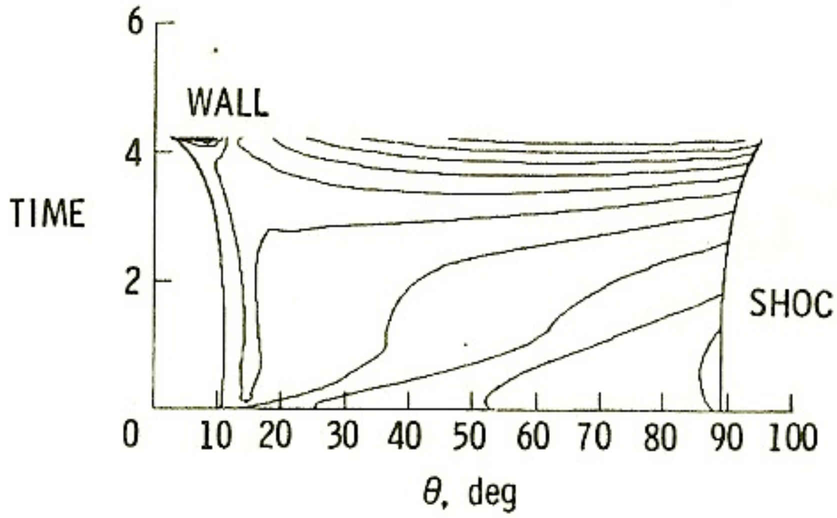

Figure 1.1 Convergence history and isobar pattern for a strong-shock solution with a fixed-pressure boundary condition for a starting cone-angle less than 12 degrees. The solution diverges as the shock waves become stronger[22].

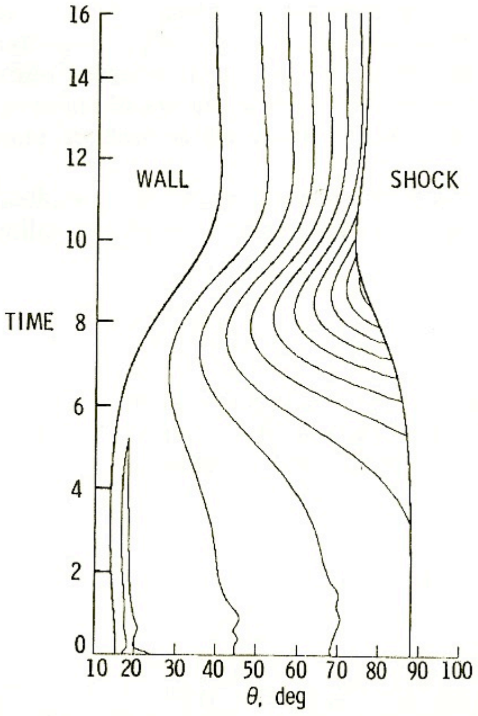

Figure 1.2 Convergence history and isobar patterns for strong-shock solution with fixed pressure boundary condition. The solution converges to the solution with the minimum entropy gain.

Salas[23] found that the solutions for the interaction of a shock wave with a channel of abrupt area change were consistent with the principle of minimum entropy production. This type of interaction may be applicable to the passage of a shock through a wire-mesh screen, the starting process in a supersonic inlet, and some phenomena that occur in pistons and jet engines. The solution of the conservation equations for this problem can include more than one wave pattern. Oppenheim, Urtiew, and Stern proposed that a minimum entropy production principle could resolve the problem to one solution[26]. Salas used a self-similar analytic model to map out the different wave patterns that occur in terms of incident shock strength and area ratio and verified his results by solving the time-dependent quasi-one-dimensional Euler equations. He found that the wave pattern that was actually observed where the conservation equations allowed for several possible solutions was in agreement with the principle of minimum entropy.

Li and Ben-Dor[24,25] applied the principle of minimum entropy to determining the solution to a shock reflection problem with multiple possible solutions. As indicated in Ben-Dor[24], there are multiple solutions possible for the problem of an oblique shock reflecting off a straight surface - either a weak or strong regular reflection or a Mach reflection - depending on the initial Mach number M_i and the wedge angle θ_w. Courant and Friedrichs[27] found that in the pseudo-steady case, a flow regime that occurs in closed reservoirs after the pressure transient have reached the reservoir boundaries, was constant three different types of Mach reflections could occur: A direct Mach reflection (D_iMR) results in the triple point moving away from the surface; a stationary-Mach reflection (StMR) results in the triple point moving parallel to the reflecting surface; and an inverse-Mach reflection (InMR) occurs when the triple point moves towards that surface. The inverse-Mach reflection is inherently unstable because the triple point will eventually meet the reflecting surface. These types of reflections are shown in Figure 3a-d.

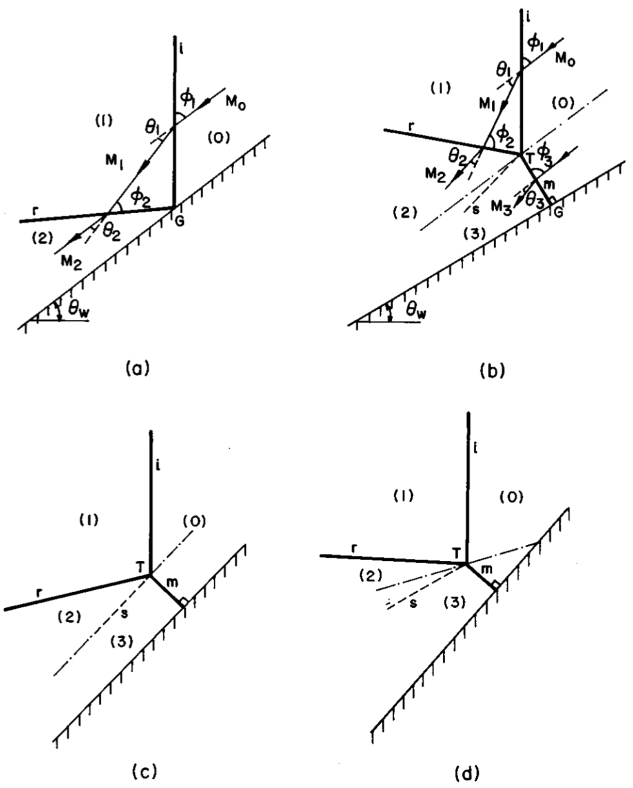

Figure 1.3. a.) Regular reflection b) Direct Mach reflection c) Stationary Mach reflection d) Inverse Mach reflection.[24]

Li and Ben-Dor employed an analytic approach using the principle of minimum entropy to choose the observed solution from among several mathematically possible solutions for the criteria for transition between shock reflection types and stability of regular reflections and Mach reflections in both steady and pseudo-steady flows. For the steady case, they develop an analytical approach to explaining experimental and numerical results found by Chpoun et. al.[28] and Vuillon, Zeitoun, and Ben-Dor [29] that contradict current understanding on regular reflection to Mach transition for steady flows.

To determine what solutions are possible for given wedge angles, there are several criteria for transitioning between different reflection types. The pressure deflection diagrams in Figure 1.4 show the possible reflections and cases with multiple solutions for different values of the angle of incidence ϕ_1. A solution of a regular reflection in the (P,θ) plane occurs at the intersection of the R-polar, reflection polar, with the P-axis where the boundary condition for regular reflection $\theta_1 - \theta_2 = \theta_3 = 0$ is satisfied. When the R-polar crosses the P-axis twice, the lower pressure value corresponds to a weak shock and the higher-pressure value, a strong shock. Locations where the incident and reflected polars intersect correspond to Mach reflections, with the type depending on whether the reflecting angle or flow deflection is negative (inverse), zero (stationary), or positive (direct).

When the R and I-polars, initial shock polar, intersect on the P-axis, either a stationary Mach reflection or regular reflection is possible. This only occurs for a specific range of reflection wedge angles. The highest wedge angle at which this occurs is θ_w^N. For $\theta_w > \theta_w^N$ only a regular reflection or inverse Mach reflection, which is unstable, is theoretically possible. The reflecting wedge angle can be decreased to less than θ_w^D, the detachment deflection angle, such that an attached solution and regular reflection is no longer possible because the R-polar no longer intersects the P-axis. (Figure 1.4d) Thus for reflection wedge angles $\theta_w^D \ge \theta_w \ge \theta_w^N$ both regular reflection and Mach reflections are possible. This situation is shown in Figure 1.4f. There is some dispute in the literature on what the exact transition criteria are between regular reflection and Mach reflection; this could be resolved with minimum entropy considerations.

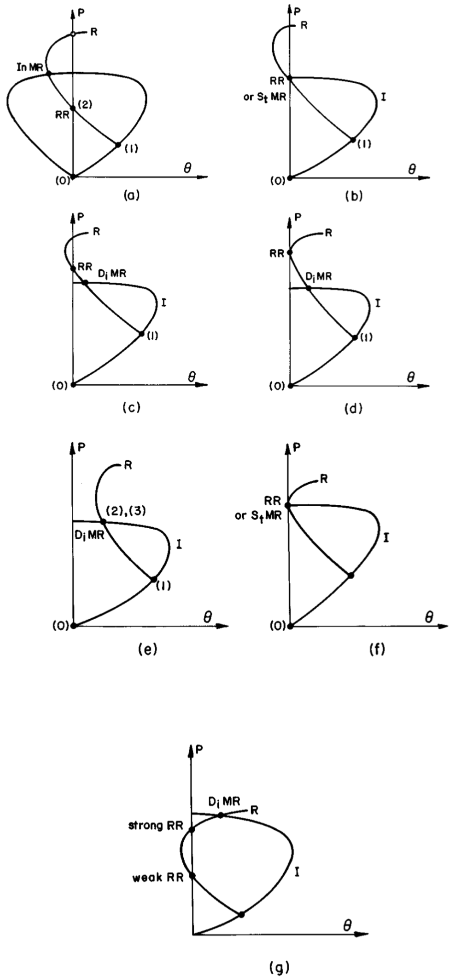

Figure 1.4. Possible I-R pressure deflection diagram combinations

These three solution domains can be further subdivided by incorporating criteria for strong or weak shocks. A point *K* where $\theta_w = \theta_w^N$ and $\theta_w = \theta_w^D$ lines as a function of the incident Mach number distinguishes between strong and weak shocks. This occurs at $M_i^k = 1.48$ and $\theta_w^k = 48.6$.

To determine the minimum entropy solution, Li and Ben-Dor used a control volume analysis for entropy for a volume containing a shock wave for steady uniform flow. The entropy production per unit time $\dot{S}$ inside the volume assuming uniform flow and the entropy change across the shock segment dy is

$$\dot{S} = \int_S \rho u \Delta s dy \tag{19}$$

$$\Delta s = C_v \left[\gamma \ln\left(\frac{2}{(\gamma+1)M^2 \sin^2\beta} + \left(\frac{\gamma-1}{\gamma+1}\right)\right) + \ln\left(\frac{2\gamma}{\gamma+1} M^2 \sin^2\beta - \frac{\gamma-1}{\gamma+1}\right)\right] \tag{20}$$

$$\sin^2\beta = \frac{1}{1+\left(dy/dx\right)^2} \tag{21}$$

where S is the curved shock surface, β is the shock angle, and γ is the ratio of specific heats. Applying the principle of minimum entropy requires that the change in entropy satisfies the following requirements:

$$\partial\dot{S}=0 \quad \text{and } \partial^2\dot{S} \geq 0. \tag{22a-b}$$

$$-\frac{\partial\Delta s}{\partial x} + \frac{\partial^2 \Delta s}{\partial y d(dx/dy)} = 0 \tag{23}$$

$$\partial^2\dot{S} = \frac{G(\gamma, M_i, dx/dy)}{H(\gamma, M_i, dx/dy)} \geq 0 \tag{24}$$

Equations 23 and 24 are the Euler-Lagrange equation and Legendre condition resulting from calculus of variations. Equation 24 is automatically satisfied because the entropy change across the shock does not depend on x or y.

Although this method was obtained from equations for a steady shock wave reflection, it can be applied for a pseudo-steady case under certain constraints. The unsteady case is limited to constant-velocity incident shock waves (i.e. the shock angle and Mach number is varied such that incident Mach number M_i is constant) and made steady by a Galilean transformation where θ_w is the wedge angle:

$$\theta_w = \frac{\pi}{2} - \phi_1 \text{ and } M_i = M_0 \sin\phi_1 \qquad \text{(25a-b)}$$

Following from solving for Equation 20 such that Equation 22a and b are satisfied, there exists a line $\theta_w = \theta_w^*$. Below this line, regular reflections are unstable, according to the principle of minimum entropy. This line follows the $\theta_w = \theta_w^D$ line until some point Q where it diverges above it. This creates a small region in the dual-solution domain $M_i \geq M_i^Q$ where the strong regular reflection is unstable but a Mach reflection is stable.

Incorporating minimum entropy considerations, Li and Ben-Dor characterized the stability of solutions in the small region in dual solution domain where $\theta_w^D \leq \theta_w \leq \theta_w^*$ and $M_i \geq M_i^Q$. Because strong stationary Mach reflections look like regular reflections, they can also be considered stable along the line $\theta_w = \theta_w^N \geq \theta_w^*$ and $M_i \geq M_i^k$ where regular reflections are considered stable. For the case of a strong direct Mach reflection, because the Mach number M_o is smaller than that for the case of a stationary Mach reflection and because a direct Mach reflection is obtained with a smaller reflecting wedge angle, the pressure behind a direct Mach reflection and the angle of incidence of the reflected shock ϕ_2 is smaller. Based on the principle of minimum entropy, if a strong stationary Mach reflection is stable, $\phi_2^{st} \le \phi_2^*$ where $G(\gamma, M_i, \phi_2^*) = 0$, then the strong direct Mach reflection is stable.

A similar analysis can be done to show that a weak direct Mach reflection is unstable above the detachment angle. Looking at a shock polar solution of a weak direct Mach reflection in Figure 1.4g, this solution has a higher pressure and reflected incidence angle than the strong regular reflection solution which was shown by Li and Ben-Dor[24] to be unstable because $\phi_2^{sRR} > \phi_2^*$. Thus, if the strong regular reflection is shown to be unstable by minimum entropy considerations, so is the weak direct Mach reflection.

Finally, in the small region in dual solution domain where the principle of minimum entropy is applied $\theta_w^D \le \theta_w \le \theta_w^*$ and $M_i \ge M_i^Q$, only the strong direct Mach reflection is stable, even though the wedge angle is higher than the detachment angle. The new criteria for transition from strong regular reflections to strong Mach reflections for $M_i > M_i^Q$ is $\theta_w = \theta_w^*$ and transition from strong Mach reflections and strong regular reflections is $\theta_w^* \le \theta_w \le \theta_w^N$.

A summary of what solutions are stable and in what domain is provided in Figure 1.5 and Table 1.1

Regular reflection			Mach reflection		
θ_w	$1 < M_i < M_i^Q$	$M_i > M_i^Q$	θ_w	weak $1 < M_i < M_i^k$	strong $M_i > M_i^k$
$\theta_w > \theta_w^*$	Stable	Stable	$\theta_w > \theta_w^*$	Unstable	Unstable
$\theta_w^* > \theta_w > \theta_w^D$	N/A	Unstable	$\theta_w^N \geq \theta_w > \theta_w^D$	Unstable	Stable
$\theta_w < \theta_w^D$	Theoretically impossible	Theoretically impossible	$\theta_w < \theta_w^D$	Stable	Stable

Table 1.1 Shock wave configurations

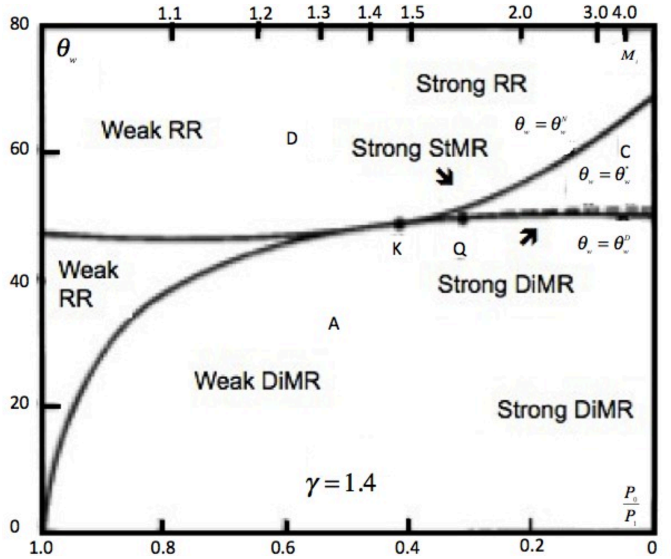

Figure 1.5. Solution domains. Region C contains both Strong Mach reflections and Strong regular reflections[24]

Li and Ben-Dor also compared their stability results in the dual-solution domain and new transition criteria based on entropy considerations to experimental data available. Their analysis suggested that the strong direct Mach reflection is theoretically stable in that region even though it has not been seen. This is because for pseudo-steady flow, a regular reflection has first appeared in many of the experimental cases with single wedges; and because it is a stable configuration, the regular reflection remains. Experimental results for a double wedge by Syschchikova and Krassovskaya[30] and Takayama and Ben-Dor[31] showed a strong direct Mach reflection in the dual-solution domain.

Horne and Karamcheti proposed a method for applying the principles of entropy extrema to unsteady flows[17,18]. They proposed examining an unsteady wall jet as a function of the mean and fluctuating components of the dissipation function below.

$$\Phi_1 = -\frac{2\mu}{\rho_0}\nabla^2 p + \mu\omega^2 \tag{26}$$

where ρ_0 is the total density, μ is the viscosity, p is the pressure, and ω is the vorticity. Writing the vorticity and pressure in terms of the mean and the fluctuation from that mean,

$$\begin{aligned} \omega &= \hat{\omega} + \omega(t) = \hat{\omega} + \omega' \\ p &= \hat{p} + p' \end{aligned} \tag{27a-b}$$

the dissipation function Φ_1 can be written as,

$$\begin{aligned} \Phi_1 &= -\frac{2\mu}{\rho}\nabla^2(\hat{p} + p') + \mu(\hat{\omega} + \omega') \\ \hat{\Phi}_1 &= -\frac{2\mu}{\rho}\nabla^2\hat{p} + \mu\left[\hat{\omega}^2 + \overline{(\omega')^2}\right] \end{aligned} \tag{28a-b}$$

They determined the relative contributions to the dissipative structure of the wall jet by finding a time average of the observed values of the field variables in the cross-stream direction[17,18]. For the steady case, they used the same process as Li and Ben-Dor to extremize the dissipation function subject to a set of constraints to show that incompressible channel flows and the cylindrical vortex are minimal dissipative distributions.

Lewis and Smith[32] used a similar method to Horne and Kamacheti[18] to apply the principle of minimum entropy to unsteady shocks to suggest that entropy considerations could be used to determine shock stability to perturbations. The non-linearity of changes in thermodynamic variables across a shock wave produces some interesting results when looking at the time-average of the total pressure ratio and entropy jump across an oscillating shock. Figure 1.6 presents the time history of the entropy jump across a shock that is oscillating about a steady-state mean with a normal Mach number of 2 subjected to a sinusoidally varying 10% plus-or-minus variation, $M_n = \hat{M}_n(1+0.1\sin(wt))$. At the beginning of the cycle, when the static pressure ratio is higher and the shock is moving towards the approaching flow, the entropy jump has a larger magnitude than later in the cycle, when the static pressure ratio is smaller and the shock is moving away from the upstream flow. Thus, for Mach 2, over the entire cycle, the net entropy rise is greater than the mean or steady case. However, as shown in Figure 1.7, for higher normal Mach numbers, the magnitude of the entropy rise compared to the mean in the beginning of the cycle when the static pressure ratio is largest is *less* than the magnitude of the entropy rise compared to the mean at the end of the cycle when the static pressure ratio is the smallest. Because of the non-linearity of the governing equations, these results suggest that, based on entropy considerations, shocks in hypersonic inlets, which have lower supersonic normal Mach numbers, will be stable to certain perturbations, while a ramjet or supersonic inlet, which will typically have normal shocks at Mach numbers around M=2.5 to M=4.5 might not be stable to perturbations.

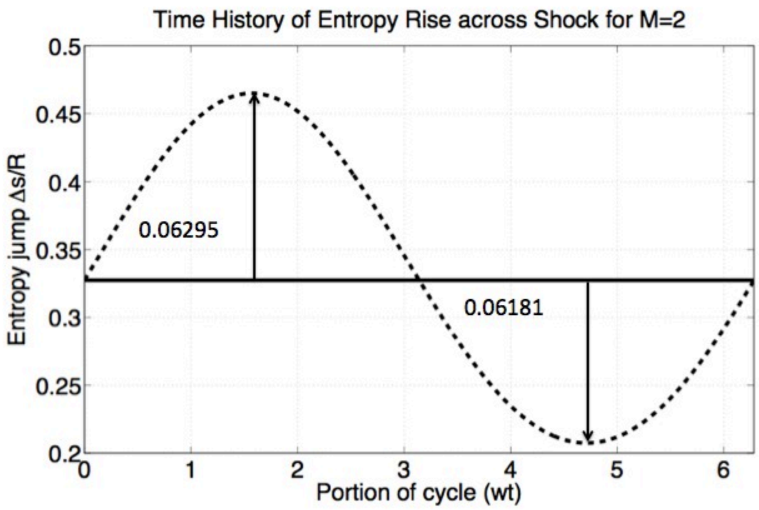

Figure 1.6. Time history of entropy jump across a shock with a normal Mach number of 2 and a 10% sinusoidal variation in normal Mach number. The entropy rise at the beginning of the cycle is higher than the entropy rise in the latter half is less than the mean.

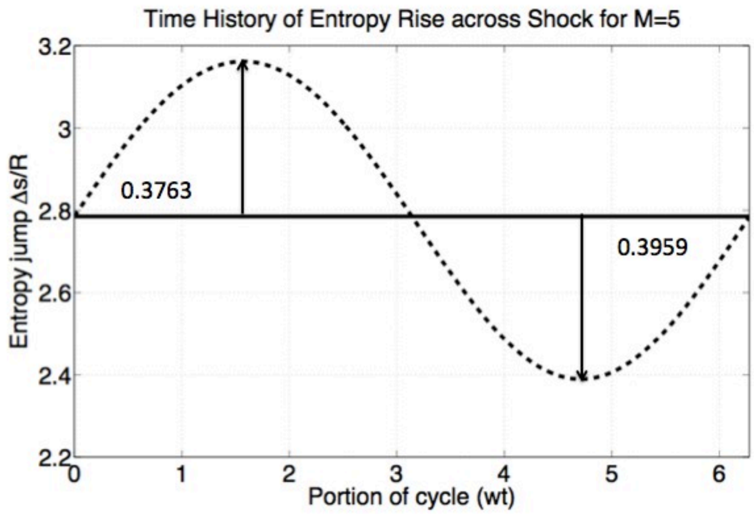

Figure 1.7. Time history of entropy jump across a shock with a normal Mach number of 5 and a 10% sinusoidal variation in normal Mach number. The entropy rise at the beginning of the cycle compared to the mean is less than the difference between the lower entropy rise in the latter half and the mean.

Lewis and Smith[32] presented analysis that includes functions that allow for the calculation time-averaged entropy rise across an unsteady shock and compare it to computational results. In their work, they looked at perturbations of the upstream normal Mach number M_1 and static pressure ratio P with a similar construction to Horne and Kamacheti[18], where $M_1 = \hat{M}_1 + M'(t)$ and $P = \hat{P} + P'(t)$. The entropy jump across a shock depends on just the upstream normal Mach number and the ratio of specific heats γ,

$$\frac{\Delta s}{R} = \ln\left\{\left[1+\frac{2\gamma}{\gamma+1}\left(M_1^2-1\right)\right]^{\frac{1}{\gamma-1}}\left[\frac{(\gamma-1)M_1^2+2}{(\gamma+1)M_1^2}\right]^{\frac{\gamma}{\gamma-1}}\right\} \qquad (29)$$

The perturbations for normal Mach number and pressure can also be expressed as $M_1 = \hat{M}_1(1+\varepsilon\sin(wt))$ and $P = \hat{P}(1+\phi\sin(wt))$ where ε and ϕ small perturbation magnitudes. Lewis and Smith chose a sinusoidal perturbation so that the solution can be integrated, but other waveforms (including a saw-tooth or square wave) would also be equally appropriate. Assuming a quasi-steady perturbation, such that at any moment in time the shock properties are only a function of the upstream normal Mach number in the shock frame of reference and the ratio of specific heats, the time-averaged quasi-steady entropy rise across the shock is

$$\frac{\Delta s}{R} = \frac{1}{T}\int_0^T \ln\left[\left(1+\frac{2\gamma}{\gamma+1}\left[\left(\hat{M}+M'(t)\right)^2-1\right]\right)^{\frac{1}{\gamma-1}}\left(\frac{(\gamma+1)\left(\hat{M}+M'(t)\right)^2+2}{(\gamma-1)\left(\hat{M}+M'(t)\right)^2}\right)^{\frac{\gamma}{\gamma-1}}\right] \qquad (30)$$

After substituting in $M_1 = \hat{M}_1(1+\varepsilon\sin(wt))$, this equation can be linearized based on several approximations and algebraic manipulations. The time average can be taken, and only terms of $\varepsilon^2\sin^2(wt)$ remain when higher order terms are dropped. The entropy rise across the shock for an unsteady flow with a sinusoidal Mach number perturbation can be expressed as

$$\left.\frac{\Delta s}{R}\right|_{avg} = \left.\frac{\Delta s}{R}\right|_{steady} - \frac{2(\gamma-1)(\gamma M^6+1)-(9\gamma^2-4\gamma-1)M^4+3(\gamma^2-4\gamma-1)M^2}{\left[([\gamma-1]M^2+2)(2\gamma M^2[\gamma-1])\right]^2}(M^2-1)\gamma\varepsilon^2$$

(31)

or

$$\left.\frac{\Delta s}{R}\right|_{avg} = \left.\frac{\Delta s}{R}\right|_{steady} + G(M,\gamma)\varepsilon^2 \qquad (32)$$

The function $G(M,\gamma)$ can be easily solved to determine whether the entropy perturbation is positive $G(M,\gamma) > 0$ or negative for a given Mach number and ratio of specific heats. It has a zero value at M=3.314 for a ratio of specific heats of 1.4. However, the time rate of change of entropy depends on entropy flux, not just the entropy gain across the shock. For an upstream perturbation in normal Mach number, the mass flux also changes in the moving shock frame, so the time-averaged entropy flux ρus is of interest and can produce higher order terms that change the results. Lewis and Smith determined that the time averaged entropy flux for an upstream Mach number perturbation is

$$\left.\frac{\rho u(\Delta s)}{\rho_1 u_1 R}\right|_{average} \cong \left.\frac{\Delta s}{R}\right|_{steady} + \left\{ -\frac{2(\gamma+1)M_1^2}{\left(2+(\gamma-1)M_1^2\right)^2}\left.\frac{\Delta s}{R}\right|_{steady} + \frac{4\gamma\left(1-M_1^2\right)^3}{\left(2+(\gamma-1)M_1^2\right)^2\left(2\gamma M_1^2-(\gamma-1)\right)} \right.$$
$$\left. -\left(M_1^2-1\right)\frac{2(\gamma-1)(\gamma M_1^6+1)-(9\gamma^2-4\gamma-1)M_1^4+3(\gamma^2-4\gamma-1)M_1^2}{4\gamma\left(\left((\gamma-1)M_1^2+2\right)\left(2\gamma M_1^2-(\gamma-1)\right)\right)^2}\right\}\varepsilon^2 \qquad (33)$$

$$\left.\frac{\rho u(\Delta s)}{\rho_1 u_1 R}\right|_{average} \cong \left.\frac{\Delta s}{R}\right|_{steady} + H(M,\gamma)\varepsilon^2 \qquad (34)$$

The qualitative behavior is similar, but the normal Mach number at which $H(M,\gamma)=0$ is at M=1.58 instead of M=3.31. Similarly for a static pressure ratio perturbation, which for downstream pressure perturbations does not produce a changing mass flux in the moving shock frame, the relation for the time-averaged entropy flux across a shock is

$$\frac{\Delta s}{R}=\left.\frac{\Delta s}{R}\right|_{steady}+\left\{\frac{1}{\gamma-1}\left\{1-\frac{4\gamma^2\hat{P}}{(\gamma-1)\hat{P}^2+2(\gamma^2-1)\hat{P}+(\gamma^2-1)}\right\}\int_0^{2\pi}\frac{\phi\sin wt}{\pi}d(wt)-\frac{1}{2(\gamma-1)}\times\right.$$
$$\left.\left[1-\frac{8\gamma^2\left[(\gamma^2-1)\hat{P}^3+(\gamma^2+1)\hat{P}\right]}{(\gamma^4-2\gamma^2+1)\left(\hat{P}^4+1\right)+4(\gamma^4-1)\left(\hat{P}^3+\hat{P}\right)+(6\gamma^4+4\gamma^2+6)\hat{P}^2}\right]\int_0^{2\pi}\frac{(\phi\sin wt)^2}{\pi}d(wt)\right\}$$

(35)

$$\frac{\Delta s}{R}=\frac{\rho u\Delta s}{\rho u_1 R}=\left.\frac{\Delta s}{R}\right|_{steady}+F(P)\phi^2 \qquad (36)$$

The zero occurs at M=2.198, suggesting that shocks with normal Mach numbers below M=2.198, where $F(P,\gamma)>0$ for $\gamma=1.4$, will be stable to downstream pressure quasi-steady perturbations, while shocks above M=2.198 will not, according to the principle of minimum entropy. While the details of how these relations in equations 31, 33, and 35 were derived was not explained in this section, they will be discussed at length in Chapter 2.4 as the current study will use these relations and derive similar relationships for other perturbations using the same methods that Lewis and Smith used. Lewis and Smith also conducted a numerical simulation of the entropy rise to confirm the validity of their approximations and found errors on the order of 10^{-6} for the difference between approximated total pressure ratio and entropy jump and numerical simulation for small perturbations (<20%).

Lewis and Smith[32] also developed similar relationships for the time-averaged total pressure ratio as a function of the mean plus a perturbation in total pressure. Because the entropy jump is the natural log of total pressure $\frac{\Delta s}{R} = -\ln \frac{p_{0,2}}{p_{0,1}}$, the total pressure should behavior qualitatively similar to the entropy rise as in Figures 6 and 7. This suggests that an unsteady shock at lower Mach numbers could have a higher total pressure ratio than the mean or steady case. However, unlike entropy, total pressure is not a state variable and is frame of reference dependent. This analysis only applies in the moving shock frame, not the absolute frame. In the absolute frame, the total pressure rise is always less for an unsteady perturbation.

While the principle of minimum entropy has been successfully applied to a variety of problems, including supersonic flows with shocks, several questions about its validity and application to unsteady shock problems still remain. Horne and Karamcheti[18] and Lewis and Smith[32] used time averaging to compare the entropy jump across an unsteady shock; however, no analysis or experimental validation was presented demonstrating that time averaging is a valid approach for time-varying flows. This research will present an argument for the suitability of time-averaging the entropy jump across a shock for a quasi-steady flow.

The qualitative difference between low supersonic normal Mach numbers and large supersonic normal Mach numbers shown by Lewis and Smith[32] suggests a fundamental difference in stability for oblique shocks in hypersonic inlets and nearly normal shocks in supersonic inlets. At low supersonic normal Mach numbers, the entropy rise is greater for the unsteady flow, suggesting that a shock in a hypersonic inlet, but not a normal shock in a supersonic inlet, could be stable to small perturbations if the principle minimum entropy applies. Previous research on applying the principle of minimum entropy to shock systems[22-25] provides some support for using this approach.

This research will also expand on the method presented in Lewis and Smith[32] by evaluating additional perturbations that an inlet shock system might be subjected to such as angle perturbations, upstream Mach number perturbations, and changes in upstream atmospheric conditions. These are upstream perturbations that result in perturbations of the upstream mass flux, which Lewis and Smith[32] either did not evaluate or analyze, and introduce higher order terms that change the normal Mach number at which an unsteady shock has a higher entropy rise than the steady shock. Finally, this research will also consider shocks representative of those seen in different inlet types.

Previous research by Li and Ben-Dor[24] and Lewis and Smith[32] only evaluated the entropy jump across the shock and applicability of entropy considerations to pseudo-steady and quasi-steady flows. For highly oscillatory perturbations with high frequencies, the quasi-steady assumptions no longer apply, and the thermodynamic time derivatives become important. In addition, at sufficiently high enough frequencies, the disturbances downstream will effectively cancel each other, resulting little effect due to the unsteadiness on the inviscid thermodynamic variables downstream. Thus, for a highly unsteady flow a different approach is needed and is presented in this work.

1.3 Previous work -- unsteady shocks and inlets

Successful hypersonic vehicle operation depends on accurate prediction of the flow into a scramjet engine and where oblique shocks form and intersect the vehicle. A typical hypersonic scramjet vehicle is shown in Figure 1.8 with the shock intersecting the inlet cowl. The aircraft forebody provides compression for the engine and acts as an external part of the inlet, and the aircraft aftbody acts as an extension of the nozzle by providing expansion to increase thrust. At the back of the inlet, the shock would intersect the shoulder before propagating through the isolator. As the flow is perturbed from its design conditions, either by changes in angle-of-attack, turns, or travel through non-uniformities, the shock angles can change. If the shock angle moves outside the cowl, spillage can occur leading to increased vehicle drag and decreased mass flow in the combustor. On the other hand, if the shock moves inside the inlet, shock boundary-layer losses can cause flow separation and intense localized heating. Control of the shock position on or near the cowl is desired to prevent destructive heating, separation losses, and maintain high enough airflow into the inlet. In addition, scramjets operate at thrust-to-drag ratios close to unity so that any additional cowl drag, spillage, changes in the flow downstream into the combustor, or excessive drag and shock losses in the inlet could be intolerable.

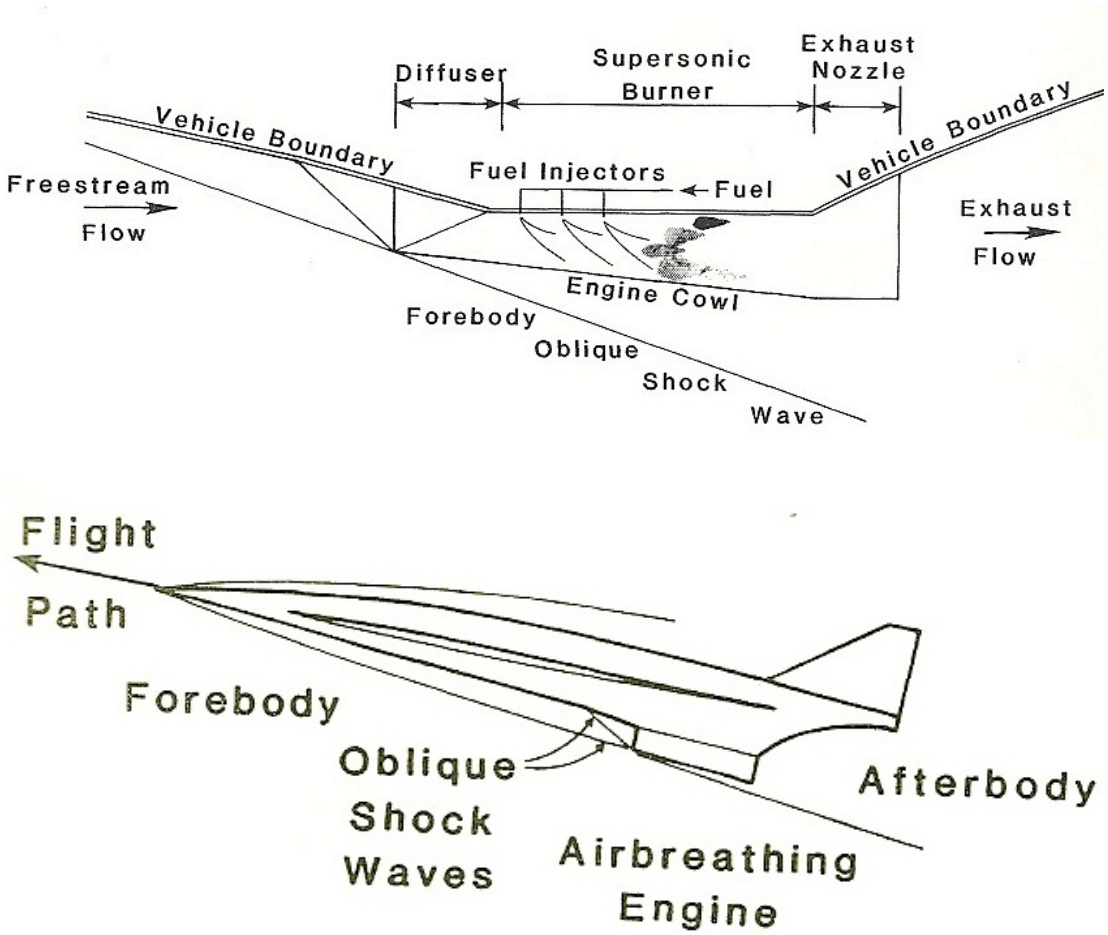

Figure 1.8. Diagram of a planar or 2D geometry scramjet engine and a scramjet-powered vehicle.[76]

Lewis presented analysis design a hypersonic inlet for bow shock location control and on which designs would be less sensitive to changes in flow conditions[44]. At low hypersonic Mach numbers, an increase in the surface angle for a 5-degree wedge causes the shock to move away from the surface of the vehicle, but causes it to move towards the surface of the vehicle for a high freestream Mach number (Mach 20). At Mach 15, this wedge is relatively insensitive to changes in angle-of-attack. If the Mach number is varied, increasing the freestream Mach number decreases the displacement for a small-angle wedge (2 degrees), but increases the displacement for a large-angle wedge (15 degrees). Generally, as the Mach number increases, the shock angle always decreases and thus is displaced towards the surface. This displacement decreases as the surface wedge angle increases. These results are from the well-known theta-beta-Mach number relation

$$\cot\theta = \tan\beta\left[\frac{\frac{\gamma+1}{2}M_1^2}{M_1^2\sin^2\beta - 1} - 1\right] \qquad (37)$$

where θ is the wedge angle, β is the shock angle, and M_1 is the upstream Mach number lead to several inlet design questions that motivated the research in Reference 44. Some of these questions outlined in Reference 44 relevant to off-design flight or the effects of unsteadiness are:

1. Is there a specific wedge angle, which minimizes relative shock displacement due to a change in flight Mach number?
2. Is there a specific wedge angle, which minimizes relative shock displacement due to a change in wedge angle?
3. What is the effect of adding an additional ramp downstream of the first?
4. What is the effect of a thick hypersonic boundary layer on the match?
5. How significant is the effect of frequency at which Mach number or angle-of-attack change?

For designing for changes in flight Mach number, Lewis made several observations based on familiar shock relations and their approximations for small angle wedges at hypersonic speeds. The Mach number or wedge angle at which the shock will be the smallest, occurs when $\frac{\partial \beta}{\partial M} = 0$. Taking Equation 37 for the theta-beta-Mach number relation, and taking the high Mach number $M >> 1$ and small-angle limit $\theta, \beta << 1$, one can use the approximations $\sin\beta \approx \beta$, $\sin\theta \approx \theta$, $\theta \approx \beta$, $\cos\beta \approx 1$, and $\cos\theta \approx 1$. quadratic relationship is derived for the shock angle

$$\frac{\beta}{\theta} = \frac{\gamma+1}{4} + \sqrt{\left(\frac{\gamma+1}{4}\right)^2 + \frac{1}{(M\theta)^2}} \tag{38}$$

The derivative of this with respect to Mach number is

$$\frac{\partial \beta}{\partial M} = \frac{1}{M^2 \sqrt{\left[(\gamma+1)/4\right]^2 (M\theta)^2 + 1}} \tag{39}$$

This equation shows that the shock motion with respect to changing Mach number will never be zero, but this derivative goes to zero as Mach number increases. At small deflection angles, the derivative becomes smaller as the shock angle decreases and the wedge angle or angle-of-attack increases. In other words, for a fixed geometry inlet, there is no way to match bow shock to the cowl at off-design Mach numbers, but these changes can be minimized at higher Mach numbers and surface angles or angle-of-attack.

A similar line of analysis can be used to show the variation in pressure ratio as the Mach number changes. For hypersonic flow at small angles, the pressure ratio is often written as

$$\frac{p_2}{p_1} = 1 + \left[\gamma(\gamma+1)/4\right](M\theta)^2 + \gamma(M\theta)^2 \sqrt{\left[(\gamma+1)/4\right]^2 + \frac{1}{(M\theta)^2}} \tag{40}$$

The change in pressure ratio with respect to Mach number is

$$\frac{\gamma(\gamma+1)M\theta\sqrt{(\gamma+1)^2(M\theta)^2+16}+\gamma(\gamma+1)^2(M\theta)^2+8\gamma}{2\sqrt{(\gamma+1)^2(M\theta)^2+16}} \tag{41}$$

Thus thermodynamic changes caused by changing Mach numbers increase as the Mach number or wedge (or angle-of-attack) increases. Lewis also used similar derivations for examining the effect of changing shock angle and adding a second compression ramp. Figure 1.9, which shows shock displacement for a 1-degree change in angle-of-attack, shows an interesting result that for wedge angles of 10 degrees at about Mach 7 and wedge angles of 5 degrees at Mach 15, the shock is not displaced.

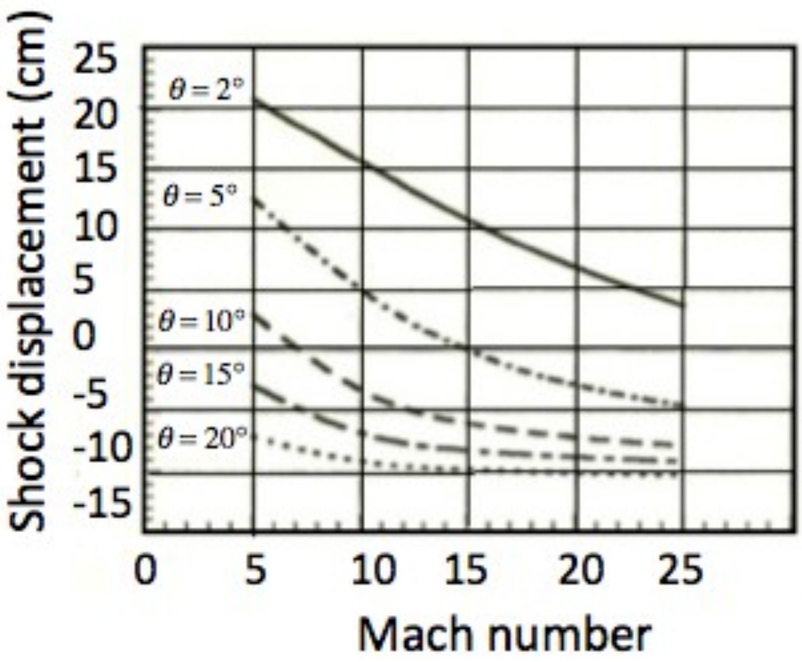

Figure 1.9. Shock displacement with 1-deg increment in angle-of-attack for a 30-meter wedge inlet.[44]

The results from Lewis' analysis indicate several interesting guidelines for inlet design. Not surprisingly, fixing the shock becomes more difficult with a thick boundary layer with the thickness varying with angle-of-attack. The shock can not be fixed with varying Mach number, so if an inlet is intended to be robust to off-design operation or fly over a range of Mach numbers, it would need to be designed with variable geometry. Lewis suggests that an inlet be designed with a fixed shock criterion where possible matched to a cruise Mach number under the boundary layer conditions for that cruise Mach number. Lewis found that the shock could be fixed against perturbations in altitude, which are more likely than variations in Mach number if a vehicle flies at its fixed design Mach number. If a secondary ramp is used, two ramps provide the most control over shock position, as multiple ramps have less control because the shock displacement decreases as shock angle and Mach number increase. However, the addition of more ramps or increasing the wedge angle, increases the sensitivity of the overall inlet pressure ratio to changes.

A shock that is less resistant to changing its angle will experience a larger increase in pressure ratio as upstream Mach number is increased. Thus, there is a trade-off between controlling the shock position and minimizing thermodynamic fluctuations that would propagate into the inlet. In related work, Lewis and Hastings[46] found that high-frequency variations tend to be transmitted directly to the bow shock so that shock motion follows surface motion closely. They also found that, even if a thick boundary layer is present, there was not a significant mismatch at reasonable frequencies despite the potential for the boundary layer to amplify the effect of the surface motion.

Lewis et al.[45] examined the effect that unsteady hypersonic vehicle motion has on its bow shock. This unsteadiness could come from vehicle plunging and pitching motions. In their work, they aimed to determine what the relative motion of the inlet bow shock at high Mach numbers in under the influence of an oscillating wall, and what that does to the thermodynamic properties of the air entering the inlet. Preferably, the shock would move with the vehicle such that the shock remains fixed relative to the vehicle. The shock's movement could be different in amplitude and/or phase, resulting in a displacement of the shock relative to the body. This problem is depicted in Figure 1.10. Typically the angular deviation differs by about 10% of the vehicle's angular displacement, which seems insignificant, but some hypersonic vehicles would have long inlets, so a small angular displacement could result in a large linear displacement at the entrance to the engine[46].

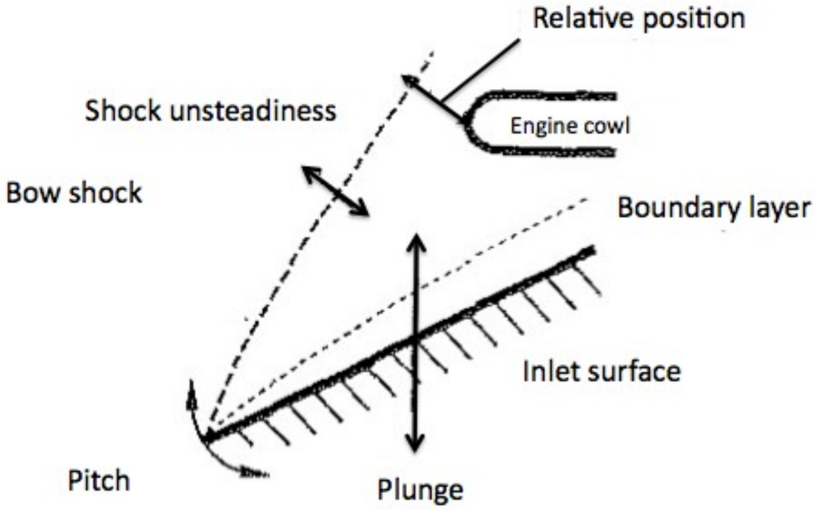

Figure 1.10. Shock motion relative to vehicle.[45]

In their study, they varied the frequency of oscillations and examine the shock and flow field responses as a function of frequency. They looked at two frequency limits - quasi-steady and highly unsteady - for their analytic approach and look at a computational solution including the intermediate region for validation using a time-accurate inviscid MacCormack scheme. Details on the qualitative differences between the quasi-steady and high frequency limit and what frequency range they include are discussed at length in Chapter 2.

The approach used in the current study for describing the two limits is similar to that used by Lewis and Surline[45]. They found good agreement between their analytic and computational results and behavior not predicted by their analysis in the intermediate region. For frequencies of 1 Hz, the shock did not move relative to the plate for Mach numbers of 5 and 10 with a normal motion relative to the surface with an amplitude of 0.5 meters and 0.1 meters, respectively. For 10 Hz, as shown in Figure 1.11, the resulting motion of the shock was sinusoidal but out of phase with respect to the vehicle motion, for the case of a Mach 10 wedge with an oscillation amplitude of 0.1 and 0.5 meters. For the 100 Hz case, which is the limit of the quasi-steady solution based on Lewis and Hastings[46], the results showed the shock tends to curve downstream of the leading edge of the surface. The maximum and minimum displacement also increased by a factor of 5 over the input amplitude, creating a non-uniform pressure profile behind the shock a shown in Figure 1.12. Figure 1.13 shows the amplification of the oscillation for a Mach 20 wedge. However, this amplification does depend on oscillation amplitude, such for a small oscillation, the shock remained almost stationary. Finally, Lewis et al. found that the shock did not move when the surface was oscillated at frequencies of 1 and 5 KHz as shown in Figure 1.14. However at high frequency oscillations, for locations closer to the leading edge where the shock sits closer to the surface, the distance at which the expansion and compression waves produced by the moving surface cancel is equal to the shock wave height, so the shock is curved and affected by the moving wall. In the intermediate region where neither the quasi-steady nor high frequency limit applies, the resulting expansion and compression waves interact with the shock and affect its location. This also resulted in a non-uniform flow field downstream, which could have serious consequences on the operation of the combustor.

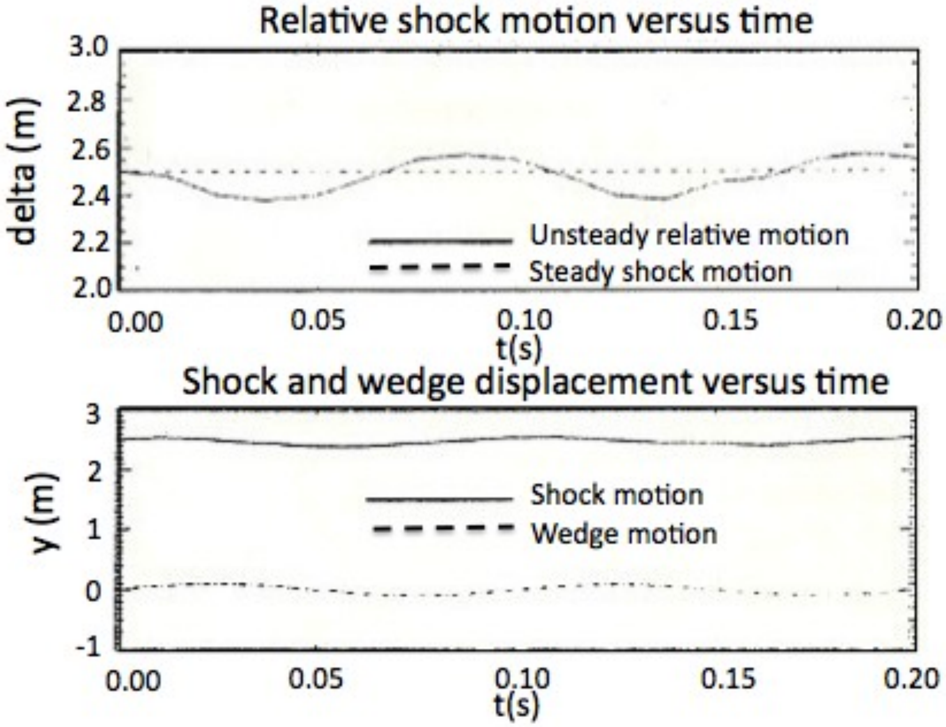

Figure 1.11. Unsteady 10 Hz Mach 10 wedge flow.[45]

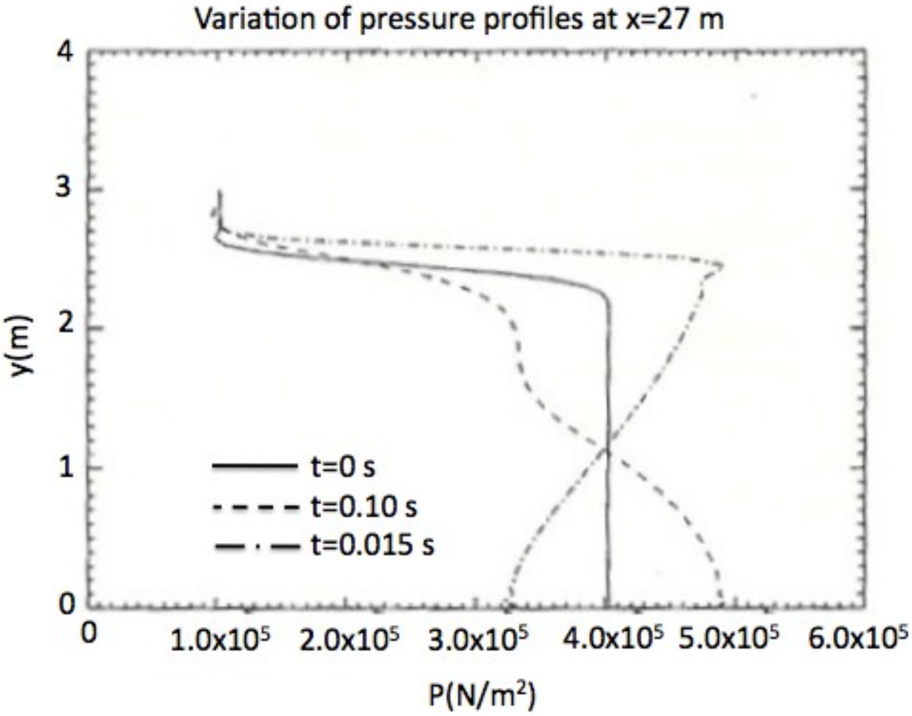

Figure 1.12. Pressure profiles for Mach 10 with a frequency of 100 Hz and displacement amplitude of 0.1 meters.[45]

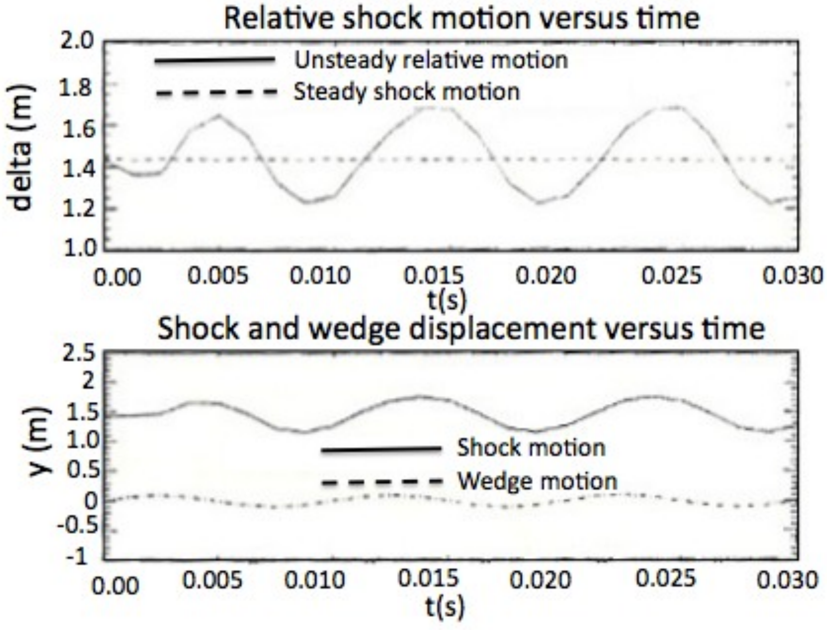

Figure 1.13. Unsteady Mach 20 wedge flow for wedge oscillating with an amplitude of 0.1 meters at a frequency of 100 Hz.[45]

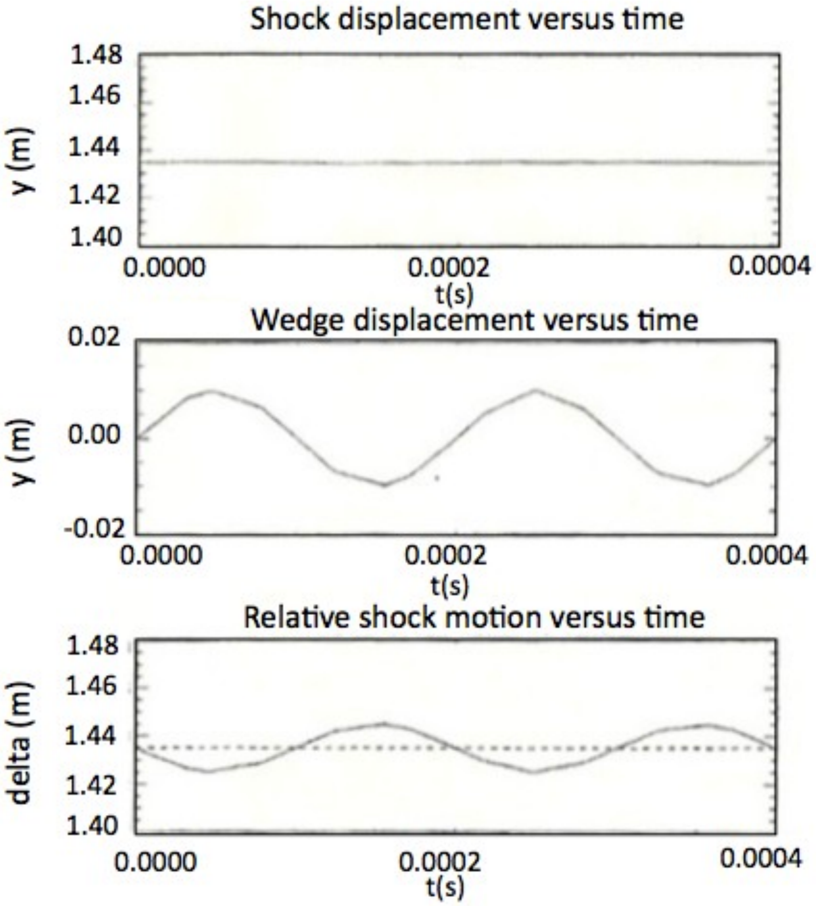

Figure 1.14. Unsteady Mach 20 wedge flow at high frequency (5 kHz).[45]

To summarize, at low frequencies, the shock motion matches the amplitude of the vehicle motion. At mid-range frequencies, a resonating effect seems to occur and the amplitude of the shock motion is several times greater than the vehicle's. At high frequencies, there is an attenuation effect and the shock does not see the vehicle's motion. As Mach number increases, the effect of the vehicle's motion decreases. This is not surprising, as it will be shown in Chapters 2.2 and 7.4, that the upper bound of the quasi-steady limit and lower bound of the high frequency limit increase with Mach number. These results and similar analysis to References 45 and 46 behind the quasi-steady and high frequency limits that will be presented in Chapter 2 are important for determining how to calculate the entropy rise across a shock subjected to perturbations at different frequencies. The computational results presented in Reference 45 also provide some validity to the two different approaches and frequency limits that will be discussed in Chapters 2 and 6.

1.3.a Type IV Shock Interactions

Accurate determination of where a hypersonic oblique shock intersects the surface of the body and resulting shock boundary-layer interactions is crucial to a successful scramjet vehicle operation. Shock-boundary layer interactions produced by the impingement of the bow shock on the cowl produces an area of intense local heating and complicated flow field[35]. Shock interactions - particularly a Type IV interaction - - also tend to be highly sensitive to shock motion, and the inherent unsteadiness also affects cowl-shock matching[33,34].

A type IV shock interaction typically occurs at the cowl of a hypersonic inlet where the weak oblique vehicle bow shock intersects the nearly normal cowl bow

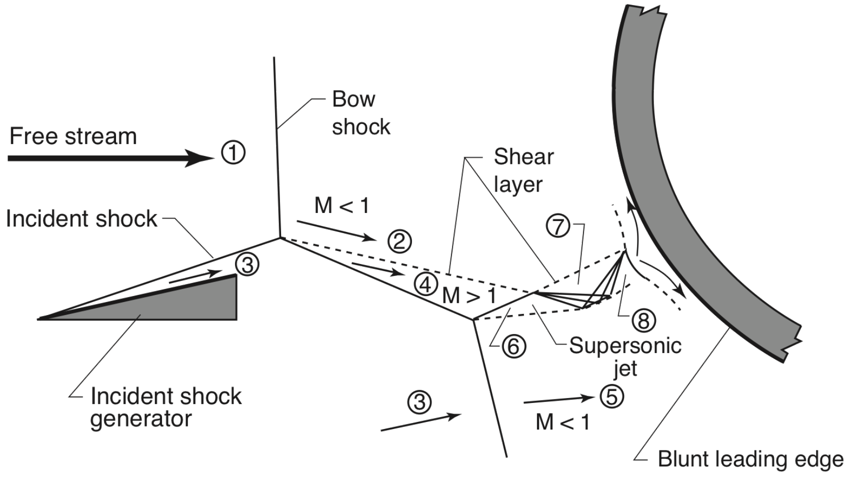

Figure 1.15. Type IV interaction.[77]

shock. This interaction produces a supersonic jet embedded in the subsonic flow region between the bow shock and the surface (Figure 1.15). When the supersonic jet impinges on the wall, a bow shock is produced. This bow shock produces a small stagnation region with intense localized heating and high pressures. The level of intense heating and maximum pressure depend on jet characteristics like size, wall impingement angle, flow state such as turbulent or laminar, and pressure. In addition, the transmitted shock and the supersonic jet is generally unsteady possibly because small variations in upstream flow propagate to large changes downstream. Several computational and experimental studies have found that these shock interactions are inherently unsteady[40-43]. A type IV interaction is one of six types of shock interactions first categorized by Edney in 1968[37]. Figure 1.16 shows the shock interference pattern on the lip of a scramjet inlet cowl. For example, types I and II occur when two weak shocks of opposite families intersect with a Type II occurring closer to the sonic point.

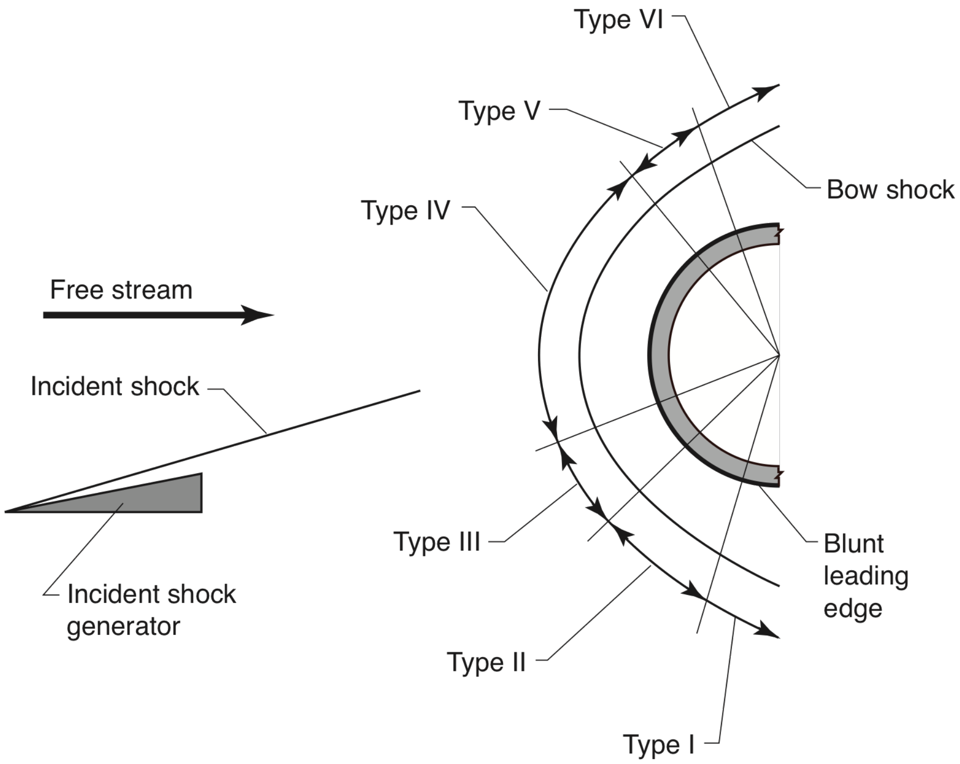

Figure 1.16. Six types of shock interference patterns.[77]

Understanding the stability of shocks to unsteadiness is of particular interest to locate and control Type IV interactions. Experimental results indicate that heating rates and pressure loads associated with a Type IV interaction can be 30 times larger than other types of shock intersections with a surface[35,36] . High heat transfer rates and high pressures resulting from these types of interactions are an important factor to consider in designing an inlet[37,38] .These large temperature gradients and thermal stresses could significantly damage structural components and could limit the duration and usefulness of the vehicle if they are not accurately predicted. These interactions could also occur on the wings or tail section of a hypersonic vehicle.

Experimental results have also shown that the maximum pressure, heat transfer rate, and surface pressure distribution are highly sensitive to upstream conditions such as Mach number, shock strength, and thermodynamic flow conditions[35,37,38].

Lind and Lewis found that slight perturbations in freestream conditions can have large effects on the type IV shock/shock interaction flowfield[34]. They examined the effect that slight perturbations in upstream flow conditions[34] and the location of the impinging bow shock have on Type IV interactions[39]. Lewis and Lind conducted a parametric analytic study to determine the effect freestream Mach number, the incident shock angle, and the bow shock angle have on the transmitted shock angle. For example, to determine the effect of different cowl radii on the transmitted shock angle, they varied the bow shock angle while keeping all other parameters constant. For examining the effects of speed changes, they varied Mach number, and to look at changes in angle of attack or different inlet designs, they varied the inlet deflection angle.

In their work[34], Lind and Lewis developed several guidelines for inlet design to mitigate the effects of Type IV interactions. In general, they found that whenever the inlet bow shock intersects the cowl bow shock near the stagnation region, the transmitted shock is effectively unsteady because small upstream variations are magnified downstream. At the limit of very high Mach numbers, the interaction and the transmitted shock angle exhibits a Mach number independence and also becomes less dependent on inlet deflection angle or angle-of-attack. However, as the Mach number decreases small changes in Mach number or incident shock angle result in large changes in the transmitted shock angle. Their results also suggested that to minimize unsteadiness of the transmitted shock, the inlet deflection angle should be small. At large inlet deflection angles or angles-of-attack, small changes in angle have a large effect on the transmitted shock angle[34].

Lind and Lewis[39] used a computational approach to examine the effect of location of the impinging shock. They used a high-resolution upwind scheme with second-order accuracy in time and space. They varied the impinging shock location on the cowl, which was modeled as a blunt body, between 168 and 186 degrees using flow conditions provided by experiments conducted by Holden[35]. Their results indicated that the location of the impinging shock strongly influenced the development of the interaction, the maximum pressure, and frequency of oscillation associated with the interaction[39]. They found that for shock impingement angles greater than 185 degrees, the Type IV interaction was unsteady. This resulted from an unstable separation region located above where the jet impinged on the wall and how the shock resulting from the jet's impingement was oriented. When the resulting shock from the jet impingement was either parallel with the surface or angled such that the flow through the shock was deflected down, the interaction would be unsteady. Shock impingement angles less than 175 degrees, produced steady Type IV interactions. Figure 1.17 shows the time history of surface pressure for a shock impingement angle on the cowl of 174 degrees. For shock angles between 175 and 185 degrees, the interaction could be steady or unsteady.

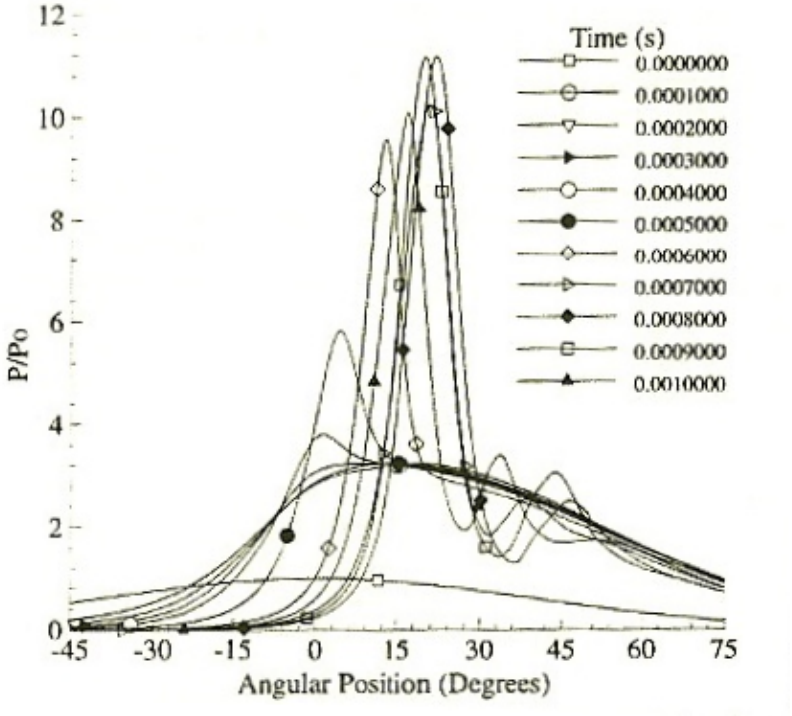

Figure 1.17. Time history of surface pressure for shock impingement angle of 174 degrees.[43]

Unsteadiness has also been studied at length for other propulsion applications, including for flow in a transonic compressor or turbine passage[47-50]. Ng and Epstein[47] identified that there are significant entropy-related consequences resulting from unsteadiness in a transonic compressor passage because of unique properties of unsteady flow compared to steady flow. Inlets of pulse detonation engines may have unsteady flows because of the detonations used in pulse detonation engines are periodic[51-54]. Cullick and Rogers[55] examine the frequency response of a normal shock in a diverging channel, a critical problem for ramjet engines subjected to pressure oscillations. Under steady conditions, a normal shock sits in the divergent section of the inlet diffuser. To a first approximation, the problem of the effect of the pressure oscillations can be treated based on the small-amplitude acoustic motion approximations. Thus the problem can be thought of as a problem of interaction between a normal shock and acoustic waves. It is well known that a normal shock is stable in a divergent channel but unstable in a converging channel. For a normal shock in a channel, if it is displaced, a disturbance propagates downstream where it could be reflected, causing it propagate upstream. Cullick and Rogers[55] examined whether this disturbance grows or decays assuming quasi-steady oscillations and small amplitudes acoustic wave and shock wave motion. They developed a linearized model for representing the unsteady behavior of a shock inlet system for a ramjet. However, their results only encompassed the acoustic field and not the velocity fluctuations that may arise.

Because hypersonic flights are sensitive to changes in flow conditions, understanding the conditions under which a flow would remain unsteady is crucial. Mitigating, accommodating, and containing the effects of Type IV shock interactions on the engine cowl or on control surfaces is critical to their survivability and use in long duration flight. Mitigating and predicting unsteady effects also facilitates maintaining sufficient airflow into the engine and preventing additional losses through shock-boundary layer interactions and non-uniform pressure and temperature profiles. This research proposes one method of predicting unsteadiness and the effect of flow perturbations on hypersonic vehicle operation based on the principle of minimum entropy production.

1.4 Previous work -- three-dimensional inlets

Much of scramjet inlet research since the late 1990’s has focused on streamline traced axi-symmetric inward-turning Busemann inlets and inlets that transition from a rectangular capture area to a circular combustor. In the 1950s, inlet designs and research focused on inward-turning axi-symmetric inlets. These designs fell out of favor with a preference for rectangular two-dimensional inlets for flight vehicles. The late 1990’s saw a renewed interest in inlets with circular or elliptical combustors specially inward-turning or shape-changing inlets.[57] The joint Australian-US Hypersonic International Flight Research Experimentation (HiFire) program will flight test a 3-D scramjet based on the REST inlet[56]

A much-studied candidate for a streamline traced axi-symmetric inlet is the Busemann inlet[58,59]. These inlets have several benefits including relatively high pressure recovery, the ability to easily blend with a circular combustor, and can be designed based on an inviscid flow field that is completely known analytically. Busemann first proposed an internal axi-symmetric flow that consisted of internal isentropic compression followed by a conical shock.[58] Molder and Szpiro[59] proposed an inlet based on using any stream surface of this flow field proposed by Busemann as the inlet wall. This flow field obeys the Taylor-Maccoll equations for axi-symmetric conical flow:

$$u_R'^2\left(u_R + u_R''\right) = \frac{(\gamma-1)}{2}\left(1 - u_R^2 - u_R'^2\right)\left(u_R'' + u_R'\cot\theta + 2u_R\right) \tag{47}$$

where u_R is the radial velocity non-dimensionalized with respect to the freestream speed[59]. The tangential velocity u_ϑ is found from the irrotationality condition

$$u_\theta = u'_R = \frac{du_R}{d\theta} \tag{48}$$

where θ is the angle emanating from the conical shock from the center of the inlet to the entrance of the inlet. The conical shock turns the flow such the flow is uniform and parallel to the inlet wall coming into the combustor. The shock then cancels at the shoulder during on-design conditions. Figure 1.18 shows the shock structure in a Busemann inlet. A numerical method for designing these inlets was developed by Van Wie and Molder[60].

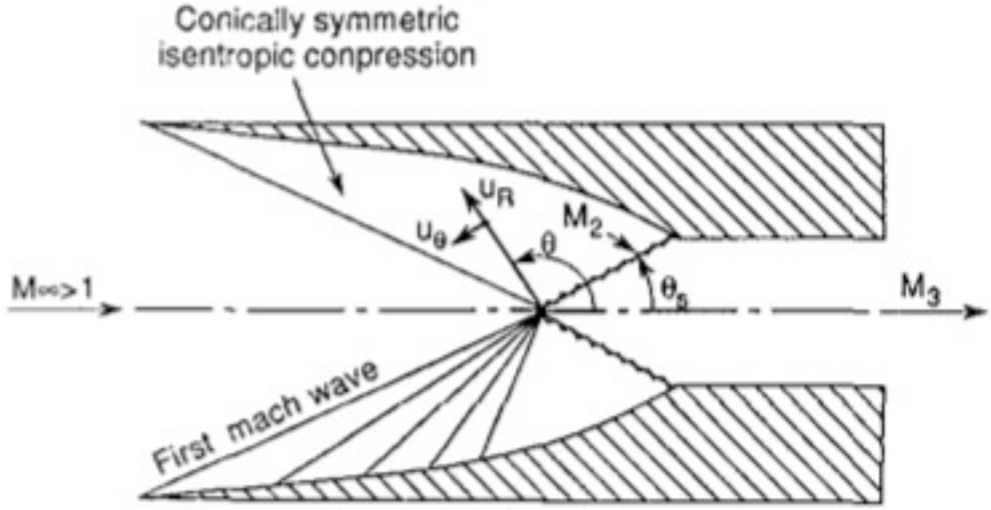

Figure 1.18. The Busemann inlet.[4]

Although these inlets have relatively high total pressure recovery, they have several drawbacks. Busemann inlets have such high contraction ratios that they will not start in steady flow. The contraction ratio determines the minimum Mach number the inlet can operate and how much the flow can be compressed before it chokes. When the inlet unstarts, a normal shock adjusts the flow and the flow becomes subsonic entering the combustor[**61**]. Several researchers have proposed modifications to the Busemann inlet to avoid contraction ratios that are too high[60,62]. Busemann inlets also tend to be very long, leading to high viscous losses due to higher boundary layer growth, which can mitigated somewhat by truncating the inlet with an initial turning angle at the leading edge with small total pressure losses due to the oblique shock formed at the sharp leading edge for small angles[63]. Busemann inlets also have poor off –design performance because of their sensitivity to flow angularity particularly if the inlet has no truncation angle or a sharp leading edge.

The design of a transition duct from a rectangular capture area to an elliptical combustor has been the focus of several efforts. Inlets with a rectangular capture area and circular combustor can combine many of the benefits of rectangular inlets and circular combustors. However, streamline tracing in a parent flow field with uniform inflow and outflow requires the same shape at freestream as at the throat. Stream-traced inlets contain the features of the parent flow-field. Most efforts to create this transition duct have involved blending together the two parent flow fields – rectangular and Busemann.

In particular, considerable work on these inlets has been done by Smart, who used a modified-streamline tracing method involving blending together multiple sets of streamlines to form the transition duct of rectangular-to-elliptical “REST” inlet.[64] The process involved calculating a pre-determined capture area and pressure ratio required for the inlet. First, an axi-symmetric compression flow field with the required pressure ratio was calculated. Several capture shapes and inlets varying from rectangular to elliptical were defined. The path of the streamlines from the inlet entrance to the exit plane was calculated. Specifically, a streamline-traced inlet with rectangular-like capture shape like in Figure 1.19.b. was determined. A second streamline traced inlet with a capture area like Figure 1.19.b. but with radiuses corners as shown in Figure 1.21.a. was then calculated. A third inlet shape with an elliptical throat with the same area as Figure 1.21.b. was calculated and similar to that shown in Figure 1.21.b. All three shapes were smoothly blended together to form a REST inlet with the rectangular capture shape of Figure 1.21.b., the cross-sectional shape of Figure 1.21.a. at the cowl closure, and the throat shape of Figure 1.21.b. A mathematical lofting procedure smoothly blended the streamlines together to produce a smooth transition from rectangular capture area to elliptical combustor.

A resulting transition is shown in Figure 1.20.

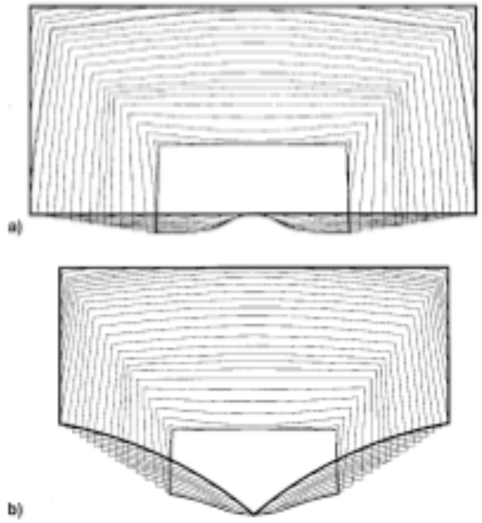

Figure 1.19. Inlet cross-sectional shape distributions for different rectangular capture areas. *a.) Rectangular capture shape b.) Rectangular shape used for REST inlets.*[64]

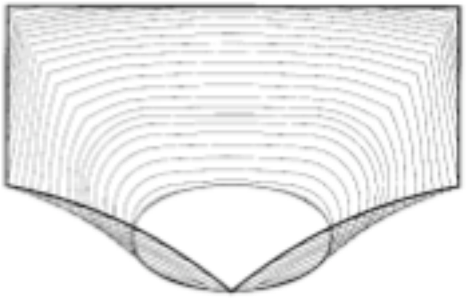

Figure 1.20. Cross-sections of a blended REST inlet.[64]

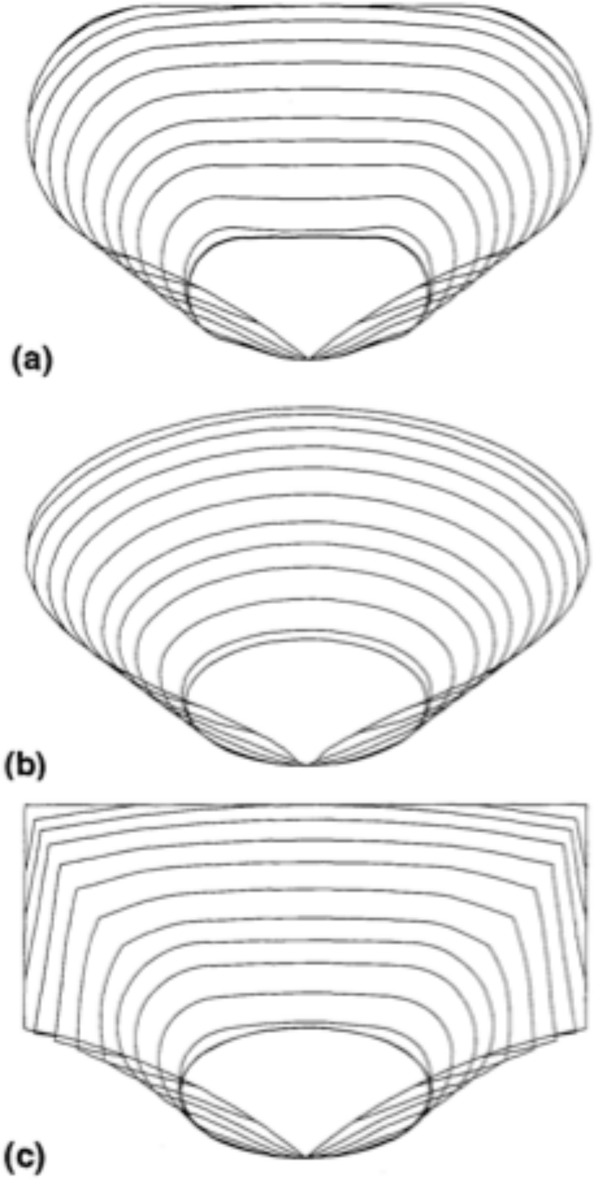

Figure 1.21. Cross-sectional shapes for the three blended inlets for constructing a REST inlet.[65]

Smart's design procedure produced an inlet that performs better than similar two-dimensional inlets[64] for a vehicle cruising at Mach 7 with Mach 6 flow entering the inlet. Tables 1.2-1.4 contain these performance values calculated with a three-dimensional CFD flow solver for Mach 6.0 REST inlet under inviscid flow assumptions for on-design and off-design Mach numbers compared to a rectangular inlet. Even at off-design conditions, the REST inlet performed better than the rectangular inlet. A Mach 6.0 REST inlet was also tested experimentally and found to have slightly lower performance than predicted but higher performance than previously-tested three-dimensional inlets.[66] The parameters typically used to evaluate the performance of scramjet inlets are static temperature ratio ψ , total pressure recovery π_c , kinetic energy efficiency η_{KE} , adiabatic compression efficiency, m_c mass capture percentage, P_R pressure ratio, L_{in}/d_h ratio of the inlet length to the hydraulic diameter, and C_D coefficient of drag.

Property	Mach 3.6	Mach 4.8	Mach 6.0
m_c	84.40%	94.00%	99.50%
P_R	14.8 +/- 3.0%	13.7 +/- 19.1%	13.8 +/- 9.8%
Ψ	2.19 +/- 2.2%	2.16 +/- 5.8%	2.16 +/- 6.4%
M_{exit}	1.77 +/- 2.7%	2.82 +/- 5/3%	3.74 +/- 4.2%

Table 1.2. Characteristics of inviscid Mach 6.0 REST inlet.

Property	Mach 3.6	Mach 4.8	Mach 6.0
π_c	0.960	0.932	0.926
η_{KE}	0.995	0.996	0.997
η_c	0.99	0.982	0.981
C_D	0.349	0.185	0.114
L_{in}/d_h	17.57	17.57	17.57

Table 1.3. Inviscid performance of Mach 6.0 REST inlet

Property	Mach 3.6	Mach 4.8	Mach 6.0
P_T	0.784	0.795	0.791
η_{KE}	0.972	0.985	0.99
η_{KD}	0.945	0.946	0.945
C_D	0.348	0.193	0.125
L_{in}/d_h	7.9	13.26	18.08

Table 1.4. Inviscid performance of 2D rectangular inlet for comparison.[64]

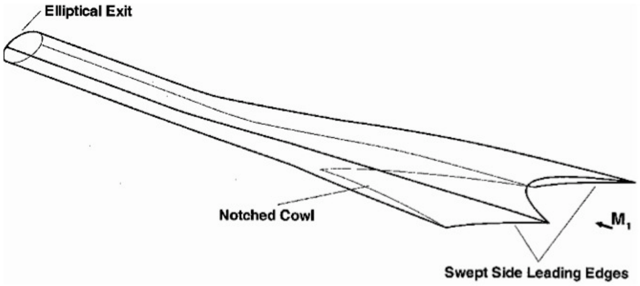

Figure 1.22. REST Inlet.[64]

Other methods for designing a three-dimensional inlet have been presented. Recent work by Bussey[67,68,79] introduces a methodology for designing a scramjet inlet with a different capture than combustor shape using compound compressible flow theory for both inviscid and viscous flow with a shock wave is presented. This is an inverse method that determines the flow through the inlet and flow at the capture plane for a chosen inlet design and flow profile into the combustor.

Three-dimensional or axi-symmetric inlets with curved shocks are of interest because they may also be more or less stable to perturbations based on entropy considerations. Similar to the physics behind the three-dimensional relieving effect of flow over a cone, the flow in a three-dimensional inlet may be inherently more stable to perturbations than an axi-symmetric or rectangular design. Steady curved shocks also have a higher entropy rise than a straight shock with a shock angle equivalent to the average angle of the curved shock, suggesting that curved shocks may be more stable to perturbations. On the other hand, the curved shock creates an ordered pressure, temperature, and entropy gradient that suggests a three-dimensional surface may decrease the rate of entropy production, which could mean a curved shock might be less stable. This research will explore using entropy considerations which three-dimensional inlet shapes, if any, are inherently more forgiving to flow perturbations and off-design effects.

Chapter 2: Quasi-Steady Shocks Analysis

2.1 Quasi-steady shocks versus highly unsteady shocks

For low frequency oscillations, the quasi-steady assumption can apply, allowing for simplifications in calculating entropy at each point in time. Following the approach of Ng and Kerrebrock[69], the continuity equation for unsteady flow evaluated for a control volume around a shock is

$$-\iint_s \rho \vec{U} \cdot \vec{n} dS = \frac{\partial}{\partial t} \iiint_v \rho dV \tag{49}$$

$$\frac{\partial}{\partial t}(\rho V) = \rho \frac{\partial V}{\partial t} + V \frac{\partial \rho}{\partial t} \tag{50}$$

where V is the control volume. Under the quasi-steady assumption, the time derivatives of thermodynamic variables are negligible so the continuity equation can be simplified to

$$\frac{\partial}{\partial t}(\rho V) \cong \rho \frac{\partial V}{\partial t} \tag{51}$$

Thus, continuity is satisfied by moving the shock at a speed of $W = \partial V / \partial t$. This quasi-steady assumption thereby treats the moving shock as if it were a steady-state solution with a constant velocity each time step. This means that the familiar shock relations from the Rankine-Hugoniot equations for the pressure ratio, temperature ratio, density ratio, down stream Mach number, and entropy change can be used. This limit is restricted to frequencies below about 100 Hz[46]. The next section will provide analysis showing how that limit is derived. For low frequencies, the entropy jump across the shock will be calculated according to the following familiar relations:

$$\frac{\Delta s}{R} = \ln\left\{\left[1+\frac{2\gamma}{\gamma-1}\left(M_1^2-1\right)\right]^{1/\gamma-1}\left[\frac{\left(\gamma-1\right)M_1^2+2}{\left(\gamma+1\right)M_1^2}\right]^{\gamma/\gamma-1}\right\} \quad (52)$$

$$\frac{\Delta s}{R} = \ln\left\{P^{\frac{1}{\gamma-1}}\left[\frac{(\gamma-1)P+\left(\gamma+1\right)}{(\gamma+1)P+\left(\gamma-1\right)}\right]^{\gamma/(\gamma-1)}\right\} \quad (53)$$

2.2 Wavy wall and piston analogy

Lewis and Smith[32] and Horne[18] both used time averaging to look at the total change in entropy production versus a steady case; however, it is not obvious whether time averaging is appropriate. This work proposes an analogy that explains the appropriateness of using time averaging and its limitations. One-dimensional piston theory and the hypersonic equivalence principle suggest that the oscillatory unsteadiness could be considered as spatial variations for calculating the entropy jump across a shock.

According to one-dimensional piston theory, a sinusoidal unsteady piston movement in one-dimension looks the same as flow over a wavy wall in two dimensions as discussed in Liepmann and Roshko[70]. The plot of the distance the shock resulting from an unsteady piston moving at a constant velocity U_{piston} travels versus time resembles that of the height above the wedge and distance downstream an oblique shock formed from a two-dimensional wedge that moves constant velocity of U_{wedge} travels. The wedge would have an angle $\theta = U_{piston}/U_{wedge}$. Figure 2.1 shows graphically this similarity between one-dimensional unsteady piston motion and supersonic flow over a wedge. For an unsteady oscillating piston, the wedge would resemble a wavy wall.

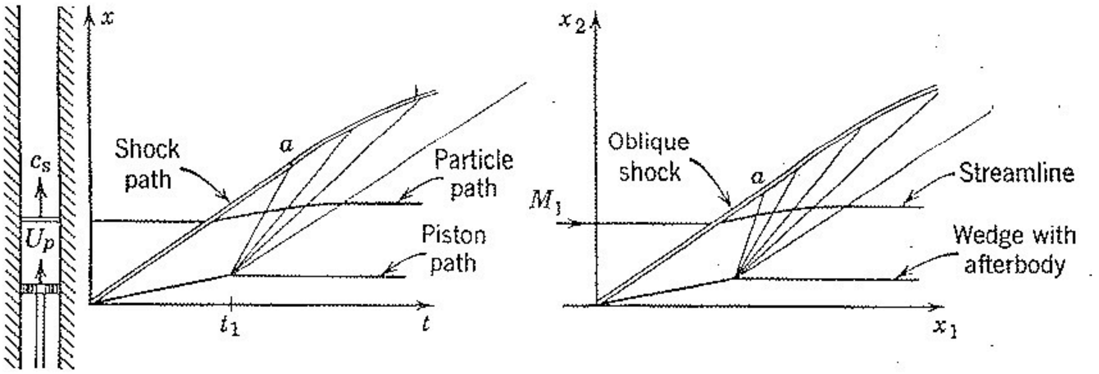

Figure 2.1. On the left is the piston and wave motion in the x-t plane. The figure on the right is the same picture, but for an oblique shock and two-dimensional wedge in the x-y plane[70].

The hypersonic equivalence principle also permits solutions of the unsteady piston problem to be used for hypersonic flow problems with small disturbances. For a slender body of length *L* traveling at hypersonic speeds with slenderness ratio of τ, the change in velocities of the flow travelling over the body can be treated as perturbations $u = V_\infty + u'$ in the x-direction and $v = v'$ and assumed to follow the surface of the body such that $\frac{v'}{u' + V_\infty}$. Each variable such is non-dimensionalized as follows

$$\tilde{x} = \frac{x}{L},\ \tilde{y} = \frac{y}{L\tau},\ z = \frac{z}{\tau L} \tag{54}$$

$$\tilde{u}' = \frac{u'}{V_\infty \tau^2}, \tilde{v}' = \frac{v'}{V_\infty \tau}, \tilde{w}' = \frac{w'}{V_\infty \tau} \tag{55}$$

$$\tilde{p} = \frac{p}{\rho_\infty V_\infty^2}, \tilde{\rho} = \frac{\rho}{\rho_\infty} \tag{56}$$

This allows for several simplifications to the Euler equations known as the hypersonic small-disturbance or hypersonic slender-body equations outlined in Rasmussen[71] :

$$\begin{aligned}
&\frac{\partial \tilde{\rho}}{\partial \tilde{x}} + \frac{\partial\left(\tilde{\rho}\tilde{v}'\right)}{\partial \tilde{y}} + \frac{\partial\left(\tilde{\rho}\tilde{w}'\right)}{\partial \tilde{z}} = 0 \\
&\frac{\partial \tilde{u}'}{\partial \tilde{x}} + \tilde{v}'\frac{\partial \tilde{u}'}{\partial \tilde{y}} + \tilde{w}'\frac{\partial \tilde{u}'}{\partial \tilde{z}} = -\frac{1}{\tilde{\rho}}\frac{\partial \tilde{p}}{\partial \tilde{x}} \\
&\frac{\partial \tilde{v}'}{\partial \tilde{x}} + \tilde{v}'\frac{\partial \tilde{v}'}{\partial \tilde{y}} + \tilde{w}'\frac{\partial \tilde{v}'}{\partial \tilde{z}} = -\frac{1}{\tilde{\rho}}\frac{\partial \tilde{p}}{\partial \tilde{y}} \\
&\frac{\partial \tilde{w}'}{\partial \tilde{x}} + \tilde{v}'\frac{\partial \tilde{w}'}{\partial \tilde{y}} + \tilde{w}'\frac{\partial \tilde{w}'}{\partial \tilde{z}} = -\frac{1}{\tilde{\rho}}\frac{\partial \tilde{p}}{\partial \tilde{z}} \\
&\frac{\partial \tilde{s}}{\partial \tilde{x}} + \frac{\partial \tilde{s}}{\partial \tilde{y}} + \frac{\partial \tilde{s}}{\partial \tilde{z}} = 0 \\
&\tilde{s} = \frac{\tilde{p}}{\tilde{\rho}^{\gamma}}
\end{aligned} \tag{57a-f}$$

An important consequence of the hypersonic small-disturbance approximations is the hypersonic equivalence principle identified by Hayes[72]. A slender body moving at hypersonic speeds causes perturbations in the axial velocity of the body of the order of τ^2 and of the order τ in the lateral direction. This means that a fluid motion caused by a slender body in the a hypersonic flow is mostly in a plane normal to the freestream and equivalent to that of an unsteady piston (Figure 2.2). These equations are equivalent to those for an unsteady flow with one less space dimension[80]. For an unsteady two-dimensional flow with time non-dimensionalized as $\tilde{t} = \frac{t}{l/V_\infty}$, which is equivalent to $\tilde{x}$, so it can be replaced in the small-disturbance equations. This substitution results in the same set of partial differential equations for two-dimensional unsteady flow as three-dimensional steady flow[73].

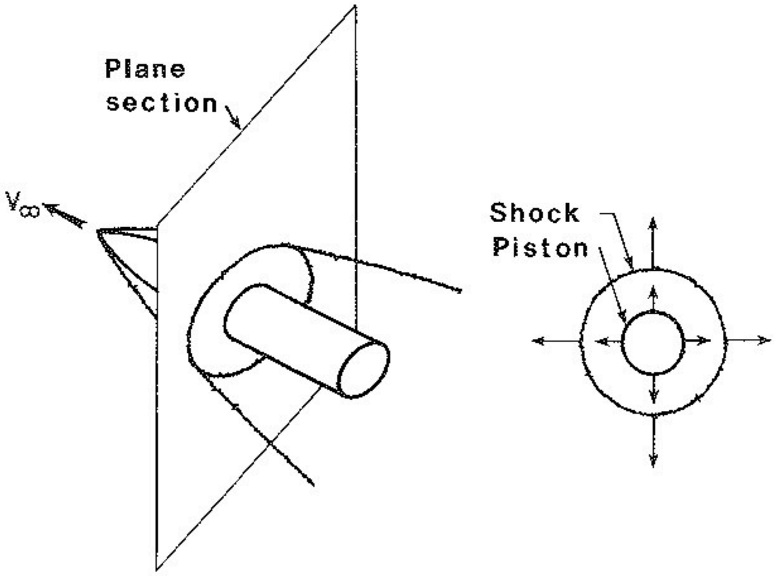

Figure 2.2. Hypersonic equivalence principle: Steady two-dimensional shock compared to unsteady piston shock motion.[71]

Using the hypersonic equivalence principle, for a sinusoidal hypersonic unsteady flow that contains a shock in an inlet, the unsteadiness can translate to a steady hypersonic flow in an inlet with an additional spatial dimension replacing the time dimension. Hypersonic inlets have small turning angles, so they can be considered slender bodies. Thus for the purposes of comparing entropy production across the shock, an unsteady flow can be considered analogous to the flow over a wavy wall.

The time-dependence in pressure and Mach number can be replaced with a new shock angle and summed up over all shock angles as shown below in Equations 58 and 59:

$$M = \hat{M}(1+\varepsilon\sin(\omega t))\sin\beta = \hat{M}\sin\beta_{ww,M} \tag{58}$$

$$P = \left(1+\frac{2\gamma}{\gamma+1}\left(M_1^2\sin^2\beta-1\right)\right)(1+\varepsilon\sin\omega t) = \left(1+\frac{2\gamma}{\gamma+1}\left(M_1^2\sin^2\beta_{ww,P}-1\right)\right) \tag{59}$$

where β_{ww} can be constructed by re-arranging Equations 58 and 59 to solve for β_{ww} and is defined below for each type of perturbation,

$$\begin{aligned} \beta_{ww,M} &= \sin^{-1}\left[\sin\beta(1+\varepsilon\sin\omega t)\right] \\ \beta_{ww,P} &= \sin^{-1}\left[\sin\beta\sqrt{1+\varepsilon\sin\omega t\left(1-\frac{1}{M^2\sin^2\beta}\left[\frac{\gamma-1}{2\gamma}\right]\right)}\right] \end{aligned} \tag{60a-b}$$

Using this transformation from time unsteadiness to changes in shock angle results in the same entropy jump across the shock because the normal Mach number is the same whether looking at the problem in spatial or time-spatial dimensions[80]. Thus, it follows that time averaging can be used for evaluating the entropy jump across the shock as it is the same as summing up the entropy jump across a shock for flow across a wavy wall. Li and Ben Dor[25] also used a transformation for unsteady shocks to deal with the time-dependence, to apply minimum entropy considerations by requiring the Mach number and wedge angle to change such that normal Mach number was constant. They found that available experimental evidence supported their conclusions[25].

2.2 Limits on wavy wall analogy and quasi-steady assumptions

This analogy is only valid for a range of frequencies and perturbation magnitudes. If the frequency is too high or the perturbation too large, the disturbances will cancel too close to the shock and the shock will not be affected by the wavy wall. From piston theory, if the piston motion is symmetric, at sufficiently high reduced frequencies, the expansion fans created from withdrawing the piston and compression waves created from pressing the piston will meet and cancel. From hypersonic small disturbance theory, a small bump in a wall results in an expansion fan and compression wave that will eventually meet and cancel as shown in Figure 2.5. Above the cancellation distance, the flow does not see the wall disturbance. In addition, if the compression waves and expansion fans cancel too close to the shock relative to the shock disturbance or the inlet height, the unsteadiness will cancel out and not enter the combustor, and a different approach to looking at entropy gain is needed.

To determine the frequency range for using the quasi-steady assumption, take an oscillating normal shock with a perturbation on the order of 1% of the freestream Mach number - perturbation size that will be shown later is well with-in the quasi-steady limit as shown in Figure 2.3. The upstream flow has a maximum velocity of $u_{1,\max} = \hat{M}_1(1+\varepsilon)a_1$ at $t = 0$. The downstream flow has a velocity of $u_{2,\max} = \dfrac{\hat{M}_1(1+\varepsilon)a_1}{(\rho_2/\rho_1)_{u1,\max}}$ where the density ratio is based on $M_1 = \hat{M}_1(1+\varepsilon)$. At a time of $t = \dfrac{\pi}{f}$ and a shock physical perturbation distance of *l*, the upstream flow has a minimum velocity of $u_{1,\min} = \hat{M}_1(1-\varepsilon)a_1$ and downstream velocity of $u_{2,\min} = \dfrac{\hat{M}_1(1-\varepsilon)a_1}{(\rho_2/\rho_1)_{u_{1,\min}}}$ where the density ratio is based on $M_1 = \hat{M}_1(1-\varepsilon)$. The position of the downstream disturbance at a time *t* associated with each shock is:

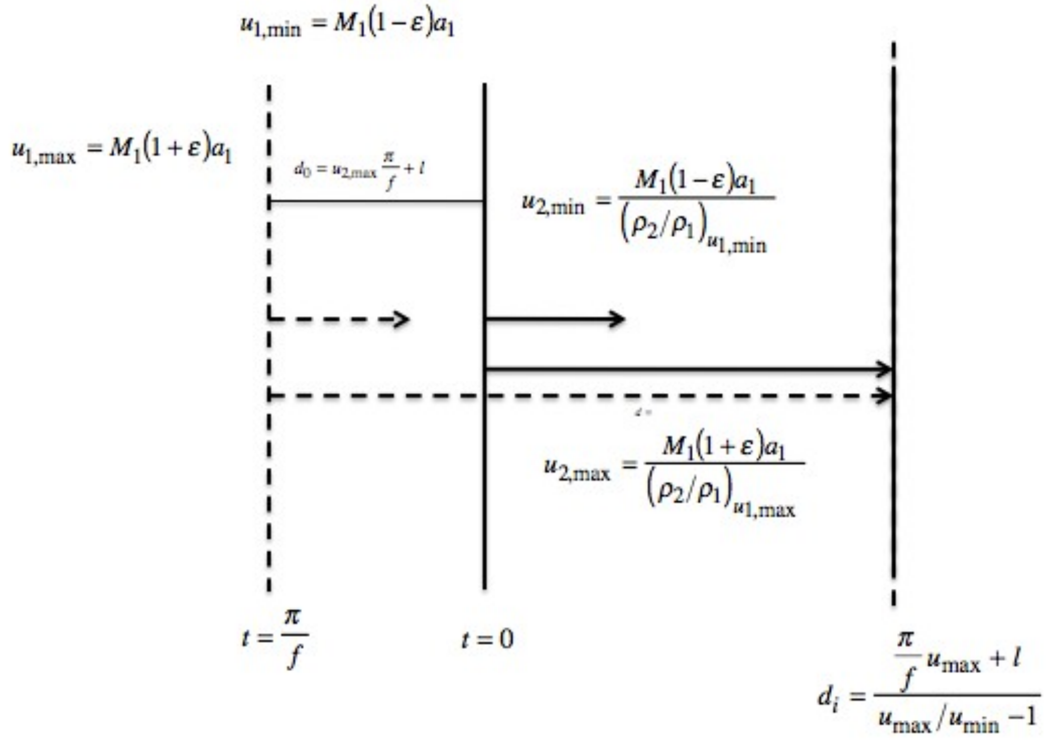

Figure 2.3. Oscillating normal shock with shock movement distance of *l*. The two shocks shown are associated with the minimum and maximum downstream flow speeds.

$$u_{2,\max}t + u_{2,\max}\frac{\pi}{f} + l = d_{\max} \tag{61}$$

$$u_{2,\min}t = d_{\min} \tag{62}$$

Cancellation occurs when the expansion wave, which corresponds to the highest downstream velocity, meets the compression wave, which corresponds to the lowest downstream velocity in the cycle. When the two intersect, the disturbances will cancel and wash out, resulting in no effect of the oscillation on the downstream flow past that point. Solving each equation for *t* and equating, the intersection of the two disturbances d_i can be determined:

$$t = \frac{d - u_{2,\max} \pi/f - l}{u_{2,\max}} \tag{63}$$

$$t = \frac{d}{u_{2,\min}} \tag{64}$$

$$d_i = \frac{u_{2,\max} \pi/f + l}{u_{2,\max}/u_{2,\min} - 1} \tag{65}$$

As expected, as the freestream Mach number increases, the intersection distance increases, and the intersection distance goes as $1/f$. Above frequencies of 1 kHz, the cancellation distance is on the order of 10s of meters or less - within the flow path of a scramjet-powered vehicle. Figure 2.4 shows the ratio of the cancellation distance for an unsteady piston to the movement of the shock for Mach 5, 7, and 10 and suggests that the wavy wall approximation is applicable for analysis in an inlet for frequencies under 100 Hz. A shock perturbation distance of 1 mm was used in this example.

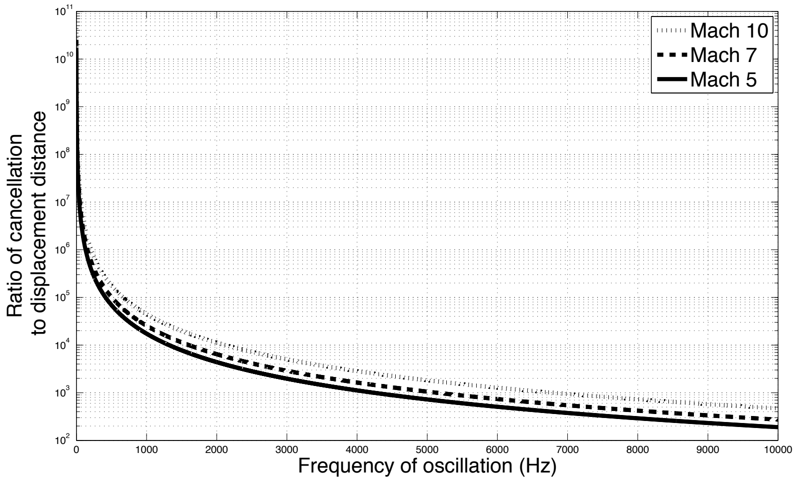

Figure 2.4. Ratio of cancellation distance to shock perturbation amplitude versus frequency for a 10% Mach number oscillation.

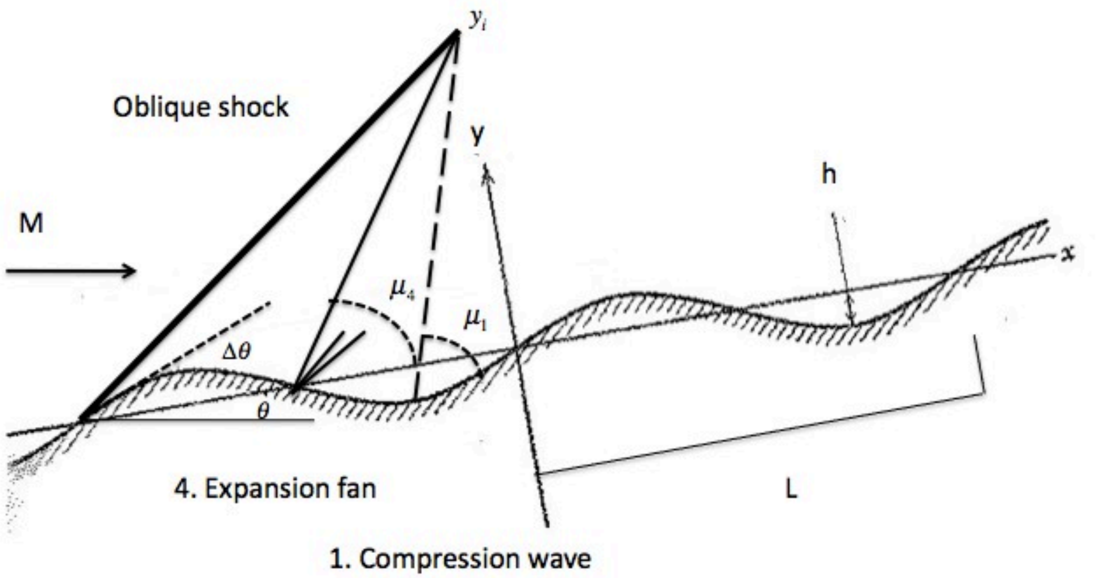

Figure 2.5 Expansion fan and compression waves over a wavy wall.

By examining flow over a wavy wall, the quasi-steady limit for perturbation sizes can be determined. Assume a wavy wall similar to that in Figure 2.5, which is angled at some angle θ. When the flow is at the peak of the cycle or at the mean the second time in the cycle at point 4, it expands, creating expansion waves. When the flow is at the minimum at point 1 until it reaches the maximum, it compresses, creating compression waves. If the wavy wall is too small, then the effect of the wavy wall will cancel under the shock, leaving the shock unaffected. A Mach number perturbation can be translated to a wedge angle perturbation by Equation 60a and the theta-beta-Mach number relation. This results in a perturbation length of $L = (2\pi/f)\hat{M}_1\hat{a}_1$ and height of $h = (L/4)\tan\Delta\theta$ where $\Delta\theta$ depends on the Mach number or pressure perturbation size. From the geometry in Figure 2.5, the height above the wall of the expansion fan and the compression waves is

$$y_4 = \tan(\mu_4 + \theta)x_4 \tag{66}$$

$$y_1 = \tan(\mu_1 + \theta + \Delta\theta)\left(x + \frac{L}{4}\right) - h \tag{67}$$

$$\mu_1 = \sin^{-1}\left(\frac{1}{\hat{M}_2}\right) \tag{68}$$

where μ_4 is determined from the Prantl-Meyer function for $\upsilon_2(M_4) = \upsilon_1(\hat{M}_2) + \Delta\theta$ and $\mu_4 = \sin^{-1}\left(\frac{1}{M_4}\right)$. The angles μ_1 and μ_4 are Mach angles associated with a compression wave in the middle of the cycle and an expansion wave at the cycle's peak, respectively. To find the location of the intersection, set $y_4 = y_1$.

$$\tan(\mu_4 + \theta)x_i = \tan(\mu_1 + \Delta\theta + \theta)(x_i + L/4) - h \tag{69}$$

$$y_i = \tan(\mu_4 + \theta)x_i \tag{70}$$

$$x_i = \frac{\pi}{2f}\hat{M}\hat{a}_1 \frac{\tan\Delta\theta - \tan(\mu_1 + \Delta\theta + \theta)}{\tan(\mu_1 + \Delta\theta + \theta) - \tan(\mu_4 + \theta)} \tag{71}$$

$$y_i = \frac{\pi}{2f}\hat{M}\hat{a}_1 \frac{\tan\Delta\theta - \tan(\mu_1 + \Delta\theta + \theta)}{\tan(\mu_1 + \Delta\theta + \theta) - \tan(\mu_4 + \theta)}\tan(\mu_4 + \theta) \tag{72}$$

Figure 2.6 shows the ratio of the cancellation height to the length of the perturbation for Mach 5, 7, and 10 and three different wedge angles for a Mach number perturbation. Examination of the equation for cancellation height shows that if it is divided by the length of the perturbation, the frequency dependence divides out. The data plotted in Figure 2.6 is independent of frequency as expected for a quasi-steady flow. For perturbations $\varepsilon > 0.1$, this ratio begins to level out to 102, suggesting that the wavy wall analogy is only applicable to small perturbations of Mach number of 10%. The limits on the wavy wall analogy are for Mach number perturbation sizes under 10%. The limits of pressure ratio of 20% or $\phi = 0.2$ can be found by the influence coefficient[74] relating pressure and Mach number,

$$\frac{dP}{P} = \left[\frac{4\gamma}{2\gamma M_1^2 - (\gamma + 1)} \right] \frac{dM_1}{M_1} \tag{73}$$

For comparison, Figure 2.7 shows the regimes applicable for the quasi-steady and high frequency solutions for the relative shock motion to the vehicle motion calculated by Lewis and Surline[45] for a 1-meter thick downstream region between the shock and surface. These limits are on the same order of magnitude (on the order of less than 100 Hz for quasi-steady and greater than 1 kHz for high frequency) as those calculated here and in section 7.4.

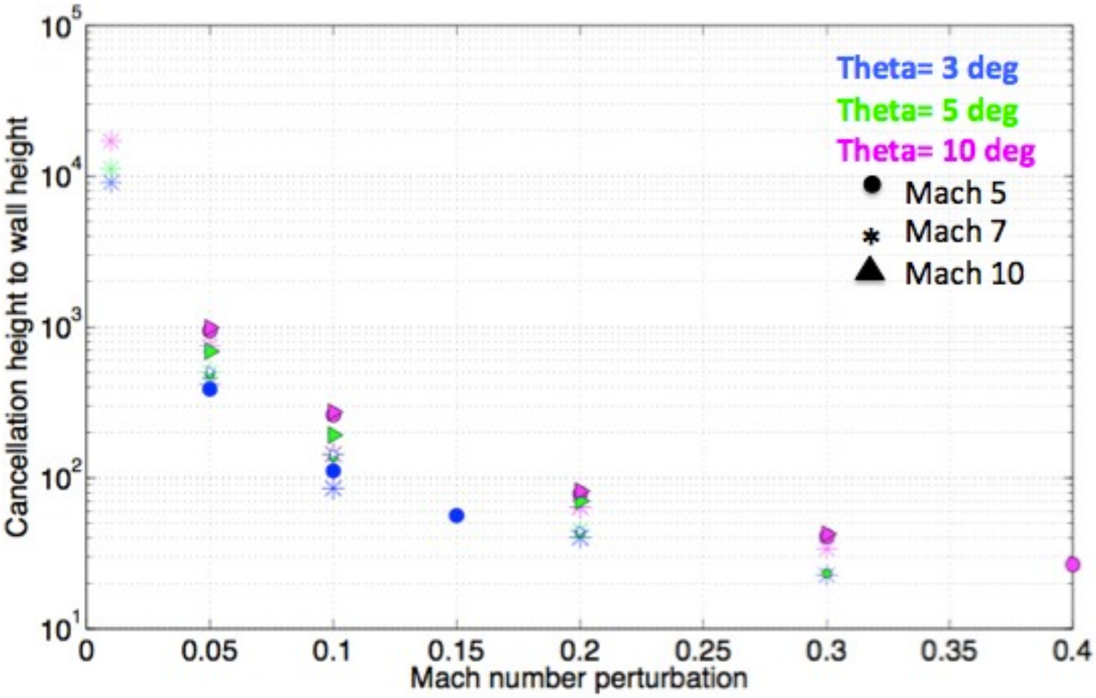

Figure 2.6. Cancellation height to wavy wall height for Mach 5,7, and 10 and average wedge angles of 3, 5, and 10 degrees versus Mach number perturbation size.

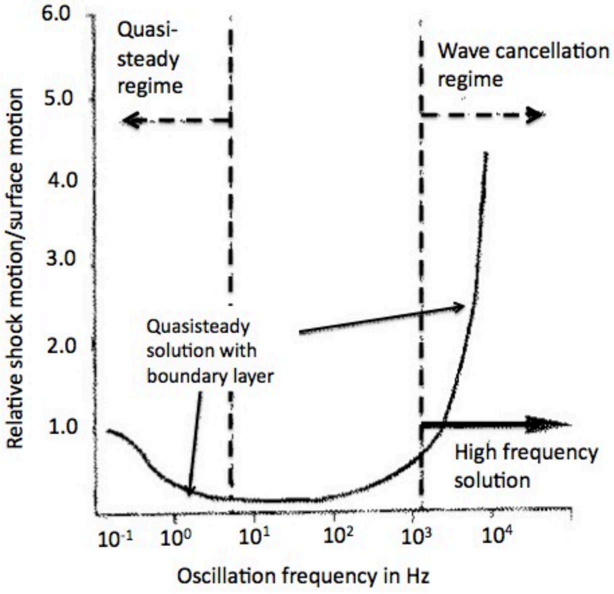

Figure 2.7. Relative shock motion to surface motion for a vehicle with a 1-meter thick downstream region between the surface and shock.[45]

2.4 Entropy flux perturbation for quasi-steady shock perturbations

Entropy considerations are used to evaluate the stability of unsteady shocks by applying it to four types of perturbations to the flow through a hypersonic three-dimensional inlet. A value of $\gamma = 1.4$ is used throughout this work for the ratio of specific heats except when varied to analyze the effect of changing gas chemistry.

2.4.a Upstream Mach number

A perturbation in normal Mach number could result from vehicle yaw, plunging motion, or speed changes. This perturbation can be represented by a steady and unsteady component

$$M = \hat{M}\left(1 + \varepsilon \sin(wt)\right) \tag{74}$$

where ε is the magnitude of the Mach number perturbation and $\hat{M}$ is the Mach number normal to the shock. The magnitude of the perturbation is small enough such that ε^3 or $\mu^3(t) = \varepsilon^3 \sin^3(wt)$ can be neglected. Inserting Equation 74 for Mach number into Equation 52 for the entropy jump across the shock, the following relationship describes the entropy jump across a shock for a sinusoidal Mach number perturbation:

$$\frac{\Delta s}{R} = \ln\left[\left(1 + \frac{2\gamma}{\gamma - 1}\left(M^2\left(1 + \mu(t)\right)^2 - 1\right)\right)^{\frac{1}{\gamma - 1}} \left(\frac{(\gamma - 1)M^2\left(1 + \mu(t)\right)^2 + 2}{(\gamma + 1)M^2\left(1 + \mu(t)\right)^2}\right)^{\frac{\gamma}{\gamma - 1}}\right] \tag{75}$$

To linearize, Equation 75 needs to be factored into the steady and unsteady components,

$$\begin{gathered}\frac{\Delta s}{R}=\frac{1}{\gamma-1}\ln\left[\left(1+\frac{2\gamma}{\gamma-1}(M^2-1)\right)\left(1+A\mu(2+\mu)\right)\right]+\\ \frac{\gamma}{\gamma-1}\ln\left[\left((\gamma-1)M^2+2\right)\left(1+B\mu(2+\mu)\right)\right]-\frac{\gamma}{\gamma-1}\ln\left[\left((\gamma+1)M^2\right)\left(1+\mu(2+\mu)\right)\right]\end{gathered} \tag{76}$$

The third term is already factored, leaving the coefficients *A* and *B* to be determined. To solve for *A*, set the polynomial equal to the expanded version of the factor in Equation 75 corresponding to the pressure ratio,

$$\left(1+\frac{2\gamma}{\gamma-1}(M^2-1)\right)\left(1+A\mu(2+\mu)\right)=\left(1+\frac{2\gamma}{\gamma-1}(M^2-1)\right)+\frac{2\gamma}{\gamma-1}M^2\mu(2+\mu) \tag{77}$$

$$A=\frac{2\gamma M^2}{\gamma M^2-(\gamma-1)} \tag{78}$$

Similarly to solve for *B*,

$$\left((\gamma-1)M^2+2\right)\left(1+\mu(2+\mu)\right)=(\gamma-1)M^2\mu(2+\mu) \tag{79}$$

$$B=\frac{(\gamma-1)M^2}{(\gamma-1)M^2+2} \tag{80}$$

Plugging in the coefficients and using the fact that the product of multiple functions in a logarithm is equal to the sum of the logarithms of each product,

$$\frac{\Delta s}{R}=\frac{1}{\gamma-1}\ln\left(1+\frac{2\gamma}{\gamma-1}\left(M^2-1\right)\right)+\frac{\gamma}{\gamma-1}\ln\left(\frac{(\gamma-1)M^2+2}{(\gamma+1)M^2}\right)$$
$$+\frac{1}{\gamma-1}\ln\left(1+\frac{2\gamma M^2\left(2\mu+\mu^2\right)}{\gamma M^2-(\gamma-1)}\right) \qquad (81)$$
$$-\frac{\gamma}{\gamma-1}\ln\left(1+2\mu+\mu^2\right)+\frac{\gamma}{\gamma-1}\ln\left(1+\frac{(\gamma-1)M^2\left(2\mu+\mu^2\right)}{(\gamma-1)M^2+2}\right)$$

The perturbation terms can be linearized because $a\varepsilon << 1$ where a is just a coefficient using the expansion $\ln(1+x)\cong x-\frac{1}{2}x^2$. The result of this linearization is in Equation 80 after grouping terms of μ and μ^2 and dropping terms of μ^3 or higher.

$$\frac{\Delta s}{R}=\left.\frac{\Delta s}{R}\right|_{steady}+\frac{2\gamma}{\gamma-1}\left[\frac{2M^2}{2\gamma M^2-(\gamma-1)}-1+\frac{(\gamma-1)M^2}{(\gamma-1)M^2+2}\right]\mu$$
$$+\frac{1}{\gamma-1}\left[\frac{2\gamma M^2}{2\gamma M^2-(\gamma-1)}-\frac{4\gamma^2M^4}{\left(2\gamma M^2-(\gamma-1)\right)^2}+3\gamma+\frac{(\gamma+1)M^2}{(\gamma-1)M^2+2}-\frac{4\gamma(\gamma+1)^2M^4}{\left((\gamma-1)M^2+2\right)^2}\right]\mu^2$$

(82)

The term corresponding to μ can be simplified as follows:

$$\frac{2\gamma}{\gamma-1}\frac{(\gamma-1)M^2\left(2\gamma M^2-(\gamma-1)\right)+2M^2\left((\gamma-1)M^2+2\right)-\left(2\gamma M^2-(\gamma-1)\right)(\gamma-1)M^2+2}{\left(2\gamma M^2-(\gamma-1)\right)\left((\gamma-1)M^2+2\right)}$$

(83)

The numerator simplifies to:

$$\frac{1}{(\gamma-1)}\left[\frac{2\gamma M^2}{2\gamma M^2-(\gamma-1)}-\frac{2\gamma^2M^4}{\left(2\gamma M^2-(\gamma-1)\right)^2}+\gamma+\frac{\gamma(\gamma-1)M^2}{(\gamma-1)M^2+2}-\frac{2\gamma(\gamma-1)^2M^4}{\left((\gamma-1)M^2+2\right)^2}\right]=$$
$$\frac{2(\gamma-1)\left(\gamma M_1^6+1\right)-\left(9\gamma^2-4\gamma-1\right)M_1^4+3\left(\gamma^2-4\gamma-1\right)M_1^2}{2\gamma\left(\left((\gamma-1)M_1^2+2\right)\left(2\gamma M_1^2-(\gamma-1)\right)\right)^2}\left(M^2-1\right)$$

(84)

So the term corresponding to μ is

$$\frac{4\gamma\left(M^2-1\right)^2}{\left(2\gamma M^2-(\gamma-1)\right)\left((\gamma-1)M^2+2\right)}\mu \tag{85}$$

$$\frac{1}{(\gamma-1)}\left[\frac{2\gamma M^2}{2\gamma M^2-(\gamma-1)}-\frac{2\gamma^2 M^4}{\left(2\gamma M^2-(\gamma-1)\right)^2}+\gamma+\frac{\gamma(\gamma-1)M^2}{(\gamma-1)M^2+2}-\frac{2\gamma(\gamma-1)^2 M^4}{\left((\gamma-1)M^2+2\right)^2}\right]=$$
$$\frac{2(\gamma-1)\left(\gamma M_1^6+1\right)-\left(9\gamma^2-4\gamma-1\right)M_1^4+3\left(\gamma^2-4\gamma-1\right)M_1^2}{2\gamma\left(\left((\gamma-1)M_1^2+2\right)\left(2\gamma M_1^2-(\gamma-1)\right)\right)^2}\left(M^2-1\right)$$

(86)

Thus, the entropy jump across a shock with a quasi-steady sinusoidal Mach number oscillation is

$$\frac{\Delta s}{R}=\left.\frac{\Delta s}{R}\right|_{steady}+\int_0^{2\pi}\frac{4\gamma\left(M^2-1\right)^2}{\left(2\gamma M^2-(\gamma-1)\right)\left((\gamma-1)M^2+2\right)}\varepsilon\sin(\theta)\frac{d\theta}{2\pi}+$$
$$\int_0^{2\pi}\frac{2(\gamma-1)\left(\gamma M_1^6+1\right)-\left(9\gamma^2-4\gamma-1\right)M_1^4+3\left(\gamma^2-4\gamma-1\right)M_1^2}{2\gamma\left(\left((\gamma-1)M_1^2+2\right)\left(2\gamma M_1^2-(\gamma-1)\right)\right)^2}\left(M^2-1\right)\varepsilon^2\sin^2(\theta)\frac{d\theta}{2\pi} \tag{87}$$

Averaged over the entire cycle, only the ε^2 remains. However, the upstream mass flux crossing the shock is time-varying for the Mach number and atmospheric conditions perturbations in the shock frame. The product of the time-varying mass flux and the entropy jump across the shock introduces higher order terms that contribute significantly to the production of entropy. For the purposes of analyzing the stability of different inlets to perturbations, the convected entropy flux will be examined in this study. The convected entropy flux pus for Mach number perturbations with the upstream velocity normal to the shock $u_1=\hat{M}(1+\varepsilon\sin wt)a_1$,

$$\rho_2 u_2 s_2-\rho_2 M_1 a_1 \mu s_2=\rho_2\left(u_2-\hat{M}a_1\mu\right)\left[\Delta s+s_1\right] \tag{88}$$

From mass conservation, substitute in the following relations to remove u_2 and ρ_2 and $u_1=\hat{u}_1(1+\varepsilon\sin wt)$,

$$\rho_1 u_1 = M a_1 (1+\mu) \tag{89}$$

$$u_2 = \frac{\rho_1 u_1}{\rho_2} \tag{90}$$

$$\begin{aligned} &\rho_2\left(\frac{u_1\rho_1}{\rho_2}(1+\mu) - \hat{M}a_1\mu\right)[\Delta s + s_1] = \rho_1 a_1 \hat{M}\left[1+\varepsilon\left(1-\frac{\rho_2}{\rho_1}\right)\right][\Delta s + s_1] = \\ &\rho_1 a_1 \hat{M}\left[1+\varepsilon\left(1-\frac{(\gamma+1)M^2(1+2\mu+\mu^2)}{(\gamma-1)M^2(1+2\mu+\mu^2)+2}\right)\right][\Delta s + s_1] \end{aligned} \tag{91}$$

Substituting in Equation 53 for the entropy jump across the shock for $\frac{\Delta s}{R}$, dropping terms of μ^2, and integrating over one cycle, where the odd μ terms integrate to zero,

$$\begin{aligned} &\left[1-\frac{(\gamma+1)M^2}{(\gamma-1)M^2+2}\right]\mu \times \frac{4\gamma\left(M_1^2-1\right)^2}{\left(2+(\gamma-1)M_1^2\right)\left(2\gamma M_1^2-(\gamma-1)\right)}\mu = \\ &-\frac{\left[\left((\gamma-1)M^2+2-(\gamma+1)M^2\right)\right]4\gamma\left(M_1^2-1\right)^2}{\left(2+(\gamma-1)M_1^2\right)^2\left(2\gamma M_1^2-(\gamma-1)\right)}\mu^2 = \\ &-\frac{\left[\left(\gamma M^2-M^2+2-\gamma M^2-M^2\right)\right]4\gamma\left(M_1^2-1\right)^2}{\left(2+(\gamma-1)M_1^2\right)^2\left(2\gamma M_1^2-(\gamma-1)\right)}\mu^2 = \\ &\frac{4\gamma\left(1-M_1^2\right)^3}{\left(2+(\gamma-1)M_1^2\right)^2\left(2\gamma M_1^2-(\gamma-1)\right)}\mu^2 \end{aligned} \tag{92}$$

$$\begin{aligned} \left.\frac{\rho u(\Delta s)}{\rho_1 u_1 R}\right|_{average} \cong \left.\frac{\Delta s}{R}\right|_{steady} + \Bigg\{ &-\frac{2(\gamma+1)M_1^2}{\left(2+(\gamma-1)M_1^2\right)^2}\left.\frac{\Delta s}{R}\right|_{steady} + \frac{4\gamma\left(1-M_1^2\right)^3}{\left(2+(\gamma-1)M_1^2\right)^2\left(2\gamma M_1^2-(\gamma-1)\right)} \\ &-\left(M_1^2-1\right)\frac{2(\gamma-1)\left(\gamma M_1^6+1\right)-\left(9\gamma^2-4\gamma-1\right)M_1^4+3\left(\gamma^2-4\gamma-1\right)M_1^2}{4\gamma\left(\left((\gamma-1)M_1^2+2\right)\left(2\gamma M_1^2-(\gamma-1)\right)\right)^2}\Bigg\}\varepsilon^2 \end{aligned}$$

(93)

This is the final result for the entropy flux across the shock for a sinusoidal Mach number perturbation that will be used for analysis. This can be written as

$$\frac{\Delta s}{R} = \left.\frac{\Delta s}{R}\right|_{steady} + G(M,\gamma)\varepsilon^2 \tag{94}$$

As defined, if $G(M,\gamma)$ is positive, then the unsteady perturbation results in higher entropy, and according to the principle of minimum entropy, should be an unstable state and should stabilize to the mean or steady state. Mach numbers at which $G(M,\gamma)$ becomes positive or negative will be of interest.

2.4.b Downstream pressure ratio

Changes in entropy can also be compared for perturbations in the pressure ratio resulting from a perturbation in the back pressure in the combustor or isolator. Changes in the pressure ratio could result from changes in back pressure in the combustor or isolator and isentropic changes in atmospheric flight conditions. In a hypersonic inlet, pressure changes in the combustor or isolator can propagate forward to the inlet through the subsonic portion of the boundary layer. A brief change in pressure imposed downstream of the shock creates an unsteady flow and an imbalance of forces across the shock, pushing the shock upstream for an increase in pressure and downstream for a decrease.

For a downstream pressure rise, the shock will have a velocity relative to the upstream velocity, resulting in the shock strength decreasing and pushing the shock back to its previous position. A downstream pressure decrease will have the opposite effect. Both result in the oscillation in pressure ratio. This oscillation in pressure ratio can be written as $P = p_2/p_1 = \hat{P}(1+\phi\sin(wt))$ where ϕ is a small fraction of the pressure ratio and can be neglected for powers of three or higher. Using Equation 53 for the entropy jump across the shock in terms of the pressure ratio, the entropy jump across the shock subjected to a perturbation in pressure ratio is

$$\frac{\Delta s}{R} = \ln\left[\hat{P}(1+\varepsilon)\right]^{\frac{1}{\gamma-1}} + \ln\left[\frac{(\gamma-1)\hat{P}(1+\varepsilon)+(\gamma+1)}{(\gamma+1)\hat{P}(1+\varepsilon)+(\gamma-1)}\right]^{\frac{\gamma}{\gamma-1}} \quad (52)$$

After factoring out the perturbation components, the entropy jump across the shock becomes,

$$\begin{aligned}\frac{\Delta s}{R} &= \frac{1}{\gamma-1}\ln\hat{P} + \frac{\gamma}{\gamma-1}\ln\left[\frac{(\gamma-1)\hat{P}+(\gamma+1)}{(\gamma+1)\hat{P}+(\gamma-1)}\right] \\ &+ \frac{1}{\gamma-1}\ln(1+\varepsilon) + \frac{\gamma}{\gamma-1}\ln\left(1+\frac{(\gamma-1)\hat{P}\varepsilon}{(\gamma-1)\hat{P}+(\gamma+1)}\right) - \frac{\gamma}{\gamma-1}\ln\left(1+\frac{(\gamma+1)\hat{P}\varepsilon}{(\gamma+1)\hat{P}+(\gamma-1)}\right)\end{aligned} \quad (95)$$

For small perturbations, the logarithms can be linearized as $\ln(1+a\varepsilon) \cong a\varepsilon - \frac{(a\varepsilon)^2}{2}$, resulting in the following relation for $\Delta s/R$,

$$\begin{aligned}&\frac{\Delta s}{R} = \left.\frac{\Delta s}{R}\right|_{steady} + \\ &\frac{1}{\gamma-1}\left[1+\gamma\frac{\left((\gamma-1)\hat{P}\right)}{(\gamma-1)\hat{P}+(\gamma+1)} - \gamma\frac{\left((\gamma+1)\hat{P}\right)}{(\gamma+1)\hat{P}+(\gamma-1)}\right]\varepsilon - \\ &\frac{1}{2(\gamma-1)}\left[1+\gamma\frac{\left((\gamma-1)\hat{P}\right)^2}{\left((\gamma-1)\hat{P}+(\gamma+1)\right)^2} - \gamma\frac{\left((\gamma+1)\hat{P}\right)^2}{\left((\gamma+1)\hat{P}+(\gamma-1)\right)^2}\right]\varepsilon^2\end{aligned} \quad (96)$$

Looking at the term associated with ε first, the common denominator of the second and third term is

$$\left[(\gamma-1)\hat{P}+(\gamma+1)\right]\left[(\gamma+1)\hat{P}+(\gamma-1)\right] = (\gamma^2-1)\hat{P}^2 + 2(\gamma^2+1)\hat{P} + (\gamma^2-1) \quad (97)$$

The numerator can be simplified as follows,

$$\gamma\left[(\gamma-1)(\gamma+1)\hat{P}^2 + (\gamma-1)^2\hat{P} - (\gamma-1)(\gamma+1)\hat{P}^2 - (\gamma+1)^2\hat{P}\right] = \left[\gamma^2-2\gamma+1-\gamma^2-2\gamma-1\right]\gamma\hat{P} = -4\gamma\hat{P}$$
(98)

Next, the second term can be simplified using a similar method,

$$\left[1+\gamma\frac{\left((\gamma-1)\hat{P}\right)^2}{\left((\gamma-1)\hat{P}+(\gamma+1)\right)^2}-\gamma\frac{\left((\gamma+1)\hat{P}\right)^2}{\left((\gamma+1)\hat{P}+(\gamma-1)\right)^2}\right]=$$
$$1+\gamma\frac{\left((\gamma-1)\hat{P}\right)^2\left((\gamma+1)\hat{P}+(\gamma-1)\right)^2-\left((\gamma+1)\hat{P}\right)^2\left((\gamma-1)\hat{P}+(\gamma+1)\right)^2}{\left((\gamma+1)\hat{P}+(\gamma-1)\right)^2\left((\gamma-1)\hat{P}+(\gamma+1)\right)^2} \qquad (99)$$

Starting by expanding out the denominator,

$$\left((\gamma+1)\hat{P}+(\gamma-1)\right)^2\left((\gamma-1)\hat{P}+(\gamma+1)\right)^2=(\gamma^2-1)\hat{P}^2+2(\gamma^2+1)\hat{P}+(\gamma^2-1)=$$
$$(\gamma^2-1)^2\hat{P}^4+(\gamma^2-1)^2+4(\gamma^2+1)(\gamma^2-1)\hat{P}^3+4(\gamma^2+1)(\gamma^2-1)\hat{P}+\left[4(\gamma^2+1)^2+2(\gamma^2-1)^2\right]\hat{P}^2=$$
$$[\gamma^4-2\gamma^2+1]\left(\hat{P}^4+1\right)+4[\gamma^4-1]\left(\hat{P}^3+\hat{P}\right)+[6\gamma^4+4\gamma^2+6]\hat{P}^2$$

(100)

The numerator simplifies to,

$$\left((\gamma-1)^2(\gamma+1)^2-(\gamma-1)^2(\gamma+1)^2\right)\hat{P}^4+\left[2(\gamma-1)^3(\gamma+1)-(\gamma+1)^3(\gamma-1)\right]\hat{P}^3+\left[(\gamma-1)^4-(\gamma+1)^4\right]\hat{P}^4=$$
$$0-8(\gamma^2-1)\hat{P}^3-8(\gamma^2+1)\hat{P}^2$$

(101)

Substituting in the results from Equations 95, 96, 98, and 99, the final result for the linearized entropy perturbation across the shock is

$$\frac{\Delta s}{R}=\left.\frac{\Delta s}{R}\right|_{steady}+\frac{1}{\gamma-1}\left[1-\frac{4\gamma^2\hat{P}}{(\gamma^2-1)\hat{P}^2+2(\gamma^2+1)\hat{P}+(\gamma^2-1)}\right]\varepsilon+$$
$$\frac{1}{2(\gamma-1)}\left[\frac{8(\gamma^2-1)\hat{P}^3+8(\gamma^2+1)\hat{P}^2}{[\gamma^4-2\gamma^2+1]\left(\hat{P}^4+1\right)+4[\gamma^4-1]\left(\hat{P}^3+\hat{P}\right)+[6\gamma^4+4\gamma^2+6]\hat{P}^2}-1\right]\varepsilon^2 \qquad (101)$$

If the entropy gain across the shock is averaged over an entire cycle, the odd terms drop out, leaving only the ε^2 terms. The odd term will become important for analyzing the entropy gain perturbation for perturbations in upstream thermodynamic variables, where the mass flux across the shock will also vary in time. Because the mass flux across a shock is not affected for a downstream pressure perturbation, the normalized entropy flux across the shock for perturbations in back pressure is

$$\frac{\Delta s}{R} = \left.\frac{\Delta s}{R}\right|_{steady} + \frac{1}{2(\gamma-1)}\left[\frac{8(\gamma^2-1)\hat{P}^3 + 8(\gamma^2+1)\hat{P}^2}{[\gamma^4-2\gamma^2+1](\hat{P}^4+1) + 4[\gamma^4-1](\hat{P}^3+\hat{P}) + [6\gamma^4+4\gamma^2+6]\hat{P}^2} - 1\right]\varepsilon^2$$

$$\frac{\Delta s}{R} = \left.\frac{\Delta s}{R}\right|_{steady} + H(\hat{P},\gamma)\phi^2$$

(103)

2.4.c Upstream pressure and atmospheric conditions

Changes in the pressure ratio can also be caused by changes in altitude or atmospheric conditions. Upstream thermodynamic changes resulting from altitude perturbations or perturbations in air density and temperature would occur isentropically. For small isentropic changes in atmospheric conditions, the upstream density and temperature also have an unsteady component and can be linearized as follows:

$$\rho_1 = \hat{\rho}_1(1+\phi\sin(wt))^{-\frac{1}{\gamma}} \approx \hat{\rho}_1\left(1 - \frac{1}{\gamma}\phi\sin(wt)\right) \quad \text{for } \phi << 1 \qquad (104)$$

$$T_1 = \hat{T}_1(1+\phi\sin(wt))^{\frac{1-\gamma}{\gamma}} \approx \hat{T}_1\left(1 - \phi\left(\frac{1-\gamma}{\gamma}\right)\sin(wt)\right) \quad \text{for } \phi << 1 \qquad (105)$$

While further calculations will be done using a perturbation in the pressure ratio, perturbations in upstream density or temperature will qualitatively have the same effect on the difference in the time-averaged and mean unperturbed entropy. The value of the entropy difference will change, but the normal Mach at which the maximum entropy difference or there is no difference between the time-averaged entropy gain across the shock and entropy gain across the shock for the unperturbed mean will not change. Unlike for back pressure perturbations, changes in the pressure ratio resulting from perturbations upstream of the shock will vary the mass flux across the shock. The changing convected mass flux re-introduces the higher order term that time-averaged to zero. Returning to the equation for convected entropy,

$$\rho us = \rho_1 a_1 \hat{M}\left[1+\varepsilon\left(1-\frac{\rho_2}{\rho_1}\right)\right]\left[\Delta s + s_1\right] \tag{91}$$

The linearized upstream density perturbation in Equation can be substituted into equation 89,

$$\rho us = \hat{\rho}_1 a_1 \hat{M}\left(1-\frac{\varepsilon}{\gamma}\right)\left[1+\varepsilon\left(1-(1+\frac{\varepsilon}{\gamma}\right)\right]\left[\Delta s + s_1\right] = \hat{\rho}_1 a_1 \hat{M}\left(1-\frac{\varepsilon}{\gamma}-\left(\frac{\varepsilon}{\gamma}\right)^3\right)\left[\Delta s + s_1\right] \tag{106}$$

After substituting in Equation 102 for $\Delta s/R$ and dropping terms of ε that time average to zero and higher order terms, the convected entropy flux for perturbations in upstream thermodynamic variables can be found by dividing the ε term by $-\gamma$,

$$\left.\frac{pu\Delta s}{p_1 u_1 R}\right|_{avg} = \left.\frac{\Delta s}{R}\right|_{steady} + \left\{\frac{1}{\gamma(\gamma-1)}\left\{\frac{4\gamma^2\hat{P}}{(\gamma-1)\hat{P}^2+2(\gamma^2-1)\hat{P}+(\gamma^2-1)}-1\right\}-\frac{1}{2(\gamma-1)}\right. \\ \left.\left[1-\frac{8\gamma^2\left[(\gamma^2-1)\hat{P}^3+(\gamma^2+1)\hat{P}\right]}{(\gamma^4-2\gamma^2+1)\left(\hat{P}^4+1\right)+4(\gamma^4-1)\left(\hat{P}^3+\hat{P}\right)+(6\gamma^4+4\gamma^2+6)\hat{P}^2}\right]\right\}\phi^2 \tag{107}$$

$$\left.\frac{pu\Delta s}{p_1 u_1 R}\right|_{avg} = \left.\frac{\Delta s}{R}\right|_{steady} + J(P)\phi^2 \tag{108}$$

2.4.d Sinusoidal angle perturbation

Perturbations in angle of attack and sideslip angle or pitching motions can result in perturbations in the shock angle relative to the vehicle. Displacement of the shock can result in increased wave drag if it moves away from the vehicle and decreased mass flow if it moves into the inlet. Perturbations in the shock angle can be written as $\beta(t)=\hat{\beta}(1+\varepsilon\sin wt)$ with $\mu\equiv\hat{\beta}\varepsilon\sin wt$ so that $M_{1,n}=\hat{M}_1\sin\left(\beta(1+\varepsilon\sin(wt))\right)$. A similar method can be used to derive the expression for the entropy perturbation due to sinusoidal perturbations in the shock angle. The shock angle perturbation can be expanded using

$$\sin\left(\beta(t)\right)=\sin\left(\hat{\beta}(1+\varepsilon\sin(wt))\right)=\left(\sin\left(\hat{\beta}\right)\cos(\mu)+\cos\left(\hat{\beta}\right)\sin(\mu)\right) \tag{109}$$

such that

$$M_{1,n}^2=\hat{M}_1^2\left[\sin^2\cos^2\mu+\cos^2\beta\sin^2\mu+2\sin\beta\cos\beta\sin\mu\cos\mu\right] \tag{110}$$

For small perturbations in the shock angle, the small angle approximation $\cos^2\mu=1-\mu^2/2$ can be used, resulting in a form that can be substituted into the original derivation for the Mach number perturbation and separated into the steady and unsteady components using $2\sin\mu\cos\mu=\sin 2\mu$,

$$M_{1,n}^2=\hat{M}_1^2\left[\sin^2\left(1-\frac{\mu^2}{2}\right)+\cos^2\beta\sin^2\mu+\sin\beta\cos\beta\sin 2\mu\right] \tag{111}$$

$$\begin{aligned}
M_{1,n}^2&=\hat{M}_1^2\sin^2\beta\left[\left(1-\frac{\mu^2}{2}\right)+\cot^2\beta\sin^2\mu+\cot\beta\sin 2\mu\right]\\
M_{1,n}^2&=\hat{M}_{1,n}^2\left[\left(1-\frac{\mu^2}{2}\right)+\cot^2\beta\sin^2\mu+\cot\beta\sin 2\mu\right]
\end{aligned} \tag{112}$$

which is analogous to $M^2 = M^2(1+2\varepsilon+\varepsilon^2)$ for Mach number perturbations, with a major difference being the non-linear dependence on the perturbation size and the mean shock angle in Equation 112. The expression for the shock angle perturbation is thus very similar to the expression found for the Mach number perturbation but with different weighting to each term based on a non-linear dependence on the perturbation size and mean shock angle.

$$\left.\frac{\rho u(\Delta s)}{R\rho_1 u_1}\right|_{average} \cong \left.\frac{\Delta s}{R}\right|_{steady}\left\{-\frac{2(\gamma+1)M_1^2}{\left(2+(\gamma-1)M_1^2\right)^2}\left.\frac{\Delta s}{R}\right|_{steady}\left(\sin^2\mu\cot^2\hat{\beta}-\mu^2\right)\right.$$
$$+\frac{2\gamma\left(1-M_1^2\right)^3}{\left(2+(\gamma-1)M_1^2\right)^2\left(2\gamma M_1^2-(\gamma-1)\right)}\left(\cos\hat{\beta}\cot\hat{\beta}\sin\mu\sin 2\mu\right)$$
$$\left.-\left(M_1^2-1\right)\frac{2(\gamma-1)\left(\gamma M_1^6+1\right)-\left(9\gamma^2-4\gamma-1\right)M_1^4+3\left(\gamma^2-4\gamma-1\right)M_1^2}{\left(\left((\gamma-1)M_1^2+2\right)\left(2\gamma M_1^2-(\gamma-1)\right)\right)^2}\gamma\left(\cot^2\hat{\beta}\sin^2\mu-\mu^2\right)\right\}$$

(113)

$$\left.\frac{\rho u\left(\Delta s\right)}{R\rho_1 u_1}\right|_{average} \cong \left.\frac{\Delta s}{R}\right|_{steady}+\left\{-\frac{2\left(\gamma+1\right)M_1^2}{\left(2+\left(\gamma-1\right)M_1^2\right)^2}\left.\frac{\Delta s}{R}\right|_{steady}\left(\sin^2\varepsilon\cot^2\hat{\beta}-\left(\varepsilon\beta\right)^2\right)\right.$$
$$+\frac{2\gamma\left(1-M_1^2\right)^3}{\left(2+\left(\gamma-1\right)M_1^2\right)^2\left(2\gamma M_1^2-\left(\gamma-1\right)\right)}\times\left(\cos\hat{\beta}\cot\hat{\beta}\sin\varepsilon\beta\sin 2\varepsilon\beta\right)$$
$$\left.-\left(M_1^2-1\right)\frac{2\left(\gamma-1\right)\left(\gamma M_1^6+1\right)-\left(9\gamma^2-4\gamma-1\right)M_1^4+3\left(\gamma^2-4\gamma-1\right)M_1^2}{4\gamma\left(\left(\left(\gamma-1\right)M_1^2+2\right)\left(2\gamma M_1^2-\left(\gamma-1\right)\right)\right)^2}\gamma\left(\cot^2\hat{\beta}\sin^2\varepsilon\beta-\left(\varepsilon\beta\right)^2\right)\right\}$$

(114)

$$\left.\frac{\rho u(\Delta s)}{\rho_1 u_1 R}\right|_{average} = \left.\frac{\Delta s}{R}\right|_{steady} + K(M,\varepsilon,\gamma)\varepsilon^2 \qquad (115)$$

2.4.e Thermodynamic derivatives with quasi-steady assumption

As a consistency check, it can be shown that the time-derivatives of the thermodynamic variables are zero under the quasi-steady assumption. Following the approach of Li and Ben-Dor[24], the equation for conservation of entropy is

$$\iiint_V \frac{\partial(\rho s)}{\partial t} dV + \iint_A \left(\rho u_j s + \frac{q}{T} \right) n_j dA - \iiint_V \sigma dV = 0 \tag{116}$$

where $\sigma = \frac{1}{T}\left[\frac{\lambda}{T}\left(\frac{dT}{dx_j}\frac{dT}{dx_j} \right) + \Phi \right]$ is the thermal conductivity, and Φ is the viscous dissipation. For the flow across a shock, this can be simplified to

$$\int_{J(x,y)} \rho u_j n_j \Delta s dw = \iiint_V \sigma dV - \iiint_V \frac{\partial(\rho s)}{\partial t} dV \tag{117}$$

$$\int_{J(x,y)} \rho u \Delta s dw = \dot{S} \tag{118}$$

where u_j is the velocity component normal to the shock, which is along *J(x,y)*.

For sinusoidal Mach number perturbations with the entropy jump calculated by Equation 5 and assuming quasi-steady flow for the oblique shock relations, those derivatives are,

$$\frac{\rho_2}{R}\frac{ds_2}{dt} = \rho_1 \frac{(\gamma+1)\hat{M}^2(1+\varepsilon\sin wt)^2}{2+(\gamma-1)\hat{M}^2(1+\varepsilon\sin wt)^2}\left[\frac{\gamma}{\gamma-1}\rho_2(t)\frac{d(\rho_1/\rho_2)}{dt} + \frac{1}{\gamma-1}\frac{1}{p_2(t)}\frac{d(p_2/p_1)}{dt} \right]$$
(119)

$$\frac{d\left(p_2/p_1\right)}{dt} = 8\hat{M}^2\varepsilon w\cos(wt)(1+\varepsilon\sin wt)\frac{\gamma}{\gamma-1} \qquad (120)$$

$$\frac{d\left(\rho_1/\rho_2\right)}{dt} = 4w\varepsilon\hat{M}^2\cos wt\frac{1}{(\gamma+1)M^2(1+\varepsilon\sin wt)^2} \qquad (121)$$

The indefinite integral of Equation 121 is

$$\int 4w\varepsilon\hat{M}\cos wt\frac{1}{(\gamma+1)\hat{M}^2(1+\varepsilon\sin(wt))^2} = -\frac{4\varepsilon\hat{M}}{(\gamma+1)\hat{M}^2(\varepsilon^2\sin(wt)+\varepsilon)} \quad (122)$$

which is the same value at the beginning and end of the cycle, so the time-average of the density ratio is zero.

For sinusoidal pressure ratio perturbations with entropy calculated by Equation 53 where T_{ref} and p_{ref} are the reference values for calculating entropy,

$$\frac{1}{R}\frac{ds_2}{dt} = \frac{\gamma}{\gamma-1}\frac{1}{T_2(t)}\frac{d\left(T_2/T_1(t)\right)}{dt} - \frac{1}{p_1 P(t)}\hat{P}\phi w\cos wt \qquad (123)$$

$$\frac{d\left(\rho_2/\rho_1\right)}{dt} = \frac{-4(\gamma+1)\hat{P}\phi w\cos(wt)}{\left[(\gamma+1)+(\gamma-1)\hat{P}(1+\phi\sin wt)\right]^2} \qquad (124)$$

$$\frac{d\left(T_2/T_1\right)}{dt} = \left(\hat{P}\phi w\cos wt\right)\frac{(\gamma-1)\frac{p_2}{p_1}+(\gamma+1)}{(\gamma+1)\frac{p_2}{p_1}+(\gamma-1)} + \hat{P}(1+\phi\sin wt)\frac{-4(\gamma+1)\hat{P}\phi w\cos wt}{\left[(\gamma-1)+(\gamma+1)\hat{P}(1+\phi\sin wt)\right]^2}$$

(125)

$$\frac{d\rho_1 s_1}{dt} = s_1\frac{d\rho_1}{dt} = -\frac{R\hat{\rho}_1\phi w\cos wt}{\gamma}(1+\phi\sin wt)^{\frac{-(\gamma+1)}{\gamma}}\left[\left(\frac{\gamma}{\gamma-1}\ln\left[\frac{\hat{T}_1}{T_{ref}}\right] - \ln\left[\frac{\hat{p}_1}{p_{ref}}\right]\right)\right] \quad (126)$$

If back pressure changes are considered, Equation 126 is equal to zero as there are no changes to the upstream density and entropy caused by changes in the downstream pressure. If perturbations in the pressure ratio from atmospheric conditions are used, then the pressure term in Equation 123 is zero because the back pressure is constant. Each derivative is evenly distributed around zero and when time-averaged is equal to zero so $\rho\left(ds/dt\right)=0$. With the exception of $s\frac{\partial \rho}{\partial t}$, it is easy to see that most derivatives would time-average to zero because their time-dependence is of the forms $\cos(wt)$, $\sin(wt)$, $\sin(wt)\cos(wt)$, or cos(wt)/(1+esin(wt), which have values of zero integrated over the whole cycle. However, it is not obvious that the time average of the time rate of change of density multiplied by the downstream entropy, which when time averaged does not equal zero or the steady state value, should also equal zero. Figure 2.8 shows that for quasi-steady flow, this term in the time rate of change in entropy production is exactly zero and the quasi-steady assumption and wavy wall analogy still applies. Each time derivative depends on the perturbation times the frequency εw, so if they are both small (w<100 Hz, $\varepsilon < 0.1$), then the density derivative would be negligible in the continuity equation and the quasi-steady assumption would hold.

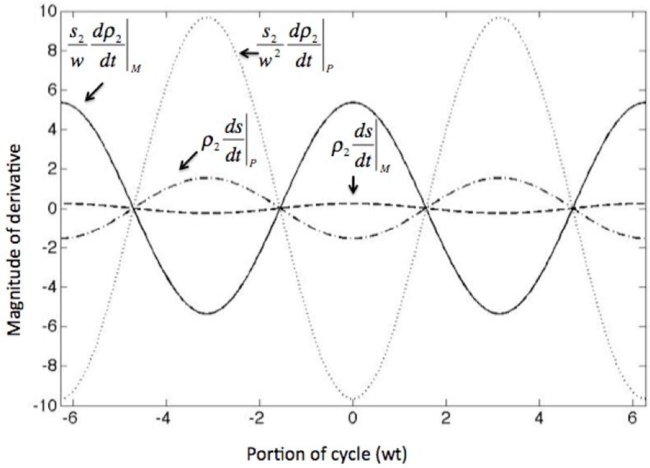

Figure 2.8. Each derivative is a sinusoid with a time-average of zero.

Chapter 3: Inlet Shock Design

Several inlet shocks will be used to study the effect of curvature and Mach number on the perturbation in the entropy gain. There are several different ways of comparing shocks that could prove useful in inlet design. For the purposes of comparing curvature and the stability of different methods of designing inlets, as the shock's curvature is increased, each shock has the same mean parameter as a straight shock and the same capture plane and cowl intersection location. Whether a shock that is designed to have a particular mean normal Mach number, pressure ratio, or temperature ratio is less stable to certain perturbations as the curvature is increased would be of interest to an inlet designer. This section will discuss how the curved shocks used for comparison were constructed.

3.1 Design parameters and methodology

Several inlets will be used to study the effect of curvature and Mach number on the perturbation in the entropy gain. Inlets are constructed for a three-degree wedge angle θ for the straight shock and Mach numbers of 5, 7, and 10. In order to compare the inlets created, each inlet has the same ratio of the inlet height to the distance to the cowl for a straight shock where the shock intersects the inlet and has either the same average Mach number normal to the shock, pressure ratio, or temperature ratio. Comparing inlets created with the same normal Mach number reverts the comparison to one of shock geometry. However, combustion rates in a scramjet are more sensitive to pressure, and hypersonic inlets are usually created with achieving a desired pressure or temperature ratio. For each method of curving the inlet shocks, the shock angle is varied as a power law as it propagates towards the inlet cowl

$$\beta(x,n) = \frac{1}{c_n} x^n + \beta_{\min,n} \tag{127}$$

where *x* is the fraction of the length to the cowl *L* divided by the height of the inlet H at the capture plane, *n* is the curvature, and c_n is a constant determined such that the mean shock angle is always the same as *n*=0, which is a straight shock. The minimum shock angle specified in the profile $\beta_{\min,n}$ is chosen such that the corresponding wedge angle at the inlet entrance is $\beta_{\min,n} = \beta_{n=0} - 10nd\beta_{\min}$ and $d\beta_{\min} = \left(\beta_{n=0} - \beta_{\min,n=1}\right)/10$. The curvatures used were n=0, 0.1, 0.2, 0.3, 0.5, 0.75, and 1.0 with n=0 as the baseline straight shock. The allowed wedge angles run from 3 degrees for n=0 to 0.5 degrees for n=1.0. For the shocks with the most curvature, the wedge angle at the capture plane was the smallest and restricted to a minimum of 0.5 degrees.

3.2 Shocks analyzed

For each design parameter like mean normal Mach number or pressure ratio, 24 inlet shocks were created. The shock angles computed for a Mach 5 inlet are shown in Figure 3.1. As shown in Figure 3.2, which shows the shock position in the inlet, the shock profiles constructed can be thought of as a string stretched from fixed end points with only the curvature changing, allowing for a comparison based primarily on curvature, with respect to the parameter of interest. The inlet length to capture height ratios were *L/H*=4.15 for Mach 5, *L/H*=5.53 for Mach 7, and *L/H*=7.27 for Mach 10, which is consistent with a straight oblique shock for a three degree wedge angle at these Mach numbers intersecting the cowl. The inlet wall can be computed from the theta-beta-Mach number relation and is shown in Figure 3.3 for the Mach 5 shock profiles. Tables 3.1- 3.9 contain the constants c_n for each inlet and maximum and minimum shock angles.

M_∞	Curvature n	c_n	$\beta_{\min}$	$\beta_{\max}$	$\theta_{\min}$	$\theta_{\max}$
5	0.1	6.129	13.39010	13.57821	2.7629	3.0240
5	0.2	3.2401	13.21938	13.62963	2.5232	3.0949
5	0.3	2.29948	13.04865	13.71513	2.2809	3.2122
5	0.5	1.5900	12.70721	13.98844	1.7876	3.5831
5	0.75	1.29722	12.28041	14.52182	1.1542	4.2905
5	1.0	1.215427	11.85360	15.2680	0.5	4.9747

Table 3.1. Constants and shock angles used to create Mach 5 inlets of varying curvature for shocks with same mean normal Mach number (shock angle).

M_∞	Curvature n	c_n	$\beta_{\min}$	$\beta_{\max}$	$\theta_{\min}$	$\theta_{\max}$
7	0.1	6.23852	10.07926	10.26945	2.7668	3.0234
7	0.2	3.3937	9.90658	10.32141	2.5303	3.0929
7	0.3	2.47845	9.73389	10.40786	2.2904	3.2080
7	0.5	1.81485	9.38852	10.68428	1.7999	3.5708
7	0.75	1.59071	8.95681	11.22382	1.1642	4.2596
7	1.0	1.601184	8.52510	11.97879	0.5	5.1854

Table 3.2. Constants and shock angles used to create Mach 7 inlets of varying curvature for shocks with same mean normal Mach number (shock angle).

M_∞	Curvature n	c_n	$\beta_{\min}$	$\beta_{\max}$	$\theta_{\min}$	$\theta_{\max}$
10	0.1	6.1969	7.65857	7.85544	2.7668	3.0229
10	0.2	3.4643	7.47993	7.90918	2.5392	3.0907
10	0.3	2.600005	7.30121	7.99862	2.3027	3.2030
10	0.5	2.0108	6.94376	8.28467	1.8159	3.5564
10	0.75	1.8871	6.49696	8.84311	1.1777	4.2242
10	1.0	2.03387	6.05015	9.62461	0.5	5.1180

Table 3.3. Constants and shock angles used to create Mach 10 inlets of varying curvature for shocks with same mean normal Mach number (shock angle).

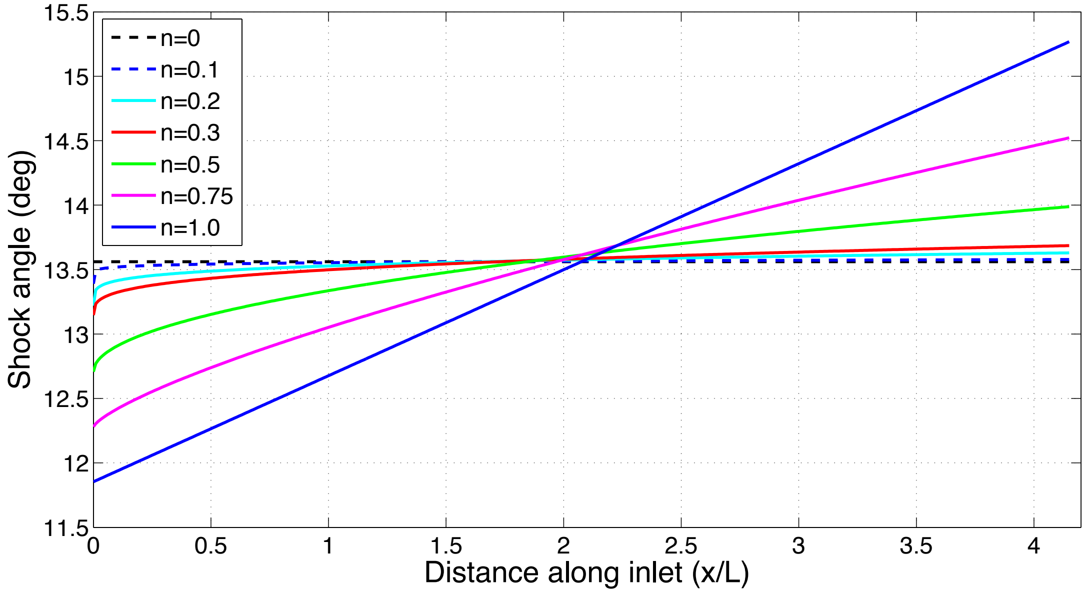

Figure 3.1. Constructed shock angles for Mach 5 inlet; Rectangular inlet has a wedge angle of 3 degrees. Each shock has the same mean angle.

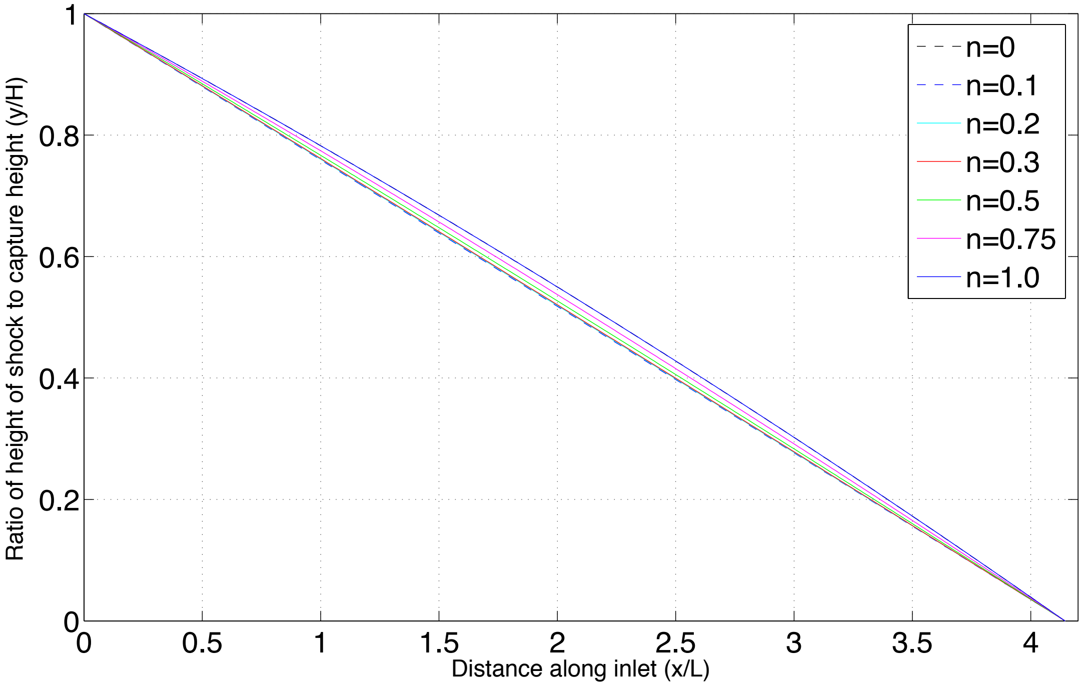

Figure 3.2. Position of shock in inlet where each shock has the same mean shock angle for Mach 5 inlet.

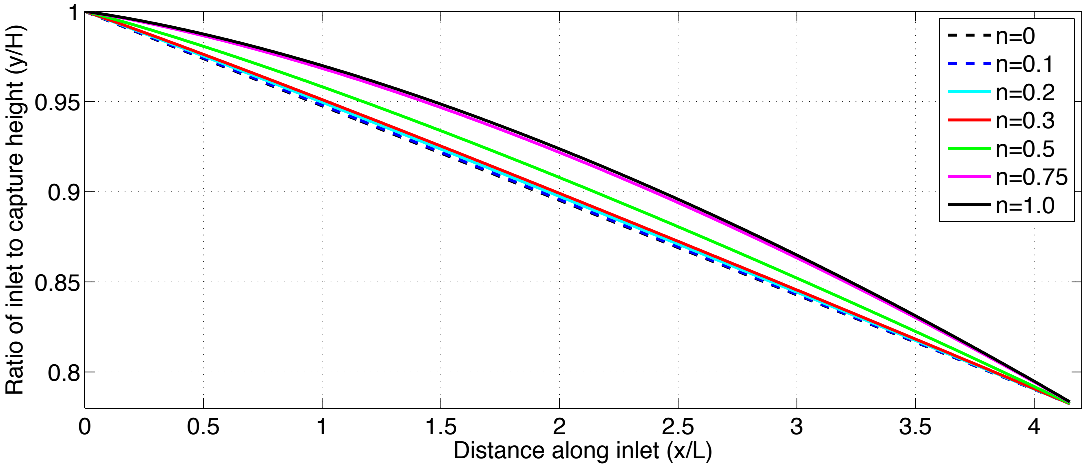

Figure 3.3. Mach 5 inlet profile along centerline constructed from each shock with the same mean shock angle.

M_∞	Curvature n	c_n	$\beta_{\min}$	$\beta_{\max}$	$\theta_{\min}$	$\theta_{\max}$
5	0.1	6.1293842	13.39010	13.57821	2.7629	3.0240
5	0.2	3.241255	13.21938	13.62963	2.5232	3.0947
5	0.3	2.3018	13.04865	13.71513	2.2809	3.2121
5	0.5	1.595831	12.70721	13.98376	1.7876	3.5768
5	0.75	1.3099357	12.28041	14.50065	1.1542	4.2620
5	1.0	1.23869875	11.85360	15.20389	0.5	5.166

Table 3.4. Constants and shock angles used to create Mach 5 inlets of varying curvature for shocks with same mean pressure ratio.

M_∞	Curvature n	c_n	$\beta_{\min}$	$\beta_{\max}$	$\theta_{\min}$	$\theta_{\max}$
7	0.1	6.23902	10.07926	10.07926	2.7629	3.0235
7	0.2	3.395332	9.90658	9.90658	2.5232	3.0927
7	0.3	2.4818837	9.73389	9.73389	2.2809	3.2067
7	0.5	1.8240337	9.38852	9.38852	1.7877	3.5624
7	0.75	1.61219644	8.956812	8.95681	1.1542	4.2216
7	1.0	1.64335119	8.525100	8.52510	0.5	5.0788

Table 3.5. Constants and shock angles used to create Mach 7 inlets of varying curvature for shocks with same mean pressure ratio.

M_∞	Curvature n	c_n	$\beta_{\min}$	$\beta_{\max}$	$\theta_{\min}$	$\theta_{\max}$
10	0.1	6.197482	7.85542	7.65866	2.7629	7.8554
10	0.2	3.4665219	7.90889	7.47993	2.5232	7.9089
10	0.3	2.6049504	7.99729	7.30121	2.2809	7.9973
10	0.5	2.0247769	8.27541	6.94376	1.7877	8.2754
10	0.75	1.92206157	8.80043	6.49696	1.1542	8.8004
10	1.0	2.10712665	9.50034	6.05015	0.5	9.5003

Table 3.6. Constants and shock angles used to create Mach 10 inlets of varying curvature for shocks with same mean pressure ratio.

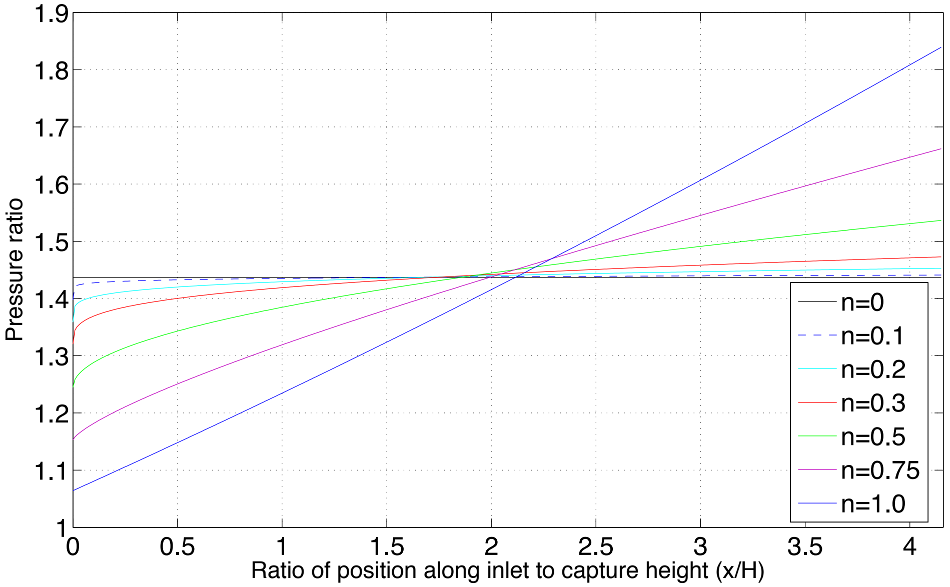

Figure 3.4. Pressure ratio along inlet for each inlet constructed with same mean pressure ratio for Mach 5 inlet.

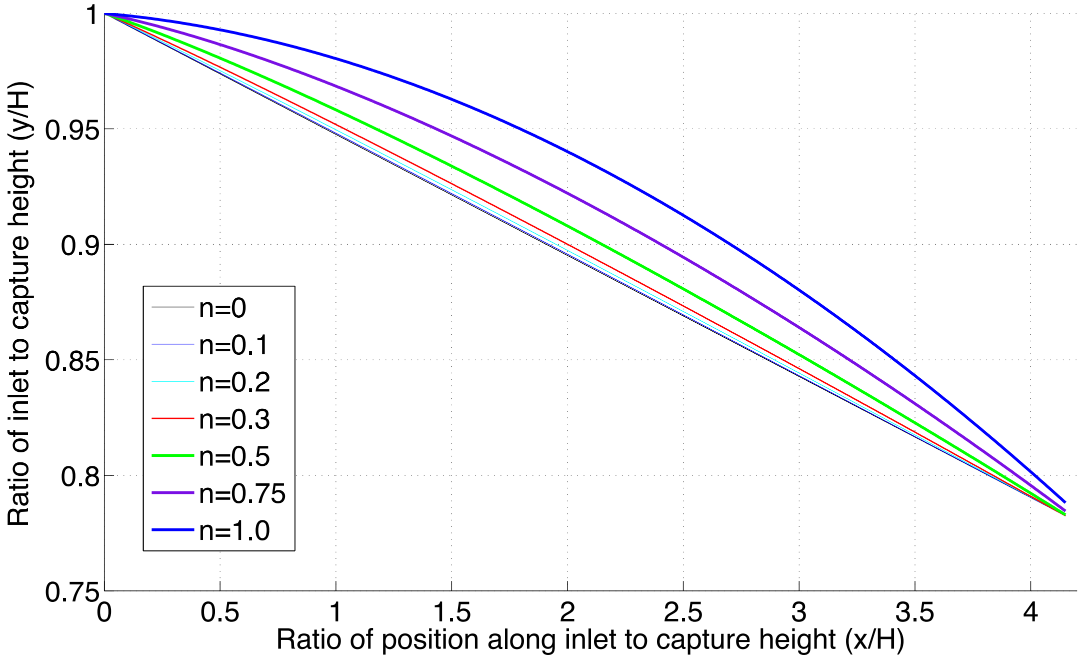

Figure 3.5. Mach 5 inlet centerline wall profile for inlets designed for same mean pressure ratio.

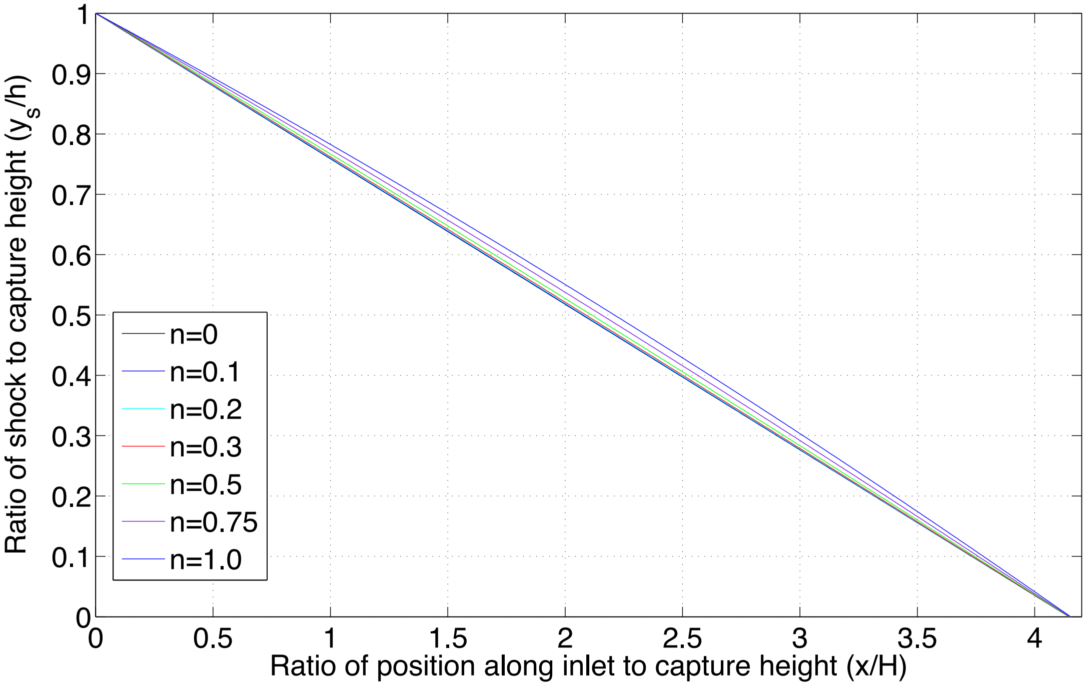

Figure 3.6. Position of shock in inlet where each shock has the same mean pressure ratio for Mach 5 inlet.

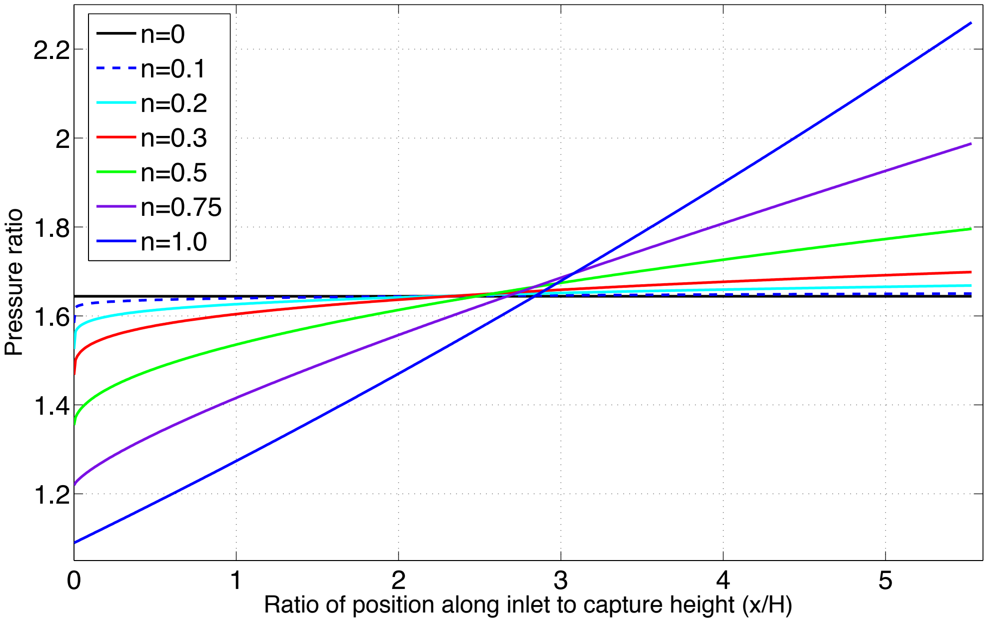

Figure 3.7. Pressure ratio along inlet for each inlet constructed with same mean pressure ratio for Mach 7 inlet.

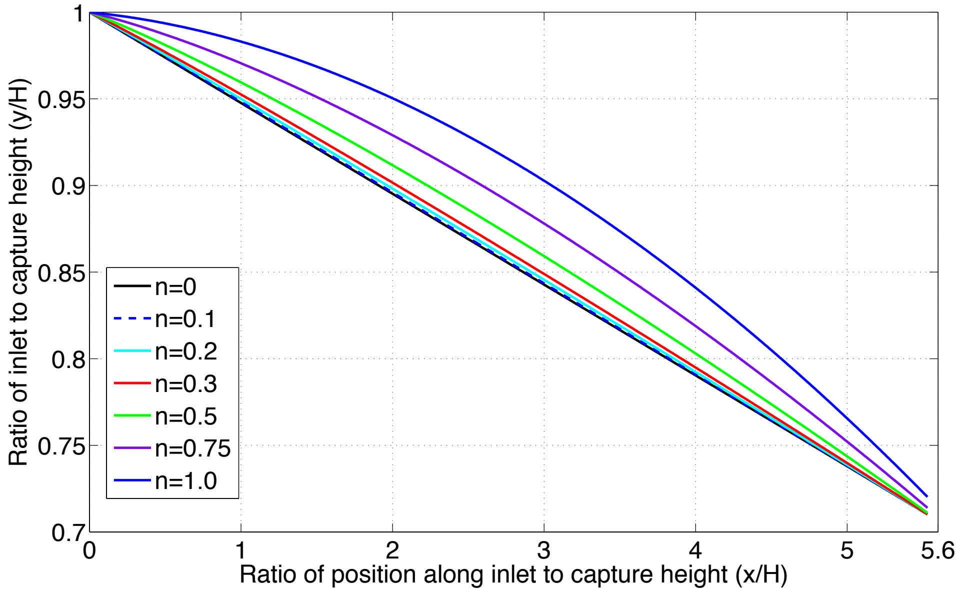

Figure 3.8 Mach 7 inlet centerline wall profile for inlets designed for same mean pressure ratio.

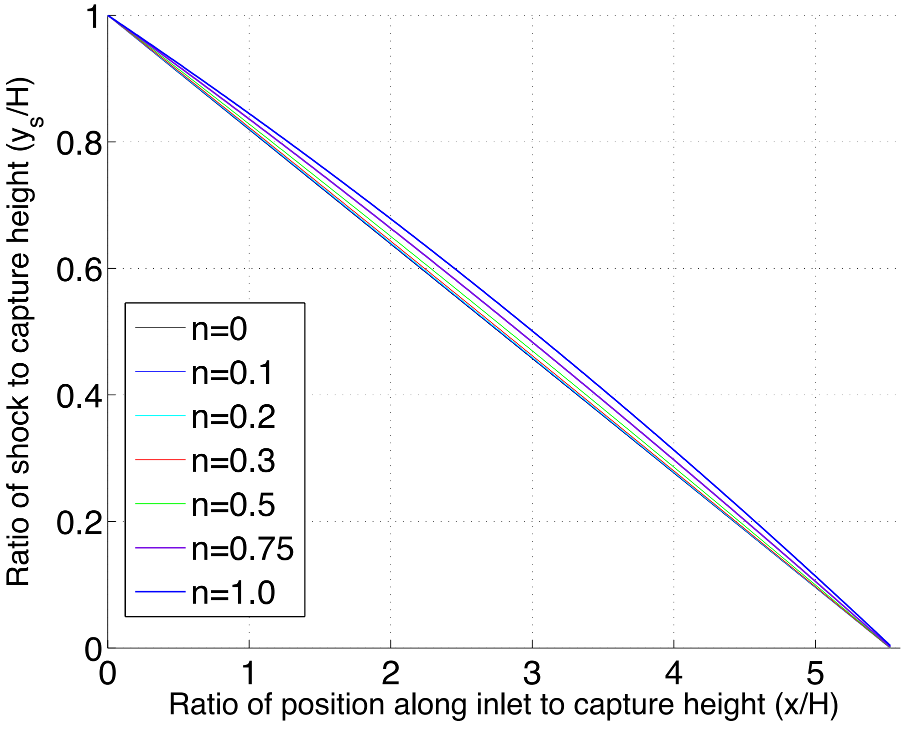

Figure 3.9. Mach 7 inlet profile along centerline constructed from each shock with the same mean pressure ratio.

M_∞	Curvature n	c_n	$\beta_{\min}$	$\beta_{\max}$	$\theta_{\min}$	$\theta_{\max}$
5	0.1	6.12895	13.39010	13.57821	2.7629	3.0240
5	0.2	3.2399155	13.21938	13.62963	2.5232	3.0949
5	0.3	2.2990725	13.04865	13.71513	2.2809	3.2123
5	0.5	1.588936	12.70721	13.98930	1.7876	3.5847
5	0.75	1.2948698	12.28041	14.52589	1.1542	4.2958
5	1.0	1.21118875	11.85360	15.27999	0.5	5.2619

Table 3.7. Constants and shock angles used to create Mach 5 inlets of varying curvature for shocks with same mean temperature ratio.

M_∞	Curvature n	c_n	$\beta_{\min}$	$\beta_{\max}$	$\theta_{\min}$	$\theta_{\max}$
7	0.1	6.238545	10.07926	10.26945	2.7629	3.0235
7	0.2	3.393774	9.90658	10.32140	2.5232	3.0929
7	0.3	2.4785935	9.73389	10.40782	2.2809	3.2079
7	0.5	1.81518032	9.38852	10.68404	1.7877	3.5705
7	0.75	1.5913986	8.95681	11.22284	1.1542	4.2583
7	1.0	1.60259635	8.52510	11.97575	0.5000	5.1817

Table 3.8. Constants and shock angles used to create Mach 7 inlets of varying curvature for shocks with same mean temperature ratio.

M_∞	Curvature n	c_n	$\beta_{\min}$	$\beta_{\max}$	$\theta_{\min}$	$\theta_{\max}$
10	0.1	6.197024	7.82921	6.19702	2.7629	3.0229
10	0.2	3.4649172	7.80235	3.46491	2.5232	3.0906
10	0.3	2.60144157	7.75510	2.60144	2.2809	3.2025
10	0.5	2.0147566	7.59848	2.01476	1.7877	3.5532
10	0.75	1.89679918	7.29567	1.89680	1.1542	4.2102
10	1.0	2.05396055	6.89729	2.05396	0.5000	5.0789

Table 3.9. Constants and shock angles used to create Mach 10 inlets of varying curvature for shocks with same mean temperature ratio.

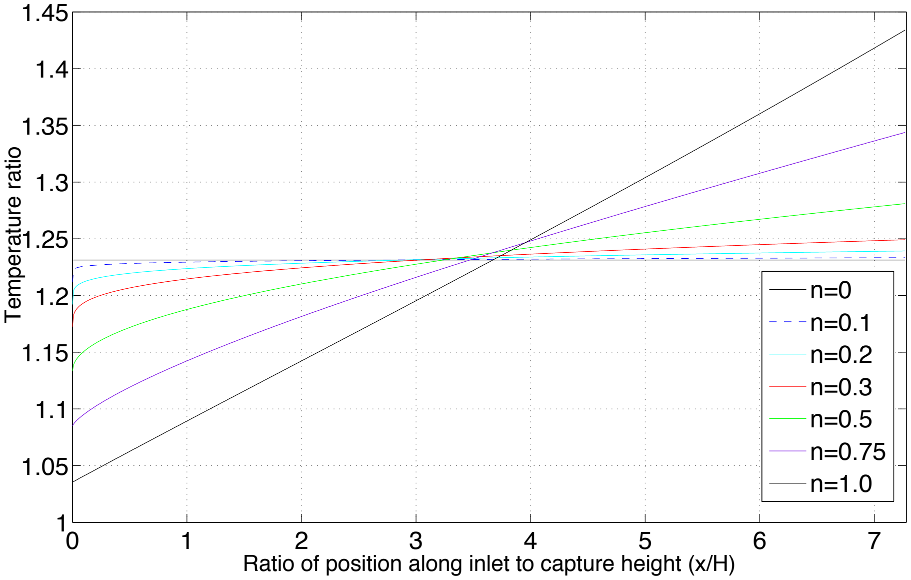

Figure 3.10. Constructed temperature ratios across a shock along each Mach 10 inlet; Rectangular inlet has a wedge angle of 3 degrees. Each shock has the same mean temperature ratio.

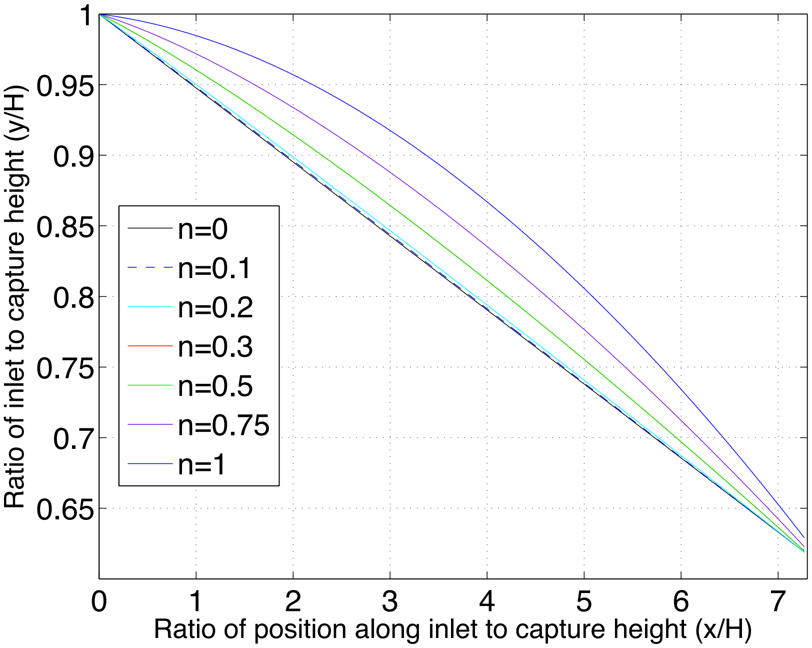

Figure 3.11. Mach 10 inlet centerline wall profile for inlets designed for same mean temperature ratio.

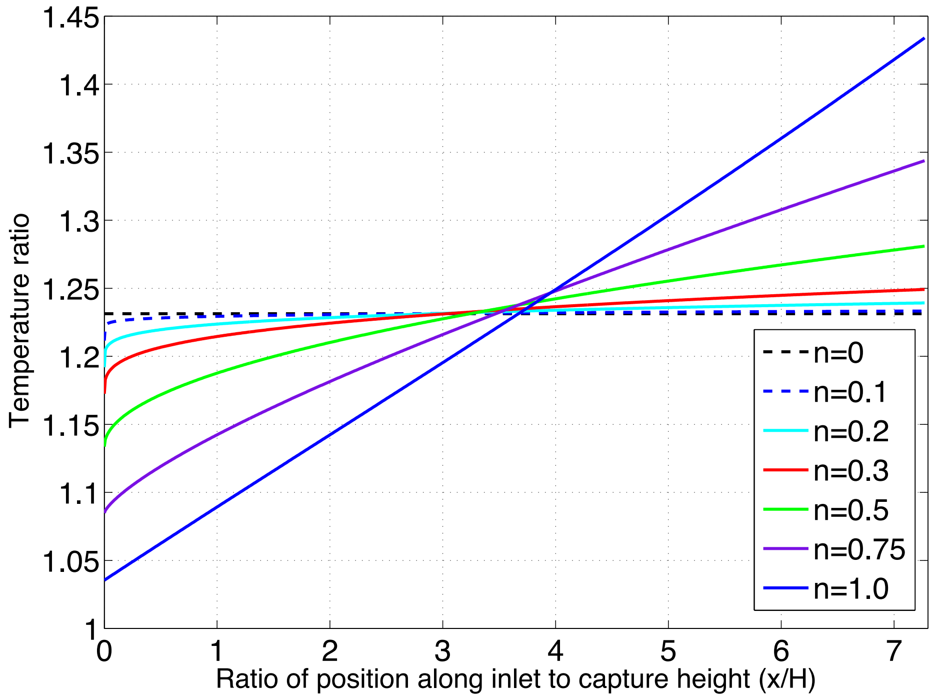

Figure 3.12. Position of shock in inlet where each shock has the same mean temperature ratio for Mach 10 inlet.

Chapter 4: Quasi-steady shock entropy analysis results

A comparison of the time average of the convected entropy flux across a shock for a straight shock in a rectangular hypersonic inlet and a curved shock in a three-dimensional hypersonic inlet reveals several interesting trends. First, results will be shown relating the entropy perturbation for Mach number, downstream pressure, upstream thermodynamic variable, and angle perturbations to normal Mach number. Because the chemistry and properties of air changes at the high temperatures corresponding to hypersonic flight, the entropy perturbation, which depends on the ratio of specific heats γ, will be compared at different ratios of specific heats. Finally, a comparison of curved shocks in general, shocks with different curvature, and shocks in inlets designed for different parameters of interest to rectangular shocks will be shown.

4.1 Upstream Mach number

Equations 93 and 94 for entropy perturbation, resulting from a sinusoidal change in normal Mach number,

$$\left.\frac{\rho u(\Delta s)}{\rho_1 u_1 R}\right|_{average} \cong \left.\frac{\Delta s}{R}\right|_{steady} + \left\{ -\frac{2(\gamma+1)M_1^2}{\left(2+(\gamma-1)M_1^2\right)^2}\left.\frac{\Delta s}{R}\right|_{steady} + \frac{4\gamma\left(1-M_1^2\right)^3}{\left(2+(\gamma-1)M_1^2\right)^2\left(2\gamma M_1^2-(\gamma-1)\right)} \right.$$
$$\left. -\left(M_1^2-1\right)\frac{2(\gamma-1)\left(\gamma M_1^6+1\right)-\left(9\gamma^2-4\gamma-1\right)M_1^4+3\left(\gamma^2-4\gamma-1\right)M_1^2}{4\gamma\left(\left((\gamma-1)M_1^2+2\right)\left(2\gamma M_1^2-(\gamma-1)\right)\right)^2} \right\}\varepsilon^2 \tag{93}$$

$$\frac{\Delta s}{R} = \left.\frac{\Delta s}{R}\right|_{steady} + G\left(M_{n,1},\gamma\right)\varepsilon^2 \tag{94}$$

can be used to determine the normal Mach number at which the shock is no longer stable to upstream Mach number perturbations, based on the principle of minimum entropy. The zero of $G\left(M_{n,1},\gamma\right)$ can be determined by re-arranging and setting the numerator of the perturbation,

$$4\gamma\left(1-M_1^2\right)^3\left(2\gamma M_1^2-(\gamma-1)\right)-\left(M_1^2-1\right)\left(2(\gamma-1)\left(\gamma M_1^6+1\right)-\left(9\gamma^2-4\gamma-1\right)M_1^4+3\left(\gamma^2-4\gamma-1\right)M_1^2\right)$$

equal to zero. This results in a zero at a normal Mach number of 1.58. For normal Mach numbers less than this, the principle of minimum entropy suggests that the unsteady flow tends to stabilize to a steady flow. For normal Mach numbers higher than 1.58, the flow should remain unsteady as a result of the perturbations or flight at off-design conditions. Thus, this result predicts that an inlet will be stable to Mach number perturbations if the turning angle is less than 8.96 degrees for a Mach 5 inlet, 6.42 degrees for a Mach 7 inlet, and 4.52 degrees for a Mach 10 inlet. The function has a maximum at M=1.32, which suggests that inlets designed near this normal Mach number might be more forgiving to speed and Mach number changes. The inflection point where the second derivative becomes positive is M=2.56. Figures 4.1 and 4.2 show a plot of Mach number versus the entropy perturbation function $G\left(M_{n,1},\gamma\right)$ and Figure 4.3 shows the first and second derivative of the entropy perturbation with respect to Mach number. As expected, the entropy flux perturbation asymptotes to a very large negative value as the normal Mach number gets large.

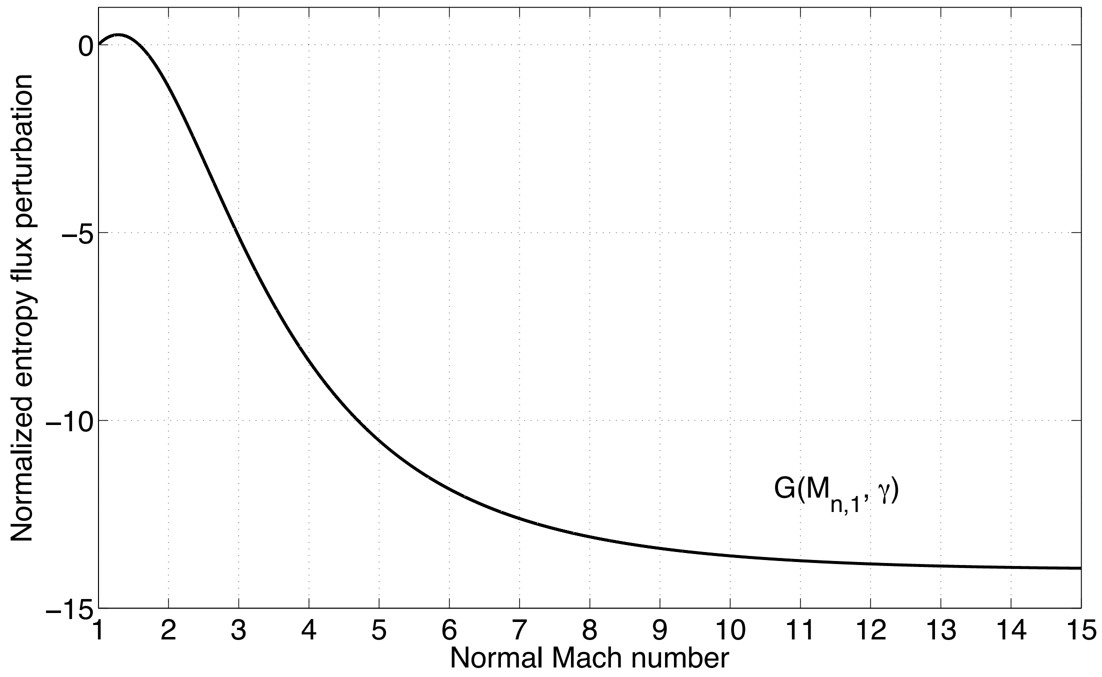

Figure 4.1 Normalized entropy flux perturbation versus normal Mach number.

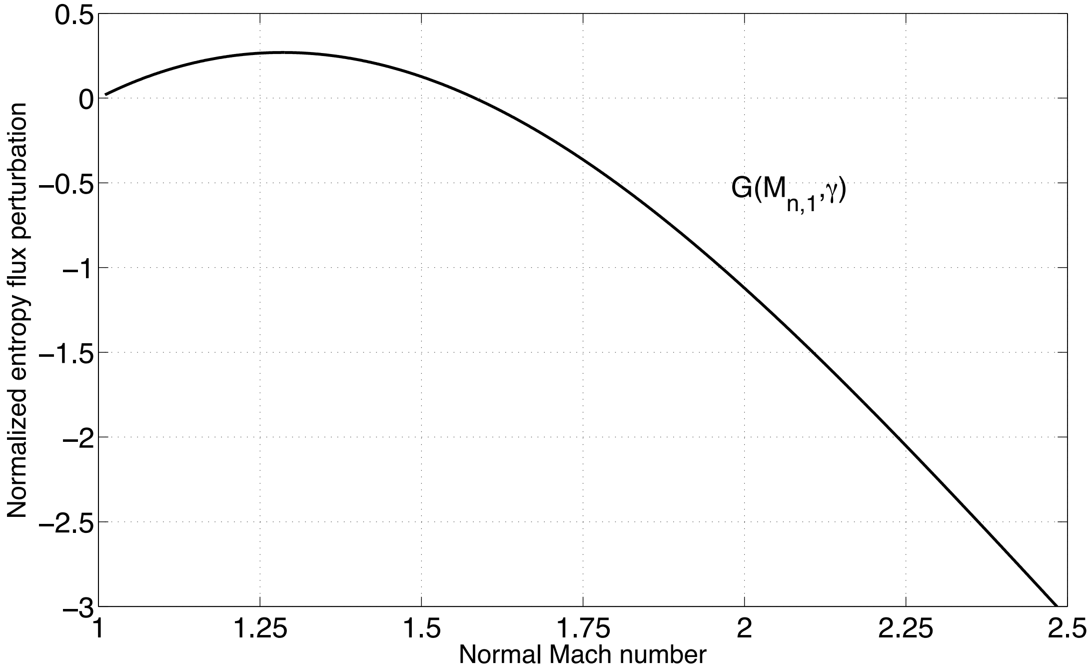

Figure 4.2. Focus on normal Mach numbers applicable to hypersonic inlets.

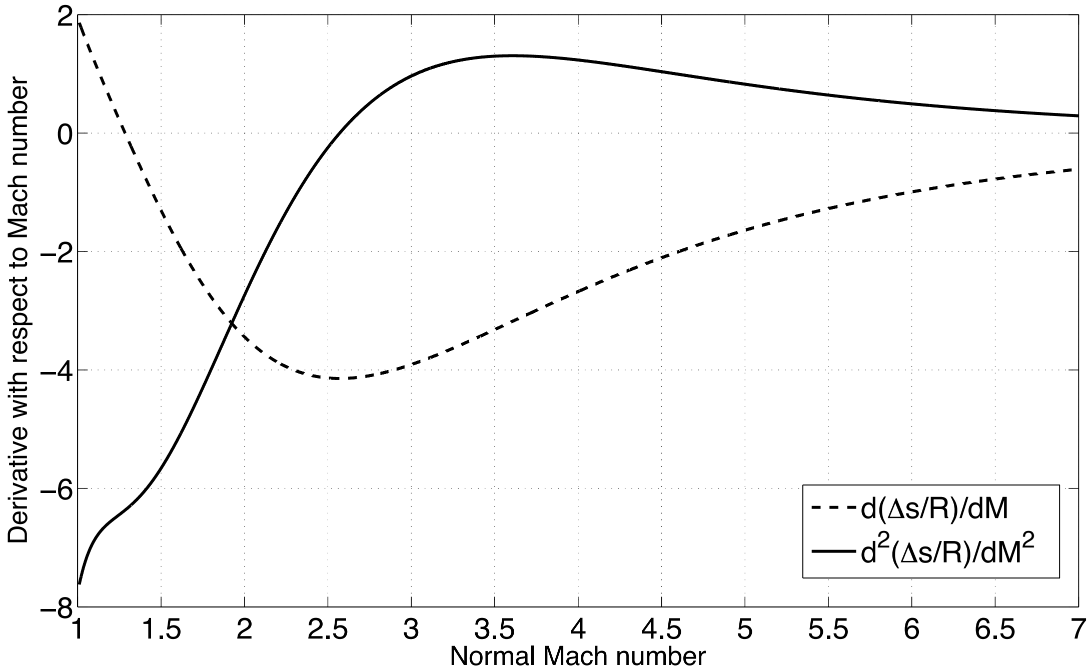

Figure 4.3. First and second derivative of entropy perturbation with respect to normal Mach number for normal Mach number perturbation.

4.2 Downstream pressure

The results for predicted stability based on the principle of minimum entropy for a downstream pressure perturbation are shown in Figures 4.4-4.6. These figures are based on Equation 103,

$$\frac{\Delta s}{R} = \left.\frac{\Delta s}{R}\right|_{steady} + \frac{1}{2(\gamma-1)}\left[\frac{8(\gamma^2-1)\hat{P}^3 + 8(\gamma^2+1)\hat{P}^2}{[\gamma^4-2\gamma^2+1]\left(\hat{P}^4+1\right) + 4[\gamma^4-1]\left(\hat{P}^3+\hat{P}\right) + [6\gamma^4+4\gamma^2+6]\hat{P}^2} - 1\right]\varepsilon^2$$

$$\frac{\Delta s}{R} = \left.\frac{\Delta s}{R}\right|_{steady} + H\left(\hat{P},\gamma\right)\phi^2$$

The normal Mach number at which a shock is no longer stable to perturbations and remains unsteady based on the principle of minimum entropy can be determined based on where $H\left(P\left(M_{n,1}\right),\gamma\right)$ equals zero. This results in a zero at a normal Mach number of 2.19 and a pressure ratio of 5.43. For normal Mach numbers or pressure ratios less than this, the principle of minimum entropy suggests that the unsteady flow tends to stabilize to a steady flow for back pressure perturbations. For normal Mach numbers higher than 2.19 or pressure ratios higher than 5.43, the flow remains unsteady to back pressure perturbations. Thus, this result predicts that an inlet will be stable to back pressure perturbations if the turning angle is less than 16.55 degrees for a Mach 5 inlet, 11.84 degrees for a Mach 7 inlet, and 8.29 degrees for a Mach 10 inlet. The function $H\left(P\left(M_{n,1}\right),\gamma\right)$ has a maximum at M=1.47. The inflection point where the second derivative with respect to Mach number d^2H/dM^2 becomes positive is M=2.62. This occurs at M=2.21 and a pressure ratio of 5.535 for the second derivative with respect to pressure ratio d^2H/dP^2. Figure 4.8 shows the first and second derivative of the entropy perturbation with respect to Mach number, while Figure 4.9 shows these derivatives with respect to pressure. As expected, the entropy flux perturbation asymptotes to a very large negative value as the normal Mach number gets large. The Mach number and pressure ratios at which a hypersonic inlet should be stable to small quasi-steady back pressure perturbations based on the principle of minimum entropy is higher than for atmospheric perturbations or other upstream perturbations. This suggests that the varying mass flux may have a de-stabilizing effect.

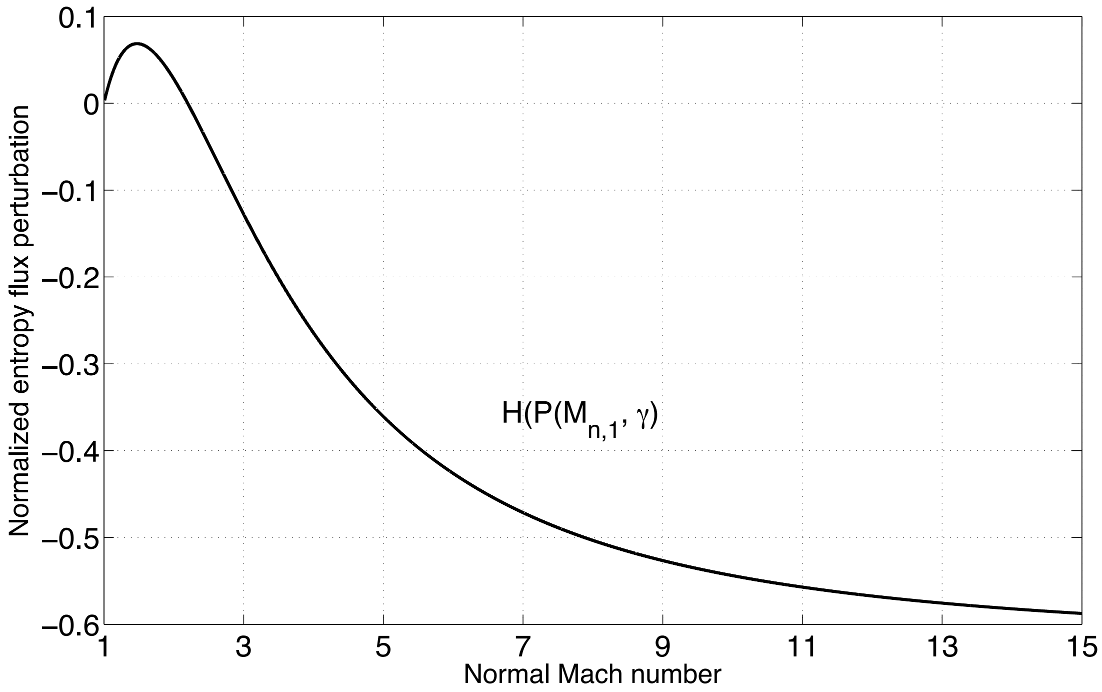

Figure 4.4 Normalized entropy flux perturbation for back pressure perturbation versus normal Mach number.

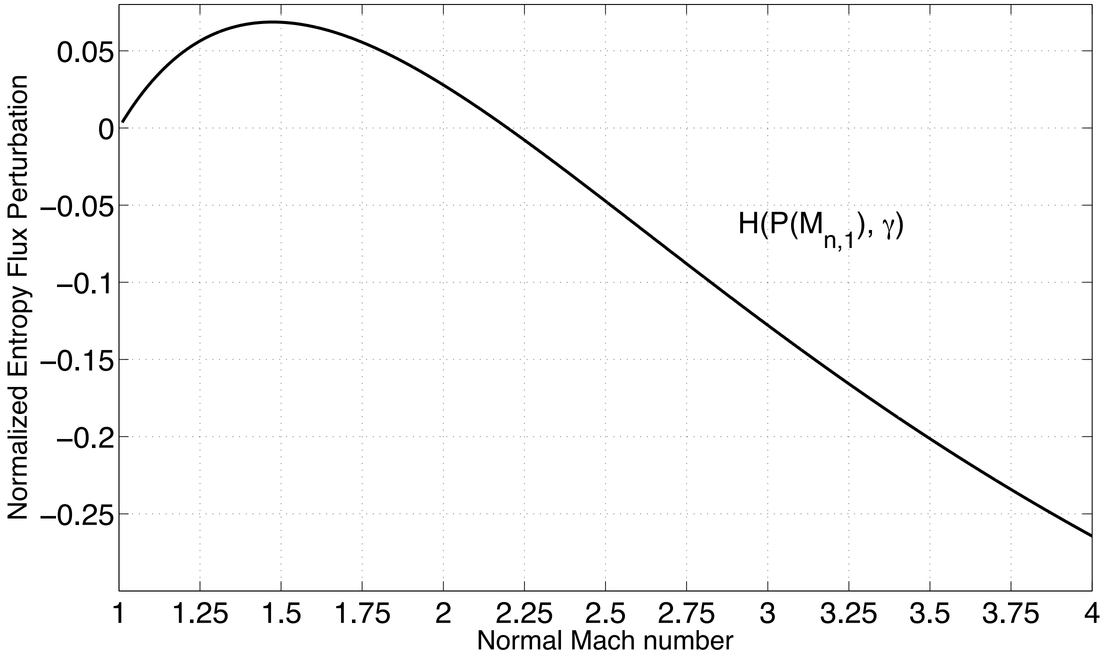

Figure 4.5. Focus on normal Mach numbers applicable to hypersonic inlets for entropy perturbation resulting from back pressure perturbations.

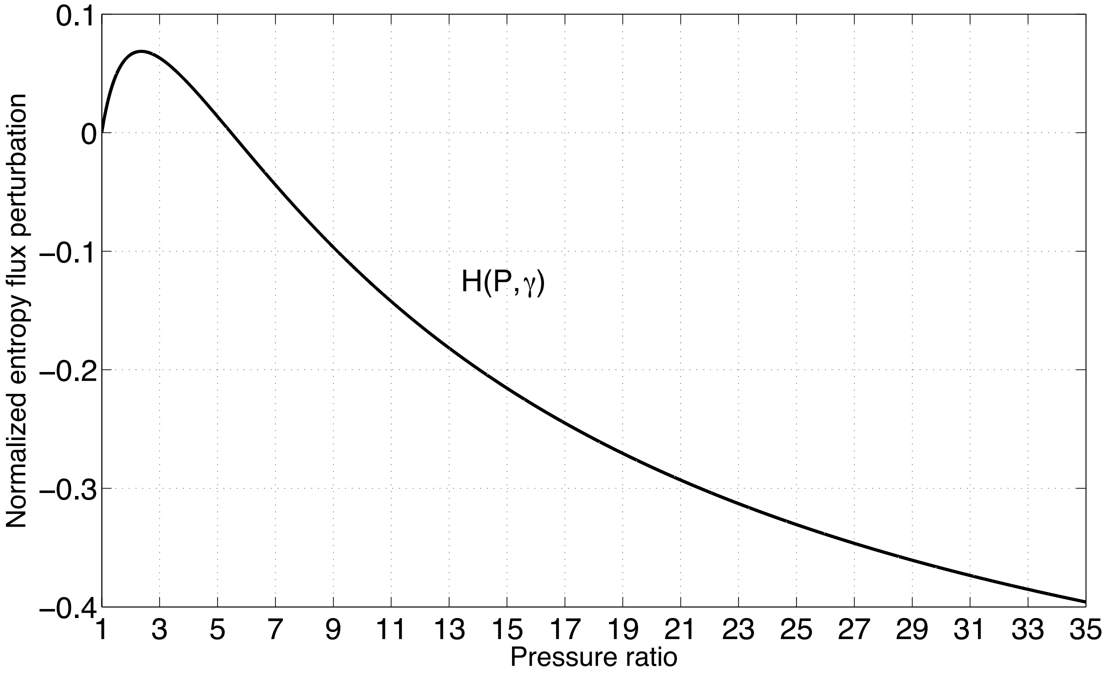

Figure 4.6 Normalized entropy flux perturbation for back pressure perturbation versus pressure ratio.

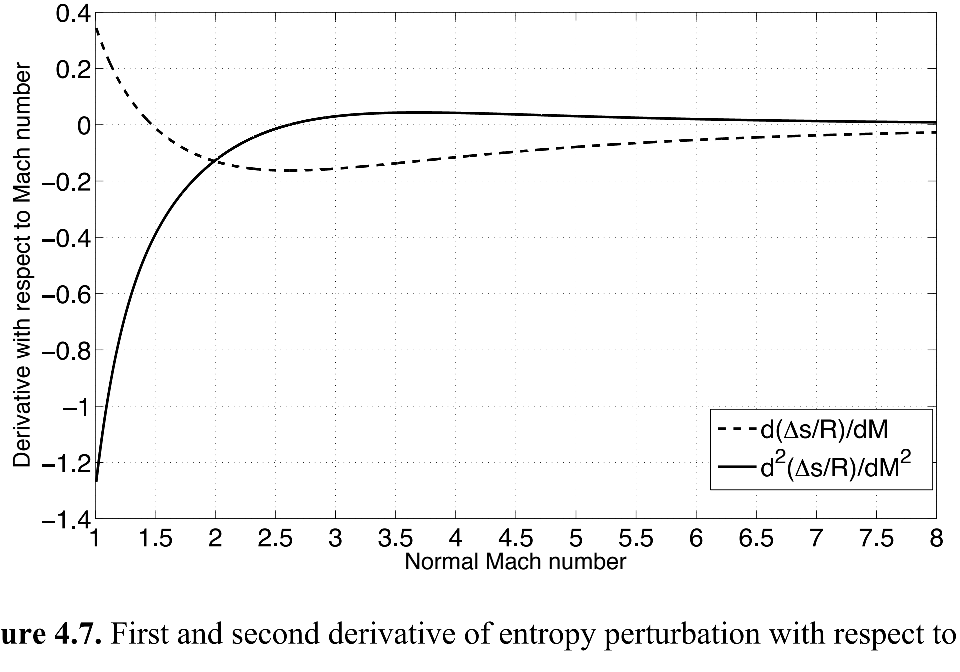

Figure 4.7. First and second derivative of entropy perturbation with respect to normal Mach number for back pressure perturbation.

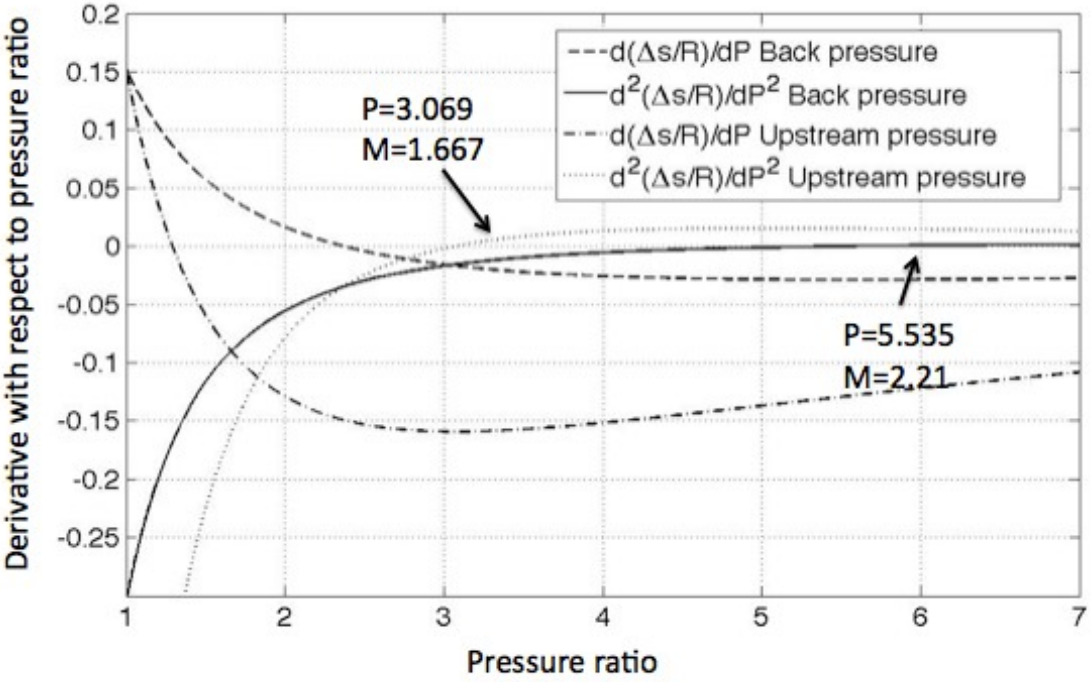

Figure 4.8. First and second derivative of entropy perturbation with respect to pressure ratio for back pressure and upstream conditions perturbations.

4.3 Upstream pressure and atmospheric conditions

Because perturbations in atmospheric conditions change the upstream mass flux, higher order terms are introduced, decreasing the entropy gain relative to the steady shock. The velocity does not change, but the upstream speed of sound and density do change isentropically. The convected entropy flux perturbation for perturbations in upstream thermodynamic variables can be determined from Equation 107 derived above,

$$\left.\frac{pu\Delta s}{p_1 u_1 R}\right|_{avg} = \left.\frac{\Delta s}{R}\right|_{steady} + \left\{ \frac{1}{\gamma(\gamma-1)} \left\{ \frac{4\gamma^2 \hat{P}}{(\gamma-1)\hat{P}^2 + 2(\gamma^2-1)\hat{P} + (\gamma^2-1)} - 1 \right\} - \frac{1}{2(\gamma-1)} \right.$$
$$\left. \left[1 - \frac{8\gamma^2\left[(\gamma^2-1)\hat{P}^3 + (\gamma^2+1)\hat{P}\right]}{(\gamma^4-2\gamma^2+1)\left(\hat{P}^4+1\right) + 4(\gamma^4-1)\left(\hat{P}^3+\hat{P}\right) + (6\gamma^4+4\gamma^2+6)\hat{P}^2} \right] \right\} \phi^2 = \left.\frac{\Delta s}{R}\right|_{steady} + J(P)\phi^2$$

This time-averaged convected entropy flux perturbation is plotted in Figures 4.9 to 4.11. This perturbation has the same behavior as the time-averaged convected entropy flux perturbation for changes in Mach number or downstream pressure, however it is smaller than the time-averaged entropy flux perturbation resulting from changes in downstream pressure and of order magnitude smaller than that resulting from changes in normal Mach number. Figure 4.9 shows the dependence on normal Mach number with Figure 4.10 showing a zoom on the area where the perturbation is positive. This equation has a zero at $M_1 = 1.25$, which is the lowest Mach number at which the theorized transition between stable and unstable based on entropy considerations occurs for any of the four perturbation types examined. This result means that only inlets with turning angles under 4.24 degrees for Mach 5, 3.04 degrees for Mach 7, and 2.15 degrees for a Mach 10 inlet would be stable to this type of perturbation. It also suggests that inlets may be less forgiving to perturbations in altitude than other expected types of perturbations; however, as Lewis' analysis[46] indicates, it is possible based on the shock equations and geometry to choose an inlet turning angle for a given speed that results in a fixed shock even if the vehicle is flying at a slightly lower or higher altitude. The increase in entropy production is the highest at $M_1 = 1.12$. Figure 4.11 shows the dependence of the time-averaged convected entropy flux perturbation *J* on the pressure ratio. Culick and Rogers' work on linearizing acoustic waves to look at the response of a normal shock in a diffuser to an upstream sinusoidal pressure oscillation found a similar result for the shock's stability[55]. Incorporating viscous effects such as separation, they found the shock should become unstable above Mach 1.48, which is not too far off the result of Mach 1.25 using the principle of minimum entropy.

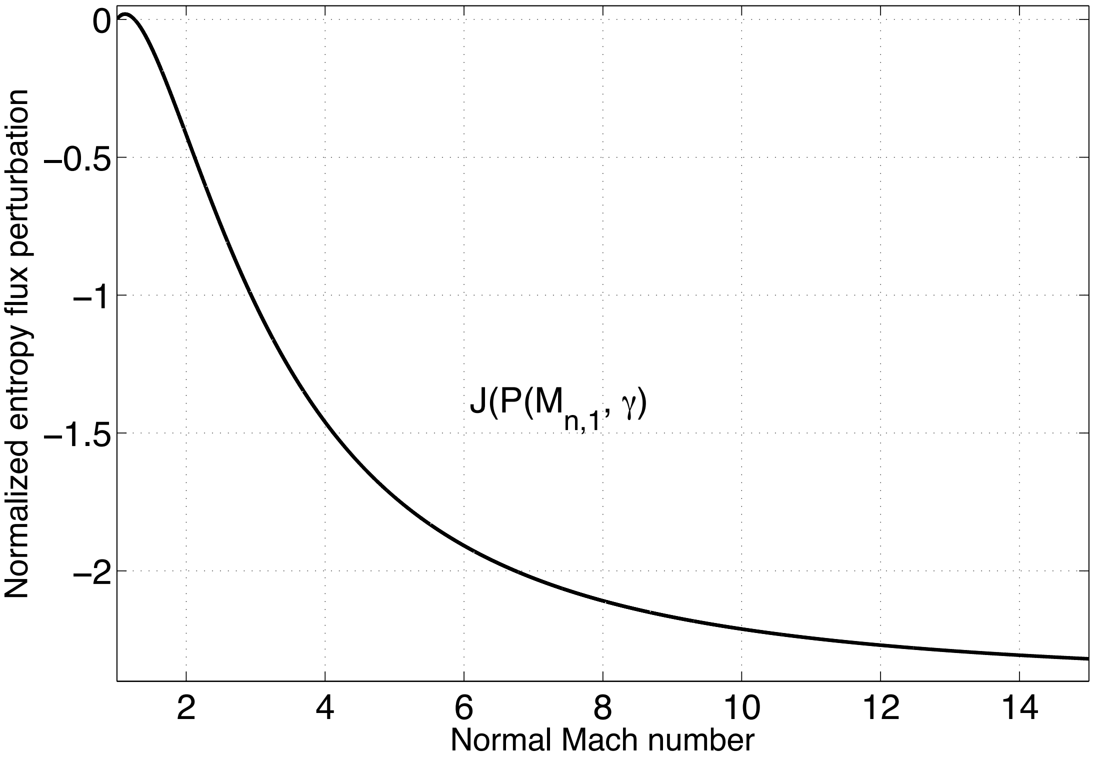

Figure 4.9 Normalized entropy flux perturbation for atmospheric perturbations versus normal Mach number.

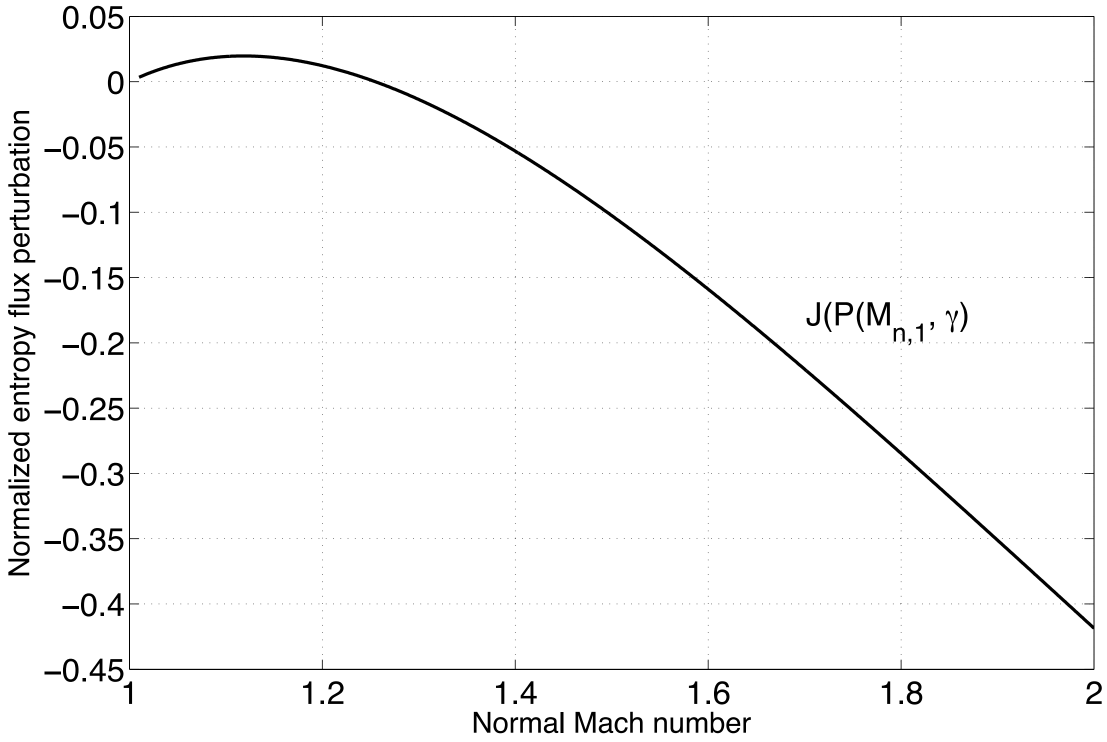

Figure 4.10. Focus on normal Mach numbers applicable to hypersonic inlets for entropy perturbation resulting from atmospheric perturbations.

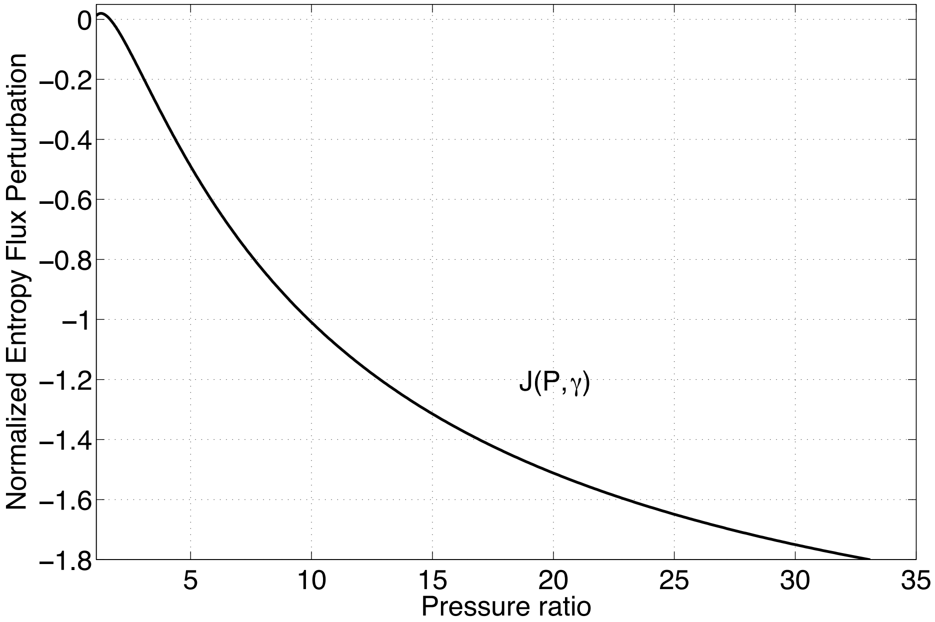

Figure 4.11. Normalized entropy flux perturbation for perturbation in upstream conditions versus pressure.

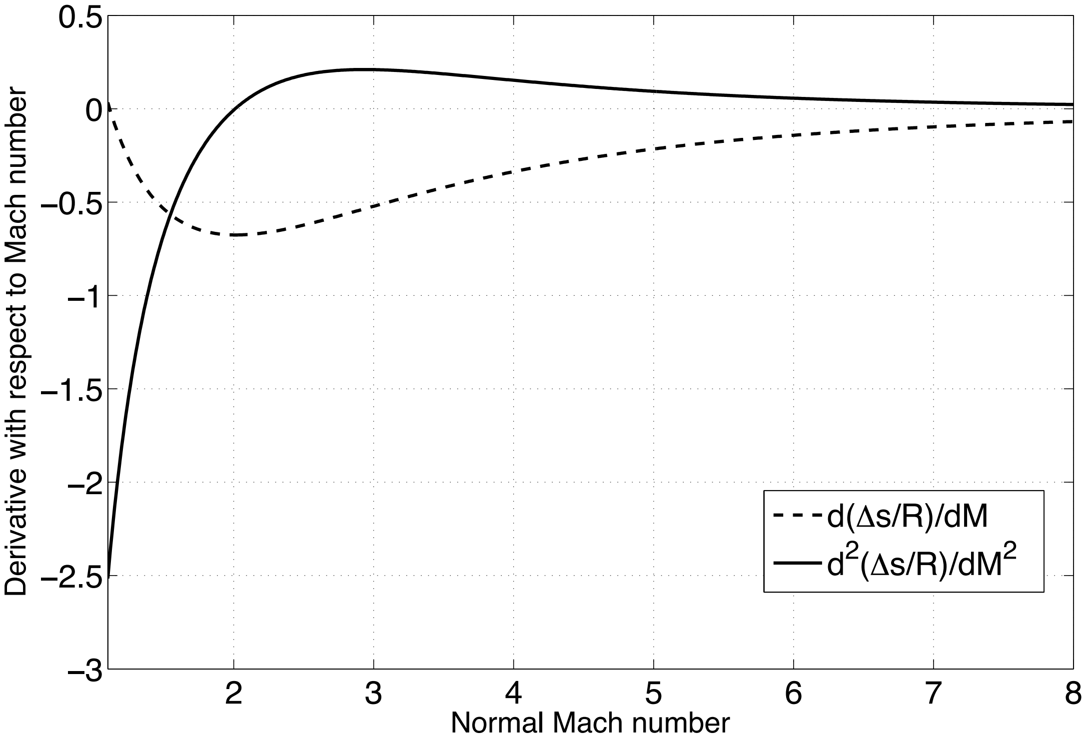

Figure 4.12. First and second derivative of entropy perturbation with respect to Mach number for upstream conditions perturbations.

The inflection point where the second derivative with respect to Mach number becomes positive occurs at *M*=2.01. This occurs at *M*=1.667 and a pressure ratio of 3.07 for the second derivative with respect to pressure ratio as shown in Figure 4.8. Figure 4.12 shows the first and second derivative of the entropy perturbation with respect to Mach number.

4.4 Sinusoidal angle perturbations

Because the expression for the shock angle perturbation is very similar to the expression found for the Mach number perturbation, the results for angle perturbations are similar to those for normal Mach number perturbations[81]. The expressions are similar, but with a different weighting to each term based on a non-linear dependence on the perturbation size and mean shock angle. This also results in a freestream Mach number dependence on the results, which was not the case for the other perturbations. The expression used for assessing the entropy perturbation derived previously is as follows,

$$
\begin{aligned}
\left.\frac{\rho u\left(\Delta s\right)}{R\rho_1 u_1}\right|_{average} \cong \left.\frac{\Delta s}{R}\right|_{steady} &+ \left\{-\frac{2\left(\gamma+1\right)M_1^2}{\left(2+\left(\gamma-1\right)M_1^2\right)^2}\left.\frac{\Delta s}{R}\right|_{steady}\left(\sin^2\varepsilon\cot^2\hat{\beta}-\left(\varepsilon\beta\right)^2\right)\right. \\
&+\frac{2\gamma\left(1-M_1^2\right)^3}{\left(2+\left(\gamma-1\right)M_1^2\right)^2\left(2\gamma M_1^2-\left(\gamma-1\right)\right)}\times\left(\cos\hat{\beta}\cot\hat{\beta}\sin\varepsilon\beta\sin 2\varepsilon\beta\right) \\
&\left.-\left(M_1^2-1\right)\frac{2\left(\gamma-1\right)\left(\gamma M_1^6+1\right)-\left(9\gamma^2-4\gamma-1\right)M_1^4+3\left(\gamma^2-4\gamma-1\right)M_1^2}{4\gamma\left(\left(\left(\gamma-1\right)M_1^2+2\right)\left(2\gamma M_1^2-\left(\gamma-1\right)\right)\right)^2}\gamma\left(\cot^2\hat{\beta}\sin^2\varepsilon\beta-\left(\varepsilon\beta\right)^2\right)\right\}
\end{aligned}
\tag{114}
$$

$$
\left.\frac{\rho u\left(\Delta s\right)}{R\rho_1 u_1}\right|_{average} = \left.\frac{\Delta s}{R}\right|_{steady} + K\left(M,\varepsilon,\hat{\beta}\right)\varepsilon^2 \tag{115}
$$

Figure 4.13 shows the behavior of the perturbation in normalized convected entropy versus upstream normal Mach number for a shock angle perturbation where $K\left(M,\varepsilon,\hat{\beta}\right)$ is the perturbation term in Equation 115 divided by the square of the perturbation size. This was done to normalize the entropy perturbation to allow for a direct comparison with the other perturbations, which will become useful when curved shocks are analyzed. As the freestream Mach number increases, so does the size of the entropy perturbation, the normal Mach number at which the maximum perturbation occurs, the range of normal Mach numbers at which the perturbation is positive, and the normal Mach number of the zero in the second derivative where the perturbation is negative. Also, as expected, as the freestream Mach number is decreased, the normal Mach number at which the inlet becomes unstable approaches the value for Mach number perturbations.

Table 4.1 contains the Mach number at which the maximum, zero entropy perturbation, and change in curvature of the entropy perturbation occurs for Mach number and shock angle perturbations. The range of stable normal Mach numbers, according to the principle of minimum entropy, is larger for a shock angle perturbation than a freestream Mach number perturbation. For example, a Mach 10 inlet with a 5-degree ramp would be stable to perturbations in the vehicle's orientation but not to changes in its speed.

	Shock angle perturbation									**Mach number perturbation**		
	Maximum			**Zero**			**Inflection point**			**Maximum**	**Zero**	**Inflection point**
M_∞	M_n	β	θ	M_n	β	θ	M_n	β	θ	M_n	M_n	M_n
5	1.31	15.19	5.15	1.63	19.02	9.62	2.32	27.65	18.08	1.32	1.58	2.56
7	1.35	11.12	4.13	1.7	14.06	7.56	2.6	21.8	15.19	1.32	1.58	2.56
10	1.36	7.82	2.97	1.75	10.08	5.62	2.78	16.14	11.6	1.32	1.58	2.56

Table 4.1. Entropy perturbation due to shock angle perturbations versus Mach number and compared to Mach number perturbations.

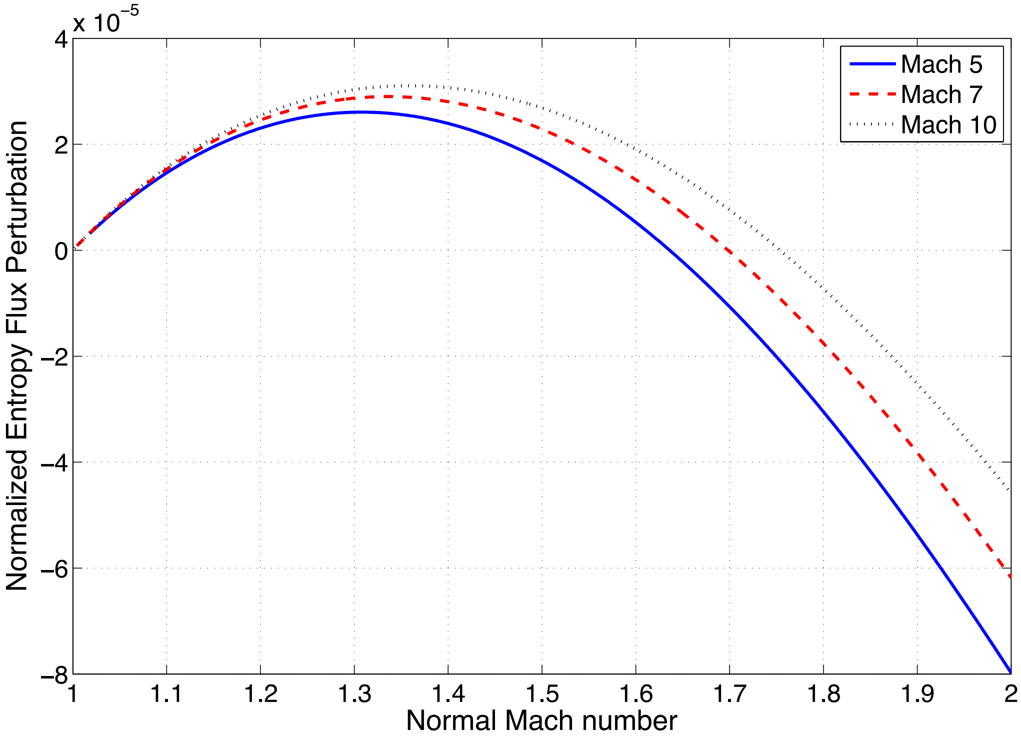

Figure 4.13. The behavior of the perturbation in convected entropy across a shock versus normal Mach number for a sinusoidal perturbation in the shock angle.

4.5 Effect of ratio of specific heats

Because at higher hypersonic speeds or at temperatures entering the isolator, in the combustor, or in the nozzle, the gas may no longer be calorically perfect or could be chemically reacting; in that case, the ratio of specific heats γ will no longer be a constant value of 1.4. Because the thermodynamic properties across the shock depend on γ, this could affect the value of the time-averaged convected entropy flux and whether an inlet or shock is stable to perturbations. As shown in Figure 4.14, as the ratio of specific heats γ increases, the Mach number at which the maximum entropy perturbation occurs very slightly increases and the Mach number at which the perturbation is equal to zero very slightly decreases. However, as can seen in Figure 4.14, this effect is insignificant and γ has a negligible effect on the entropy perturbation for shock angle perturbations. A similar result was found for Mach number and upstream thermodynamic perturbations.

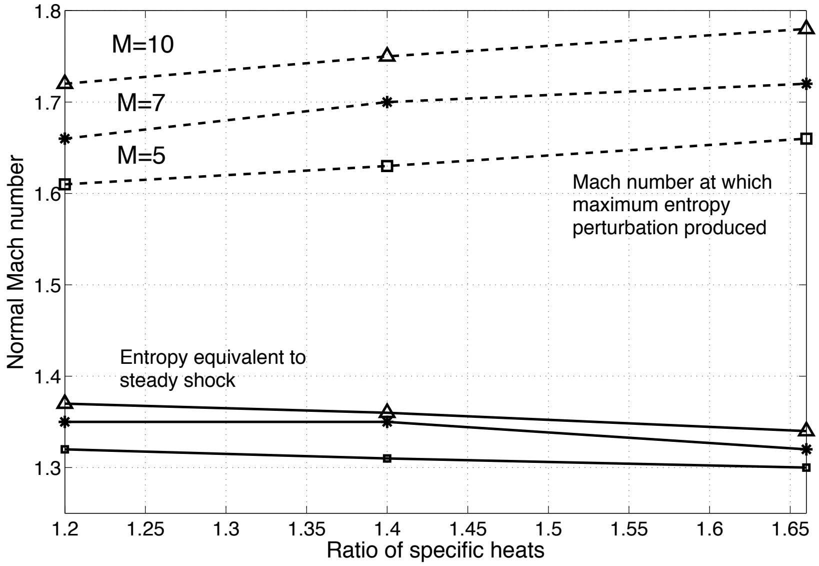

Figure 4.14. Effect of changing ratio of specific heats on stability range in normal Mach number for angle perturbations. The dashes represent the location of maximum entropy production

However, as shown in Figure 4.15 for back pressure perturbations, γ had a significant effect on the entropy perturbation. Because the back pressure perturbation does not depend on a time-varying upstream convected entropy flux, which introduces higher order terms unlike the other perturbations studied, perturbations in downstream conditions may be more sensitive to changes in the ratio of specific heats while perturbations in upstream conditions might not.

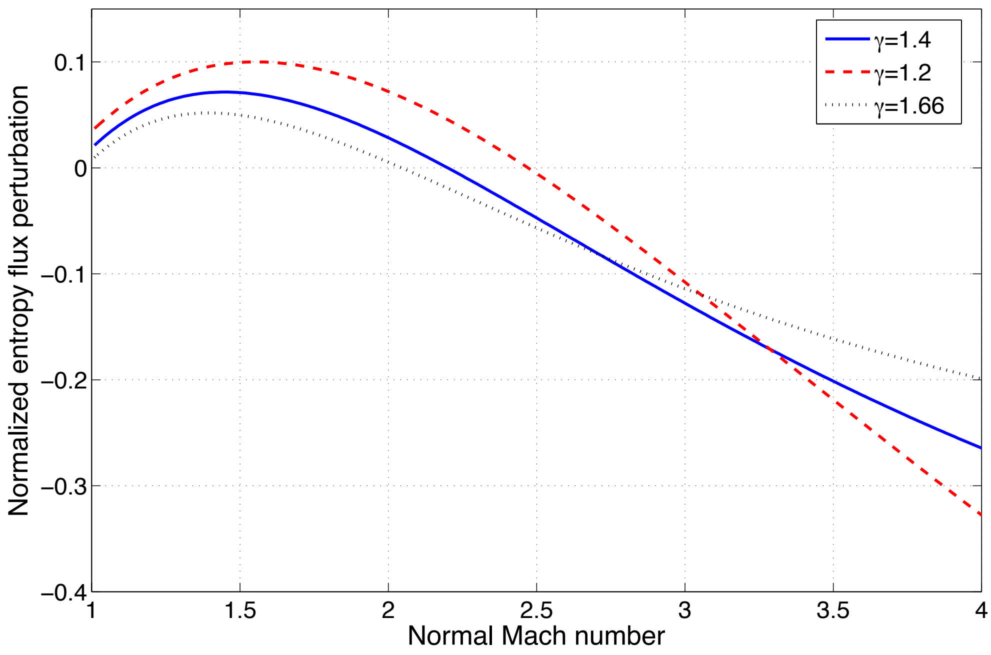

Figure 4.15. A comparison of the effect of ratio of specific heats on the change in entropy production for unsteady versus steady flow at various normal Mach numbers for a sinusoidal perturbation in the back pressure.

4.6 Results for curved shocks

4.6.a Curved versus straight

The results shown in Table 4.2 for each perturbation and curvature and second derivative of each perturbation shown in Figures 4.3, 4.7, 4.8, and 4.12 indicate that a curved shock will likely be *less* stable than a comparable straight shock to any perturbation. This is because there will be a smaller entropy flux gain across a curved unsteady shock than the unsteady straight shock even though the curved steady shock has a higher entropy flux gain than the straight shock. Similar to entropy, these perturbations are also concave down functions where $\frac{d^2G(M_1)}{dM_1^2} \leq 0$, $\frac{d^2H(M_1)}{dM_1^2} \leq 0$,

	Maximum	Zero	Inflection point	
Perturbation			**Second derivative**	
M_∞	1.32	1.58	$d^2G(M,\gamma)/dM^2$	2.56
β M=5	1.31	1.63	$d^2K(M,\gamma,\varepsilon)/dM^2$	2.32
M=7	1.35	1.7		2.6
M=10	1.36	1.75		2.78
$\left.\frac{p_2}{p_1}\right\|_{Backpressure}$	1.47	2.19	$d^2H(P(M),\gamma)/dM^2$	2.62
			$d^2H(P,\gamma)/dP^2$	2.21
$\left.\frac{p_2}{p_1}\right\|_{Upstream}$	1.12	1.25	$d^2J(P(M),\gamma)/dM^2$	2.01
			$d^2J(P,\gamma)/dP^2$	1.667

Table 4.2. The normal Mach numbers at which a shock subjected to each perturbation should have the highest entropy flux difference from the steady case, have an entropy flux gain equivalent to that of the steady case, and where the second derivative of the entropy flux perturbation function becomes positive. Note that the second derivative is everywhere negative where the difference in entropy gain between the unsteady and steady shocks is positive.

$\frac{d^2J(P(M_1))}{dM_1^2} \leq 0$, and $\frac{d^2K(M_1,\hat{\beta},\varepsilon)}{dM_1^2} \leq 0$ where the entropy perturbation $G(M_1)$, $H(\hat{P})$, $J(\hat{P})$, or $K(M_1,\varepsilon,\hat{\beta})$ is positive. At normal Mach numbers above 2.56, 2.62, 2.01, and 2.32 to 2.78, the second derivative with respect to Mach number is positive for Mach number, back pressure, atmospheric condition perturbations, and shock angle perturbations (depending on Mach number). However, in this regime, the unsteady shock is the lowest entropy gain solution, and there is no curved inlet that would result in the unsteady flow having a higher entropy rise than the steady solution.

A property of concave functions is that the mean of two values of the function is always less than the function evaluated at the mean between two points. This can be expressed as $\frac{G\left(M_{1,a}\right)+G\left(M_{1,b}\right)}{2} \leq G\left(\frac{M_{1,a}+M_{1,b}}{2}\right)$. This means that summing the entropy perturbations along a curved shock and finding the total entropy perturbation will produce a smaller increase/larger decrease in entropy production above that of its corresponding steady shock than for a straight shock with the same average shock angle. The higher the curvature is, the smaller the increase and the larger the decrease. However, at regions where the entropy flux perturbation is negative, a curved shock may have a smaller decrease in the entropy flux gain than the straight shock. It is not clear if the magnitude of the entropy flux perturbation translates to greater or less stability, but if it does, this could mean a curved shock that is unstable to flow perturbations might be more forgiving to off-design conditions than the straight shock even though both would remain unsteady.

The second derivatives with respect to pressure for back pressure or upstream conditions entropy flux perturbations have a zero much closer to the pressure ratio and normal Mach number where the shock should no longer be stable to those perturbations. The entropy perturbation has the same trend in the second derivative for the temperature ratio and pressure ratio, but the mean pressure ratio of a curved shock is not the same as the pressure ratio found using the mean Mach number, and in some cases may correspond to a smaller normal Mach number. Thus, it is also useful to look at the second derivative with respect to pressure ratio - particularly if a shock is designed to have the same mean pressure ratio as a straight shock rather than the same mean normal Mach number. As stated above, even though curved shocks created with the same mean pressure or temperature ratio as a corresponding straight shock could have a higher entropy perturbation than an unsteady straight shock, the concavity of the second derivative is still concave down where the entropy perturbation is positive, such as the second derivative with respect to Mach number. However, there are some notable differences aside from the lower normal Mach number at which the second derivative with respect to the pressure ratio is zero occurs.

Comparing the first derivatives with respect to pressure in Figure 4.8 to the derivatives with respect to Mach number in Figures 4.3, 4.7, and 4.12 show that the first derivative with respect to pressure is an order of magnitude smaller. This isn't surprising as $dP/dM = 4\gamma M/(\gamma+1)$, meaning slight changes in normal Mach number are magnified by 2 to 2.33 and slight changes in pressure ratio translate to even smaller changes in normal Mach number. The smaller first derivative with respect to pressure and location of the zero of the second derivative suggest that curved shocks that produce the same mean pressure ratio as a straight shock with a normal Mach number or pressure ratio near that zero may be more stable to these perturbations than inlets designed for another parameter. In other words, at pressure ratios or normal Mach numbers near the transition from stable to unstable--particularly for back pressure perturbations, curvature has little effect.

This effect can also be shown effectively by looking at curved shocks created with varying curvatures based on different mean parameters. Figures 4.16 to 4.18 show the increase and decrease in entropy production along each of the Mach 5, 7, 10 inlets created for each curvature with each shock having the same mean normal Mach number or shock angle for a Mach number perturbation. The distance is normalized to the inlet height and is the length along the inlet from the entrance to the cowl. As shown in Figure 4.16, although for part of the inlet, the entropy production is higher than for an unsteady straight shock, the amount below the line corresponding to the rectangular inlet is always greater. For higher curvatures at Mach 7, part of the middle of the inlet has a higher entropy production than the straight shock, but the normal Mach number passes through the maximum and the entropy production is less than for a straight shock.

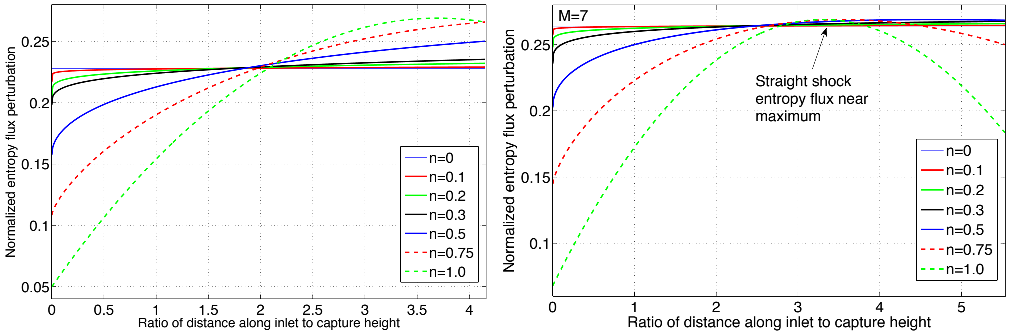

Figures 4.16 and 4.17. Entropy flux perturbation for Mach 5 and Mach 7 inlets with various curvature designed with the same mean normal Mach number versus a straight 3-degree baseline wedge inlet.

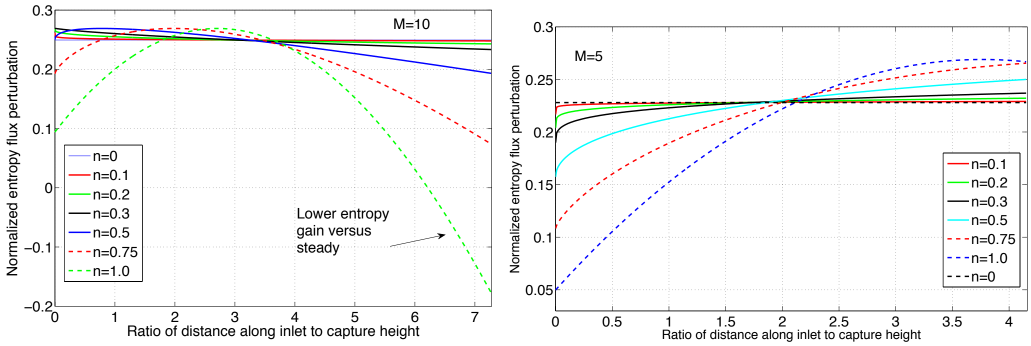

Figures 4.18 and 4.19. Normalized entropy flux perturbation from normal Mach number perturbation for inlets of various curvature. The shocks on the left all have the same mean normal Mach number and shock angle for a Mach 10 inlet. The shocks on the right all have the same mean pressure ratio for a Mach 5 inlet.

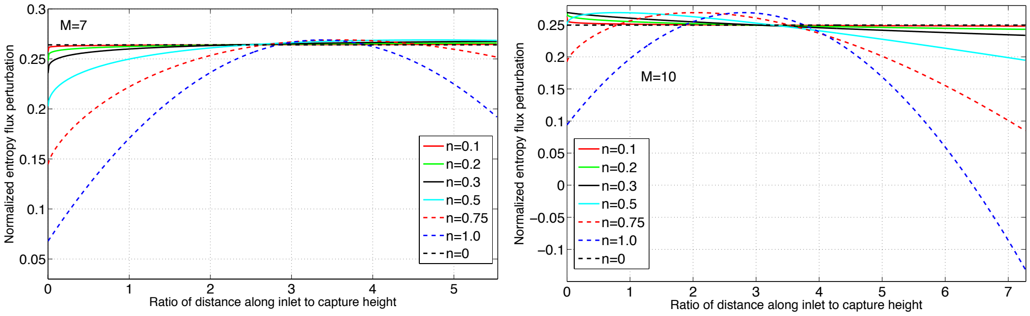

Figures 4.20 and 4.21. Normalized entropy flux perturbation from normal Mach number perturbation for inlets of various curvatures for Mach 7 and 10. Each shock has the same mean pressure ratio.

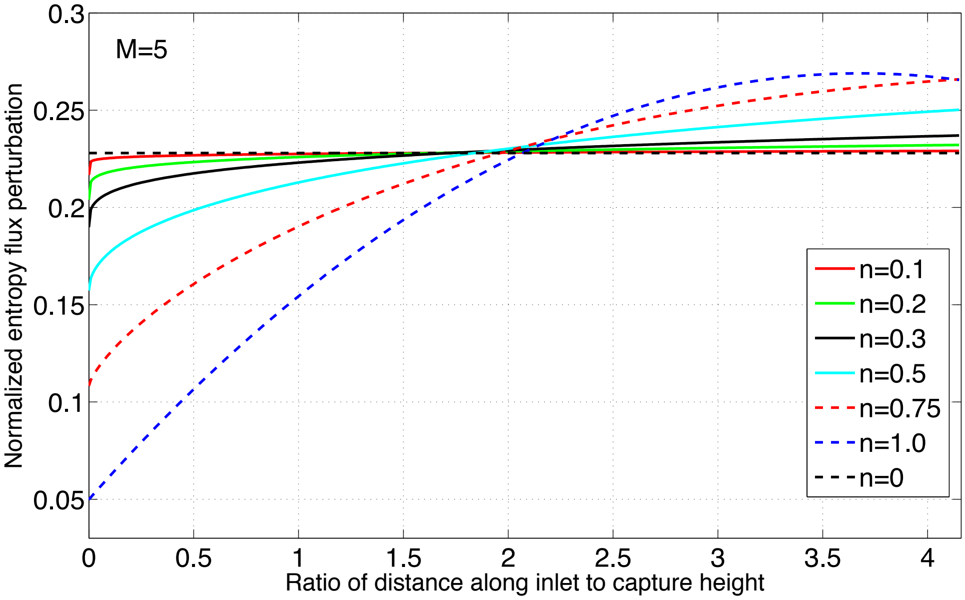

Figure 4.22. Normalized entropy flux perturbation from normal Mach number perturbation for inlets of various curvatures for Mach 5 inlets. Each shock has the same mean temperature ratio.

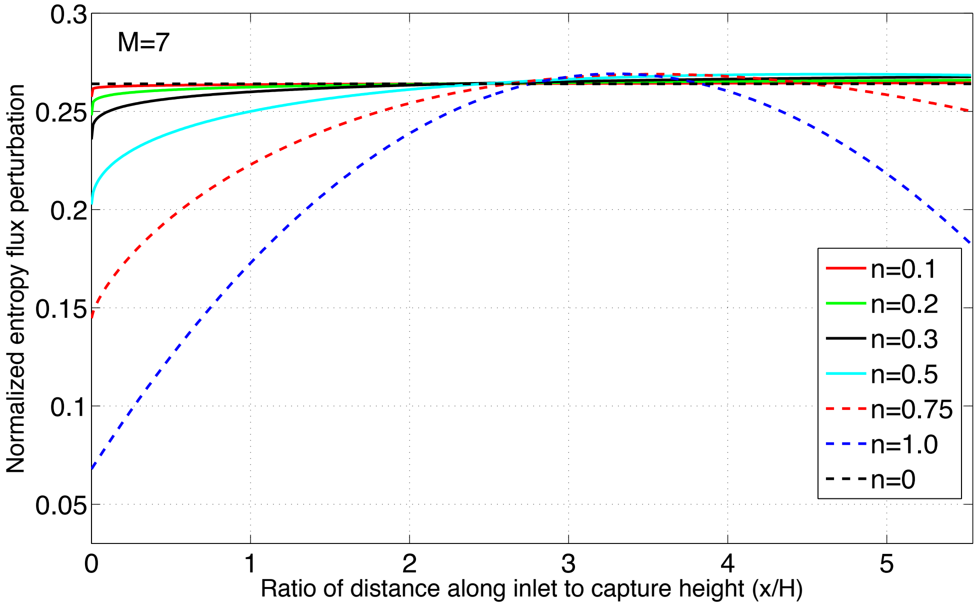

Figure 4.23. Normalized entropy flux perturbation from normal Mach number perturbation for inlets of various curvatures for Mach 7 inlets. Each shock has the same mean temperature ratio.

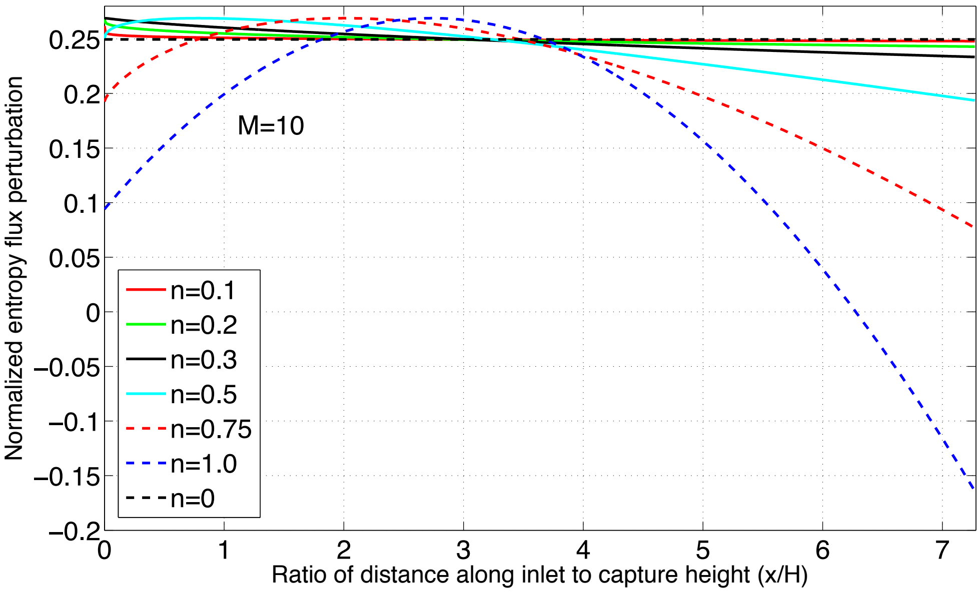

Figure 4.24. Normalized entropy flux perturbation from normal Mach number perturbation for inlets of various curvatures for Mach 10 inlets. Each shock has the same mean temperature ratio.

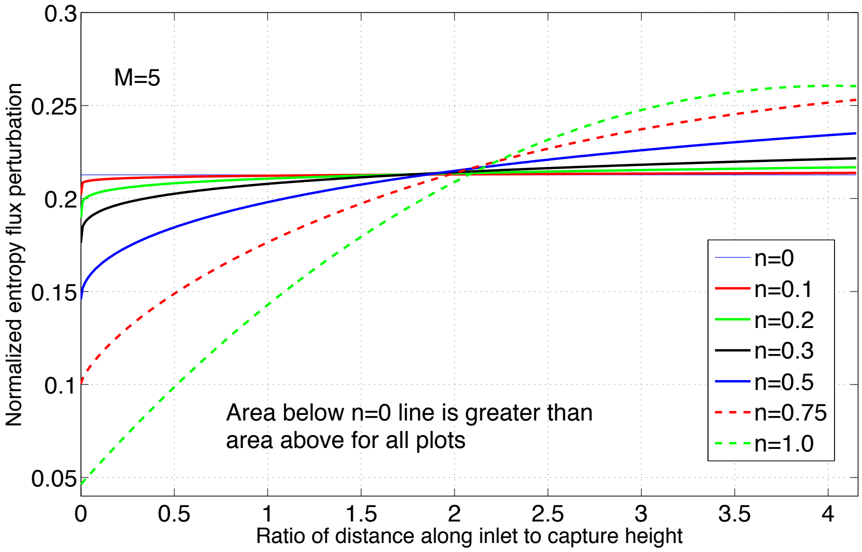

Figure 4.25. Normalized entropy flux perturbation from shock angle perturbation for inlets of various curvatures for Mach 5 inlets. Each shock has the same mean normal Mach number.

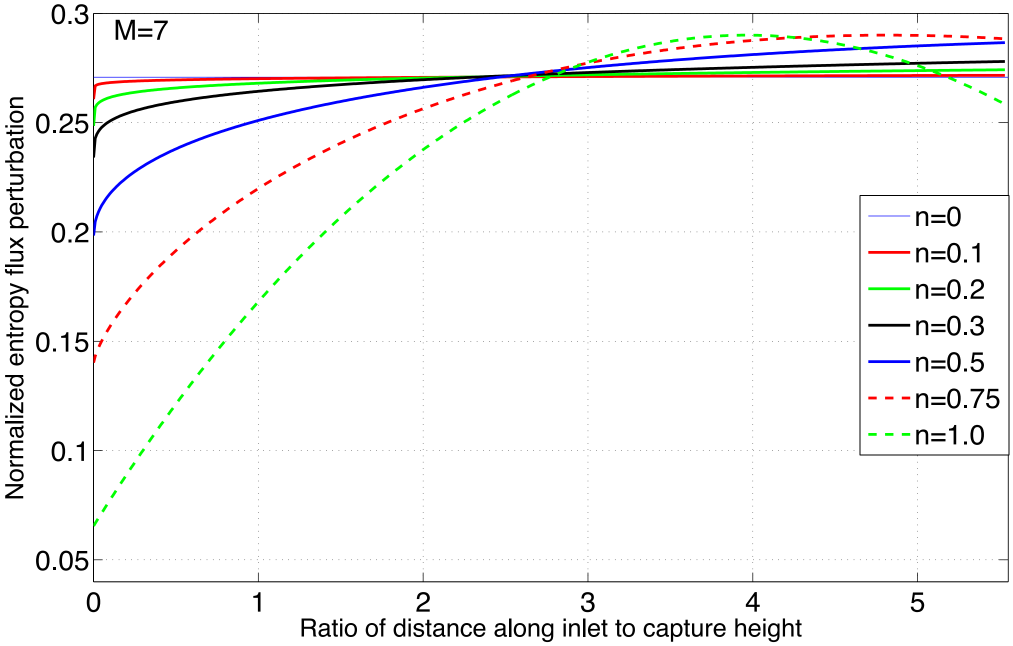

Figure 4.26. Entropy flux perturbation for a Mach 7 inlet of various curvatures versus a baseline 3 degree rectangular inlet for shock angle perturbation.

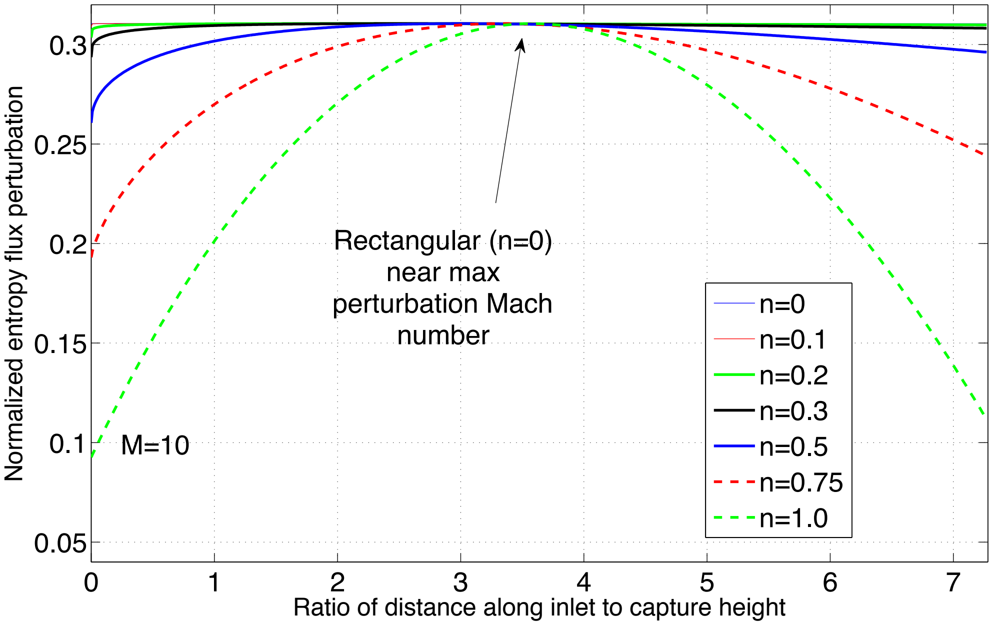

Figure 4.27. Entropy flux perturbation for a Mach 10 inlet of various curvatures versus a baseline 3 degree rectangular inlet for shock angle perturbation. Almost no part of any of the curved inlets is above the straight shock.

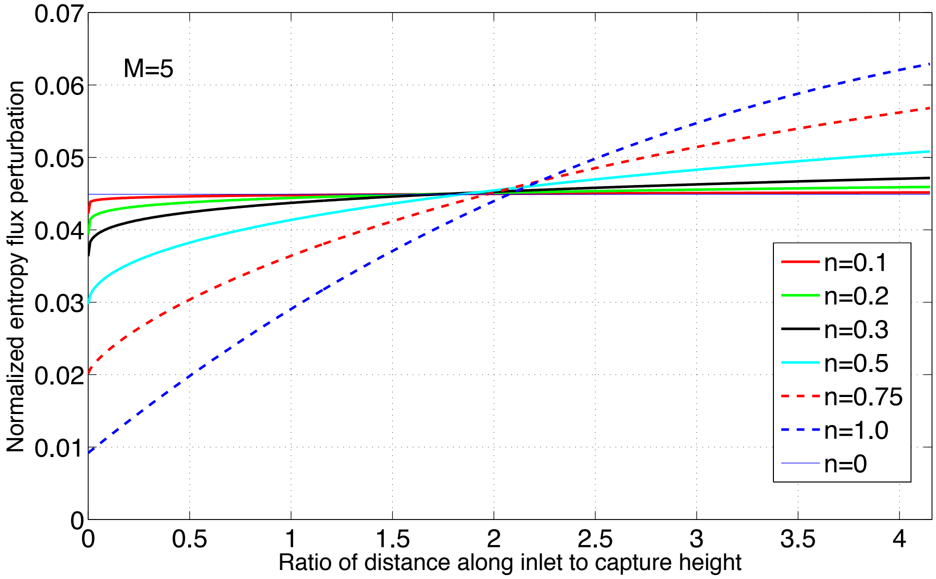

Figure 4.28. Entropy flux perturbation for a Mach 5 inlet of various curvatures versus a baseline 3 degree rectangular inlet for back pressure perturbation.

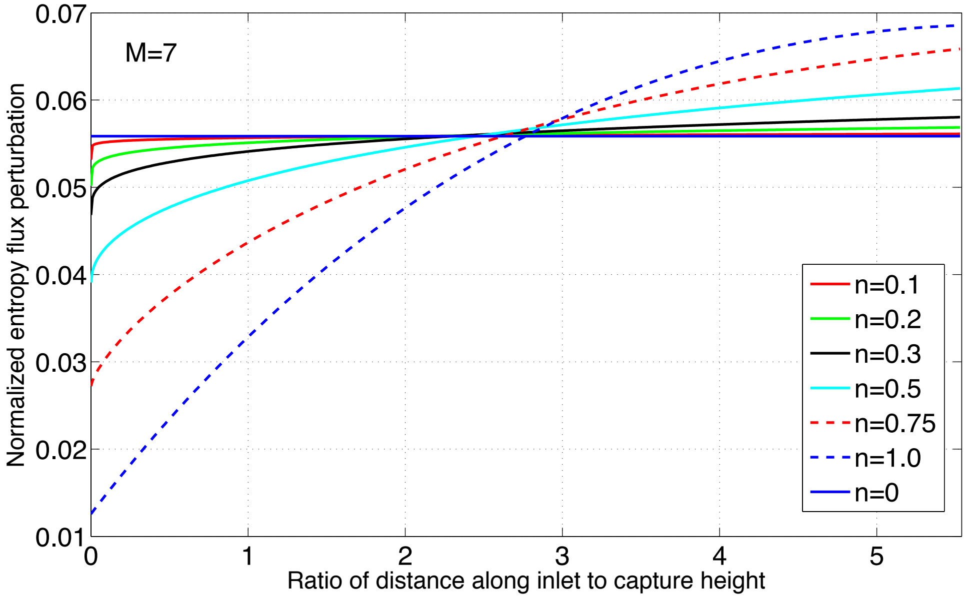

Figure 4.29. Entropy flux perturbation for a Mach 7 inlet of various curvatures versus a baseline 3 degree rectangular inlet for back pressure perturbation.

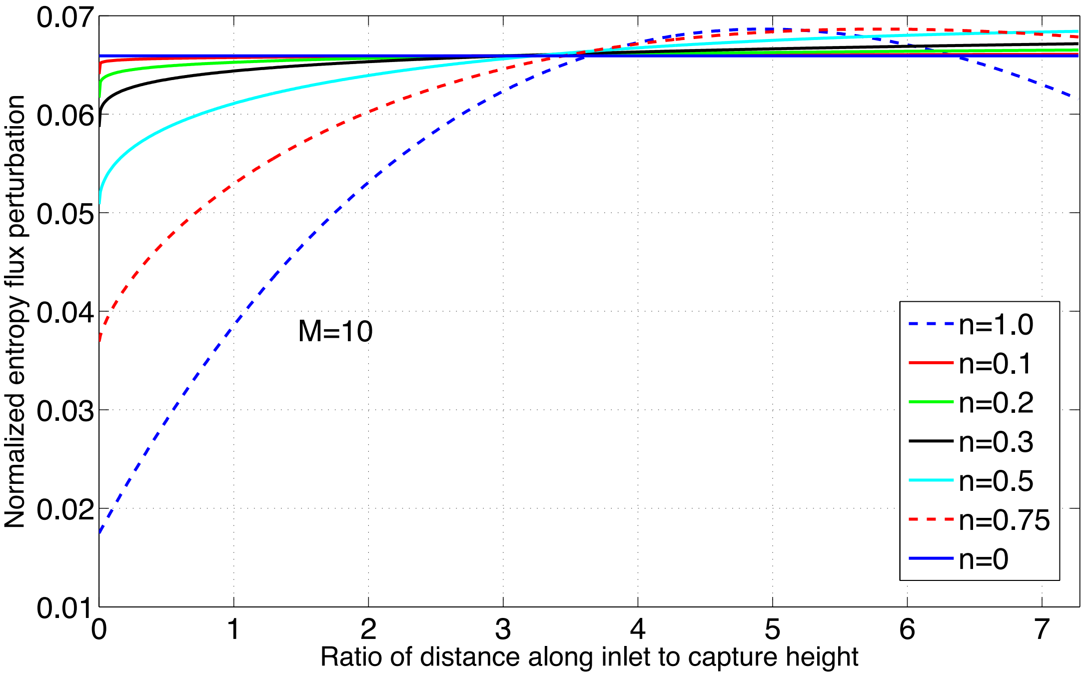

Figure 4.30. Entropy flux perturbation for a Mach 10 inlet of various curvatures versus a baseline 3 degree rectangular inlet for back pressure perturbation.

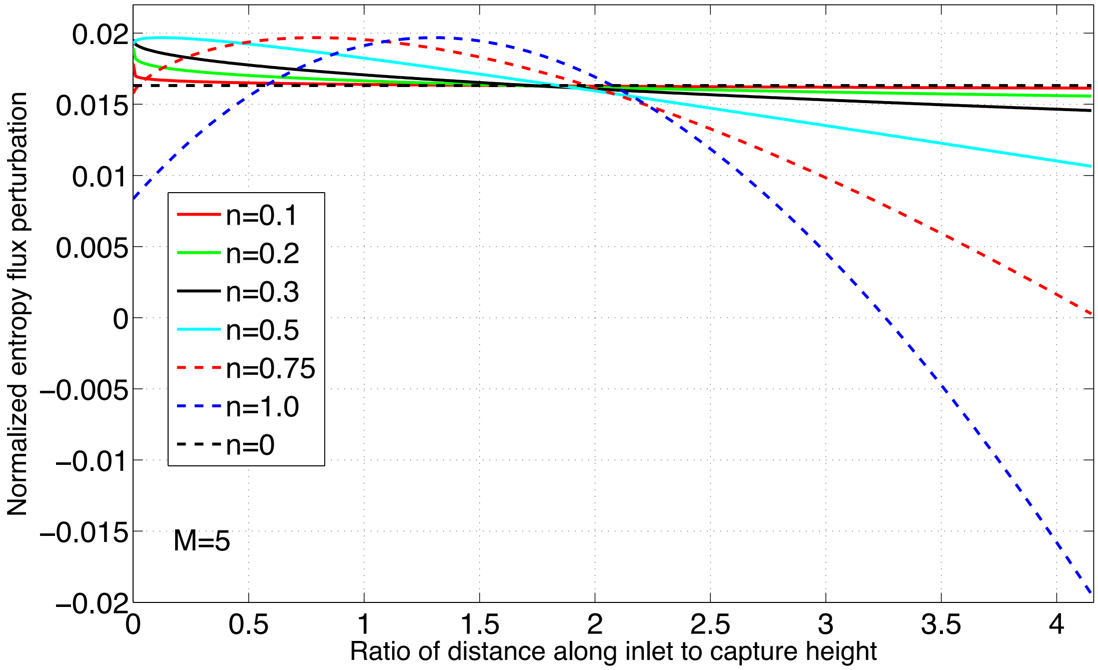

Figure 4.31. Entropy flux perturbation for a Mach 5 inlet of various curvatures versus a baseline 3 degree rectangular inlet for upstream conditions perturbation.

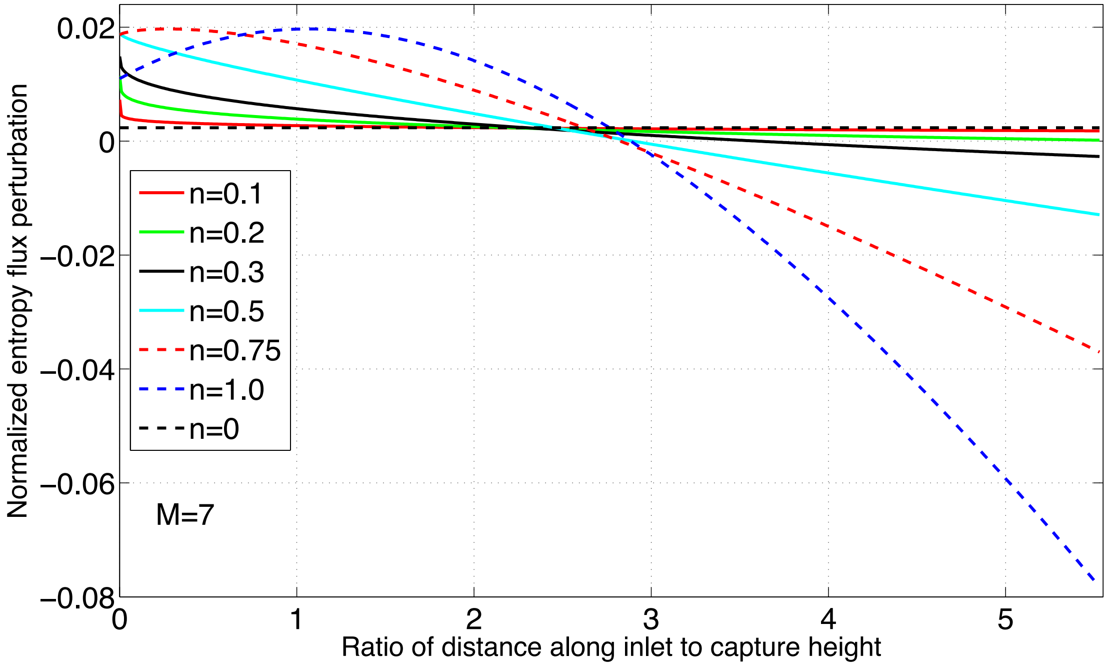

Figure 4.32. Entropy flux perturbation for a Mach 7 inlet of various curvatures versus a baseline 3 degree rectangular inlet for upstream conditions perturbation.

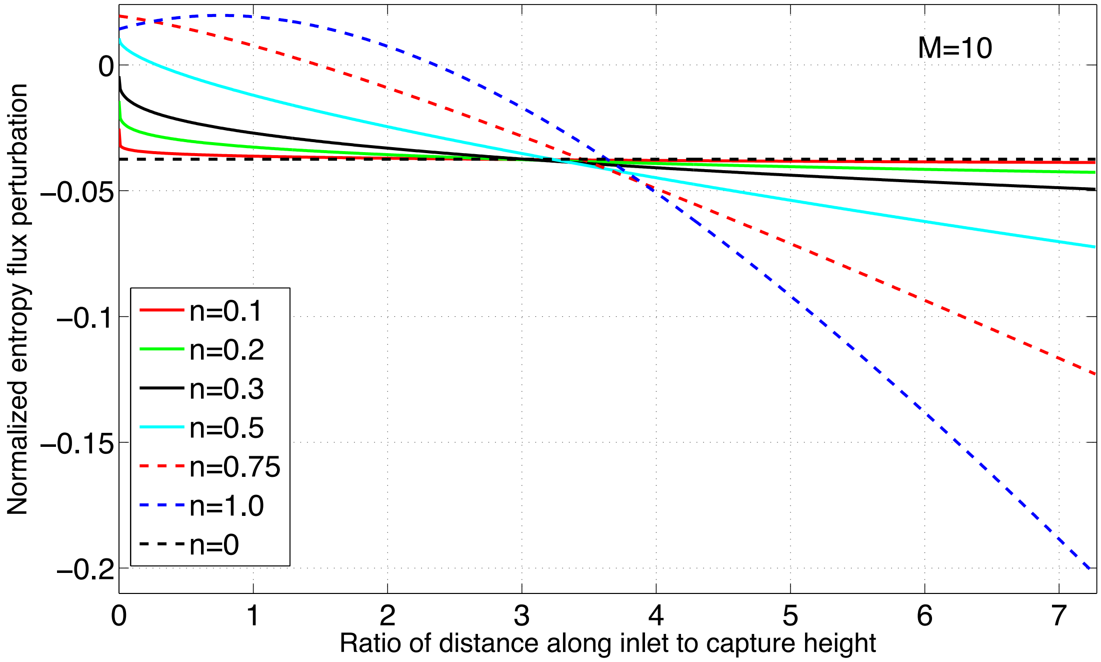

Figure 4.33. Entropy flux perturbation for a Mach 10 inlet of various curvatures versus a baseline 3 degree rectangular inlet for upstream conditions perturbation.

As shown in Figures 4.19 to 4.33, the same trend is present whether the shocks are curved based on the same mean normal Mach number or pressure or temperature ratio. As shown in Figures 4.19 to 4.33, the entropy flux perturbation below the n=0 line is always greater than that above for all perturbation types and all curvatures. In Figure 4.27 for a Mach 10 shock angle perturbation, no part of any of the curved shocks has a higher entropy flux perturbation than the straight shock. This indicates that the straight shock's shock angle or normal Mach number are where the maximum entropy perturbation for shock angle perturbations occurs.

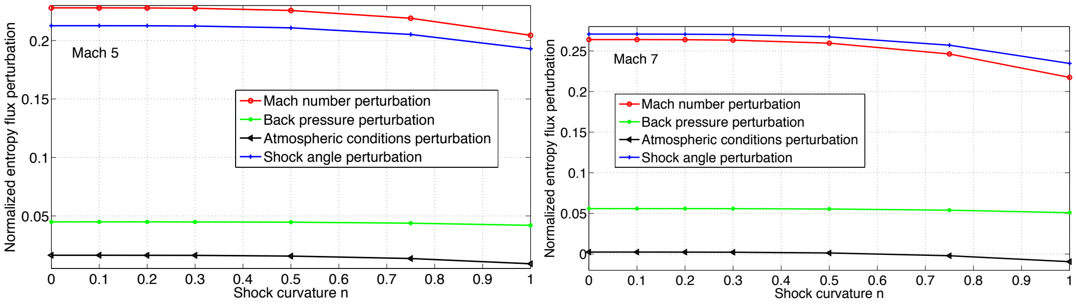

Figures 4.34. and 4.35. A comparison of the total entropy perturbation for shocks of varying curvature for Mach 5 and Mach 7 inlets. Each shock has the same mean normal Mach number.

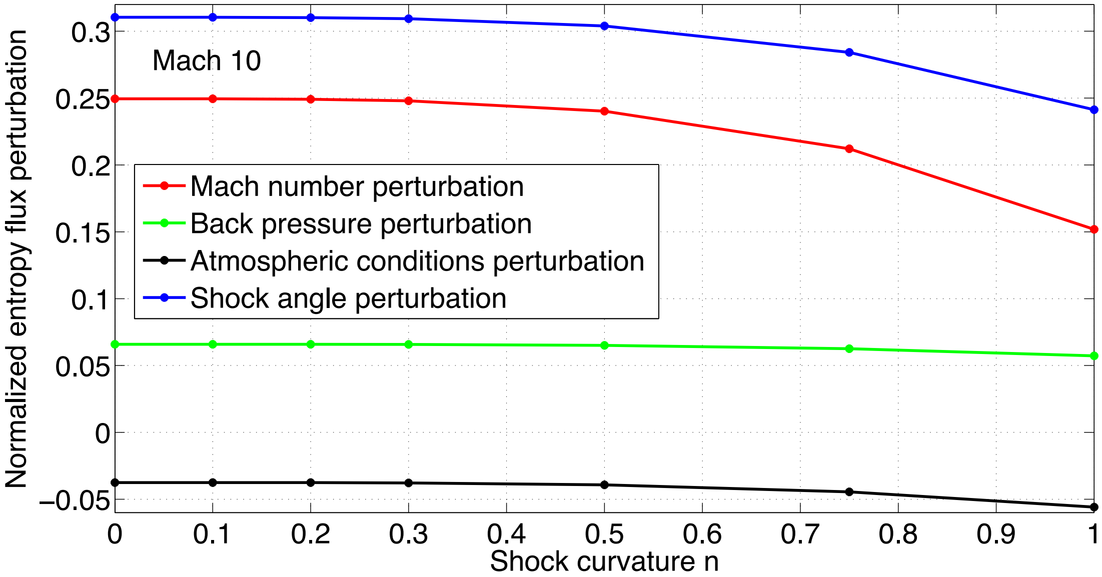

Figure 4.36. A comparison of the total entropy perturbation for shocks of varying curvature for Mach 10 inlets. Each shock has the same mean normal Mach number. Note that at higher Mach numbers, the results are more sensitive to curvature for Mach number or angle perturbations.

Figures 4.34 to 4.42 show the total entropy production perturbations compared to the steady shock for each inlet created with the same mean normal Mach number and Mach 5, 7, and 10. For inlets created with the same mean normal Mach number shown in Figures 4.34 to 4.36, the size of the entropy perturbation is much more sensitive to curvature and is magnified as the Mach number increases. Of note is that for the Mach 7 inlet, the inlet is no longer stable to perturbations in atmospheric conditions for the inlets with more curvature. In Figure 4.36, the Mach 10 inlet seems the most stable to back pressure changes and has almost no difference in entropy gain compared to the rectangular inlet.

The difference in entropy gain between the curved inlets and the rectangular inlets increases as Mach number decreases. This is likely because the average Mach number is increasing towards the maximum of the entropy perturbation. As shown in Figures 4.18, 4.21, and 4.24 for Mach 10, the entropy gain perturbation for a Mach number perturbation increases as n increases to $n = 0.5$ and then decreases. This is because the normal Mach number of the rectangular inlet is very close to the maximum value of the entropy production perturbation.

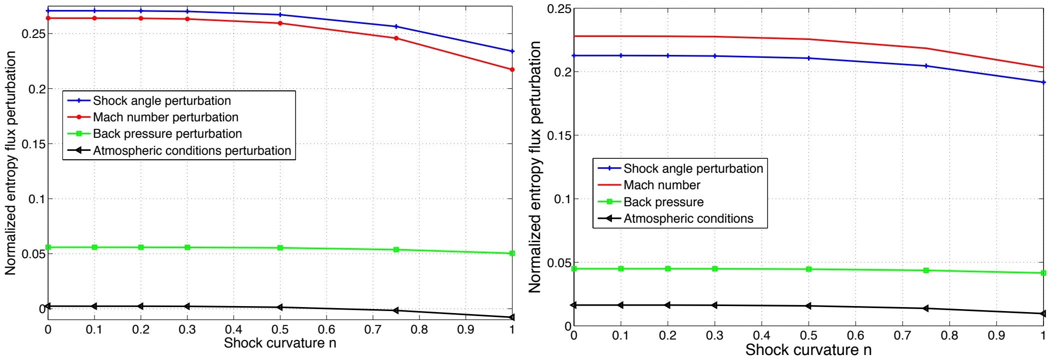

Figures 4.37 and 4.38. Entropy flux perturbation compared to the steady case for Mach 5 and Mach 7 inlets with curved shocks of varying curvature and the same mean pressure ratio.

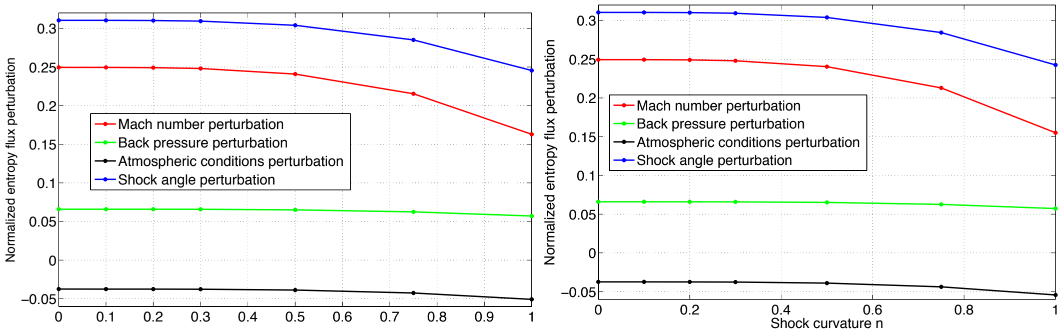

Figures 4.39. and 4.40. Entropy flux perturbation for inlets at Mach 10 of varying curvature. The shocks on the left are generated with the same mean pressure ratio, and the shocks on the right are generated with the same mean temperature ratio.

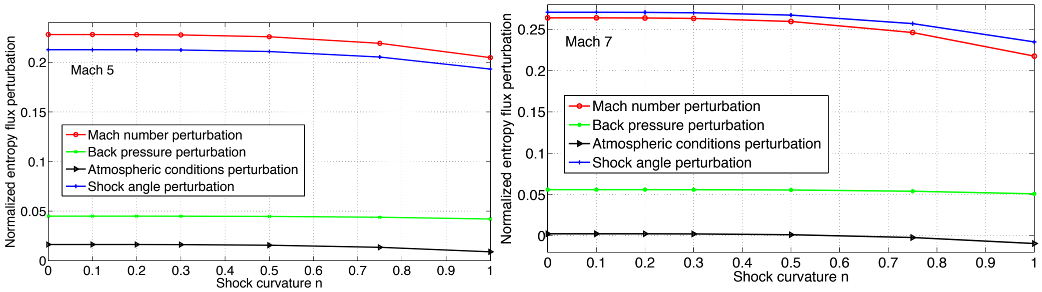

Figures 4.41. and 4.42. Entropy flux perturbation for inlets at Mach 5 and 7 of varying curvature. Each shock has the same mean temperature ratio.

Figures 4.37 to 4.39 show the same for inlets created with the same mean pressure ratio. Figures 4.40 to 4.42 show the total entropy production perturbation for each perturbation for Mach 5,7, and 10 inlets created with the same temperature ratio. In addition, for all methods of designing the shocks, the entropy flux perturbation was higher for Mach number perturbations than shock angle perturbations for Mach 5 inlets but not Mach 7 and 10.

Figures 4.43 to 4.45 show the difference in entropy production perturbation between the curved shocks and the straight shock for Mach 5, 7, and 10 for each type of perturbation and each method of curving the shocks. As Mach number and curvature increases the difference between entropy flux perturbation for an unsteady straight shock and an unsteady curved shock increases with the unsteady straight shock always having a higher entropy perturbation. This is true regardless of whether the shocks all have the same mean normal Mach number, pressure ratio, or temperature ratio.

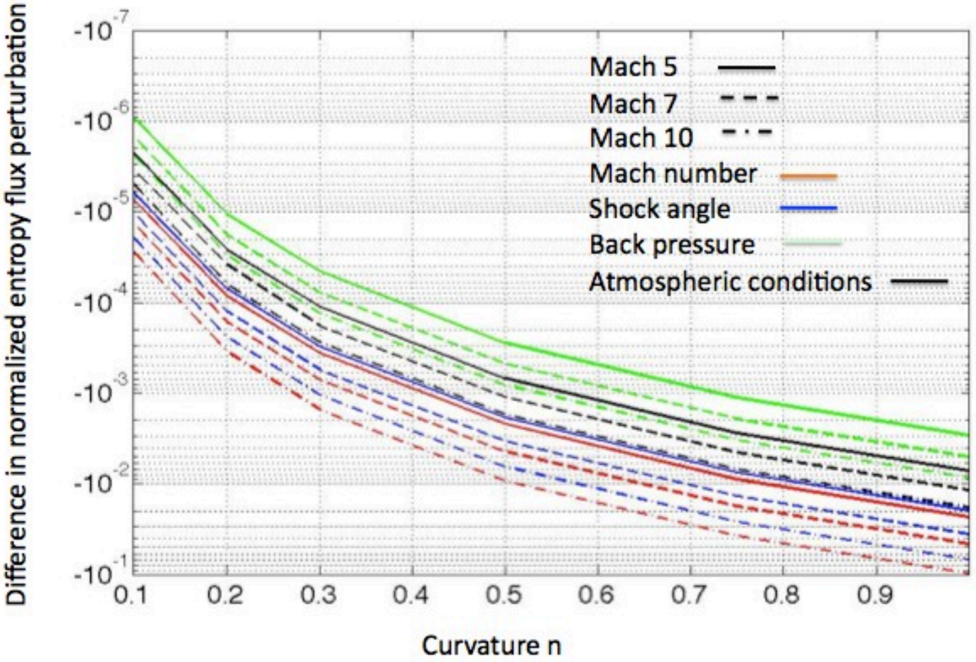

Figure 4.43. Difference in entropy perturbation for shocks of varying curved and straight shocks with the same mean normal Mach number or shock angle.

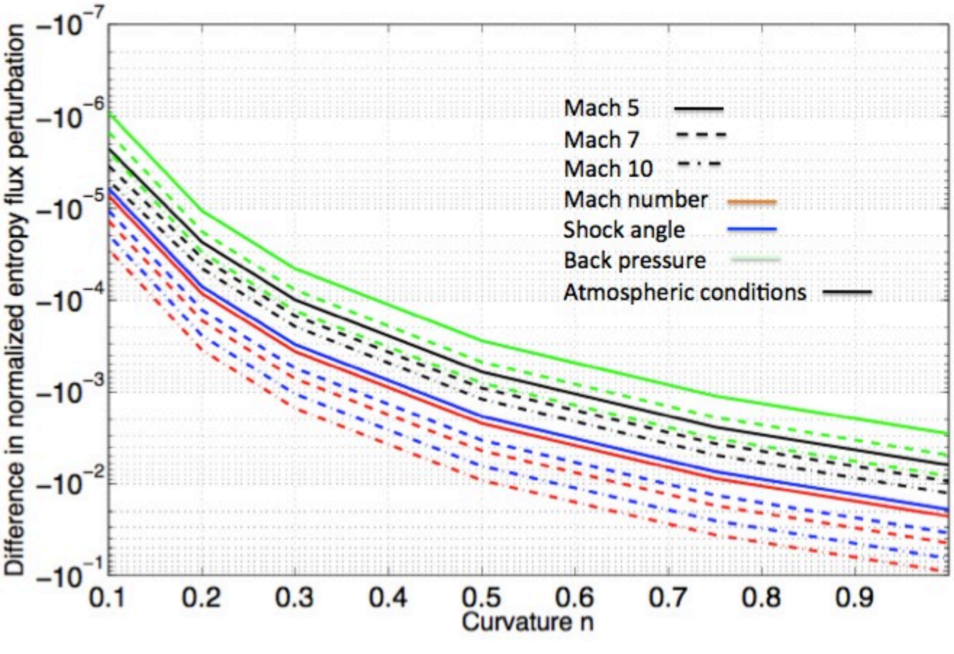

Figure 4.44. Difference in entropy perturbation for shocks of varying curved and straight shocks with the same mean pressure ratio. These curves have the same trends as for shocks with the same mean normal Mach number and temperature ratio.

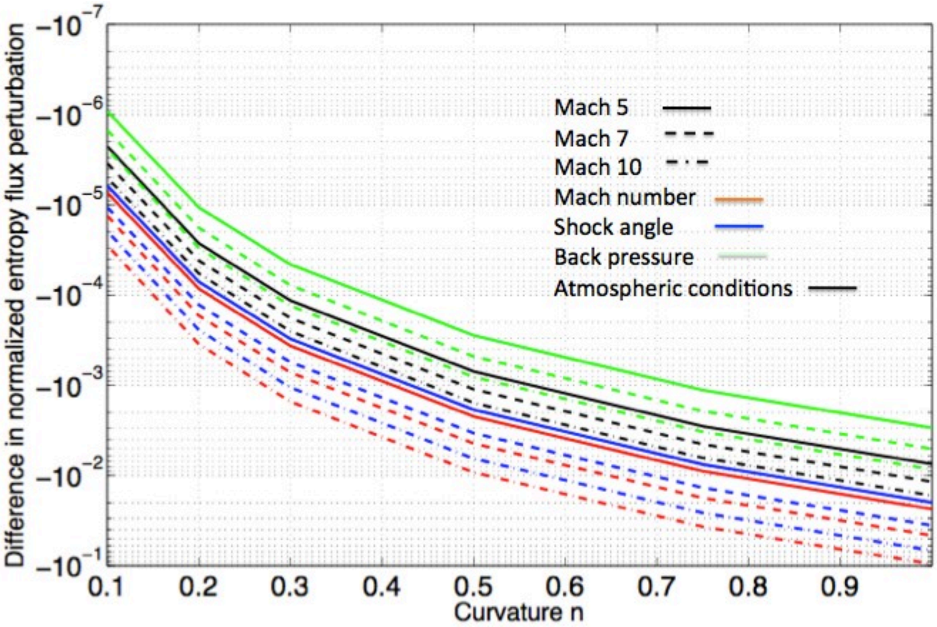

Figure 4.45. Difference in entropy perturbation for shocks of varying curved and straight shocks with the same mean temperature ratio.

4.6.b Comparison of stability for shocks designed with different mean physical parameters

Figures 4.46 to 4.57 show that three-dimensional inlets, whose curvature varies such that the mean pressure ratio or temperature are the same, have the same general decrease in entropy perturbation with respect to the straight shock. However, as shown each of these figures with the exception of 4.46, 4.56, and 4.57, the size of the entropy perturbation generally decreases when each curved shock has the same mean of the perturbed quantity. For positive entropy perturbations, this means curvature has more of an effect, and less of an effect for negative entropy perturbations. For example, if each curved shock has the same mean shock angle, then the positive entropy perturbation for Mach number or shock angle perturbations is less as curvature increases than if each curved shock had the same mean pressure or temperature ratio.

For lower Mach number shocks subjected to a Mach number or shock angle perturbation, the shocks designed with the same mean pressure ratio were more sensitive to curvature. For back pressure or atmospheric conditions, designing for either the same pressure or temperature ratio as curvature increases generally resulted in the smallest entropy perturbations. At Mach 7 and 10, the inlets created with the same mean pressure ratio had a noticeably smaller entropy increase, while there was little difference between the inlets created with the same mean Mach number and temperature ratios. This suggests that designing for a certain pressure can result in shocks more stable to Mach number or shock angle perturbations at higher normal Mach numbers. Designing for a certain Mach number can result in shocks more stable to back pressure perturbations. For perturbations in atmospheric conditions, the mean pressure ratio inlets had the smallest entropy perturbations at Mach 10, but the largest at Mach 5.

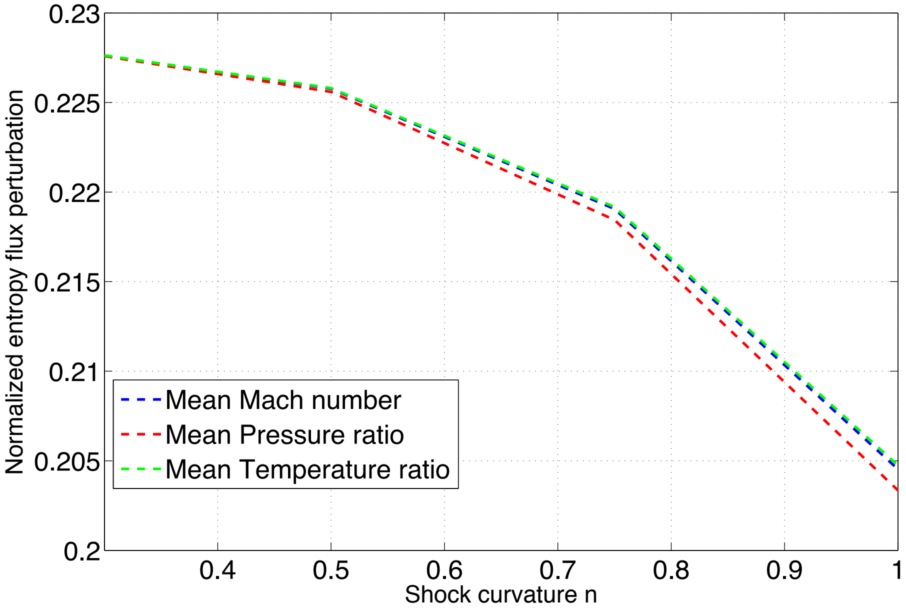

Figure 4.46. Comparison of entropy gain over steady shock for Mach number perturbations versus curvature for a Mach 5 inlet with overall wedge angle of 3 degrees for each method designing the curved shocks.

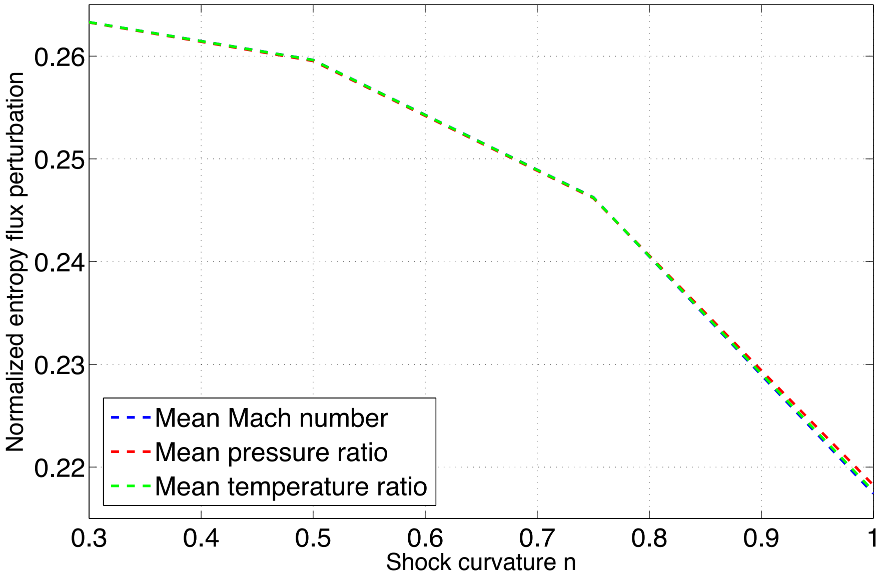

Figure 4.47 Comparison of entropy gain over steady shock for Mach number perturbations versus curvature for a Mach 7 inlet with overall wedge angle of 3 degrees for each method designing the curved shocks.

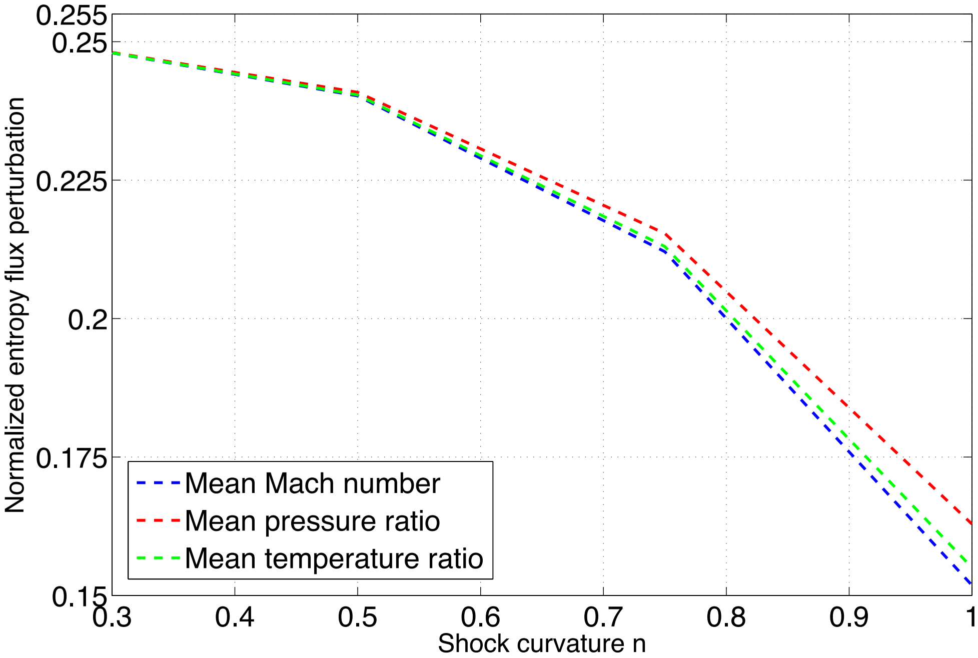

Figure 4.48. Comparison of entropy gain over steady shock for Mach number perturbations versus curvature for a Mach 10 inlet with overall wedge angle of 3 degrees for each method designing the curved shocks.

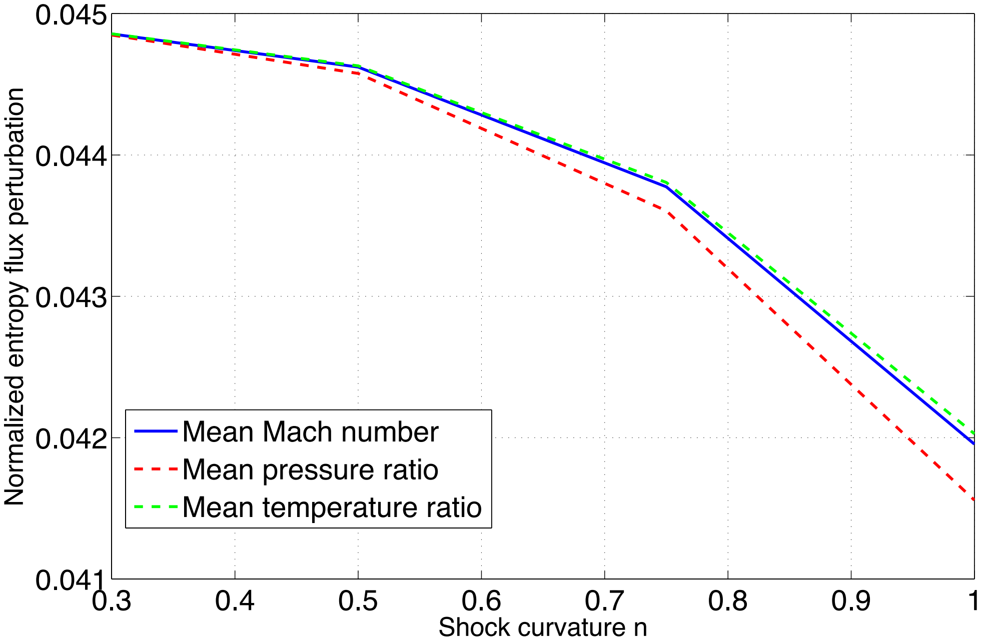

Figure 4.49. Comparison of entropy gain over steady shock for back pressure perturbations versus curvature for a Mach 5 inlet with overall wedge angle of 3 degrees for each method designing the curved shocks.

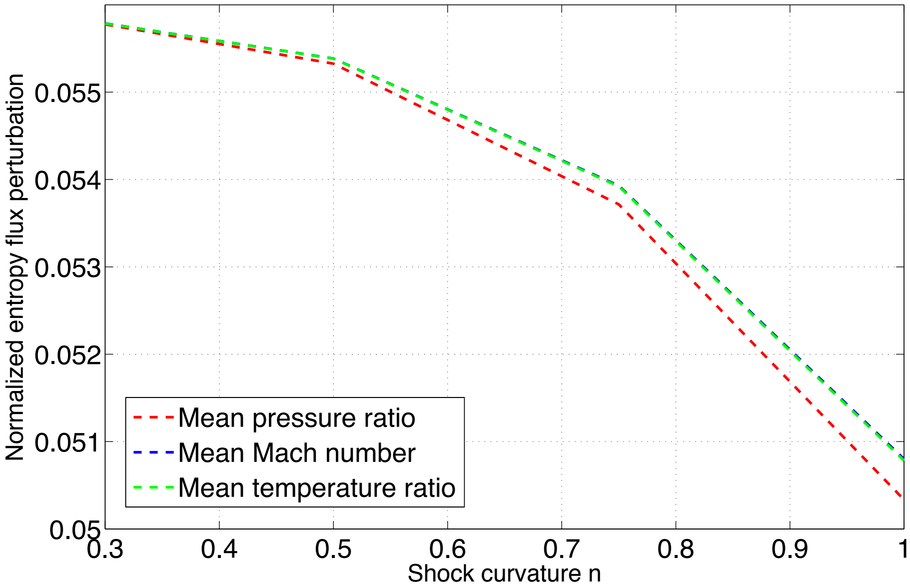

Figure 4.50. Comparison of entropy gain over steady shock for back pressure perturbations versus curvature for a Mach 7 inlet with overall wedge angle of 3 degrees for each method designing the curved shocks.

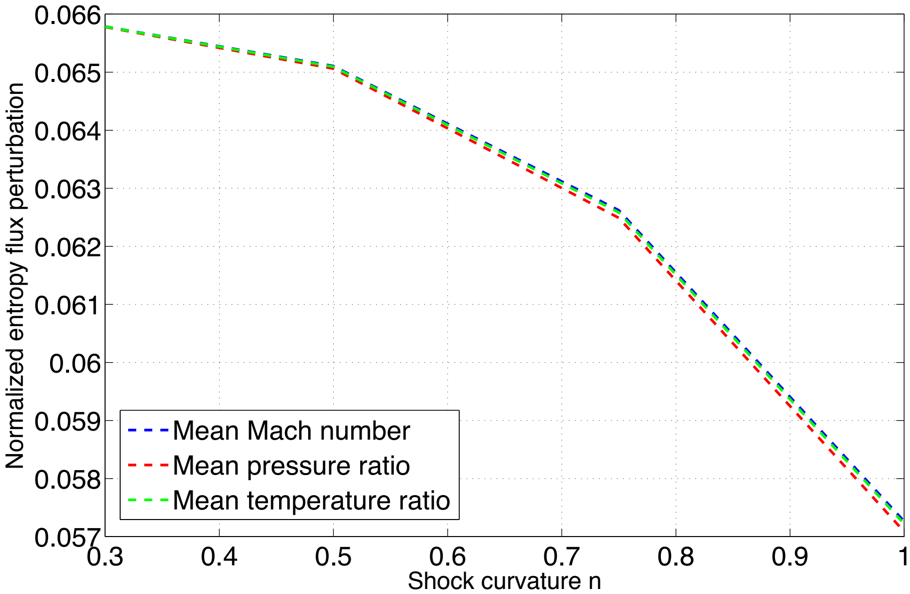

Figure 4.51. Comparison of entropy gain over steady shock for back pressure perturbations versus curvature for a Mach 10 inlet with overall wedge angle of 3 degrees for each method designing the curved shocks.

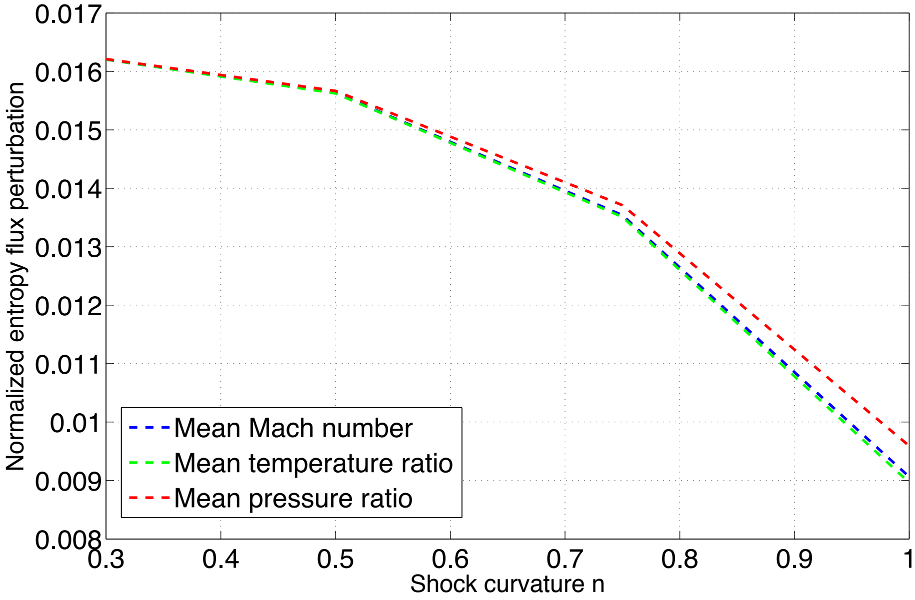

Figure 4.52. Comparison of entropy gain over steady shock for upstream atmospheric perturbations versus curvature for a Mach 5 inlet with overall wedge angle of 3 degrees for each method designing the curved shocks.

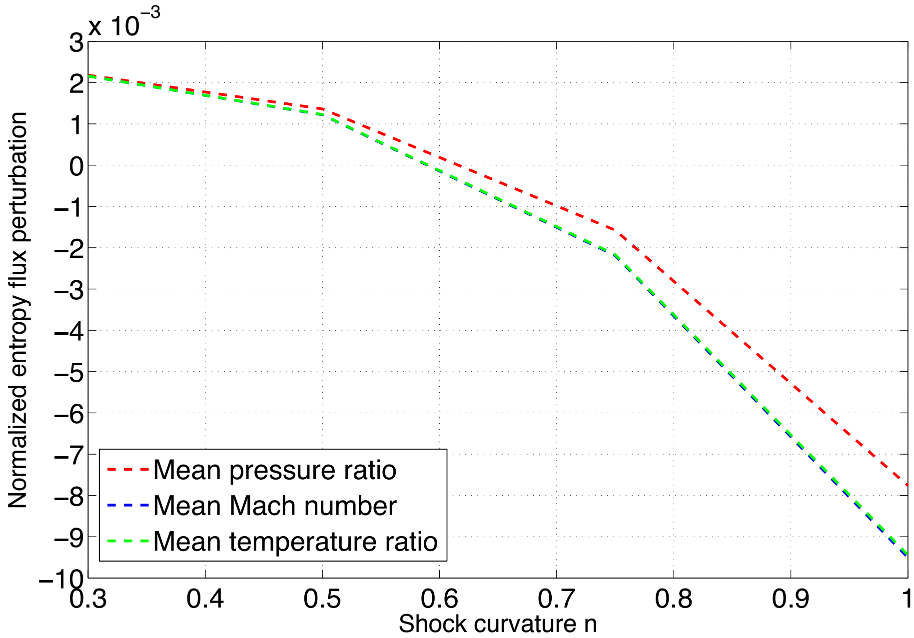

Figure 4.53. Comparison of entropy gain over steady shock for upstream atmospheric perturbations versus curvature for a Mach 7 inlet with overall wedge angle of 3 degrees for each method designing the curved shocks.

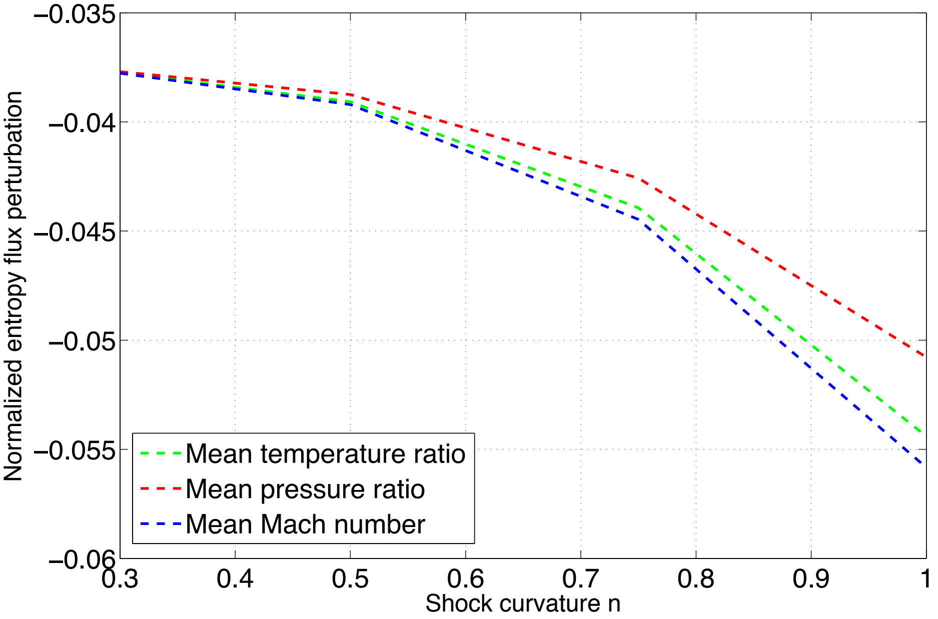

Figure 4.54. Comparison of entropy gain over steady shock for upstream atmospheric perturbations versus curvature for a Mach 10 inlet with overall wedge angle of 3 degrees for each method designing the curved shocks.

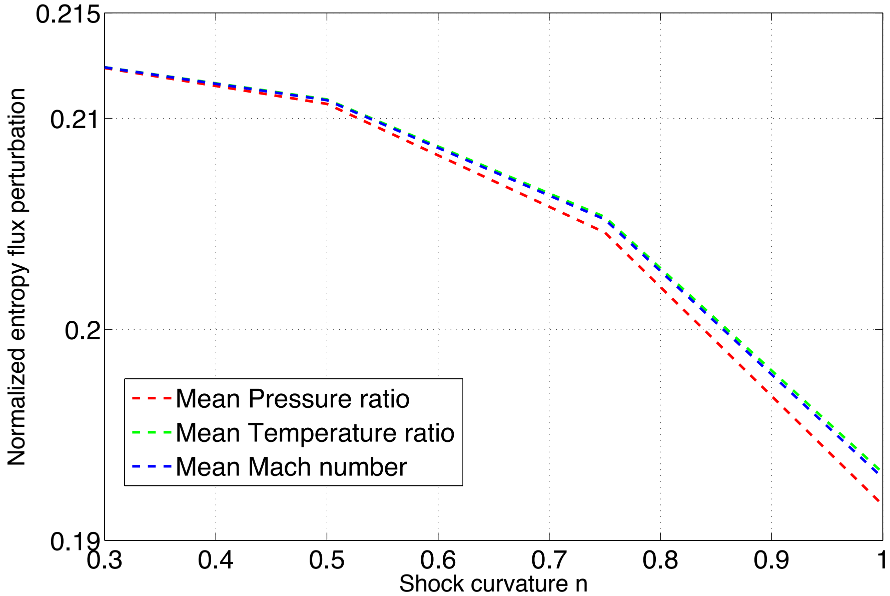

Figure 4.55. Comparison of entropy gain over steady shock for shock angle perturbations versus curvature for a Mach 5 inlet with overall wedge angle of 3 degrees for each method designing the curved shocks.

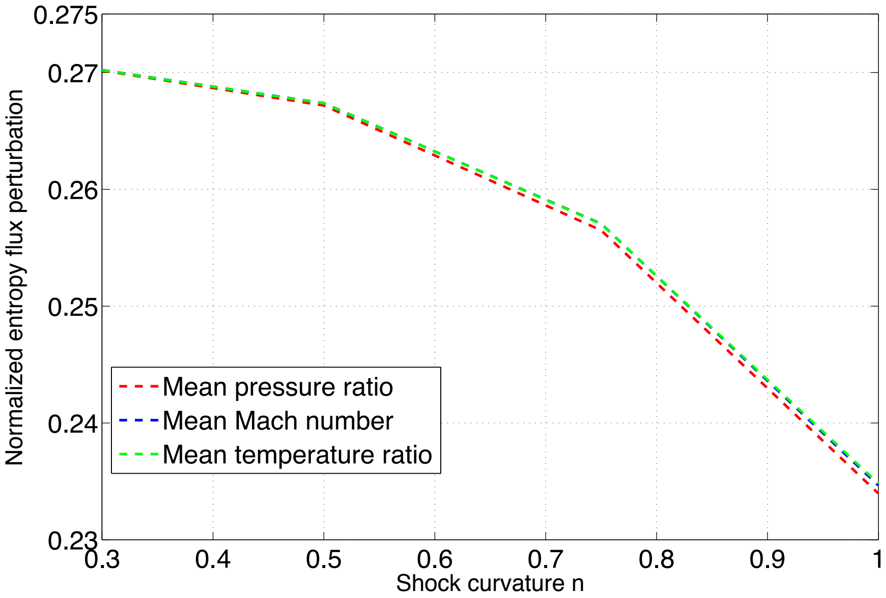

Figure 4.56. Comparison of entropy gain over steady shock for shock angle perturbations versus curvature for a Mach 7 inlet with overall wedge angle of 3 degrees for each method designing the curved shocks.

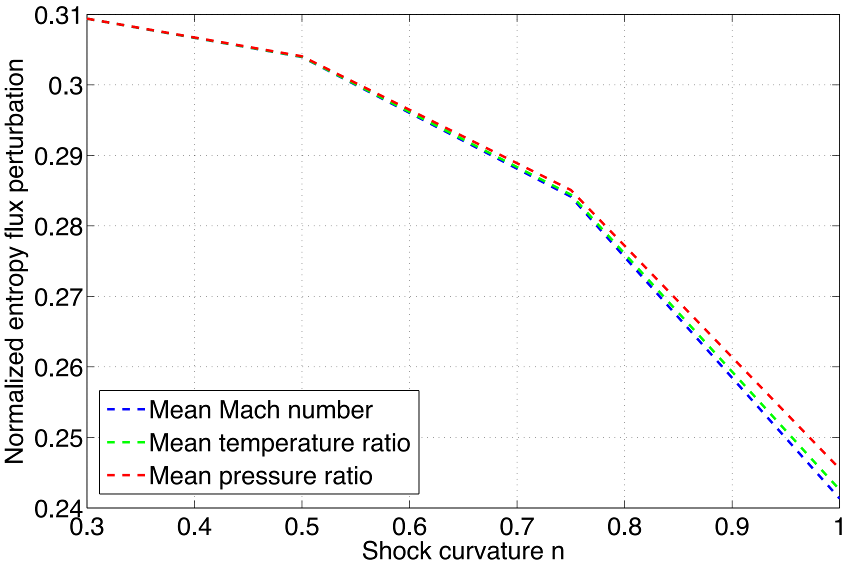

Figure 4.57. Comparison of entropy gain over steady shock for shock angle perturbations versus curvature for a Mach 10 inlet with overall wedge angle of 3 degrees for each method designing the curved shocks.

Chapter 5: Experimental Results

Data from an experiment run at Arnold Engineering Development Center's (AEDC) Hypervelocity Tunnel 9 was used to provide preliminary experimental validation of the application of the principle of minimum entropy to the stability of shock waves to unsteady effects or perturbations.

5.1 Facility

AEDC Hypervelocity Tunnel 9 is a hypersonic wind tunnel capable of running at Mach 7, 8, 10, and 14 at high Reynolds numbers that match flight conditions. The facility is a blow-down tunnel that uses nitrogen as its working fluid. It is capable of pressures up to 144.8 MPa and temperatures up to 1944 K. Because the facility has relatively long run times of up to 15 seconds, researchers can conduct an angle-of-attack sweep with a model during one run. The facility has a 1.5 meter diameter test section that can accommodate larger test articles.[78]

5.2 Experimental Setup

The goal was to acquire readily available data from a simple geometry model undergoing an angle-of-attack sweep at hypersonic speeds that covered a range of normal Mach numbers above and below the theorized transition point between stable and unstable. A run with Reynolds number of $1.16\text{x}10^6$ and the Mach 10 nozzle that fit this criteria using a blunted wedge was chosen. Data from a run with a low Reynolds number was chosen to minimize the effect of unsteadiness in a turbulent boundary layer on the bow shock near the nose. Table 5.1 shows freestream test conditions for the Mach 10 nozzle with a Reynolds number of $1.16\text{x}10^6$. Because of the boundary layer in the tunnel nozzle, which depends on Reynolds number, the effective size of the wind tunnel nozzle changes so the Mach number for the Mach 10 nozzle could differ between 9.44 and 10.23 depending on Reynolds number. For a Reynolds number of 1.16×10^6, the Mach number in the test section is M=9.55. A blunted wedge with a half-angle of 5.38 degrees pitching through -5 degrees to +15 degrees angle-of-attack at these conditions was used. Because the top also pitches through a range of angles that include the transition point, the shock off the top of the vehicle can be examined in addition to the shock off the bottom. If the calculations based on the principle of minimum entropy are correct, the transition from stable to unstable should occur at -0.6552 degrees angle-of-attack for a sinusoidal normal Mach number perturbation ($M_{n,1} = 1.58$) or 0.4376 degrees for a sinusoidal angle perturbation ($M_{n,1} = 1.74$). Schlieren flowfield imagery is used to determine when the bow shock near the nose becomes unsteady relative to the vehicle's motion.

Re/ft (10^6)	P0 (psia)	T0 (F)	H0 (BTU/lbm)	M_∞	P_∞ (psia)	T_∞ (K)
1.160	730	1310	441	9.55	2.15×10^{-2}	51.2

Table 5.1. Test conditions for Re=1.16×10^6 with Mach 10 nozzle

5.3 Data and Results

Initial results from this test run indicate that the shock did become unsteady relative to the vehicle's motion near the normal Mach number predicted for a normal Mach number perturbation. Unsteadiness was determined by looking at schlieren images taken about 250 times every second compiled into a video. It was difficult to determine precisely when the shock became unsteady because the unsteady oscillations in this region were small and difficult to see near the hypothesized transition angle-of-attack. Thus, a range of image frames and angles was found for when this transition occurred. The approximate point of transition was first determined by two different observers without any knowledge of what the model's angles were or where the transition should occur for this test run. The transition occurred at an angle-of-attack between -0.538 degrees (Frame 538) and +0.390 degrees (Frame 560 bottom) for normal Mach numbers of 1.596 and 1.731 for the bottom. This is 1 percent above to 9.6 percent above the theoretized transition normal Mach number of 1.58. For a sinusoidal angle perturbation, this transition would occur around 1.74 for Mach 9.55. So this range is 8.2 percent under to 0.5 percent under the normal Mach number at which it should become unsteady to angle perturbations. A normal Mach number of 1.58 occurred in Frame 536 and a normal Mach number of 1.74 occurred in Frame 561.

Looking at the shock on the top, the transition occurred at normal Mach numbers and angles between 1.587 and -0.60 degrees (Frame 565) and 1.741 and 0.453 degrees (Frame 540). The experimental results are in good agreement with the theory. Differences would also result from tunnel noise, viscous boundary layer interaction near the nose and an increased deflection angle because of the boundary layer, and any unsteadiness in the boundary layer that may have propagated upstream. Figures 5.1 and 5.2 show the model at minus 5 degrees angle of attack and plus 5 degrees angle-of-attack. For the first figure, the top shock is less straight and unsteady and the bottom is straighter and steady. The reverse is true for the second figure.

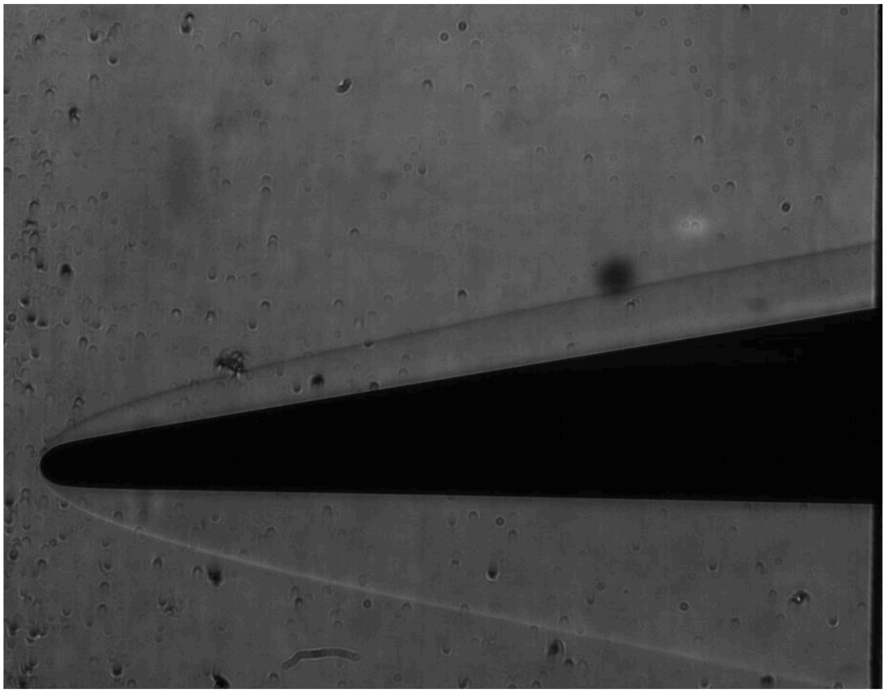

Figure 5.1. Minus 5 degrees AOA. The top has a more developed boundary layer and is unsteady. The shock is not as straight and some of the darker regions compared to Figure 5.2 correspond to places where the shock wobbles slightly.

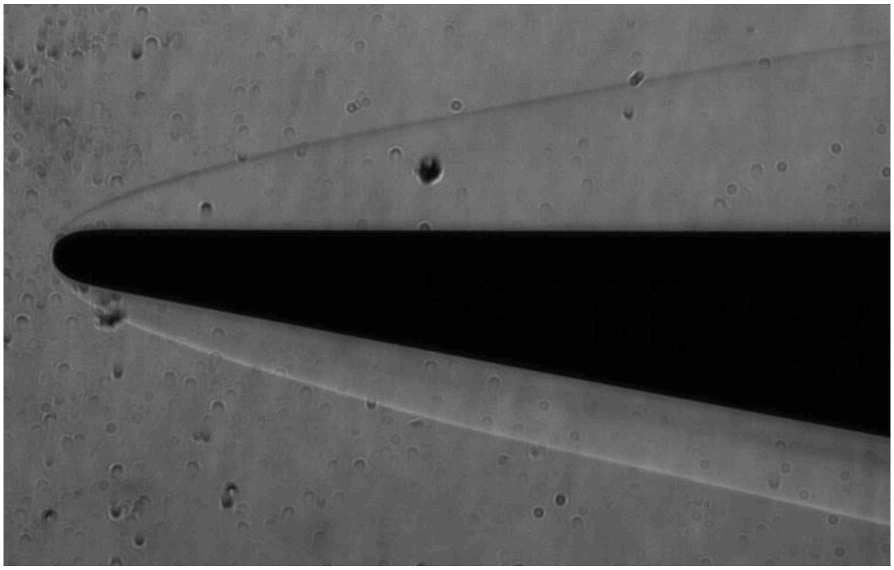

Figure 5.2. Plus 5 degrees AOA. The shock on the bottom is darker in spots and less straight, indicating shock unsteadiness. The boundary layer is also significant.

Chapter 6: Highly Unsteady Shocks Analysis

Based on the analysis in Chapter 2, perturbations at higher frequencies will require a different treatment that those at lower frequencies. The entropy flux perturbations derived in Chapter 3 and the results discussed in Chapter 4 would no longer apply beyond the quasi-steady limit. Thus, a different model is needed for high frequency oscillations. Very high frequency oscillations could result from vehicle pitching or plunging motion or oscillations in the combustor propagating forward.

6.1 Highly Unsteady Shock Relations

For very high frequency oscillations, the assumption of a stationary shock can apply, allowing for simplifications in calculating the entropy at each point in time. Following the approach of Ng and Kerrebrock[69] for quasi-steady flow across a shock, shock relations in the high frequency limit can be determined. From the unsteady continuity equation,

$$\partial(\rho u) = \frac{\partial V}{\partial t} d\rho + dV \frac{\partial \rho}{\partial t} \tag{128}$$

where V is the control volume around the shock, as argued in Chapter 2, the second term can be neglected in the quasi-steady limit and the entropy rise evaluated according to the steady oblique shock relations at each point in the cycle. For the high frequency limit, the first term can be neglected as the thermodynamic derivatives become large relative to the motion of the shock represented in the first term. At high frequencies, the shock is relatively stationary, with $dV = L$ corresponding to the shock displacement and on the order of a few millimeters at hypersonic speeds. Thus, continuity is satisfied by large density changes rather than the motion of the shock and the density change accommodates all of the unsteadiness. As discussed in Chapter 2.2, the high frequency regime can be understood with a one-dimensional piston. The piston oscillates at a high enough frequency such that the compression and expansion waves meet and cancel, so a shock's position is not affected by vehicle motion.

For high frequency oscillations, this study analyzes downstream density perturbations $\rho_2(t) = \hat{\rho}_2(1 + \varepsilon \sin wt)$ corresponding to flow perturbations downstream, possibly from the combustor, or $\rho_1(t) = \hat{\rho}_1(1 + \varepsilon \sin wt)$ from changes in the upstream conditions. As found in the quasi-steady case, results for changing upstream density should be qualitatively similar to pressure, temperature, or normal Mach number perturbations. For the case of changing conditions upstream where $\frac{d\rho_2}{dt} = 0$, continuity of mass evaluated for highly unsteady flow under this approximation becomes,

$$\rho_2 u_2 - \rho_1 u_1 = -L \frac{d\rho_1}{dt} \tag{129}$$

Divide by ρ_1,

$$\frac{\rho_2}{\rho_1} u_2 - u_1 = -\frac{L}{\rho_1} \frac{d\rho_1}{dt} \tag{130}$$

Add u_1 to both sides,

$$\frac{\rho_2}{\rho_1} u_2 = u_1 - L \frac{d \ln \rho_1}{dt} \tag{131}$$

Divide by u_2 to get the result for density ratio across the shock in terms the upstream and downstream Mach numbers in terms of upstream conditions, the rate of change of upstream density, and the small distance the shock moves,

$$\frac{\rho_2}{\rho_1} = \frac{u_1 - \frac{L}{\rho_1}\frac{d\rho_1}{dt}}{u_2} = \frac{\rho_2}{\rho_1} = \frac{M_1 - \frac{L}{a_1}\frac{d(\ln\rho_1)}{dt}}{M_2'} \tag{132}$$

Similarly for $\frac{d\rho_1}{dt} = 0$,

$$\rho_2 u_2 - \rho_1 u_1 = L\frac{d\rho_2}{dt} \tag{133}$$

$$u_2 - \frac{\rho_1}{\rho_2}u_1 = \frac{L}{\rho_2}\frac{d\rho_2}{dt} \tag{134}$$

$$\frac{\rho_1}{\rho_2} = \frac{u_2 - L\frac{d\ln\rho_2}{dt}}{u_1} \tag{135}$$

$$\frac{\rho_2}{\rho_1} = \frac{u_1}{u_2 - L\frac{d\ln\rho_2}{dt}} = \frac{M_1}{M_2' - \frac{L}{a_1}\frac{d\ln\rho_2}{dt}} \tag{136}$$

From the conservation of momentum and substituting in the above expressions for continuity, a relationship for the downstream Mach number in terms of the upstream conditions, M_2' can be found for both cases. For a perturbation in upstream density, where $\frac{d\rho_2}{dt} = 0$, conservation of momentum can be written as,

$$\rho_2 u_2^2 - \rho_1 u_1^2 + p_2 - p_1 = -u_1 L\frac{d\rho_1}{dt} \tag{137}$$

Mass conservation represented by Equation 128 can be used to remove ρ_2,

$$\rho_2 u_2^2 = \left(\rho_1 u_1 - L\frac{d\rho_1}{dt}\right)u_2 \tag{138}$$

$$\rho_1 u_1 \left(u_2 - u_1\right) + p_2 - p_1 - u_2 L \frac{d\rho_1}{dt} = -u_1 L \frac{d\rho_1}{dt} \tag{139}$$

$$p_2 - p_1 = L \frac{d\rho_1}{dt}\left(u_2 - u_1\right) - \rho_1 u_1 \left(u_2 - u_1\right) \tag{140}$$

to find the pressure ratio in terms of the time rate of change in upstream density, upstream density, and velocities,

$$\frac{p_2}{p_1} = 1 + \frac{\rho_1 u_1}{p_1}\left(u_1 - u_2\right) + \frac{L}{p_1}\frac{d\rho_1}{dt}\left(u_2 - u_1\right) \tag{141}$$

$$\frac{p_2}{p_1} = 1 + \frac{\gamma}{a_1^2}\left(u_1 - u_2\right)\left(u_1 - \frac{L}{\rho_1}\frac{d\rho_1}{dt}\right) \tag{142}$$

$$P \equiv \frac{p_2}{p_1} = 1 + \gamma\left(M_1 - M_2'\right)\left(M_1 - \frac{L}{a_1 \rho_1}\frac{d\rho_1}{dt}\right) \tag{143}$$

From this relation for the pressure ratio *P*, the Mach number across the shock in terms of the upstream speed of sound is

$$M_2' = M_1 + \frac{1-P}{\gamma}\frac{1}{M_1 - \frac{L}{a_1}\frac{d\ln\rho_1}{dt}} \tag{144}$$

Similarly, for a perturbation in downstream density, where $\frac{\partial\rho_1}{\partial t} = 0$, conservation of momentum can be written as,

$$\rho_2 u_2^2 - \rho_1 u_1^2 + p_2 - p_1 = u_2 L \frac{d\rho_2}{dt} \tag{145}$$

Mass conservation represented by equation 128 can be used to remove ρ_2,

$$u_2 L \frac{d\rho_2}{dt}\left(\rho_2 u_2 - \rho_1 u_1\right) u_2 \tag{146}$$

$$p_2 - p_1 - \rho_1 u_1^2 = -\rho_1 u_1 u_2 \tag{147}$$

to find the pressure ratio in terms of the time rate of change in upstream density, upstream density, and velocities,

$$\frac{p_2}{p_1} 1 + \frac{u_1 \rho_1}{p_1}\left(u_1 - u_2\right) \tag{148}$$

$$\frac{p_2}{p_1} = 1 + \gamma M_1\left(M_1 - M_2'\right) \tag{149}$$

From this relation for the pressure ratio P, the Mach number across the shock in terms of the upstream speed of sound is

$$M_2' = M_1 + \frac{1-P}{\gamma M_1} \tag{150}$$

The highly unsteady energy equation in the absence of heat addition or work produces another relation for the pressure ratio. For $\frac{\partial \rho_1}{\partial t} = 0$,

$$\left(\rho_2 u_2 T_{t,2} - \rho_1 u_1 T_{t,1}\right) = T_{t,2} L \frac{d\rho_2}{dt} - \frac{\gamma - 1}{\gamma} L T_2 \frac{d\rho_2}{dt} \tag{151}$$

$$T_2\left[\left(1 + \frac{\gamma-1}{2} M_2^2\right)\left(u_2 \rho_2 - L\frac{d\rho_2}{dt}\right) - \frac{\gamma-1}{\gamma} L \frac{d\rho_2}{dt}\right] = T_1 u_1 \rho_1 \left(1 + \frac{\gamma-1}{2} M_1^2\right) \tag{152}$$

Divide out ρ_2 on the left hand side to bring it to the front,

$$T_2 \rho_2\left[\left(1 + \frac{\gamma-1}{2} M_2^2\right)\left(u_2 \rho_2 - L\frac{d\ln\rho_2}{dt}\right) - \frac{\gamma-1}{\gamma} L \frac{d\ln\rho_2}{dt}\right] = T_1 u_1 \rho_1 \left(1 + \frac{\gamma-1}{2} M_1^2\right) \tag{153}$$

Divide by $T_1 \rho_1$ and the expression on the left containing $\frac{d\ln\rho_2}{dt}$ and use the ideal gas equation $P = \rho R T$ to find the pressure ratio,

$$P = \frac{p_2}{p_1} = \frac{u_1\left(1 + \frac{\gamma-1}{2} M_1^2\right)}{\left(1 + \frac{\gamma-1}{2} M_2^2\right)\left(u_2 - L\frac{d\ln\rho_2}{dt}\right) - \frac{\gamma-1}{\gamma} L \frac{d\ln\rho_2}{dt}} \tag{154}$$

$$P = \frac{p_2}{p_1} = \frac{M_1\left(1+\frac{\gamma-1}{2}M_1^2\right)}{\left(1+\frac{\gamma-1}{2}M_2^2\right)\left(M_2' - \frac{L}{a_1}\frac{d\ln\rho_2}{dt}\right) - \frac{\gamma-1}{\gamma}\frac{L}{a_1}\frac{d\ln\rho_2}{dt}} \tag{155}$$

Although total temperature of the flow is not constant for an unsteady flow, total temperature is constant for each particle of the flow, so a constant total temperature can be assumed in this derivation. From equations 136 for the density ratio and 150 for the downstream Mach number in terms of the upstream conditions,

$$M_2^2 = M_2'^2 \frac{1}{P}\frac{\rho_2}{\rho_1} = \frac{1}{P}\left(M_1 + \frac{1-P}{\gamma M_1}\right)^2 \left(\frac{M_2}{M_1 - (1-P)/\gamma M_1 - \left(L/a_1\rho_2\right)d\rho_2/dt}\right) \tag{156}$$

For perturbations in upstream density,

$$\left(\rho_2 u_2 T_{t,2} - \rho_1 u_1 T_{t,1}\right) = -T_{t,1} L\frac{d\rho_1}{dt} + \frac{\gamma-1}{\gamma} L T_1 \frac{d\rho_1}{dt} \tag{157}$$

$$T_2 u_2 \rho_2 \left(1+\frac{\gamma-1}{2}M_2^2\right) = T_1\left[\left(1+\frac{\gamma-1}{2}M_1^2\right)\left(u_1\rho_1 - L\frac{d\rho_1}{dt}\right) + \frac{\gamma-1}{\gamma}L\frac{d\rho_1}{dt}\right] \tag{158}$$

$$P = \frac{\left(M_1 - \frac{L}{a_1\rho_1}\frac{d\rho_1}{dt}\right)\left(1+\frac{\gamma-1}{2}M_1^2\right) + \frac{\gamma-1}{\gamma}\frac{L}{a_1\rho_1}\frac{d\rho_1}{dt}}{M_2'\left(1+\frac{\gamma-1}{2}M_2^2\right)} \tag{159}$$

$$M_2^2 = M_2'^2 \frac{1}{P}\frac{\rho_2}{\rho_1} = \frac{1}{P}\left(M_1 + \frac{1-P}{\gamma_1\left(M_1 - \left(L/a_1\right)d\rho_1/dt\right)}\right)^2 \left(\frac{M_1 - \left(L/a_1\rho_1\right)d\rho_1/dt}{M_2'}\right) \tag{160}$$

Equations 155 with 156 and 159 with 160 cannot be solved in closed form, but do provide unique solutions for the shock pressure ratio and downstream conditions as a function of upstream conditions and Mach number and the perturbed density derivative. These can be solved at each time step, and then an average entropy flux gain can be calculated. When the density derivatives are equal to zero, the solutions revert to the Rankine-Hugoniot equations. For quasi-steady flow, the density derivatives are very small, and the entropy perturbation is zero to machine precision, justifying the use of the Rankine-Hugoniot equations for quasi-steady perturbations in Mach number, shock angle, or pressures calculated at each time step.

Figures 6.1, 6.2, and 6.3 show upstream and downstream density derivatives, pressure ratio for both perturbation types, and the entropy flux across the shock for both perturbation types throughout the cycle for a Mach 5 flow with a 10% upstream or downstream density perturbation and a frequency of 15 kHz.

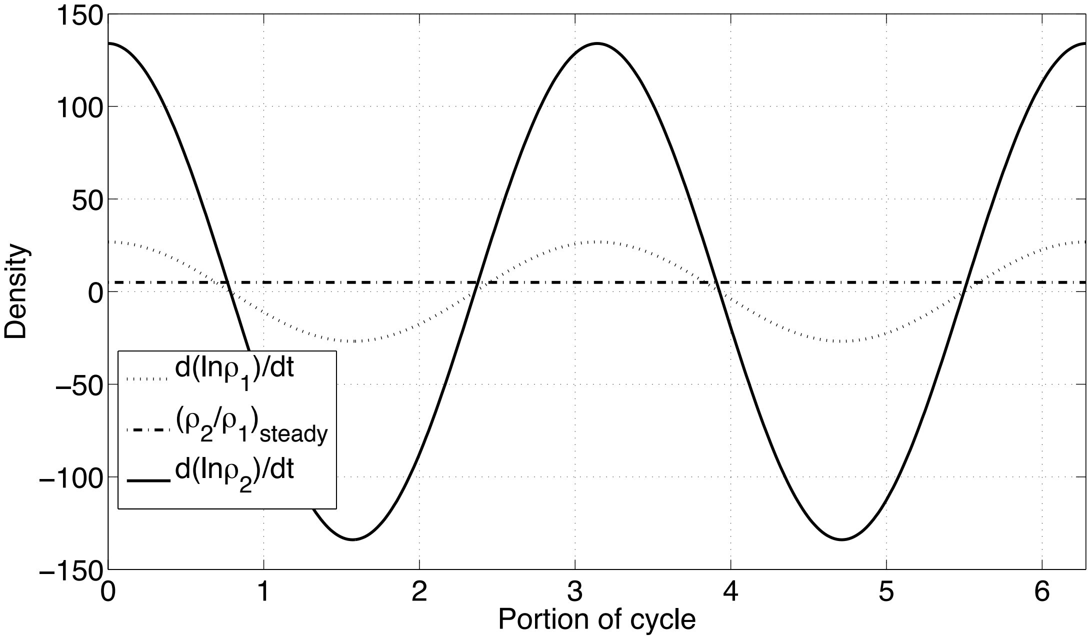

Figure 6.1. Perturbed logarithmic density derivatives upstream and downstream.

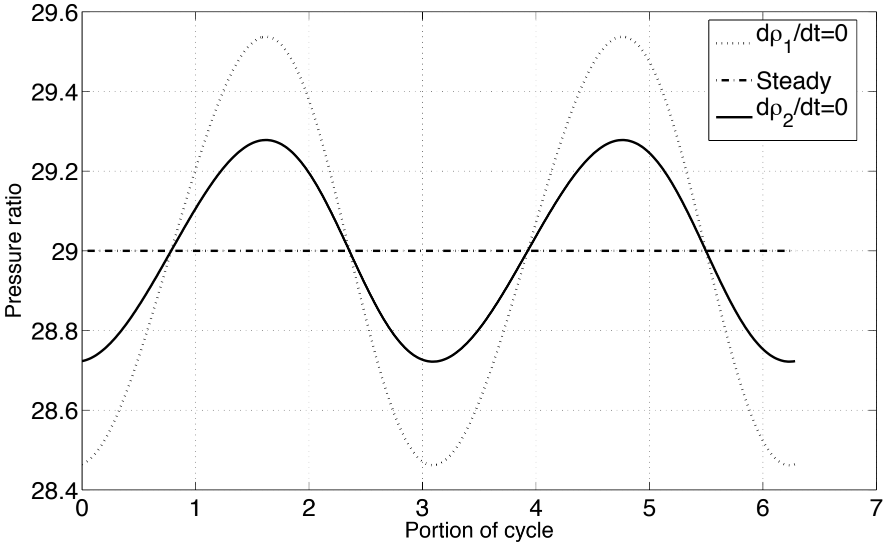

Figure 6.2. Time-varying pressure ratio for upstream and downstream density perturbations versus steady Mach 5 flow. Frequency is 15 kHz and perturbation size is 10% of upstream or downstream density.

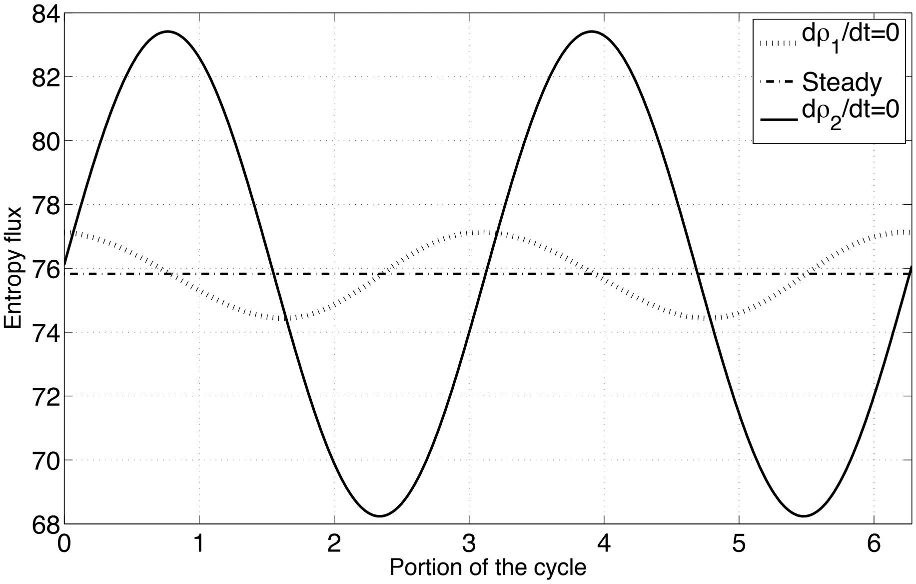

Figure 6.3. Entropy flux for upstream or downstream density perturbations at 15 kHz for a Mach 5 flow. For both upstream and downstream density perturbations at this Mach number, frequency, and perturbation size, the time-averaged entropy flux is less than the entropy flux for the steady case.

6.2 High Frequency Perturbation Methodology

6.2.a Perturbations

This study examines the entropy gain flux relative to the steady case for downstream and upstream density perturbations as a function of the perturbation size ε and a non-dimensional pseudo-Mach number M_p that characterizes the speed of the shock. Unlike the quasi-steady case, the entropy flux perturbation depends on two non-dimensional variables with the additional variable describing how much the shock is moving. In each equation for flow across a highly unsteady shock, there is a non-dimensional term

$$\frac{L}{a_1\rho_1}\frac{d\rho_1}{dt}=\frac{L}{a_1}\frac{d(\ln\rho_1)}{dt}=\frac{Lw}{a_1}\left(\frac{\varepsilon\cos(wt)}{1+\varepsilon\sin wt}\right)=M_p\left(\frac{\varepsilon\cos(wt)}{1+\varepsilon\sin(wt)}\right)\qquad(161)$$

for a sinusoidal perturbation defined as $\rho_2(t)=\hat{\rho}_2(1+\varepsilon\sin wt)$ or $\rho_1(t)=\hat{\rho}_1(1+\varepsilon\sin wt)$. Hypersonic high frequency shock oscillation amplitudes are typically are the order of 1 mm[75]. For this study, a value of 1 mm will be used for *L*. Upstream parameters were the same as those used for the quasi-steady analysis and are based on the assumption of a vehicle flying at an altitude of 30 kilometers.

This analysis used a range of frequencies and perturbations with the majority of cases run well within the high frequency limit. Frequencies varied between 1 kHz and 50 kHz, with the bulk of analysis occurring for frequencies well within the high frequency regime (5 kHz to 30 kHz). This corresponds to a pseudo-Mach number with the parameters used of 0.1 to 1.0. Perturbation sizes varied between 0.05 and 0.3, with the majority of analysis occurring with perturbation sizes between 0.1 and 0.3 with frequencies above 5 kHz. Several cases were run and compared with the same factor of εw to directly compare the effect of frequency and perturbation size. The lower limit at various Mach numbers for the high frequency limit for both perturbation sizes at a given frequency and also frequencies at a given perturbation size is also examined.

6.2.b Calculations of Time-Averaged Entropy Gain for High Frequency Oscillations

A root-finding method was used to iterate a solution for the pressure ratio across the shock at a given freestream Mach number, M_p, and perturbation size. Appendix B contains the Matlab code used for these calculations. For each freestream Mach number, M_p, and perturbation size, there is a unique pressure ratio and downstream Mach number.

Unlike for the quasi-steady case, numerical integration is required, as there are no closed form solutions for the time-averaged entropy flux. Matlab, Mathematica, and Microsoft Excel's averaging or mean functions were used to find the time-average initially. Each program uses the same numerical integration method. As found when finding the time-average of $\frac{d}{dt}(\rho s)$ for the quasi-steady case, these numerical integrators do a poor job of averaging sinusoidal functions. For example, these programs gave non-zero averages for functions that have easily derived analytic expressions that can be shown to be zero over one cycle. The results using these numerical integrators also did not make physical sense. It predicted that all upstream density perturbations at all frequencies, Mach numbers, and perturbation sizes had a higher entropy rise than the steady case and would revert back to the steady case prior to the perturbation. This is not physical as research on Type IV interactions discussed in Chapter 1.3 shows that there are stable unsteady high frequency shock systems that are not transient phenomena. For downstream density perturbations, this method predicted that no shock would be stable to high frequency downstream density perturbations. For both types of perturbations, as the Mach number increased, the mean or average entropy perturbation using these functions decreased towards zero, as expected. The pressure ratio and entropy flux across the shock has a very nearly sinusoidal response to a sinusoidal input, only varying from a sinusoid at the maximum and minimums. Given this, the time average can be calculated by subtracting the difference from the minimum in entropy flux to the steady entropy flux from the difference from the maximum in entropy flux from the steady entropy flux,

$$\left[\left.\frac{\rho u(t)\Delta s(t)}{\rho_1 u_1 R}\right|_{\max} - \left.\frac{\rho u\Delta s}{\rho_1 u_1 R}\right|_{steady}\right] - \left[\left.\frac{\rho u(t)\Delta s(t)}{\rho_1 u_1 R}\right|_{\min} - \left.\frac{\rho u\Delta s}{\rho_1 u_1 R}\right|_{steady}\right]$$

If this quantity is greater than zero, then the principle of minimum entropy states that the shock should be stable to perturbations and will become steady again. If this quantity is less than zero, then the shock would be unstable to perturbations and remain unsteady. This method produced curves of entropy flux perturbation versus normal Mach number that had a similar shape to those produced for quasi-steady perturbations. Limits found usually this method were also consistent with predictions in Chapter 2 for the high frequency limits.

Chapter 7: Results for entropy perturbation across shocks for highly unsteady perturbations

Analysis of the entropy flux across a shock subjected to high frequency perturbations shows several interesting trends, including some not observed for a quasi-steady perturbation[82]. The analysis presented indicates that shocks in hypersonic inlets may be stable to upstream perturbations at normal Mach numbers up to Mach 3.5 for very high frequencies, but not stable to any downstream perturbations in the high frequency limit. The entropy flux depends on frequency such that increasing the frequency increases the normal Mach number at which the entropy flux perturbation is positive. The size of the density perturbation has a much smaller inverse effect. The lower limit of the high frequency approximation for frequency (or pseudo-Mach number M_p) and perturbation at a given Mach number is also presented and is generally consistent with previous work and the analysis presented in Chapter 2 for quasi-steady shocks.

7.1 Downstream density perturbations

Unlike for the quasi-steady case where shocks were stable to downstream pressure perturbations at higher normal Mach numbers, unsteady shocks because of downstream density perturbations were found to be unstable for any high frequency (greater than 1 kHz) perturbation at any normal Mach number. Figure 7.1 shows a plot of the entropy flux perturbation resulting from a downstream density perturbation for frequencies between 10 and 30 kHz ($0.3 < M_p < 1.0$) and perturbations between

0.1 and 0.3. Results were normalized by the upstream mass flux and the square of the perturbation size ε to allow for comparisons for different Mach numbers, perturbation sizes, and the quasi-steady results. As expected and consistent with theory, the entropy flux perturbations all go to zero as Mach number goes to infinity.

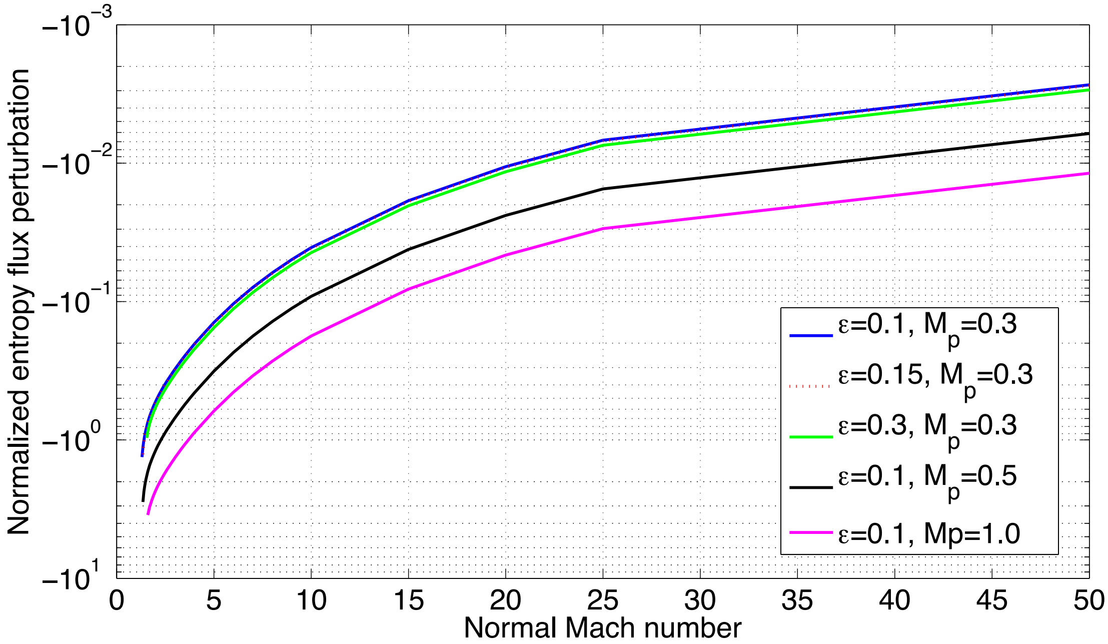

Figure 7.1. Normalized entropy gain relative to steady solution across shock for downstream density perturbation plotted against Mach number at different M_p and perturbation sizes.

As expected and consistent with theory, the entropy flux perturbations all go to zero as Mach number goes to infinity. However, this went to zero much slower with respect to Mach number than for upstream density perturbations. This is likely because $\frac{\partial \ln \rho_2}{\partial t} >> \frac{\partial \ln \rho_1}{\partial t}$ as shown in figure 6.1. In addition, the entropy flux perturbation for downstream density perturbations was several orders of magnitude larger. This is also likely because at a given normal Mach number, the larger downstream density derivative magnifies the difference from the steady case. The entropy jump across the shock for a downstream perturbation is also not multiplied by a counteracting sinusoidal change in mass flux that would decrease the difference in entropy flux from the steady case.

Finally, increasing the frequency or M_p increased the difference in normalized entropy flux perturbation from the steady case by an order of magnitude as shown in Figure 7.1. However, this resulted in the normalized entropy flux becoming more negative and could translate to the shock being less stable to downstream perturbations in thermodynamic variables. Increasing the perturbation size ε slightly decreased the difference from the steady case or increases the entropy flux gain, but this effect is many times smaller than changing the frequency or M_p.

Figure 7.1 does not start at Mach 1 because the root solver was not able to find a solution for low normal Mach numbers typically under 1.25. This may be because at high frequencies part of the flow is subsonic relative to the shock and thus a solution for the pressure ratio is not possible for that Mach number. This was an issue also for upstream density perturbations and did depend on frequency with higher frequencies increasing the lower bound for a solution. For some cases, at lower Mach numbers at which a solution was possible, the entropy flux was not positive throughout the cycle. However, entropy can decrease during a process as long as the process must finish and finishes with an entropy gain. A well-known example of this is that as flow crosses the very small region of a shock, the entropy decreases in the shock before increasing again such that the overall process results in an entropy gain. For frequencies of 10 kHz, some portions of the cycle at M=1.41 had a negative entropy flux. At 15 kHz and 30 kHz, this occurred below M=1.50 and M=1.72 respectively.

7.2 Upstream density perturbations

Unlike for the case with downstream density perturbations, the entropy flux perturbation from the steady state was positive for some normal Mach numbers for upstream density perturbations. The entropy flux perturbation's dependence on upstream normal Mach number was similar to that for a quasi-steady with a region at lower normal Mach numbers where the entropy flux perturbation was positive and the principle of minimum entropy predicts the shock should be stable to perturbations. However, as shown in the next section, the normal Mach number at which the steady entropy flux is equal to the perturbation depends highly on perturbation frequency.

Figure 7.2 shows the relationship between normalized entropy flux perturbation and normal Mach number for a perturbation of 10% of the upstream density at a frequency of 10 kHz. As with the downstream density perturbations, the entropy flux was also normalized by the square of the perturbation size and upstream steady mass flux. Figure 7.3 shows the normalized entropy gain flux perturbation for a 10% perturbation in upstream density at almost the lowest frequency at which the high frequency approximation would still apply. At 1 kHz, the relationship is very similar, but the zero occurs at a lower normal Mach number and the entropy gain flux is several orders of magnitude less. The effect of frequency and perturbation size will be discussed in more detail the next section. The general trend and shape of the graph is the same for perturbation sizes and frequencies at which the high frequency approximation is applicable.

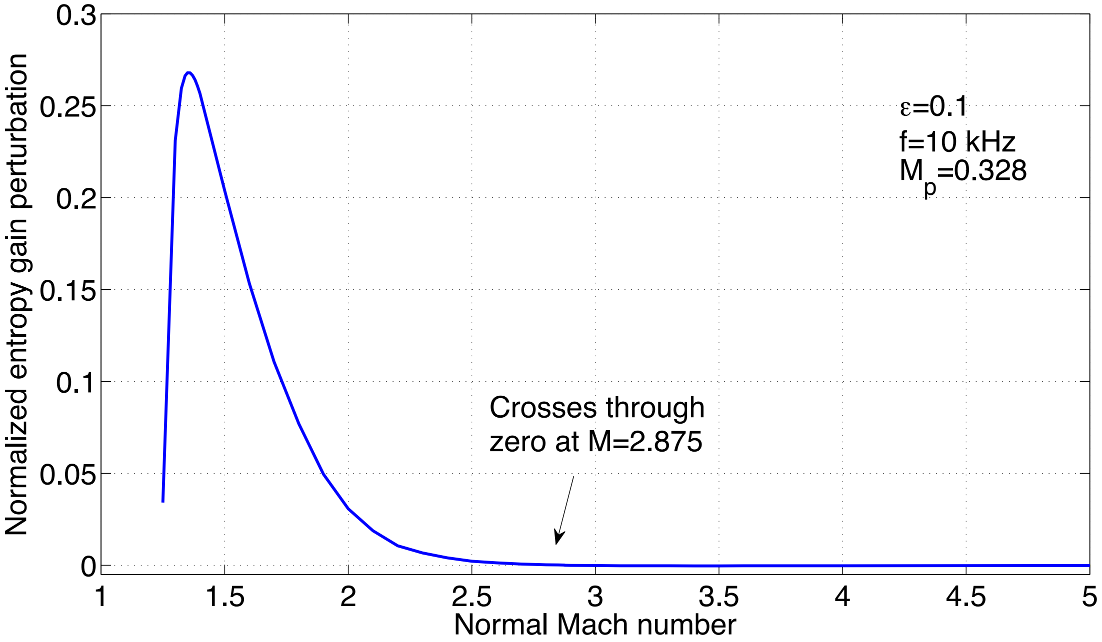

Figure 7.2. Normalized time-averaged entropy gain flux perturbation for a 10% perturbation in upstream density at a frequency of 10 kHz.

Just as with downstream perturbations, calculations at the lowest supersonic normal Mach numbers was not possible or inaccurate. Using the range of frequencies and perturbation sizes over which the high frequency approximation applied, the lowest normal Mach number at which a solution could be found was typically around Mach 1.2. As shown in Figure 7.3, at normal Mach numbers slightly above where solutions can be found with the root-finding algorithm ($1.19 < M_{n,1} < 1.27$), the entropy flux perturbation is negative for all frequencies and perturbation sizes at which the high frequency approximation was valid.

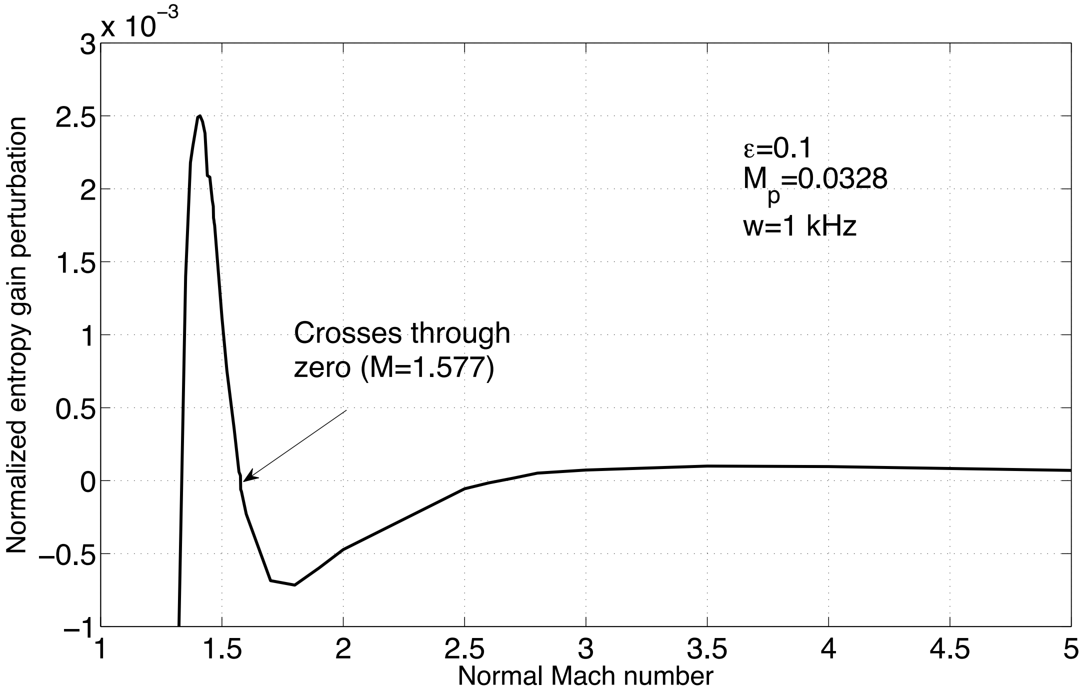

Figure 7.3. Normalized time-averaged entropy gain flux perturbation for a 10% perturbation in upstream density at a frequency of 1 kHz.

These negative entropy flux perturbations may not be accurate and could be due to numerical error and limitations with the root-finding algorithm and the method used to determine the time-average at lower normal Mach numbers. Figure 7.4 shows the pressure ratio response to a sinusoidal upstream density perturbation for a normal Mach number of 1.19 compared to a cosine function with the same mean and same distance between the mean and minimum of the function. This comparison shows that the pressure ratio is not sinusoidal and that at the peaks in the cycle, the pressure ratio is much less. Figure 7.5 shows the same comparison but for the entropy flux gain. The entropy flux response is also not a good approximation of a sinusoid and has a minimum much lower than for a sinusoid that has an amplitude equivalent to the distance between the maximum in entropy flux perturbation and its mean. Thus, finding the difference between the maximum and mean and the minimum and mean of the normalized entropy flux perturbation and determining which difference is larger is not appropriate for these lower normal Mach numbers and another method of time-averaging is needed. Figures 7.6 and 7.7 show the pressure ratio versus time and entropy flux per time for a Mach 5 flow. All of these figures used a frequency of 10 kHz and a perturbation of 10%. Comparing these figures to those for Mach 1.19 show that as Mach number increases, the pressure ratio and entropy flux more closely resemble a sinusoid. This is not surprising and is to be expected.

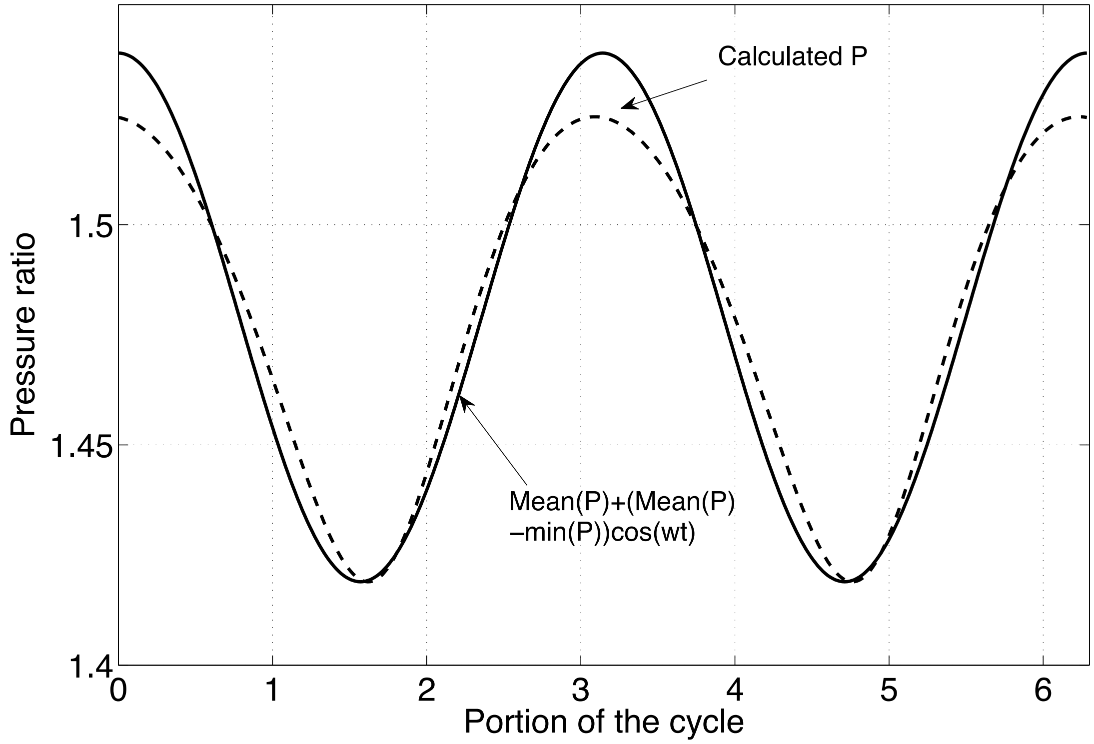

Figure 7.4. Pressure ratio at Mach 1.19 during cycle with frequency of 10 kHz.

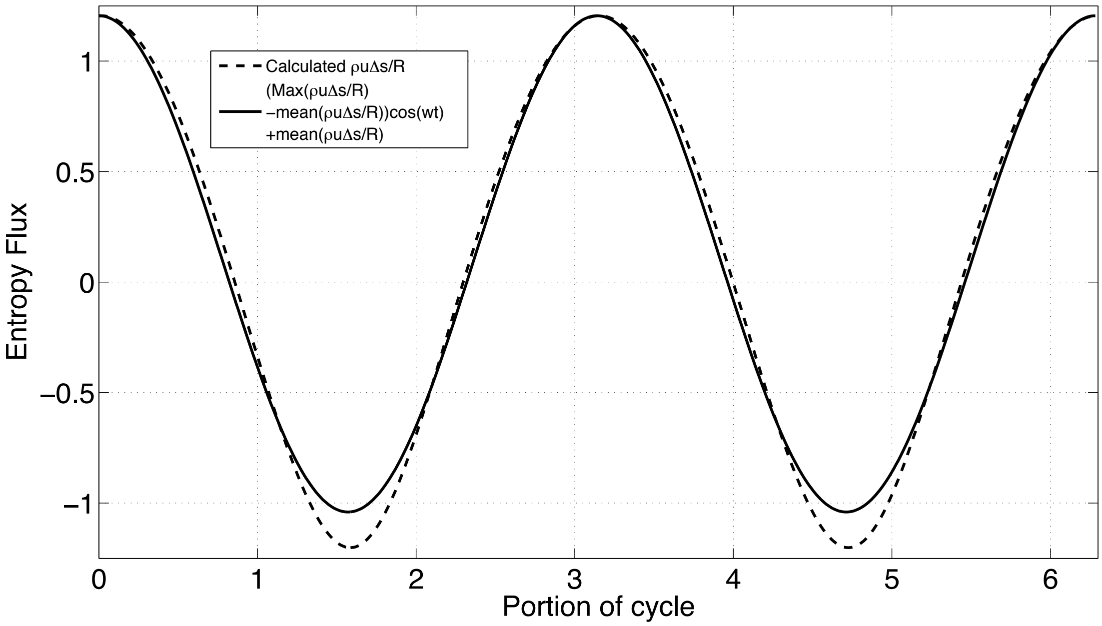

Figure 7.5. Entropy flux at Mach 1.19 during cycle with frequency of 10 kHz.

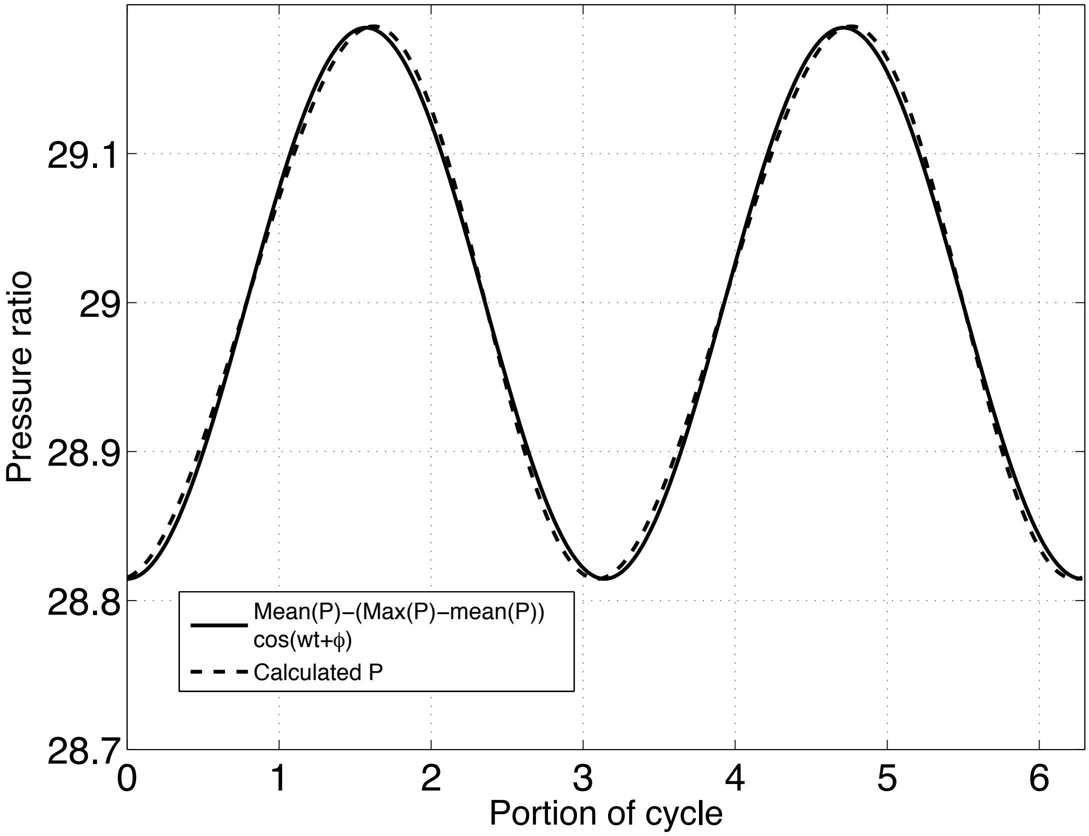

Figure 7.6. Pressure ratio at Mach 5 during cycle with frequency of 10 kHz.

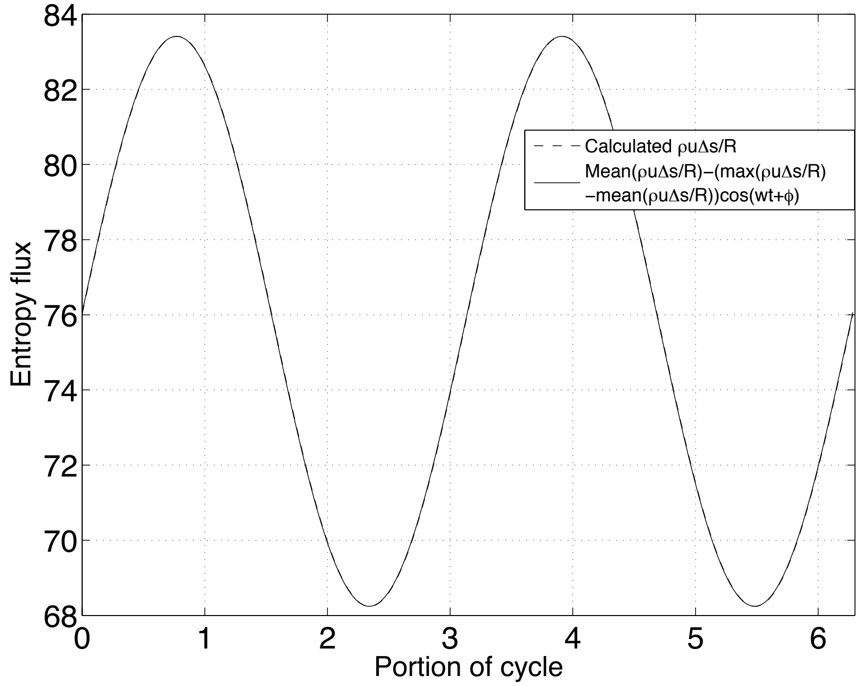

Figure 7.7. Entropy flux at Mach 5 during cycle with frequency of 10 kHz.

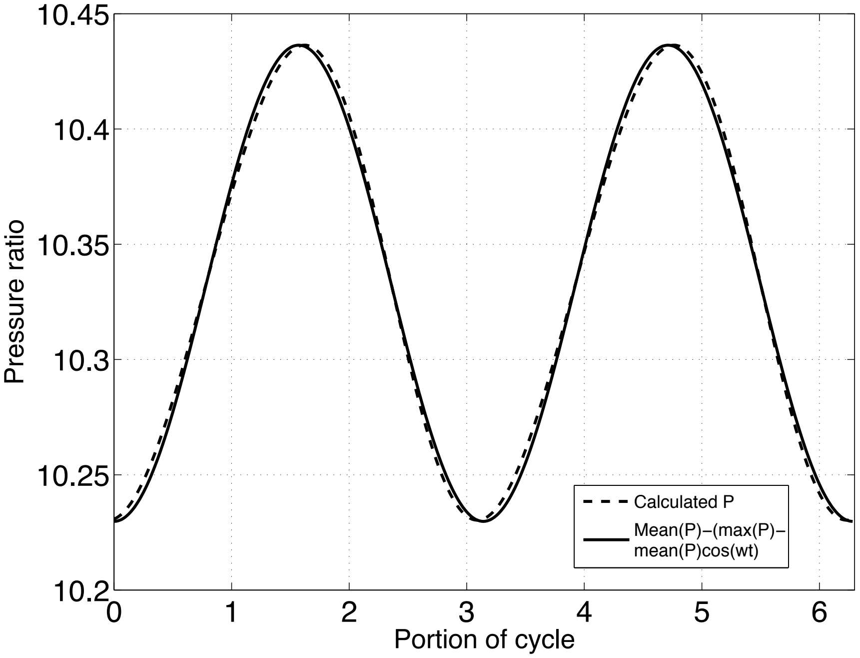

Figure 7.8. Pressure ratio at Mach 3 during cycle with frequency of 10 kHz.

In addition, as shown also in Figure 7.8, as the freestream Mach number increases, the phase of the pressure ratio and entropy flux perturbation shifts. Like with downstream density perturbations, portions of the cycle at lower normal Mach numbers had a negative entropy flux. The Mach numbers at which this occurred increased with frequency. For the frequencies looked at, the lowest normal Mach number at which the entropy flux was positive for all portions of the cycle was between M=1.53 and M=1.65. This may also be contributing to some of the inaccuracy at the lower normal Mach numbers because there may be portions of the cycle where the flow is subsonic and a solution should not be possible.

7.2.a Frequency and Pseudo-Mach number dependence

The entropy perturbation and normal Mach numbers at which a steady shock should be stable to high frequency upstream density perturbation had a significant dependence on the movement of the shock. Figure 7.9 shows three combinations of perturbation sizes and frequencies or pseudo-Mach numbers for the normalized entropy flux. The plots correspond to $\varepsilon = 0.2, M_p = 0.5$, $\varepsilon = 0.1, M_p = 1.0$, and $\varepsilon = 0.3, M_p = 0.33$ where $\varepsilon M_p = 0.1$ or $\varepsilon w = 3$ kHz. Even though the product of the perturbation size and frequency or pseudo-Mach number is the same, the perturbations corresponding to a higher frequency are of higher value and positive longer.

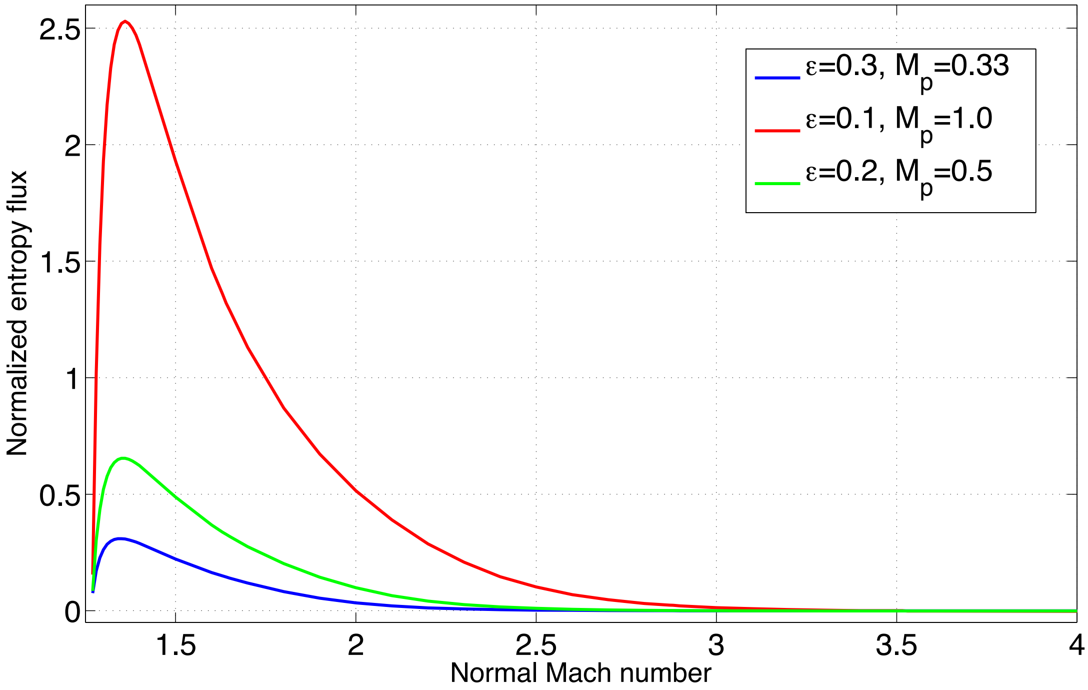

Figure 7.9. Normalized entropy flux for upstream density perturbations. The product of the perturbation size and pseudo-Mach number was the same for each at 0.1.

For shocks subjected to high-frequency density perturbations, the magnitude of the entropy flux perturbation and the normal Mach numbers at which it is positive for only upstream perturbations increases significantly as the frequency or pseudo-Mach number increases. Doubling the frequency or pseudo-Mach number resulted in an increase in the normal Mach number at which the steady entropy flux equaled the time-averaged perturbation by several tenths of a normal Mach number. Increasing the frequency has the effect of increasing the peak and broadening it. Figure 7.10 shows the normalized entropy gain relative to the steady solution versus normal Mach number for six frequencies between 800 Hz and 30 kHz with a 10% perturbation. Figure 7.11 is the same relation but with the time-averaged entropy flux divided by frequency so that the difference in where the entropy perturbation relation for each frequency crosses zero can be seen. Figure 7.12 is a zoom on the x-axis. These figures show how much the cross-over between stable and unstable and magnitude of the entropy flux perturbation decrease as frequency decreases. This is also consistent with the quasi-steady results for perturbations in upstream thermodynamic variables, which had a zero at M=1.25. Table 7.1 includes the location of the zero and maximum entropy gain versus steady for the different perturbation sizes and frequencies studied. The lowest normal Mach number at which the shock would no longer be stable to high frequency upstream thermodynamic variable perturbations was 800 Hz ($M_p = 0.0264$) and $\varepsilon = 0.1$ at M=1.461. The highest normal Mach number at which this occurred was M=3.525 for 30 kHz perturbations of 5 percent.

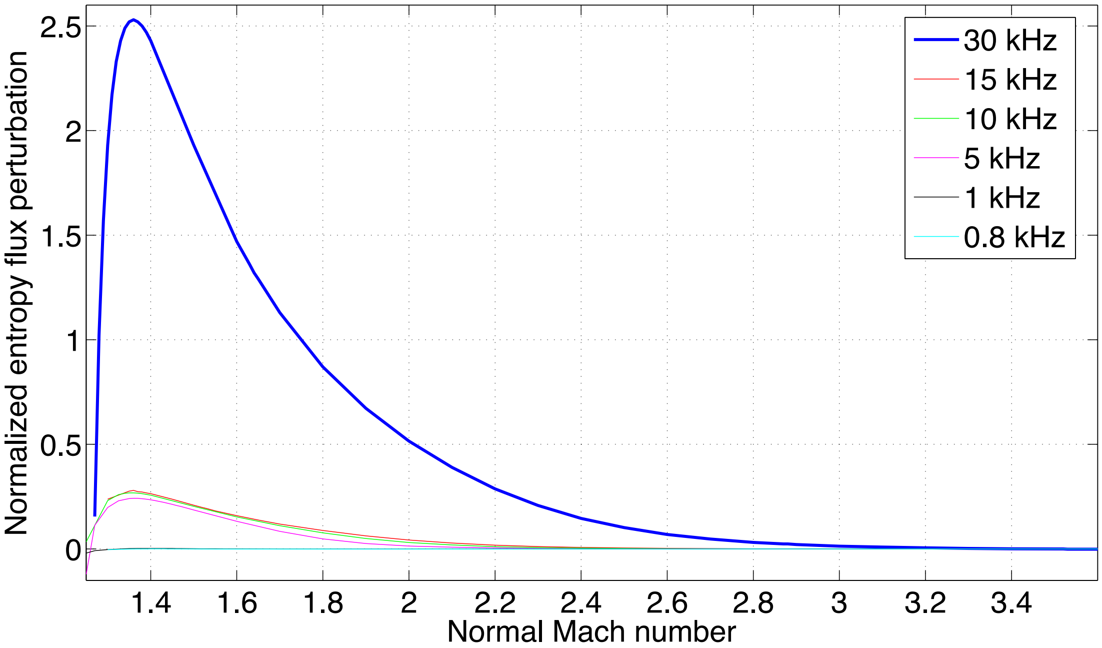

Figure 7.10. Normalized time-averaged entropy gain relative to steady solution across shock for upstream density perturbation of 10%.

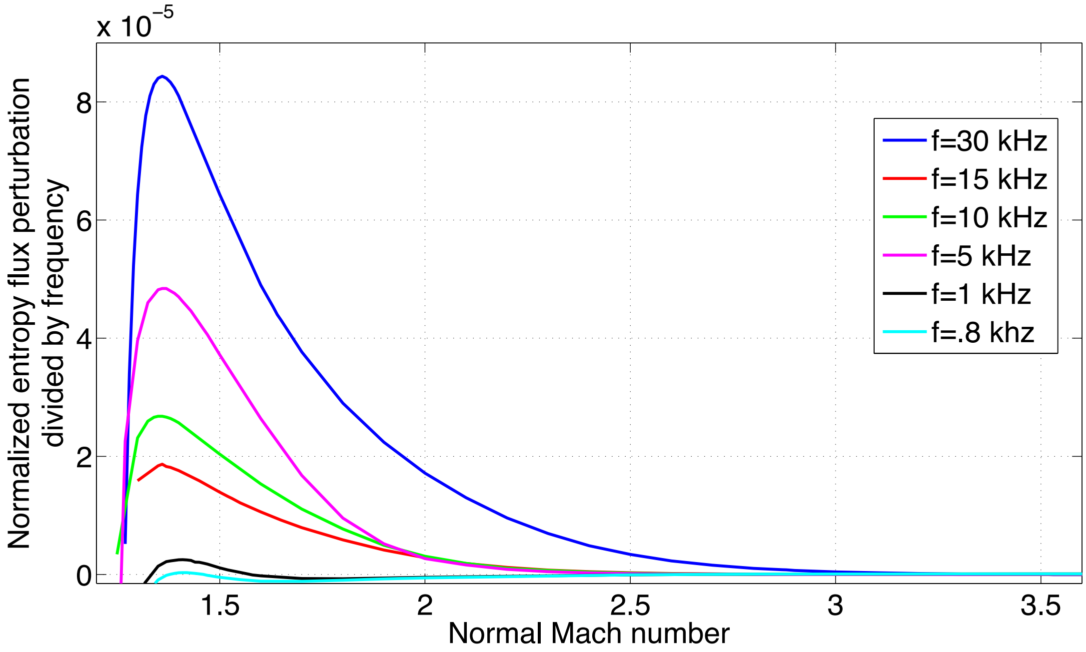

Figure 7.11. Normalized time-averaged entropy gain relative to steady solution across shock for upstream density perturbation of 10%. Results divided by frequency to facilitate viewing of the effect of frequency on the stability region.

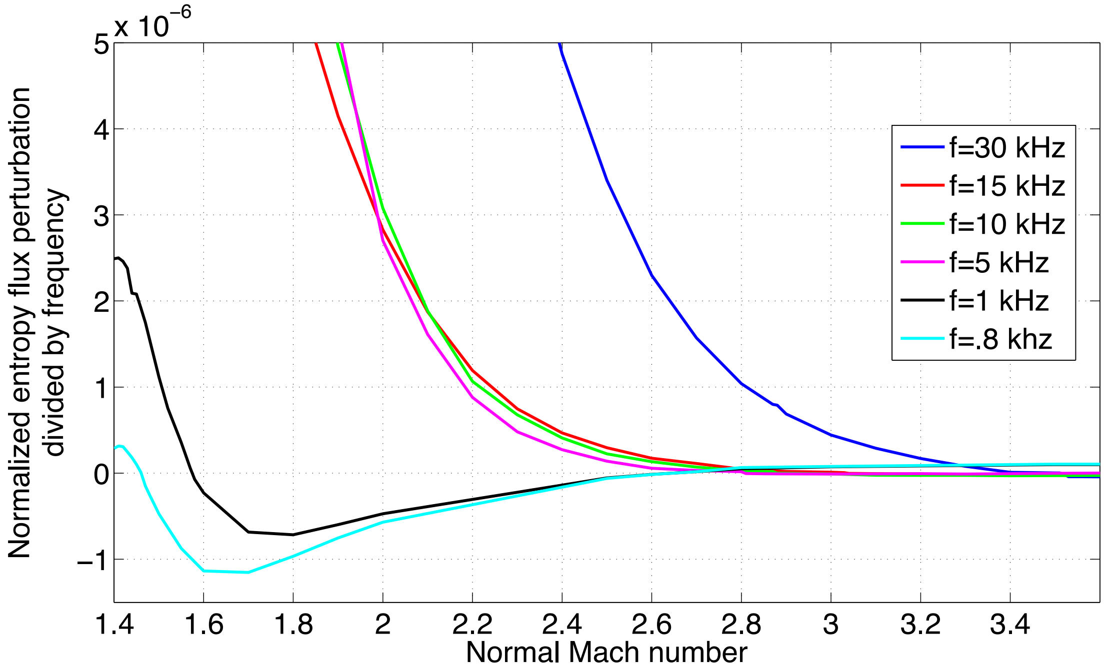

Figure 7.12. Zoom on the horizontal axis of Figure 7.11.

Perturbation size	M_p	Frequency (kHz)	Normal Mach number of maximum entropy gain versus steady	Normal Mach number of entropy gain equal to steady
0.1	0.0264	0.8	1.41	1.461
0.1	0.0328	1	1.41	1.577
0.1	0.164	5	1.375	2.804
0.1	0.328	10	1.37	2.880
0.15	0.328	10	1.37	2.876
0.3	0.328	10	1.36	2.873
0.1	0.492	15	1.36	3.033
0.2	0.492	15	1.37	3.029
0.05	0.984	30	1.37	3.525
0.1	0.984	30	1.37	3.516

Table 7.1. Predicted normal Mach number at which the shock becomes unstable according to the principle of minimum entropy as a function of perturbation size and frequency M_p.

7.2.b Perturbation size dependence

The size of the perturbation also affects the size of the time-averaged entropy flux perturbation and the Mach number stability region, but in a different way and an order of magnitude smaller than the frequency. From Table 7.1, doubling the frequency could increase the stability region by several tenths of a Mach number. This is 16% of Mach 3.033 to Mach 3.516 if the frequency increases from 15 kHz to 30 kHz. However, doubling the perturbation size slightly decreased the stability region but increases the entropy flux perturbation magnitude. The normal Mach number at which the shock no longer becomes stable decreased by several thousandths of a normal Mach number. This is 0.13% of Mach 3.033 for a 15 kHz perturbation if the perturbation size is doubled. Increasing the perturbation size increases the peak but brings the zero in closer to a lower normal Mach number. Decreasing the perturbation size broadens the graph--lowering the peak but spreading it out such that the zero is at a higher normal Mach number. The effect compared to frequency is different because the effect of the perturbation size varies during the cycle between $\frac{\varepsilon}{1+\varepsilon}M_p < \varepsilon M_p < \frac{\varepsilon}{1-\varepsilon}M_p$. Figure 7.13 shows three different perturbation sizes of 10%, 20%, and 30% for an upstream density perturbation at 30 kHz. Figure 7.14 shows several different perturbation sizes and frequencies to show the scale of the effect of changing perturbation size compared to changing the frequency or the amount the shock moves by. Figure 7.15 is a plot of Table 7.1 and the location of the zero versus M_p at different perturbation sizes showing a clear relationship between the zero and M_p or frequency and that the effect of perturbation size relative to frequency or M_p is minimal.

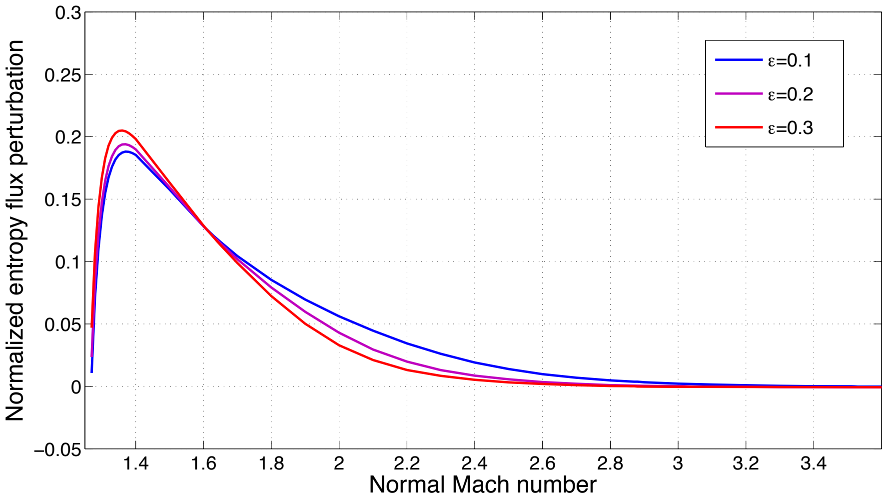

Figure 7.13. Normalized time-averaged entropy flux for frequency of 30 kHz and M_p=1.0. Increasing perturbation size has a small effect compared to changing frequency.

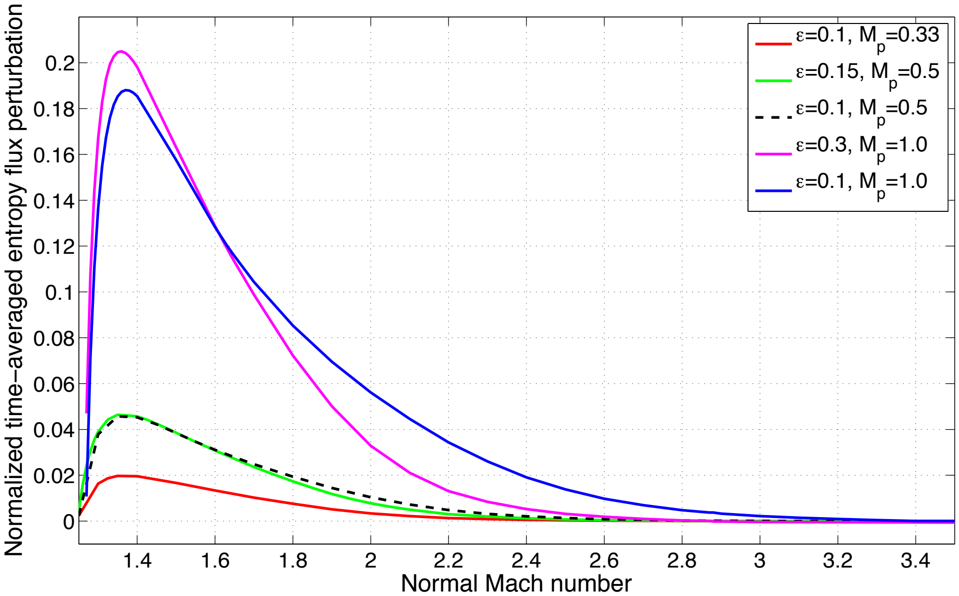

Figure 7.14. Comparison of effect of frequency or pseudo-Mach number and perturbation size on normalized time-averaged entropy flux perturbation.

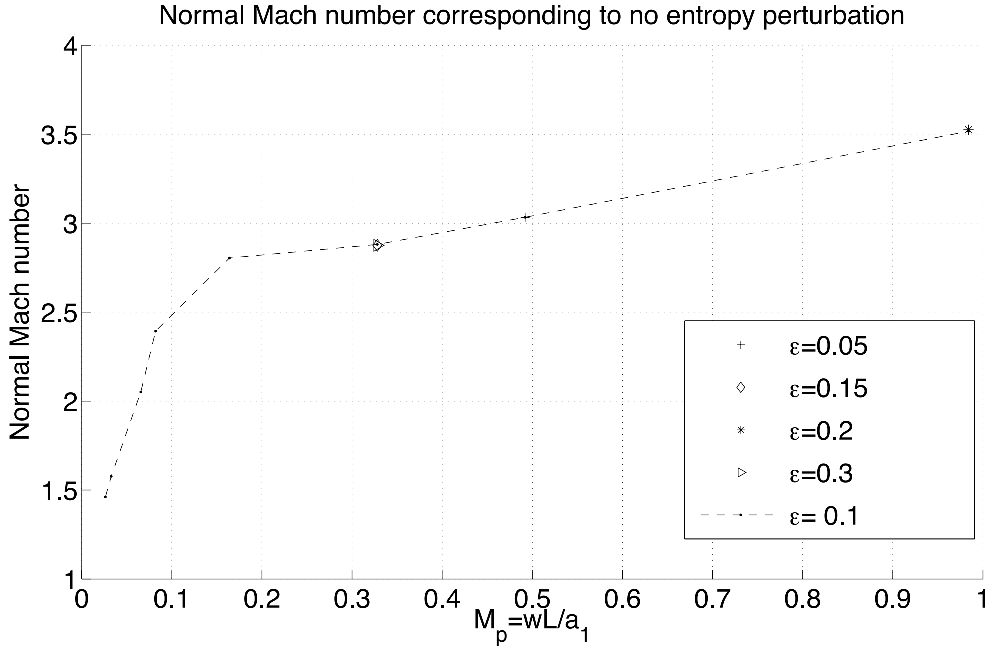

Figure 7.15. Location of transition from stable to unstable versus frequency and perturbation size.

7.3 High Mach limit

At high Mach numbers, the entropy flux perturbation goes to zero for upstream and downstream density perturbations. As shown in Figure 7.3 for upstream density perturbations, the entropy flux reaches a maximum negative value, and then unlike for the quasi-steady case, instead of becoming more negative, increases and crosses the horizontal axis again. When it crosses the horizontal axis again, the entropy flux is many orders of magnitude lower than the peak entropy flux perturbation and then decreases asymptotically to zero. Given the size and behavior of the entropy flux perturbation for high frequency upstream density perturbations at high normal Mach numbers, the positive entropy flux perturbation observed at higher normal Mach numbers is due to numerical error.

It is expected that the model would be inaccurate at higher normal Mach numbers and the entropy flux perturbation would go to zero as Mach number increases. This is because, when the density derivative, perturbation size, or frequency is zero, the equations for pressure ratio and downstream Mach number derived in Section 6 provide the same entropy jump, pressure ratio, and downstream Mach number as for a steady shock. This is the quasi-steady solution, where the shock is assumed stationary at each moment in time and the flow properties across the shock can be calculated with the steady shock equations. In the equations for pressure ratio and downstream Mach number, the perturbation appears either subtracted from or added to the normal Mach number or normal Mach number squared. If the ratio of the perturbation to normal Mach number $\frac{\varepsilon M_p}{M_{n,1}} <<< 1$, then according to the high frequency model, the high frequency perturbation will have no discernable effect on the properties of the flow across the shock and the entropy flux, so the quasi-steady approximation applies. However, it does not make physical sense that a high frequency perturbation would not affect the shock at high Mach numbers when the quasi-steady approximation predicted it would significantly decrease the entropy flux relative to the steady case. From the control volume approach, where

$$\partial(\rho u) = \frac{\partial V}{\partial t} d\rho + dV \frac{\partial \rho}{\partial t} \tag{128}$$

the first term dominated for high normal Mach numbers with the frequencies studied. This means that any relation of the entropy perturbation with respect to Mach number will include all three regimes at frequencies above the high frequency limit for lower normal Mach numbers. The region of normal Mach numbers somewhere between the minimum (most negative) entropy flux perturbation and the normal Mach number at which the entropy flux perturbation is a small negative value approximately equal to the second but essentially zero peak is an intermediate region where neither the shock movement nor the thermodynamic derivative terms dominate. Thus, the graphs presented in 7.3 and 7.12 contain all three frequency regimes--quasi-steady, intermediate region where a computational solution is required, and the high frequency regime.

7.4 Frequency and pseudo-Mach number limit at a given normal Mach number

This analysis suggests that as the normal Mach number increases, the frequency or pseudo-Mach number at which the high frequency limit applies increases. For example, while the high frequency model may adequately determine the entropy flux perturbation for a Mach 1.5 shock with a 10% density oscillation frequency of 1 kHz, the quasi-steady model will be needed to described whether this shock is stable to a upstream density perturbation at Mach 3 and what the entropy flux perturbation is. Figures 7.16 and 7.17 show a plot of the time-averaged entropy flux versus frequency for a 10% density perturbation at Mach 2.5.

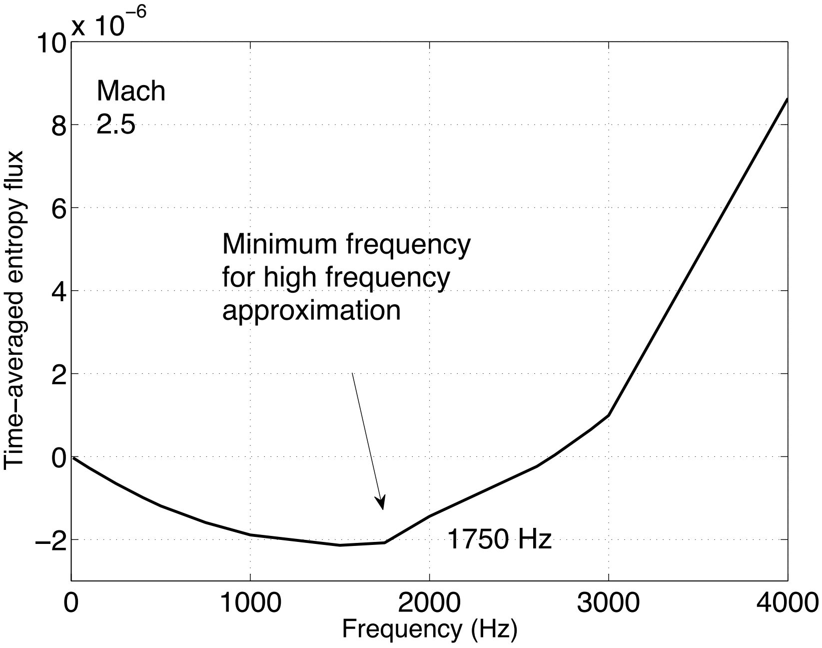

Figure 7.16. Time-averaged entropy flux versus frequency at Mach 2.5. The minimum frequency for the high frequency approximation is the maximum negative value or the function's minimum.

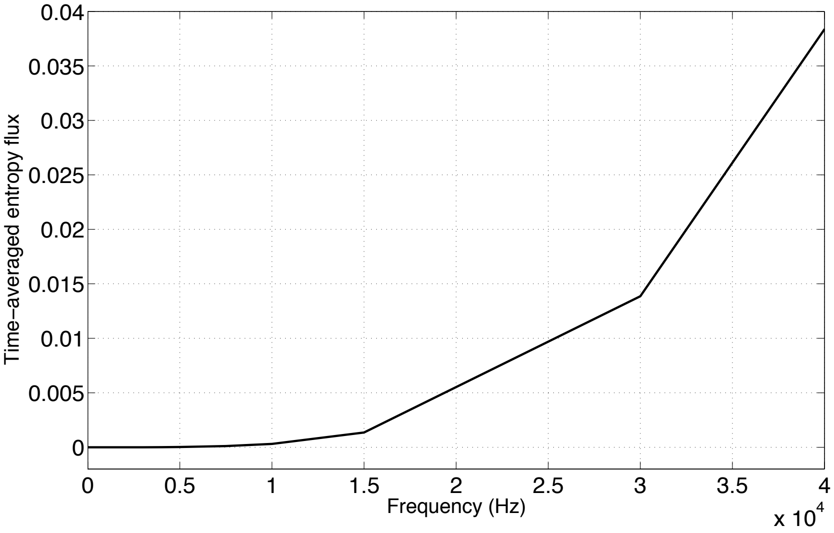

Figure 7.17 Time-averaged entropy flux versus frequency at Mach 2.5 from 10 Hz to 40 kHz.

The minimum or highest negative value occurs where the high frequency approximation is no longer valid. The full computational solution will be necessary at frequencies below this point until the thermodynamic density derivatives are very small compared to the shock velocity and the quasi-steady assumption holds. While the time-averaged entropy flux asymptotes to zero with this model, the quasi-steady limit can be approximated based on where the time-averaged entropy flux becomes small enough or is at least an order of magnitude smaller than its value at the minimum frequency at which the high frequency model still applies. This analysis for the two limits is consistent with the relation for normalized time-averaged entropy flux versus Mach number as shown in Figures 7.18 and 7.19 for a 10% density perturbation of at Mach 2 flow at 1 kHz. Figure 7.18 is a log-log plot of magnitude of the normalized time-averaged entropy flux versus frequency for Mach 2. On the log-log plot, the dip in the graph is when the entropy flux perturbation becomes positive.

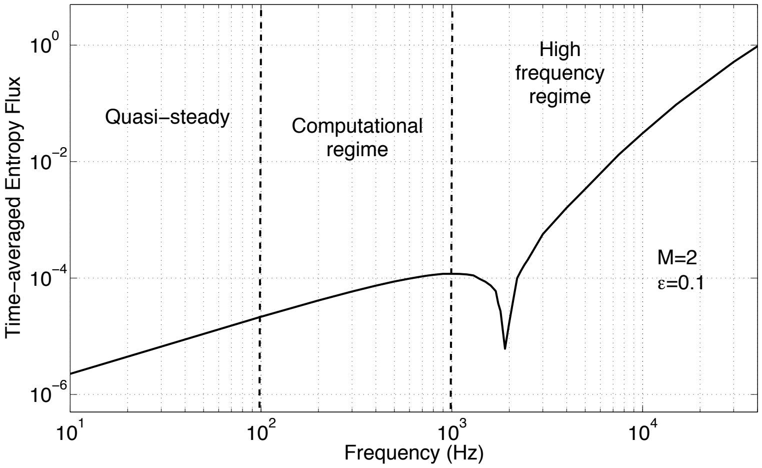

Figure 7.18. Log-log plot of magnitude of time-averaged entropy flux for Mach 2 flow with a 10% density perturbation. The maximum before the function goes through the zero is the high frequency limit.

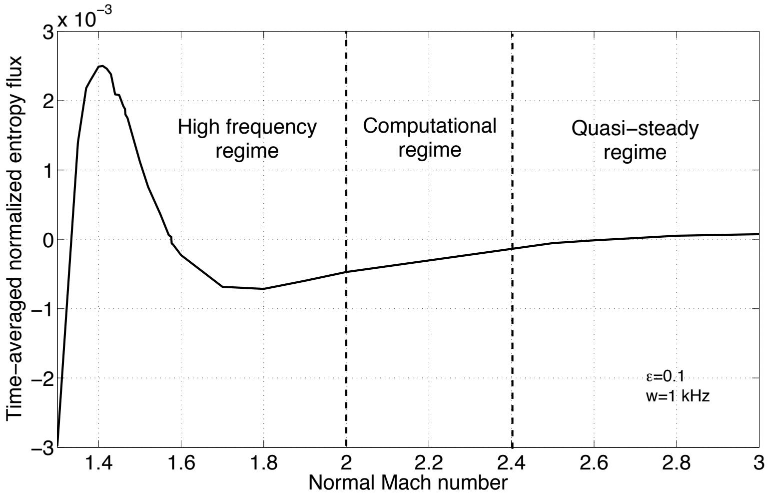

Figure 7.19. Plot of normalized time-averaged entropy flux for a 10% upstream density flux at 1 kHz and what regions might require a different treatment than the high frequency approximation.

Some care is required for finding the entropy flux for frequencies below the high frequency limit for Mach 1.5 at lower normal Mach numbers. As mentioned in Section 7.2, normal Mach numbers below 1.3 require a different method of time-averaging. Below 800 Hz for $\varepsilon = 0.1$ and 1.5 kHz for $\varepsilon = 0.05$, the entropy flux perturbation was negative or essentially zero for all normal Mach numbers. This is unlikely valid given that for quasi-steady and high frequency perturbations there is a region at lower normal Mach numbers where the entropy flux is positive and the shock should be stable to that type of perturbations. At frequencies just below this limit, such as 1.4 kHz for $\varepsilon = 0.05$ in Figure 7.20, the plots have the same shape but are below the horizontal axis and slightly distorted because the higher normal Mach numbers are going to have the same trend because the quasi-steady limit would apply. This error may be more because a different and more accurate calculation method is needed to determine the time-averaged entropy flux below at least Mach 1.3 and also because more terms in Equation 126 are needed and a fully computational solution is necessary to produce an adequate result. Also, as shown in Figure 7.20, the entropy flux perturbation for $\varepsilon = 0.1$ and 100 Hz using the high frequency method is nearly zero and also is a similar relation as that for the entropy flux with a downstream density perturbation. This suggests that the quasi-steady limit would apply for a upstream density perturbation at this frequency and of this size. This is consistent with the previous analysis on the quasi-steady limits.

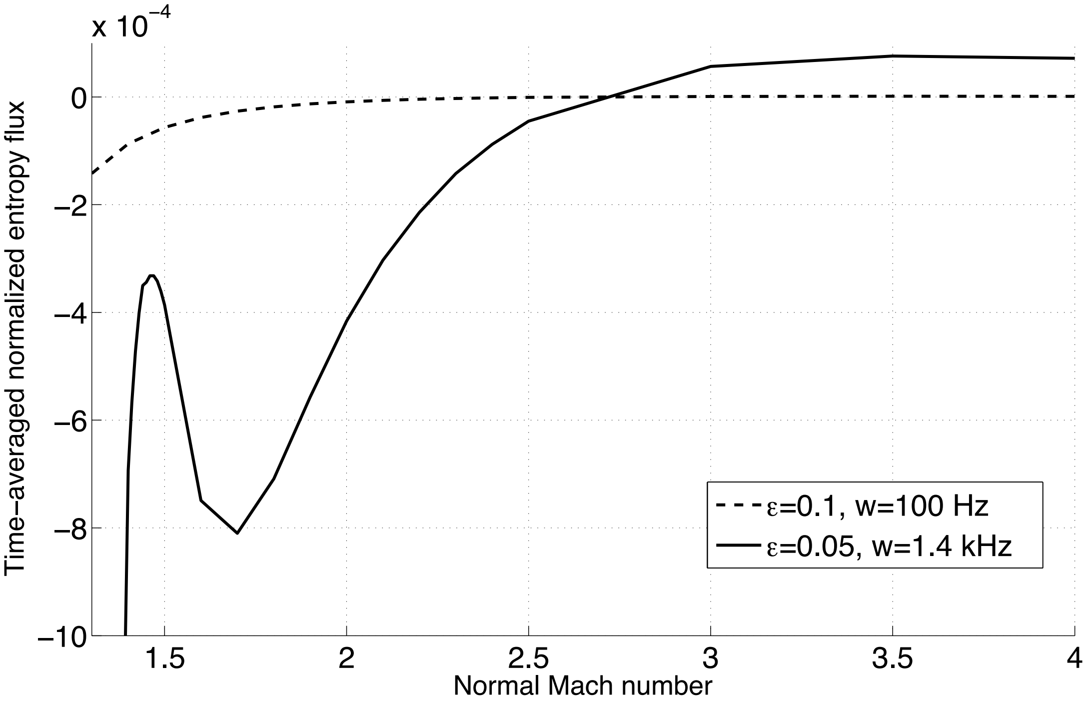

Figure 7.20. Invalid use of high frequency approximation and application of time-averaging method with lower frequencies.

As expected, the frequency or M_p required to use the high frequency approximation increases as normal Mach number increases. The relationship between normalized entropy flux perturbation and frequency is shown in Figure 7.21 for normal Mach numbers of M=1.5, 2, 2.5, 3.5, and 5 with a 10% upstream density perturbation. As the normal Mach number increases, the dip on the log-log plot of normalized entropy flux where the function reaches a minimum and trends back towards zero, crosses the horizontal axis, and turns back towards zero moves to the right towards high frequencies. For higher normal Mach numbers, the second dip at higher frequencies corresponds to where the entropy flux perturbation goes from positive (shock stable to upstream density perturbations) to negative (unstable). Figure 7.22 shows the same relationship but versus M_p instead of frequency.

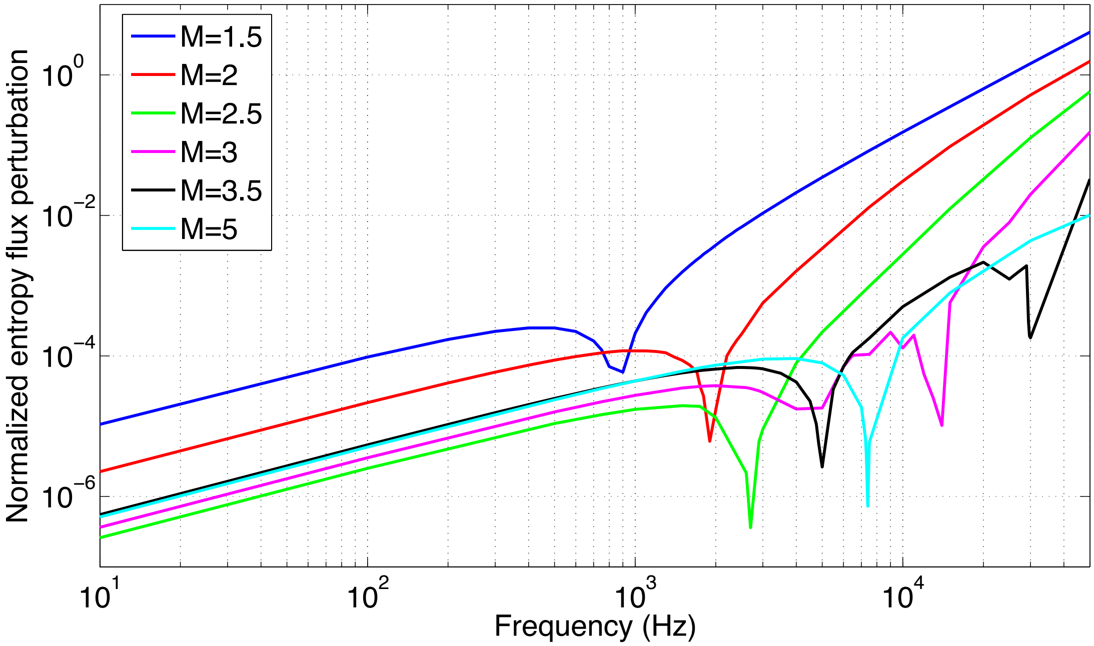

Figure 7.21 Time-averaged normalized entropy flux perturbation versus frequency at different normal Mach numbers for a 10% upstream density perturbation.

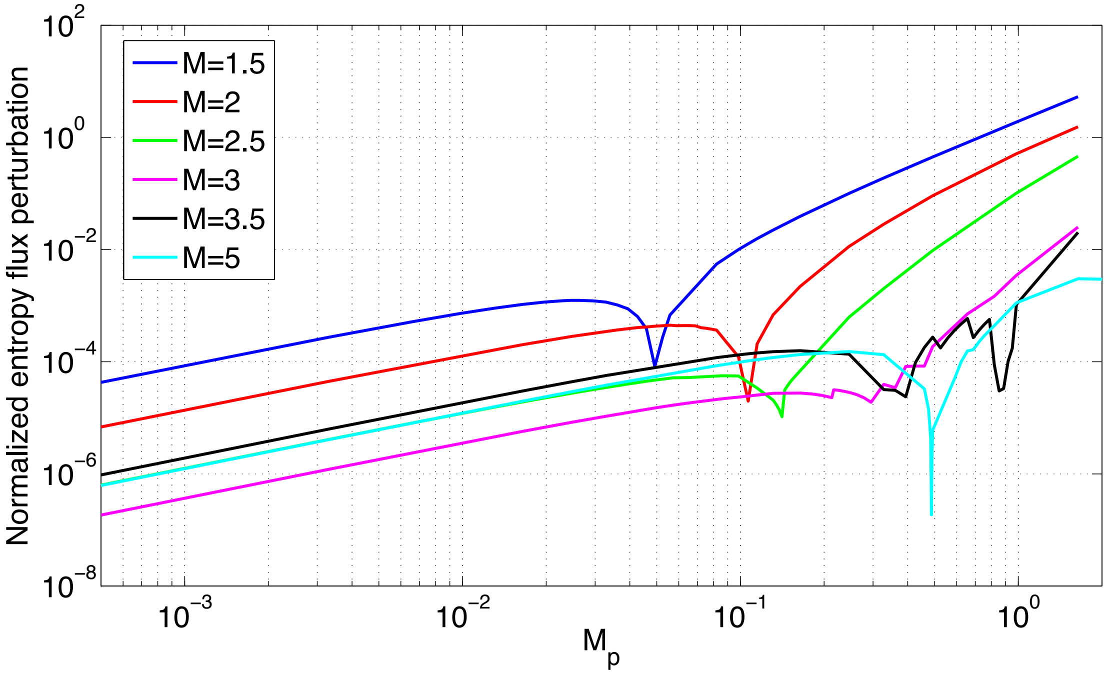

Figure 7.22. Time-averaged normalized entropy flux perturbation versus frequency at different normal Mach numbers for a 10% upstream density perturbation.

The minimum frequency for the high frequency approximation also depends inversely on the upstream density perturbation size. This is because M_p is always multiplied by $\frac{\varepsilon}{1+\varepsilon\sin(wt)}$. So it should be expected that as the perturbation size decreases, the required frequency should increase. Figure 7.23 shows the same relationship as Figure 7.21 and 7.22, but each plot for a different Mach number is shifted to the right towards higher frequencies. This is more clearly shown in Figure 7.24 where the normalized entropy flux perturbation is plotted against frequency at Mach 2 for perturbation sizes of 5%, 10% and 20% of upstream density. Finally, Table 7.2 provides the minimum frequencies for the high frequency approximation at upstream density perturbations of 0.5 and 0.1 and Mach numbers of 1.5, 2, 2.5, 3, 3.5, and 5.

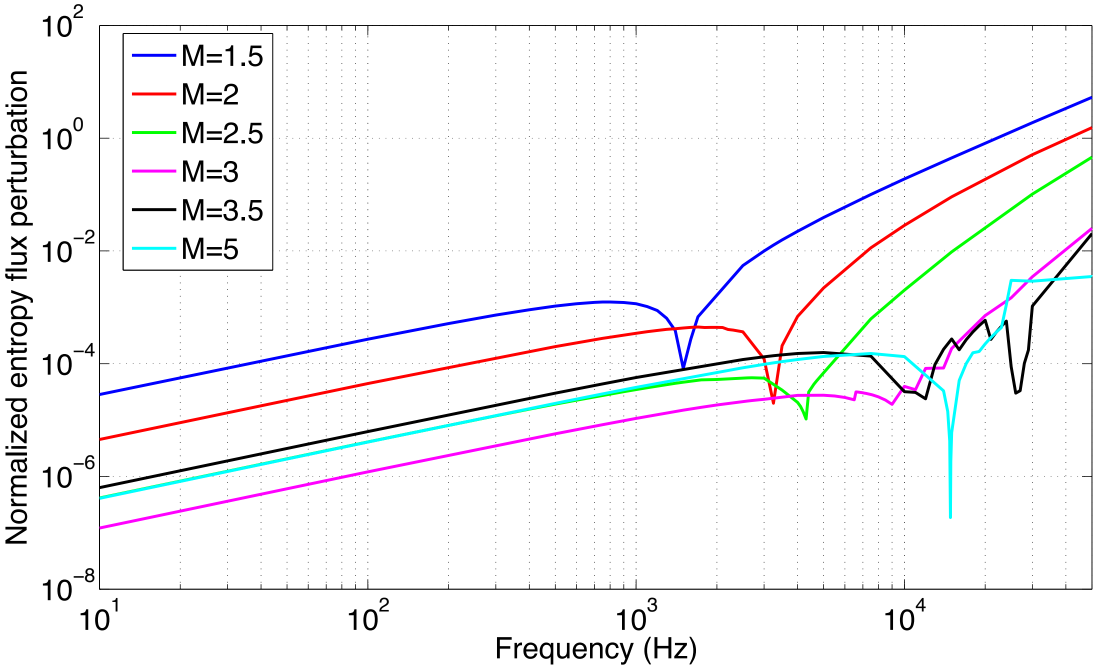

Figure 7.23. Normalized time-averaged entropy flux perturbation for 5% perturbation versus frequency at different normal Mach numbers.

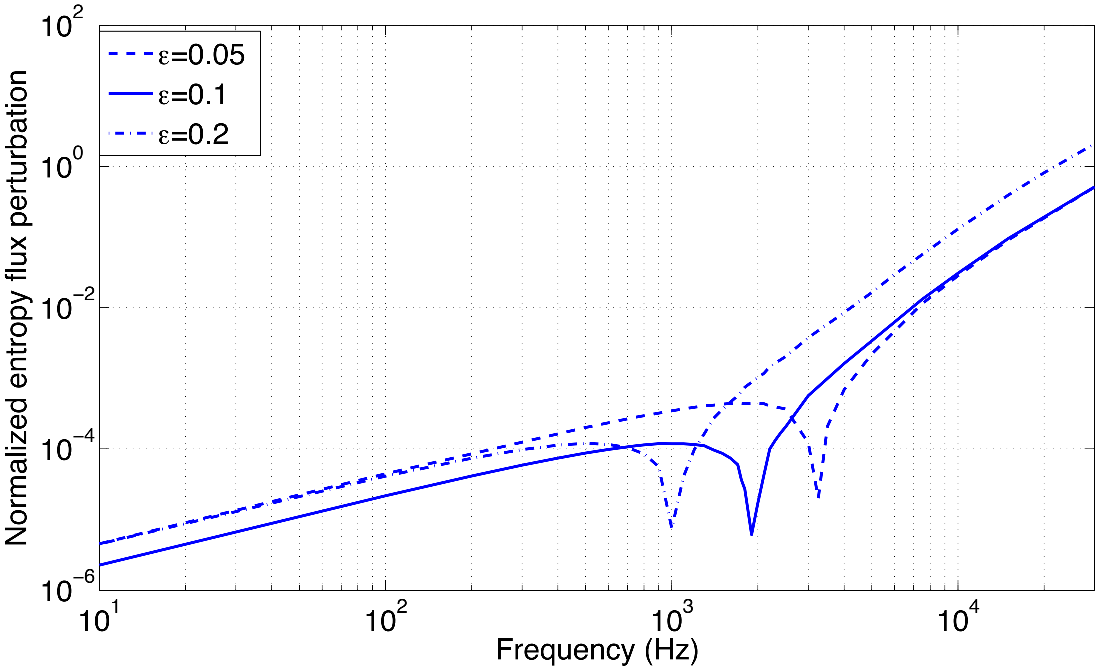

Figure 7.24. Normalized time-averaged entropy flux perturbation at Mach 2 versus frequency and perturbation size.

Perturbation size ε	**Normal Mach number** $M_{n,1}$	**Frequency (kHz)**	$\mathbf{M_p}$	$\frac{\varepsilon M_p}{M_{n,1}}$
0.2	2	0.5	0.0164	0.00082
0.1	1.5	0.8	0.0262	0.00175
0.1	2	1.0	0.0321	0.00164
0.1	2.5	1.75	0.0574	0.00229
0.1	3	6.3	0.2067	0.00688
0.1	3.5	6.3	0.2067	0.006
0.1	5	10.0	0.328	0.00656
0.05	1.5	1.5	0.0492	0.00164
0.05	2	2.0	0.0656	0.00164
0.05	2.5	2.6	0.0853	0.00170
0.05	3	6.6	0.2165	0.00361
0.05	3.5	16.0	0.5249	0.00750
0.05	5	19.0	0.6889	0.006888

Table 7.2 Minimum frequencies for high frequency limit at different perturbation sizes and normal Mach numbers

7.5 Perturbation size limit at a given normal Mach number

The validity of the high frequency approximation would also depend on the perturbation size for a given normal Mach number and frequency. However, as shown in table 7.3 and figure 7.25, this is only really applicable at lower frequencies and lower normal Mach numbers. At high enough frequencies (greater than 5 kHz), the high frequency limit applies for any size perturbation at lower normal Mach numbers. At Mach 2 and 1 kHz, this method found 10% as the minimum perturbation size, which is consistent with the finding of 1 kHz as the minimum frequency for Mach 2 with a 10% perturbation. 10% and 15% for Mach 2 and Mach 2.5 perturbations at 1 kHz is also consistent with the finding for the quasi-steady limit for perturbation size in Section 3. As figure 7.25 shows, as the frequency increases, the allowable perturbation size decreases. As Mach number increases, the minimum perturbation size also increases. The same method to determine the minimum frequency was used to determine the minimum perturbation size allowed for the high frequency approximation at a given normal Mach number.

Frequency (kHz)	**Normal Mach number** $M_{n,1}$	M_p	**Perturbation size** ε	$\frac{\varepsilon M_p}{M_{n,1}}$
1	1.5	0.0328	0.045	0.00098
1	2	0.0328	0.1	0.00164
1	2.5	0.0328	0.15	0.00197
5	1.5	0.164	0.0075	0.00082
5	2	0.164	0.015	0.00164
5	2.5	0.164	0.019	0.00025
5	3	0.164	0.15	0.00164
10	1.5	0.328	0.003	0.00066
10	2	0.328	0.003	0.00049
10	2.5	0.328	0.004	0.00052
10	3	0.328	0.035	0.00383

Table 7.3 Minimum perturbation sizes for high frequency limit at different frequencies and normal Mach numbers.

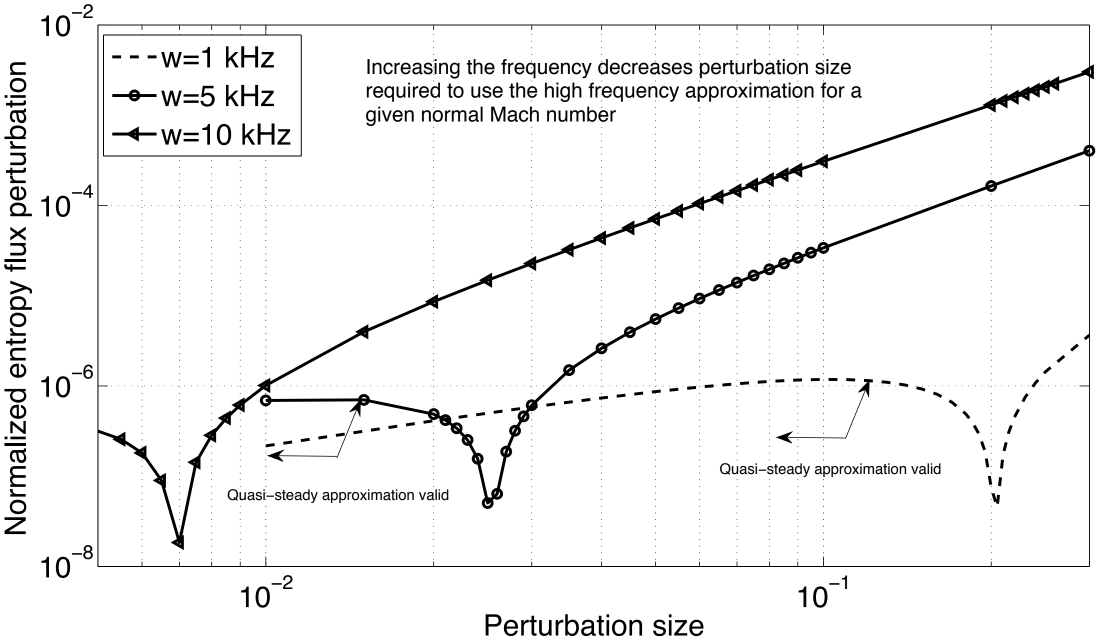

Figure 7.25. Time-averaged normalized entropy flux perturbation dependence on perturbation size at a given frequency for a Mach 2 shock.

At higher normal Mach numbers and frequencies at or above 5 kHz, perturbations below 10% generally did not produce consistent results. For perturbations below 0.1, instead of crossing the horizontal axis, the function never crossed but still had the same behavior of reaching a local minima, increasing to another near zero local maxima and then trending towards zero. This is shown in Figure 7.26 for a 0.5% perturbation at 5 kHz. This is most likely due to numerical error and is also consistent with the limits on the quasi-steady approximation of perturbations up to 10%. None of the frequencies examined above the high frequency limit had this issue for perturbation sizes above 10%.

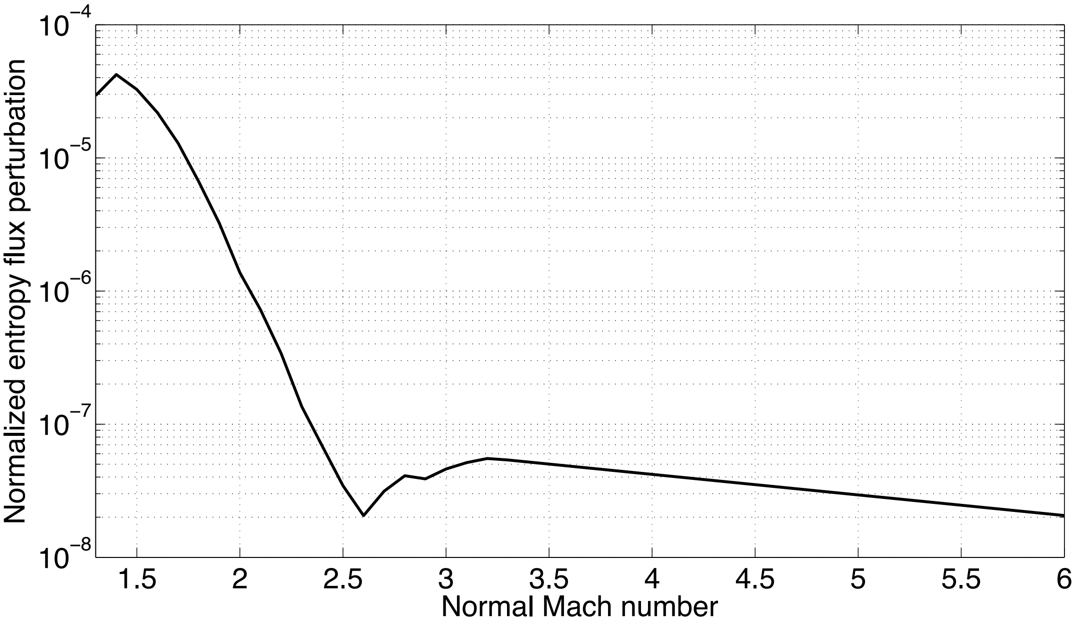

Figure 7.26. Plot of normalized time-averaged entropy flux perturbation for a 0.5% upstream density perturbation at 5 kHz.

Chapter 8. Conclusions and Summary

A method has been presented for analytically determining the unsteadiness in hypersonic inlets resulting from flow perturbations based on the principle of minimum entropy. Following this principle, if a perturbation applied to the flow results in a higher entropy increase across the shock than the unperturbed flow, then the shock would eventually revert back to its original steady state.

Analytic expressions were found for the entropy perturbation across the shock for a flow undergoing quasi-steady Mach number, angle, back pressure, and upstream thermodynamic variables perturbations. This entropy perturbation became negative, and thus the shock unstable at normal Mach numbers of 1.58, 2.19, and 1.25 for quasi-steady Mach number, back pressure, and upstream thermodynamic variables perturbations, respectively. Shock angle perturbations depend on freestream Mach number such that at Mach 5, the shock was unstable to perturbations at a normal Mach number of 1.63 and 1.75 for Mach 10. Based on this analysis, hypersonic inlets are more accommodating to quasi-steady back pressure changes than upstream perturbations. They are also more accommodating to orientation changes than speed changes. The figure below shows a Mach number and wedge angle map of where a shock in an inlet would be stable or unstable to these perturbations. These values indicate that shocks in inlets operating at hypersonic but not supersonic speeds may be stable to these types of perturbations.

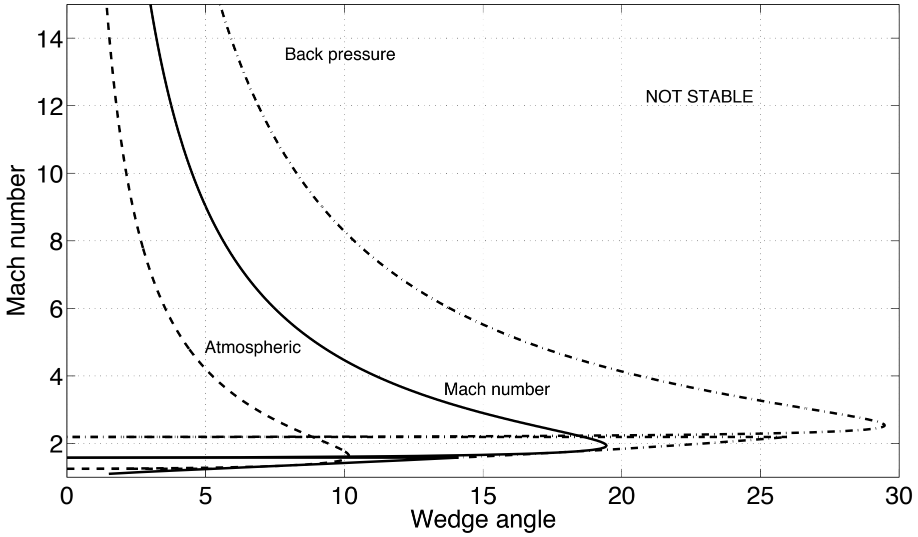

Figure 8.1. Angle and freestream Mach numbers at which the shock is stable to perturbations. Each line represents the normal Mach number at which the shock becomes unstable to perturbations. To the right, it is unstable.

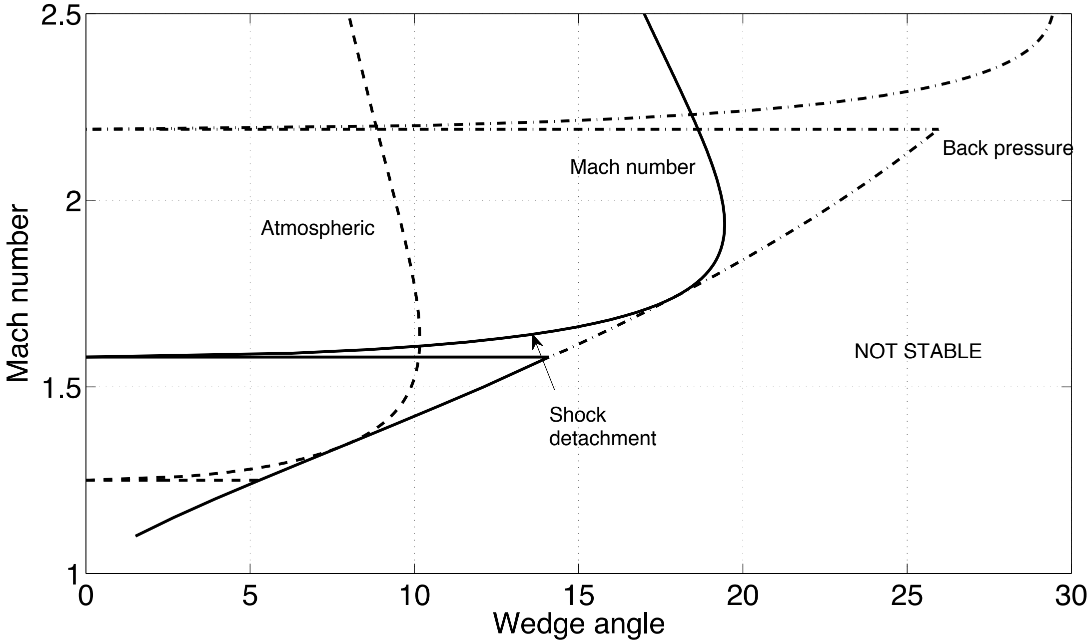

Figure 8.2. Zoom to shock detachment region. Below the freestream Mach number corresponding to the normal Mach number that the shock becomes unsteady to perturbations, all attached oblique shocks are stable to that perturbation.

A curved shock is less likely to be stable to perturbations than a comparable straight shock as defined in Chapter 3 as having the same mean pressure or temperature ratio or normal Mach number. Although a steady curved shock produces a higher entropy gain than a steady straight shock, a curved unsteady shock has a lower entropy gain or higher entropy decrease with respect to the steady shock than for an unsteady straight shock with the same average normal Mach number, shock angle, temperature ratio or pressure ratio. This is because the second derivative of the entropy perturbation is always negative for quasi-steady perturbations where the entropy perturbation is positive. Although the curved unsteady shock has a lower entropy gain than the unsteady straight shock for low normal Mach numbers, this might explain why an unsteady shock would settle to a steady straight shock rather than a curved straight shock when geometry permits either case, such as in a transmitted shock Type IV interaction. However, for a 3D curved inlet or shock, 3D effects would have to be considered, which was beyond the scope of this study.

Curved shocks constructed according to different parameters of interest were also compared to determine how sensitive different curved shocks were to certain perturbations. Shocks were constructed such that they had the same length and height and mean parameter of interest, such as pressure ratio, as a straight shock. Unsurprisingly, a shock designed to have a certain mean parameter such as pressure ratio was found to be generally more sensitive to perturbations in that parameter.

A primary contribution of this research is the development of a highly unsteady shock model. Because the above results only apply to the quasi-steady limit, a model was constructed for determining the flow downstream from a highly unsteady shock. This method was restricted to highly unsteady density perturbations on only one side of the shock. Although density perturbations were used, other perturbations more appropriate to inlets would produce qualitatively similar results. Only high frequency upstream density perturbations produced a positive entropy perturbation, suggesting that a shock is only stable to upstream but not downstream highly oscillatory or large density perturbations. For both types of perturbations, this has a significant dependence on the frequency or a pseudo-Mach number, which characterizes how much the shock moves, by increasing the range of normal Mach numbers at which the shock is stable if the frequency increases. For example, the shock may become unstable to a 30 kHz upstream 10% density perturbation at Mach 3.516 but if the frequency is 10 kHz, it would become unstable at Mach 2.880. Increasing the size of the density perturbation, decreased the normal Mach number at which the shock became unstable to perturbations by a few thousandths of a Mach number.

Limits for the validity of the upstream density perturbation were found to be consistent with our analysis of the quasi-steady limits and entropy perturbations and other numerical studies of these limits. For example, at a normal Mach number of M=1.5 and a 10% upstream density perturbation, the high frequency limit applies above 800 Hz. For a normal Mach number of M=5, the high frequency limits applies above 10 kHz. Analyzing the entropy perturbation for high frequency density oscillations will require more accurate numerical integration than used for normal Mach numbers under 1.3 and might not have physical solutions for normal Mach numbers under 1.2.

From this study, several guidelines for inlet construction were developed:

1. The flow in hypersonic inlets is likely most stable to unsteadiness in back pressure compared to unsteadiness in angle, speed, or upstream thermodynamic variables.

2. The flow in hypersonic inlets is likely more stable to unsteadiness in angle or orientation than speed.

3. Inlets with unsteadiness and with a small amount of curvature, defined as n=0.75 in this study, will still have an entropy gain over the steady case if the straight shock does.

4. Curved shocks with the same mean parameter as a straight shock are generally less stable to perturbations of that parameter.

5. No shocks are stable to high frequency downstream perturbations.

6. Stability to perturbations is sensitive to the ratio of specific heats only for downstream perturbations.

This work provides additional validation of the use of the principle of minimum entropy production for time-varying systems. In addition, this theory was applied specifically to shocks and in a problem applicable to hypersonic system design. An analogy was presented explaining a theoretical basis using piston theory for quasi-steady flows on which the principle of minimum entropy could be applied to time-varying shock systems. Experimental data from a wind tunnel run in AEDC's Tunnel 9 showed that a bow shock on a simple geometry became unsteady at the hypothesized normal Mach number, providing some initial validity to the use of the principle of minimum entropy to analyzing time-varying shock systems. This data suggests some value in exploring applying the principle of minimum entropy to other aerodynamics problems, especially if they involve time-varying systems or shocks.

Chapter 9. Future Work

This research presents several opportunities for future work. Although this study presented data that provides some initial experimental validation of the idea of using the principle of minimum entropy to determine unsteadiness as a result of perturbations, additional experiments could strengthen the validity of this application. Unsteadiness is difficult to test in wind tunnels because of tunnel noise, so additional validation could be provided if similar results are found in a quiet tunnel or another facility. Additional experimental data with more curved shapes, at different freestream Mach numbers, or with different perturbation types would be useful.

Several questions also arise that are beyond the scope of this paper. For instance, for the multi-shock system, does the principle of minimum entropy require examining each shock separately or does it require minimizing the entropy gain across the whole system? In a multi-shock system, having a minimum entropy gain across the first shock would result in a lower normal Mach number at the second shock. Then the entropy jump across the second shock might be higher at that lower normal Mach number, resulting in a higher entropy gain for the whole system. Intuitively, each shock should be treated separately, but effects can propagate upstream through a boundary layer, which couples the shocks. This question as well as shock-boundary layer interaction effects is worth further consideration.

A few topics related to specific inlet and perturbation types could also be explored. Exploration of three-dimensional effects for 3D inlets by experimentation or computational fluid dynamics could provide interesting results. Perturbations in the intermediate range could also be looked at with computational fluid dynamics to bridge the gap between the quasi-steady and highly unsteady results. Also, it might be worthwhile to develop a high frequency model for pressure or Mach number perturbations and see if the trends for the entropy gain perturbation are the same as for quasi-steady or the high frequency density perturbations. However, the ultimate goal of this type of future work is to come up with inlets with stable shock solutions.

Appendices

A. Inlet performance parameters

The parameters typically used to evaluate the performance of scramjet inlets are static temperature ratio ψ, total pressure recovery π_c, kinetic energy efficiency η_{KE}, and adiabatic compression efficiency η_c. These are defined below[76]:

$$\psi = \frac{T_{throat}}{T_\infty} = \left[\frac{1+\frac{\gamma-1}{2}M_{throat}^2}{1+\frac{\gamma-1}{2}M_\infty^2}\right] \tag{1}$$

Because the compression procession is adiabatic, total temperature is conserved.

$$\pi_c = \frac{P_{0,throat}}{P_{0,\infty}} = \frac{P_{throat}}{P_\infty}\left[\frac{1+\frac{\gamma-1}{2}M_{throat}^2}{1+\frac{\gamma-1}{2}M_\infty^2}\right] \tag{2}$$

$$\eta_c = \frac{\psi - \left(\frac{1}{\pi_c}\right)^{\frac{\gamma}{1-\gamma}}}{\psi - 1} \tag{3}$$

Adiabatic compression efficiency is the ratio of the change in static enthalpy to the ideal, isentropic change in static enthalpy. The dependence of adiabatic compression efficiency on total pressure ratio is such that even a modest decrease in adiabatic compression results in a large decrease in total pressure. This is partially why the total pressure ratio is not always the best figure of merit for determining performance of scramjets. This can be determined knowing the total pressure recovery and static temperature ratio ψ

$$\eta_{KE} = 1 - \frac{2}{(\gamma-1)\overline{M}_{\infty}^{2}}\left[\left(\frac{1}{\pi_c}\right)^{\frac{\gamma-1}{\gamma}} - 1\right] \tag{4}$$

Kinetic energy efficiency is defined as the ratio of the square of the velocity that the exit flow would have if it were isentropically expanded to the freestream pressure to the square of the freestream velocity. Because of the high velocities in hypersonic flow, large changes in adiabatic compression efficiency result in only modest changes in kinetic energy efficiency. Kinetic energy efficiency needs to be calculated to three decimal places in order to be accurate.

B. High frequency perturbation code

```
%This is the program to compute the properties across a
highly oscillatory
%shock for changes in the density ratio caused by changes
upstream or
%downstream.
%
%
%
%M=input('Enter Mach number:  ');
flag=input('Enter 1 for dr1dt=0 or Enter 2 for dr2dt=0:'
);
w=input('Frequency:  ');
e=input('Epsilon:  ');
%n=input('Index:  ');

MachN=1.3:.05:3.5;
for j=1:length(MachN)
    M=MachN(j);

g=1.4;          %Ratio of specific heats
R=287.058;      %Real gas constant
T=231.24;       %Temperature at 30 km
V=1*10^(-2);    %Shock movement distance
a1=sqrt(g*R*T); %Speed of sound
```

```
tf=pi/w;
tstep=tf/100;
t=[-2*tf:tstep:2*tf];
roe1=1.7861*10^(-2);     %Atmospheric density at 30 km
P1=roe1*R*T;             %Atmospheric pressure at 30 km
roe2roe1=((g+1).*M.^2)./(2+(g-1).*M.^2); %Steady density
ratio across shock
roe2=roe1*roe2roe1*(1+e*sin(w*t));  %Downstream density
roe2s=roe1*roe2roe1;  %Steady downstream density

P2P1s=1+(2*g)/(g+1).*(M.^2-1); %Steady pressure ratio
steadySR=(log((P2P1s).^(1/(g-1)))+log((roe2roe1).^(-g/(g-
1)))); %Steady entropy gain

top=P2P1s+.7;  %Search limits for root finder
bottom=P2P1s-.7;
z=[];
y=[];

if(flag==1)
    droedt=e*w*cos(w*t)*roe2s;
    X=V./(a1*roe2).*droedt;
for i=1:length(X)
Dir=X(i);
z(i)=fzero(@(P) gilliansolver(P,M,Dir,g),[bottom top]);
end
L=[];

M2=sqrt(1./z.*(M+(1-z)./(g*M)).^2.*(M./(M+(1-z)/(g*M)-
X)));
M2p=M+(1-z)/(g*M);
r2r1=M./(M2p-X);
roe1t=roe1;

P2P1s=1+(2*g)/(g+1).*(M.^2-1);
deltasR=(log((z).^(1/(g-1)))+log((r2r1).^(-g/(g-1))));
%Unsteady entropy gain
steadySR=(log((P2P1s).^(1/(g-1)))+log((roe2roe1).^(-g/(g-
1))));
pusteadySR=steadySR.*roe1.*M.*a1; %Steady entropy flux
pudeltasR=roe1t.*M.*a1.*deltasR; %Unsteady entropy flux

%droe2/dt=0

else

    droedt=e*w*cos(w*t)*roe1;
    X=V./(a1*roe1*(1+e*sin(w*t))).*droedt;
```

```
    droe2dt=e*w*cos(w*t)*roe2s;
for i=1:length(X)
Dir=X(i);
z(i)=fzero(@(P) gilliansolver3(P,M,Dir,g),[bottom top]);
end
%k=fzero(fun1,1)
L=[];

%For droe2/dt=0
M2=sqrt(1./z.*(M+(1-z)./(g*(M-X))).^2.*((M-X)./(M+(1-
z)/(g*(M-X))-X)));
M2p=M+(1-z)/(g*(M-X));
r2r1=(M-X)./(M2p);
roe1t=roe1*((1+e*sin(w*t)));

P2P1s=1+(2*g)/(g+1).*(M.^2-1);
deltasR=(log((z).^(1/(g-1)))+log((r2r1).^(-g/(g-1))));
steadySR=(log((P2P1s).^(1/(g-1)))+log((roe2roe1).^(-g/(g-
1))));
pusteadySR=steadySR.*roe1.*M.*a1;
pudeltasR=roe1t.*M.*a1.*deltasR;

a=[-2*tf:tstep:2*tf-tstep];
roe2a=roe1*roe2roe1*(1+e*sin(w*a));
i=diff(deltasR)./tstep.*roe2a;
i=[roe2a.*diff(deltasR)./tstep, i(1,1)];

A(1,j)=mean(pudeltasR);
A(2,j)=max(pudeltasR)-pusteadySR-(pusteadySR-
min(pudeltasR));
%A(3,i)=e;
A(3,j)=M;
A(4,j)=pusteadySR;

end

end

function output=gilliansolver(P,M,Dir,g)
M12=M+(1-P)/(g*M);
M22=1/P*(M+(1-P)/(g*M))^2*(M/(M+(1-P)/(g*M)-Dir));
output=M*(1+((g-1)/2)*M^2)./((M12-Dir)*(1+((g-1)/2)*M22)-
(g-1)/g*Dir)-P;
end


function output=gilliansolver3(P,M,Dir,g)
M12=M+(1-P)/(g*(M-Dir));
```

```
M22=1/P*(M+(1-P)/(g*(M-Dir)))^2*((M-Dir)/(M+(1-P)/(g*(M-Dir))));
output=((M-Dir)*(1+((g-1)/2)*M^2)+(g-1)/g*Dir)./((M12)*(1+((g-1)/2)*M22))-P;
end
```

Bibliography

1. Prigogine, I. *Introduction to Thermodynamics of Irreversible Processes.* Charles C. Thomas, Springfield, 1955, Chapter 6.

2. de Groot, S.R. and Mazur, P. *Non-Equilibrium Thermodynamics.* Dover Publications, Inc., N.Y., 1984. Chs. 4-9.

3. Horne, Clifton W., Charles A. Smith, and Krishnamurty Karamcheti. "Aeroacoustic and Aerodynamic Applications of the Theory of Nonequilibrium Thermodynamics." *NASA Technical Paper 3118.* 1991.

4. Prigogine, I. *From Being to Becoming.* W.H. Freeman and Co, 1980.

5. Ziegler, H. *An Introduction to Thermomechanics.* North-Holland, 1983, pp 253-269.

6. De Donder, Th. *L'Affinite*. Paris, Gauthier-Villars. 1928.

7. Donnelly, R. J., Hermann, R. and Prigogine, I. Non-Equilibium Thermodynamics: Variational Techniques and Stability. University of Chicago Press, Chicago, 1965.

8. Meijer, Paul H.E., and Edwards, John C. "Modification of the Minimum-Entropy-Production Principle" *Physical Review A,* Vol 1., pp 1527.

9. Tadmor, Eitan. "A Minimum Entropy PRinciple in the Gas Dynamics Equations." NASA-CR-178123, 1986.

10. Biot, M., A. "New Variational-Lagrangian Irrerversible Ther- modynamics with Applications to Viscous Flow, Reaction-Dif- fusion, and Solid Mechanics." Advances in AppliedMechanics, vol. 24, 1984, Academic Press, Inc. N.Y., pp. 1-91.

11. Kiss, Endre. "On the Principle of Minimum Entropy Production in Quasilinear Case and Its Connection to Statistical Mechanics" *Periodica Polytechnica, Chemical Engineering.* Vol 41, No. 2, 1997, pp 205-211.

12. Borovkov, I. S. "Principle of minimum entropy-production". *Inzhenerno-Fizicheskii Zhurnal*, Vol. 35, 1978, pp. 531-539

13. Bartelt, P., and Buser, O., "The principle of minimum entropy production and snow structure." *Journal Of Glaciology,* Vol 50,2005, pp. 342-352.

14. Andriesse, C.D. and M.J. Hollestelle. "Minimum entropy production in photosynethesis." *Biophysical Chemistry.* Vol. 90, 2001, pp. 249-253.

15. Henderson, L.F. and Atkinson, J.D., "Multi-Valued Solutions of Steady-State Supersonic Flow. Part 1. Linear Analysis," *Journal of Fluid Mechanics,* Vol. 75, Pt.4, 1976, pp. 751-764.

16. Batchelor, G. K., *An Introduction to Fluid Dynamics*. Cambridge University Press, 1973, pp. 227-228.

17. Horne, W., Smith, C., & Karamcheti, K. "Aeroacoustic and aerodynamic applications of the theory of nonequilibrium thermodynamics".NASA-TP-3118; A-90084; NAS 1.60:3118).Washington, 1991.

18. Horne, W.C., and Karamcheti, K. "Extreme Principles of Entropy Production and Energy Dissipation in Fluid Mechanics.," *AIAA 88-3830*. 1988.

19. Shi, S., and Zhou, M. "The application of minimum entropy generation principle to the thermodynamics in fluid mechanics." *Acta Aerodynamica Sinica*, Vol. 7, 1989, pp. 112-116.

20. Kalugin, V. T. "Entropy method for calculating the parameters of separated flows." *Rossijskaya Akademiya Nauk, Izvestiya, Mekhanika Zhidkosti i Gaza,* Vol 1, 1997, pp. 122-132.

21. Carrier, G.F., "On Stability of the Supersonic Flows Past a Wedge," *Quarterly of Applied Mathematics,* Vol. 6, 1949, pp. 367-378.

22. Salas, M.D., and Morgan, B.D., "Stability of Shock Waves Attached to Wedges and Cones," *AIAA Journal,* Vol. 21, No. 12, 1983, pp. 1611-1617.

23. Salas, Manuel D. "Shock Wave Interaction with an Abrupt Area Change." NASA Technical Paper 3113, 1991.

24. Li, H. and Ben-Dor, G., "Applications of the Principle of Minimum Entropy Production to Shock Wave Reflections. Part 1. Steady Flows," Journal of Applied Physics, Vol. 80, No. 4, 1996, pp. 2027-2037.

25. Li, H. and Ben-Dor, G., "Applications of the Principle of Minimum Entropy Production to Shock Wave Reflections. Part II. Pseudo-steady Flows," Journal of Applied Physics, Vol. 80, No. 4, 1996, pp. 2038-2048.

26. Oppenheim, A. K., Urtiew, P.A., and Stern, R. A., "Pecularity of Shock Impingement on Area Convergence." *Phys. Fluids,* vol. 2, no. 4, 1959. pp. 437-431.

27. Courant, R. and K.O. Friedrichs. Supersonic Flow and Shock Waves. Interscience, New York, 1948.

28. A. Chpoun, D. Passerel, H. Li, and G. Ben-Dor. "Reconsideration of oblique shock wave reflections in steady flows. Part 1. Experimental investigation," *Journal of Fluid Mechanics,* Vol. 301, 1995. pp. 19-35.

29. Vuillon, J., Zeitoun, D. and Ben-Dor, G. "Reconsideration of oblique shock wave reflections in steady flows. Part 2. Numerical investigation." *Journal Fluid Mechanics,* Vol. 301, 1995. pp. 37-50.

30. Syshchikova, M.P. and Krassovskaia, I.V. "Some properties of regular and irregular interaction of shock waves." *Archiwum Mechnaiki Stosowanej,* Vol. 31, No. 1, pp. 135-145. 1979.

31. K. Takayama and G. Ben-Dor, "State-of-the-art in research on Mach reflection of shock waves." *Sadhana*, Vol. 18, No. 3-4, 1993. pp 695-710.

32. Lewis, M.J. and K.A. Smith. "Time-Averaged Entropy and Total Pressure Ratios Across Unsteady Inlet Shock Waves" Journal of Propulsion and Power, Vol. 21, No.6, 2005, pp. 997-1007.

33. Lewis, M.J., "Designing Hypersonic Inlets for Bow Shock Location Control," Journal of Propulsion and Power, Vol. 9, No. 2, 1993, pp.313-321

34. Lind, C., and Lewis, M.J., "Unsteady Characteristics of a Hypersonic Type IV Shock Interaction, " Journal of Aircraft, Vol. 32, No.6, 1995, pp. 1286-1293.

35. Holden, M.S., Weiting, A.R., Moselle, J.R., and Glass, C., "Studies of Aerothermal Loads Generated in Regions of Shock/Shock Interaction in Hypersonic Flow." AIAA 88-0477, January 1988.

36. Weiting, A.R., "Experimental Study of Shock Waves Interference Heating on a Cylindrical Leading Edge." PhD Dissertation, Old Dominion University, 1987; also NASA TM-100484, May 1987.

37. Edney, B., "Anomalous Heat Transfer and Pressure Distributions on Blunt Bodies at Hypersonic Speeds in the Presence of an Impinging Shock, " FFA Report 115, Aeronautical Research Institute of Sweden, 1968.

38. Keyes, J.W. and Hains, F.D., "Analytical and Experimental Studies of Shock Interference Heating in Hypersonic Flow," NASA Report TN D-7139, May 1973.

39. Lind, Charles A. and Lewis, Mark J. "The Effect of Shock/Shock Interactions on the Design of Hypersonic Inlets," AIAA-1990-2217, July 1990.

40. Prabhu, R. K., Stewart, J.R., and Thareja, R. R., "Shock Interference Studies on a Circular Cylinder at Mach 16," AIAA Paper 90-0606, January 1990.

41. Klopfer. G.H. and Yee, H.C., "Viscous Hypersonic Shock-on-Shock Interaction on Blunt Cowl Lips." AIAA Paper 88-0233, January 1988

42. Lind, C.A., "A Computational Analysis of the Unsteady Phenomena Associated with a Hypersonic Type IV Shock Interaction." Ph.D. Dissertation, Department of Aerospace Engineering, University of Maryland, College Park, MD. 1994.

43. Lind, C.A., and Lewis, Mark J. "A Numerical Study of the Unsteady Processes Associated with the Type IV Shock Interaction," AIAA Paper 93-2479, June 1993.

44. Lewis, M.J., "Designing Hypersonic Inlets for Bow Shock Location Control," *Journal of Propulsion and Power,* Vol. 9, No. 2, 1993, pp.313-321

45. Lewis, M.J., Surline, Y., and Anderson, J.D., "Analytical and Computational Study of Unsteady Shock Motion on Hypersonic Forebodies," *Journal of Aircraft,* Vol. 28, No. 8, 1991, pp. 532-539.

46. Lewis, M.J., and Hastings, D.E., "Bow Shock Matching with Viscous Effects on Hypersonic Forebodies," AIAA Paper 89-2678, July 1989.

47. Ng, W.F., and Epstein, A.H., "Unsteady Losses in Transonic Compressors," *Journal of Engineering for Gas Turbines and Power,* Vol.107, No.2, 1985. pp. 345-353

48. Handa, T., Masuda, M., and Matsuo, K., “Mechanism of Shock Wave Oscillation in Transonic Diffusers,” AIAA Journal, Vol. 41, No. 1, 2003, pp. 64–70.

49. Berthouze, P., and Bur, R., “Experimental Investigation of the Response of a Transonic Shock-Wave to Downstream Perturbations,” AIAA Paper 2001-3295, July 2001.

50. Bogar, T. J., Sajben, M., and Kroutil, J. C., “Characteristic Frequencies of Transonic Diffuser Flow Oscillations,” AIAA Journal, Vol. 21, No. 9, 1983, pp. 1232–1240.

51. Mullagiri, S., Segal, C., and Hubner, P. J., “Oscillating Flows in a Model Pulse Detonation Engine Inlet,” AIAA Journal, Vol. 41, No. 2, 2003, pp. 324–326.

52. Mullagiri, S., and Segal, C., “Oscillating Flows in Inlets of Pulse Det- onation Engines,” AIAA Paper 2001-0669, Jan. 2001.

53. Nori, V., Lerma, N., and Segal, C., “Oscillatings Flows in Inlets for Pulsed Detonation Engines,” AIAA Paper 2003-886, Jan. 2003.

54. Gustavsson, J., Nori, V., and Segal, C., “Inlet/Engine Interactions in an Axisymmetric Pulse Detonation Engine System,” Journal of Propulsion and Power, Vol. 19, No. 2, 2003, pp. 282–286.

55. Culick, F. E. C., and Rogers, T., “The Response of Normal Shocks in Diffusers,” AIAA Journal, Vol. 21, No. 10, 1983, pp. 1382–1390.

56. Smart, M.K., and Suraweera, M.V., "HIFiRE 7 - Development of a 3-D Scramjet for Flight Testing," AIAA Paper 2009-7259, 2009.

57. Siebenhaar, A. and Bogar, T.J. “The Impact of Round Combustors on TBCC Propulsion and Hypersonic Cruise Vehicles, “ AIAA Paper 2006-7986, Nov. 2006.

58. Busemann, A. “Die achsensymmetrische kegeligeUebershallstromung,” Luftfahrforschung 19, 137-144 (1942).

59. Molder, Sannu and Szpiro, Edward J. “Busemann Inlet for Hypersonic Speeds.” *Journal of Spacecraft and Rockets.* Vol. 3, mo.8 Aug 1966. pp 1303-1304.

60. Van Wie, David and Molder, Sannu. “Applications of Busemann Inlet Designs for Flight at Hypersonic Speeds,” AIAA Paper 22-1210. Feb 1992.

61. Kantrowitz, A. and Donaldson, C., “Preliminary Investigation of Supersonic Diffusers,” NACA ACR L5D20, May 1945.

62. Billig, Frederick and Kothari, Ajay P. “Streamline Tracing: Technique for Designing Hypersonic Vehicles.” *Journal of Propulsion and Power,* Vol 16, No.3, May – June 2000.

63. Drayna, Travis W., Nompelis, Ioannis, and Candler, Graham V. “Hypersonic Inward Turning Inlets: Design and Optimization”

64. M.K. Smart, “Design of Three-Dimensional Hypersonic Inlets with Rectangular-to- Elliptical Shape Transition.” *Journal of Propulsion and Power.* Vol. 15, No.3 May- June 1999.

65. M.K. Smart, “Design of Three-Dimensional Hypersonic Inlets with Rectangular-to- Elliptical Shape Transition, “ AIAA-1998-960-848, 1997.

66. Smart, M.K. “Experimental Testing of a Hypersonic Inlet with a Rectangular-to-Elliptical Shape Transition.” AIAA Aerospace Sciences Meeting and Exhibit, January 1999.

67. Bussey, G.H., *Application of Compound Compressible Flow to Hypersonic Three-Dimensional Inlets*. Master's Thesis, University of Maryland Department of Aerospace Engineering, 2009.

68. Bussey, Gillian H. and Mark J. Lewis, "Application of Compound Compressible Flow to Hypersonic Three-Dimensional Inlets. " AIAA-2009-7403, 16th AIAA/DLR/DGLR International Space Planes and Hypersonic Systems and Technologies Conference, October 2009.

69. Ng, W. *Time Resolved Measurements in a Transonic Compressor Stage.* Phd thesis, MIT Department of Mechanical Engineering, 1983.

70. Liepmann, H.W. and Roshko, A. *Elements of Gas Dynamics*. Dover Publications, New York, 2001.pp 91, 212-215.

71. Rasmussen, Maurice. *Hypersonic Flow.* John Wiley & Sons, Inc., New York, 1994. Chapter 7.

72. Hayes, W.D. and Probstein, R.F., *Hypersonic Flow Theory,* Academic Press, New York, 1959.

73. Anderson, J.D., *Hypersonic and High-Temperature Gas Dynamics, 2nd Edition.* AIAA, Reston, Virginia, 2006. Chapter 4.

74. Shapiro, Asner. The Dynamics and Thermodynamics of Compressible Fluid Flow. Ronald Press, New York. 1953. Ch. 8.

75. Marineau, Eric C. and Hans G. Hornung, "Study of Bow-Shock Wave Unsteadiness in Hypervelocity Flow from Reservoir Fluctuations." *AIAA-201-0382-165,* 48th AIAA Aerospace Sciences Meeting, Orlando, Florida, January 4-7 2010.

76. Heiser, W.H. and Pratt, D. T. *"Hypersonic Airbreathing Propulsion."* American Institute of Aeronautics and Astronautics, 1994.

77. Christopher E. Glass, "Numerical Simulation of Low-Density Shock-Wave Interactions." NASA TM 1999 209358, July 1999.

78. http://www.arnold.af.mil/library/factsheets/factsheet.asp?id=13884

79. Bussey, Gillian H. and Mark J. Lewis, "Application of Compound Compressible Flow to a Boundary Layer in a Hypersonic Three-Dimensional Inlet." AIAA-2007-74, 49th AIAA Aerospace Sciences Meeting including the New Horizons Forum and Aerospace, January 2011.

80. Bussey, Gillian H. and Mark J. Lewis, "Comparison of Stability of Hypersonic Rectangular and Three-Dimensional Inlets to Unsteady Perturbations Using Entropy

Considerations." AIAA-2011-3363, 29th AIAA Applied Aerodynamics Conference, June 2011.

81. Bussey, Gillian H. and Mark J. Lewis, "Principle of Minimum Entropy Analysis Applied to Unsteady Flow in Three-Dimensional Hypersonic Inlets." 17th AIAA International Space Planes and Hypersonic Systems and Technologies Conference, April 2011.

82. Bussey, Gillian H. and Mark J. Lewis, "Analysis of Highly Unsteady and Quasi-steady Shocks in Hypersonic Inlets Based on the Principle of Minimum Entropy." AIAA-2012-5938, 18th AIAA/3AF International Space Planes and Hypersonic Systems and Technologies Conference. September 2012.